annual progress

HEAVY VEHICLE PROPULSION MATERIALS

FreedomCAR and Vehicle Technologies Program

Less dependence on foreign oil today, and transition to a petroleum-free, emissions-free vehicle tomorrow.

U.S. Department of Energy
Energy Efficiency and Renewable Energy
Bringing you a prosperous future where energy is clean, abundant, reliable, and affordable

FreedomCAR & Fuel Partnership

21st CENTURY TRUCK PARTNERSHIP

U.S. Department of Energy
Office of FreedomCAR and Vehicle Technologies
1000 Independence Avenue S.W.
Washington, DC 20585-0121

FY 2006

Progress Report for Heavy Vehicle Propulsion Materials

Energy Efficiency and Renewable Energy
Office of FreedomCAR and Vehicle Technologies
Advanced Materials Technologies

Edward J. Wall **Program Manager, OFCVT**
Rogelio A. Sullivan **Advanced Materials Technologies Team Leader**
Jerry L. Gibbs **Technology Development Manager**

January 2007

CONTENTS

1. INTRODUCTION..... 1

2. MATERIALS FOR ADVANCED FUEL SYSTEMS..... 5

A. Mechanical Reliability of Piezo Stack Actuators 5

3. MATERIALS FOR EXHAUST AFTERTREATMENT..... 11

A. Materials for Exhaust Aftertreatment..... 11
B. Characterization of Catalyst Microstructures and Deactivation Mechanisms……. 27
C. Development of NO_x Sensors for Heavy Vehicle Applications..... 35
D. Development of Materials Analysis Tools for Studying NO_x Adsorber Catalysts (CRADA No. ORNL-02-0659 with Cummins, Inc.) 39
E. Catalysis by First Principles..... 51
F. Durability of Diesel Particulate Filters (CRADA with Cummins, Inc.) 67

4. MATERIALS FOR AIR HANDLING AND THERMAL MANAGEMENT..... 75

A. Austenitic Stainless Steel Alloys for Exhaust Manifold (CRADA with Caterpillar, Inc.)..... 75
B. Friction and Wear Reduction in Diesel Engine Valve Trains……..... 81

5. MATERIALS FOR STRUCTURAL COMPONENTS…… 87

A. Cost-Effective Machining of Titanium and HCCI Fuel Systems Spray Hole Drilling ……..... 87
B. Synergistic Processing-Enhanced Grinding of Advanced Engine Materials…… 97

6. MATERIALS FOR HOT SECTION COMPONENTS…….. 101

A. NDE of Diesel Engine Components…… 101
B. Life Prediction of Diesel Engine Components..... 109
C. Engineered Surfaces for Diesel Engine Components..... 121
D. High-Temperature Advanced Materials for Lightweight Valve Train Components…….. 125

7. CHARACTERIZATION OF PHYSICAL AND MECHANICAL PROPERTIES……. 143

A. IEA - Implementing Agreement for a Programme of Research and Development on Advanced Materials for Transportation Applications…… 143
B. IEA- Rolling Contact Fatigue…….. 147

8. EMERGING TECHNOLOGIES……. 153

A. Processing and Characterization of Structural and Functional Materials for Heavy-Vehicle Applications …… 153
B. Powder Processing of Nanostructured Alloys Produced by Machining..... 161
C. Deformation Processes for the Next-Generation Ceramics……..... 169

1. INTRODUCTION

Heavy Vehicle Propulsion Materials

Advanced materials are an enabling technology for fuel-efficient commercial vehicle engines. Heavy Vehicle Propulsion Materials supports the engines and emissions activities in the FreedomCAR and Vehicle Technologies Program to provide enabling materials technologies in a timely fashion.

Presently, the fuel system represents a significant portion of the cost of a heavy-duty diesel engine. Enabling materials and cost-effective, precision manufacturing processes are instrumental in developing improved fuel injection systems. In addition to new and improved materials, improved manufacturing and inspection methods for the injector components are being developed.

The use of piezoelectric stack actuators as diesel fuel injectors has the potential to reduce injector response time, provide greater precision and control of the fuel injection event, and lessen energy consumption (e.g., for use in homogeneous charge compression ignition, HCCI, engines). However, the piezoelectric stacks are brittle and potentially subject to premature failure. A new R&D effort was begun to apply established brittle material probabilistic design and reliability analyses to piezo-stack actuators, generate the required mechanical property data for the design and reliability analysis, and identify minimum mechanical performance requirements for fuel injector piezo-stack actuators.

Novel scuffing tests to evaluate fuel injector materials in diesel fuel and biodiesel fuel environments have been developed and are in beneficial use for evaluating fuel system materials. The testing system is available to High Temperature Materials Lab (HTML) users as well as to the Propulsion Materials Program.

The reduction of nitrogen oxides (NO_x) and particulate emissions is critically important to OFCVT's program and is highly materials dependent. The U.S. Department of Energy (DOE) goals for improved efficiency of commercial vehicles are greatly complicated by engine and exhaust aftertreatment technologies designed to meet the mandatory U.S. Environmental Protection Agency (EPA) emission regulations for 2010 and 2012. Materials and systems research is being conducted to minimize the potentially negative effects of emission-reduction technologies on fuel economy and to result in cleaner and more efficient engines.

Durability of exhaust aftertreatment systems in commercial vehicles is a concern. A lifetime of at least 500,000 miles is expected, and a 1,000,000-mile lifetime is desired (compared with 100,000 miles for automobiles). Exposure of the aftertreatment systems to high temperatures, vibration, erosion, and chemical attack by species in the oil and fuel results in degradation of performance. The effects of exposure in service on the microstructure and microchemistry of the aftertreatment systems are being characterized, and this research may lead to development of more durable systems. The development of advanced NO_x sensors is being conducted to facilitate optimal engine and aftertreatment control strategies.

The characterizations of new materials from various stages of the catalyst's life cycle were continued this year. X-ray diffraction, X-ray photoelectron Spectroscopy and Scanning Transmission Electron Microscopy were used to evaluate the thermal degradation of a NO_x storage and reduction (NSR) catalyst within the catalyst support brick as a function of macroscopic position, catalyst history and operating conditions. Two studies characterizing a new catalyst system and a diesel oxidation catalyst in the unused and aged states were completed.

We have used Density Functional Theory (DFT) methods to investigate formation and adsorption energies as well as reaction energy profiles. Formation energies were calculated for $Pt_{1-3}O_y$ on MgO(100), while adsorption energies of O and CO on Pt_xO_x and Pt_xO_{2x} and O, O_2, CO, CO_2, NO, and NO_2 on Pt_x were calculated. We also calculated reaction energy profiles for $CO+1/2O_2 \rightarrow CO_2$ and $NO+1/2O_2 \rightarrow NO_2$. In concert with the first principles calculations we completed the synthesis of a series of supported Pt catalysts and evaluated them for CO oxidation.

The atomic-scale resolution of the aberration-corrected scanning transmission electron microscope (ACEM) was used to characterize the nature of platinum catalyst structures on alumina, silica and titania support materials, including the imaging of platinum species dispersed as single atoms and in precrystalline clusters known as "rafts." In particular, the different behavior of the Pt atoms, clusters and rafts on the support materials was characterized, as a function of electron beam excitation.

The development of test techniques to characterize the physical and mechanical properties of ceramic diesel particulate filters (DPFs) and develop analysis and inspection tools for assessing their reliability and durability was continued. Probabilistic design tools were used to model the durability and expected life of DPF ceramic substrates. Physical and mechanical property measurements were made on DPF substrates to better understand the time dependant fracture mechanics behavior.

Caterpillar continued to assess durability of various catalyst technologies in terms of phosphorous, sulfur and thermal degradation, and to identify materials that have high diesel particulate filtration efficiency, low pressure drop, and comply with future emission regulations for commercial diesel engines. The effort was focused on identifying the impact of phosphorus (P) exposure on diesel particulate filters (DPF) and diesel oxidation catalysts and of P plus sulfur (S) exposure on selective catalytic reduction (SCR) catalyst formulations.

Diesel engine components that require durability and low friction in order to improve propulsion system energy-efficiency and reduce emissions were identified. These include wastegate bushings for exhaust gas recirculation (EGR) components, fuel injector plungers, and valve and valve seat materials. Test methods, data analysis methodology, and models to evaluate and quantify the performance of candidate materials under simulated use conditions were developed.

Caterpillar developed high-velocity oxygen fueled (HVOF) coating processes to apply amorphous steels and quasicrystal materials to engine pistons and cylinder heads for use as thermal barrier coatings in homogenous charged combustion ignition (HCCI) engine designs. The diffusion stability of the new materials at engine operating temperatures was determined by means of diffusion couples and microprobe analysis.

Caterpillar and ORNL continued the development of CF8C-Plus cast stainless steel for near-term applications in diesel engine exhaust manifolds and turbocharger housings. Highlights include demonstrating that CF8C-Plus cast stainless steel is far superior to SiMo cast iron at 600°C and above. CF8C-Plus also shows strength, creep resistance and aging resistance benefits compared with other commercial cast stainless steels being considered for heavy-duty diesel turbocharger housings at 750°C. Significant progress has been made in commercializing the alloy. Creep-rupture resistance was determined for CF8C-Plus Cu/W and CF8C-Plus to further the interest of major diesel turbocharger OEMs to upgrade housings. ASTM weldability was characterized, along with castability of thin-walled CF8C-Plus and CF8C-Plus Cu/W in support of exhaust component applications.

Caterpillar, in collaboration with Argonne National Laboratory and ORNL, has a project to design and fabricate prototype engine valves from silicon nitride and titanium aluminide materials. The objective is valves that are 30% lighter than steel valves, provide a 200% increase in service lifetime, and potentially increase fuel efficiency in advanced engines by 10%. A probabilistic design approach was developed for the high-hardness valve materials. The friction welding of TiAl valve heads and Ti-6V-4Al valve stems was

successfully optimized. The effects of surface finish on the performance of silicon nitride valves was evaluated and indicated that valves with good surface finish performed well in bench tests.
This year a 500-hr durability test of the light-weight valves was successfully completed. A Caterpillar C15 ACERT™ engine was donated to the National Transportation Research Center (NTRC) for future component testing.

Efforts in cost-effective manufacturing were carried out by ORNL, the University of Michigan, Purdue University and Third-Wave Systems. The machining characteristics of difficult materials such as fuel injection plungers and wear-resistant engine parts were characterized and modeled in order to develop high-speed, cost-effective manufacturing processes.

Rogelio A. Sullivan
Team Leader, Materials Technologies
Office of FreedomCAR and Vehicle Technologies
Energy Efficiency and Renewable Energy

Jerry L. Gibbs
Technology Development Manager
Office of FreedomCAR and Vehicle Technologies
Energy Efficiency and Renewable Energy

2. MATERIALS FOR ADVANCED FUEL SYSTEMS

A. Mechanical Reliability of PZT Piezo-Stack Actuators for Fuel Injectors

Andrew A. Wereszczak and Hong Wang
Ceramic Science and Technology Group (CerSaT)
Oak Ridge National Laboratory
P.O. Box 2008, MS 6068
Oak Ridge, TN 37831-6068
(865) 576-1169; fax: (865) 574-6098; e-mail: wereszczakaa@ornl.gov

DOE Technology Development Manager: Jerry L. Gibbs
(202) 586-1182; fax: (202) 586-1600; e-mail: Jerry.gibbs@ee.doe.gov
ORNL Technical Advisor: D. Ray Johnson
(865) 576-6832; fax: (865) 574-6098; e-mail: johnsondr@ornl.gov

---

Contractor: Oak Ridge National Laboratory, Oak Ridge, Tennessee
Contract No.: DE-AC05-00OR22725

Objectives

- Apply established structural ceramic probabilistic design and reliability analysis to piezo-stack actuators.
- Generate the required mechanical property data for the design and reliability analysis.
- Identify minimum mechanical performance requirements for fuel injector piezo-stack actuators.

Approach

- Develop finite element models that estimate service stress states in piezo-stack actuators.
- Measure strength and fatigue distributions of piezoelectric ceramics that comprise piezo-actuators as a function of electric field and loading rate, and combine with FEA modeling to predict performance of whole stacks.
- Evaluate piezoelectric and mechanical response of whole piezo-stack actuators and compare to predictions.

Accomplishments

- Created preliminary FEA models to predict stress states in piezo-stack actuators.
- Established miniature mechanical test setup to measure strength of thin (~200 micron or 0.008” thick) piezoceramics.
- Designed and procured hardware that will enable mechanical testing of piezoceramics as a function of electric field, and cyclic fatigue testing of piezostacks with concurrent confined load.

Future Direction

- Refine FEA models.
- Characterize effect of electric field on piezoceramic mechanical performance.
- Destructively evaluate piezo-stack actuators to identify performance limiting stresses and flaw types.

Introduction

The use of piezoelectric stack actuators as diesel fuel injectors has the potential to reduce injector response time, provide greater precision and control of the fuel injection event, and lessen energy consumption (e.g., for use in homogeneous charge compression ignition, HCCI, engines). Examples of piezo-actuators are shown in Fig. 1. Though piezoelectric function is the obvious primary function of lead zirconate titanate (PZT) ceramic stacks for fuel injectors, their mechanical reliability can be a performance and life limiter because PZT is brittle, lacks high strength, and may exhibit fatigue (i.e., slow crack growth) susceptibility. That brittleness and relatively low strength can be overcome with proper design though. This project combines in-situ micromechanical testing, mechanical characterization of full piezo-stack actuators, microstructural-scale finite element analysis, probabilistic design sensitivity, and structural ceramic probabilistic life prediction methods to systematically characterize and optimally design PZT piezoelectric stack actuators that will enable maximized performance and operational lifetime.

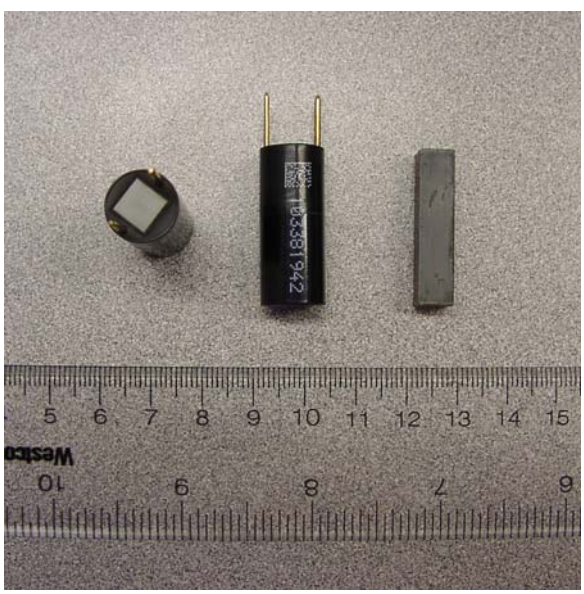

Figure 1. Examples of piezo-stack actuators. Left is a top view, middle is a side view, and right is a stack removed from the protective covering.

A significant portion of this project is devoted to understanding the link between the microstructural and macroscopic responses of a piezo-stack. A multilaminate architecture comprises these piezo-stack with alternating layers of electrode and piezoceramic. Such an internal architecture is shown in Fig. 2. Cracking can initiate in the piezo-stacks detrimentally affecting the actuation, so concerted efforts are underway to understand that cracking from a structural ceramic perspective.

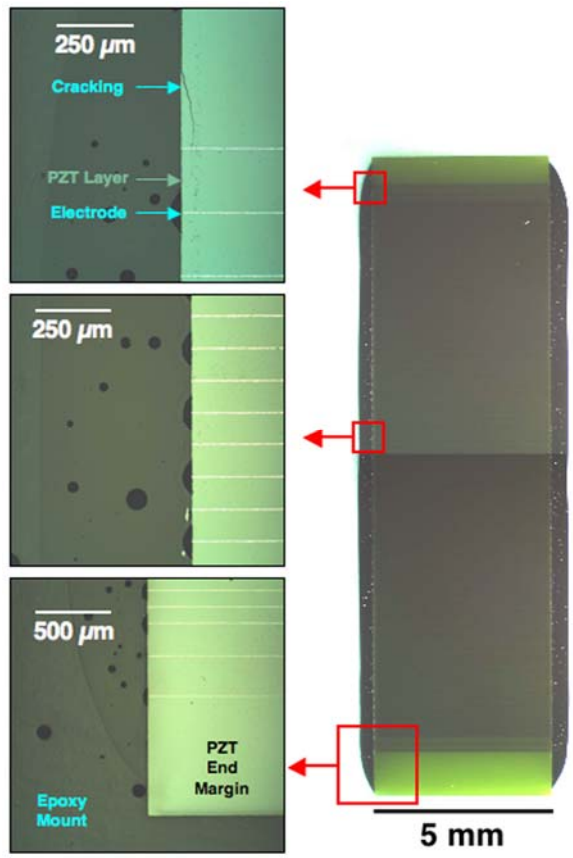

Figure 2. Cross-section of a piezo-stack actuator.

Approach

The strength test setup (see Fig. 3) consists of a micromechanical test frame that has integrated load and acoustic emission measuring capabilities. Load and acoustic histories for a typical test are shown in Fig. 4. Interestingly, the specimens do not always fracture catastrophically and Fig. 4 can illustrate that. The first acoustic event (occurring at the ~ 90s

mark) is associated with crack initiation and that corresponding load was used to calculate strength after Shetty *et al.* [1]. That fracture does immediately run through the whole specimen causing the specimen to withstand additional loading. The second event is undergoing further interpretation and the third event is associated with complete specimen fracture.

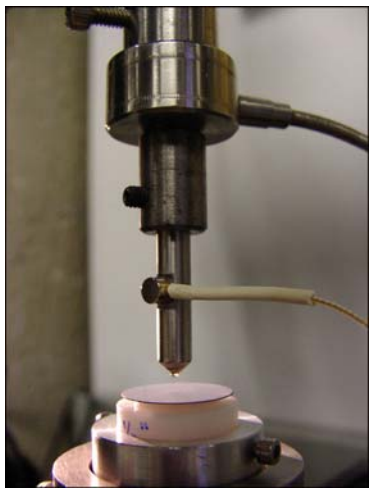

Figure 3. Micromechanical ball-on-ring biaxial flexure strength test setup. Load and acoustic activity are continuously measured during each test. A thin disk specimen is shown whose thickness is approximately 200 microns.

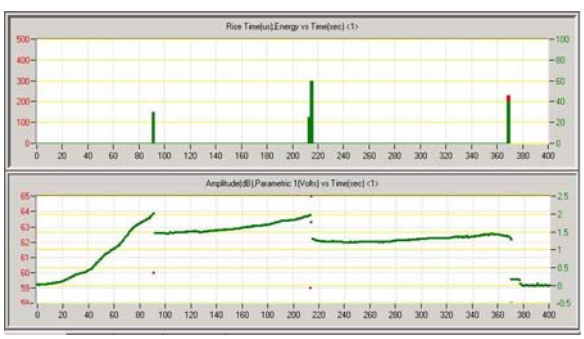

Figure 4. The upper graph shows acoustic signal rise time as a function of time and the lower is a double-Y graph that shows acoustic events (red dots) and load in Newtons as a function of time. The first event is associated with crack initiation and the corresponding load is used to calculate strength.

In order to confidently estimate strength of the PZT films tested with the configuration shown in Fig. 3, finite element analysis (FEA) was conducted of the ball-on-ring tested films, and then compared against the typically used formula for this loading configuration. This validation was an important task because measured strength is perhaps the most prominent dependent parameter being measured.

To initiate the study of the translation of piezoceramic strength and probabilistic life prediction and design of piezoactuators, industry type 5A4E and 5H4E piezoceramic sheets were sectioned into square specimens and flexure tested in ball-on-ring testing. The manufacturer's reported d33 for the 5A4E and 5H4E dielectrics were 390 x 10^{-12} m/V and 650 x 10^{-12} m/V, respectively while their reported Curie temperatures were 350 and 230°C, respectively.

To start to bridge mechanical responses between discrete PZT ceramic films and the macroscopic piezo-stack actuators, FEA modeling of the latter was initiated that will facilitate the effect of applied voltage on resulting stress in the piezo-stacks.

Lastly, hardware (amplifier, loading platens, capacitance gages, data acquisition system, dead weight loading system, etc.) were acquired in preparation for piezostack testing that will enable concurrent mechanical loading and piezoactuation. This use of this equipment will play key roles in this project's FY07 work.

Results

The calculated strength underwent scrutiny through comparisons of stresses predicted from finite element analysis (Fig. 5). Based on those results, it appears that the more classical calculation of failure stress [1] was overestimating the stresses as shown in Fig. 6. Strength-size-scaling relationships were developed and will be used to integrate strengths of these thin film PZT test coupons into the predicted performance of piezo-stack actuators comprising them.

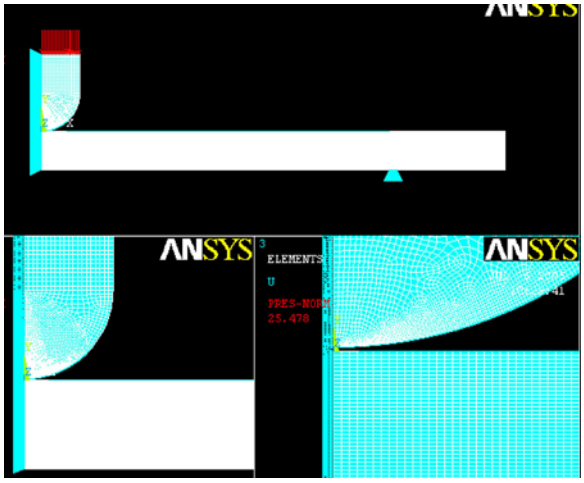

Figure 5. Finite element analysis was performed to accurately estimate "ball-on-ring" biaxial bending stresses in the thin PZT piezoceramic specimens.

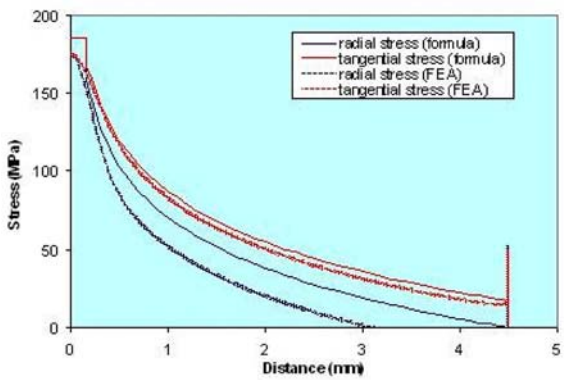

Figure 6. Finite element analysis results showed that the classical formula for determining biaxial flexure stress overestimates actual stress.

The 5A4E PZT dielectric had a higher strength than the 5H4E as illustrated in Figs. 7-8. The Weibull moduli of both materials were statistically equivalent. Preliminary optical fractography has showed failure initiation is at the surface indicating that a surface-type flaw or volume-type flaw located at the surface was the strength-limiter.

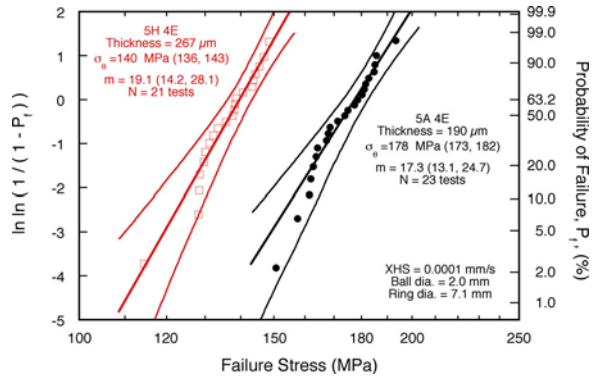

Figure 7. Weibull strength distributions for the 5H4E and 5A4E piezoceramics. The same loading fixture was used to test both materials. The 5H4E specimens were approximately 50% thicker than the 5A4E.

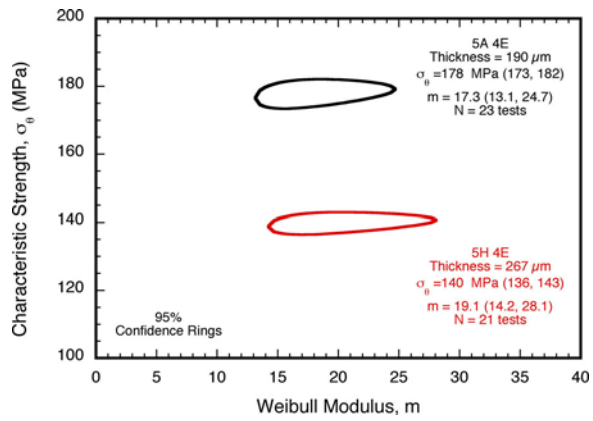

Figure 8. 95% confidence ratio rings for characteristic strength and Weibull modulus

A one-quarter FEA model was created of a piezo-stack to aid in our interpretations of the link between voltage and resulting stress. An example of that relationship is illustrated in Figs. 9-10. For structural ceramic components, the greatest concern for reliability compromise is the magnitude of the first principal tensile stresses. This project will examine the design the existing piezo-stack actuators and strive to make educated changes so to lessen those tensile stresses and improve their reliability.

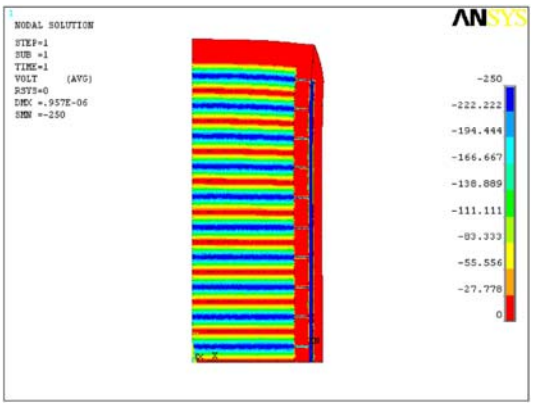

Figure 9. Voltage profile in an actuated piezo-stack.

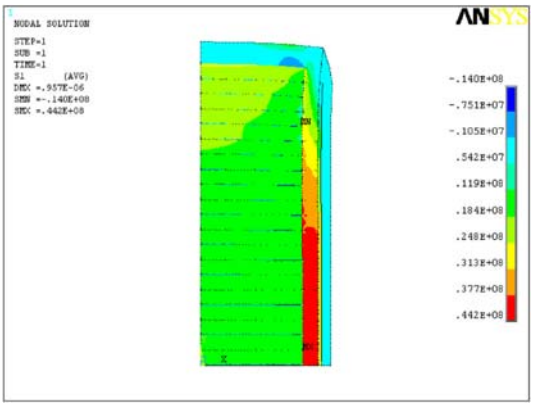

Figure 10. Resulting first principal stress field from the applied voltage field shown in Fig. 9.

Conclusions

FY06 was this project's first year and a great deal was accomplished that will enable design optimization and reliability enhancements of ceramic piezo-stack actuators for heavy duty diesel engine fuel injectors. An ultimate goal is to link systematic micromechanical property data of the piezoceramic materials to mechanical performance of piezo-stack actuators. Toward that, in FY06 micromechanical test facilities were established and are being used to measure strength and fatigue responses of the piezoceramics. The bridge between the micro and macro will be supported through modeling, and finite element models were developed to both validate stress fields in mechanical testing and stress fields in an actuated piezo-stack. Hardware was identified and procured that will enable the commencement of piezo-stack reliability analyses in FY07 and linking to property data of the PZT ceramic films.

References

[1] D. K. Shetty, A. R. Rosenfield, P. McGuire, G. K. Bansal, and W. H. Duckworth, "Biaxial Flexure Tests for Ceramics," *Ceramic Bulletin*, 59:1193-97 (1980).

Presentations and Publications

H. Wang and A. A. Wereszczak, "Effects of Electric Field on the Biaxial Strength of Poled PZT," to be given at 31st International Cocoa Beach Conference and Exposition on Advanced Ceramics and Composites, Daytona Beach, FL, 21-26 January, 2007.

3. MATERIALS FOR EXHAUST AFTERTREATMENT

A. Materials for Exhaust Aftertreatment

Corey Shannon, Herbert DaCosta, Matt Stefanick, Ronald Silver, Tom Paulson, and Craig Habeger
Caterpillar Inc.
P.O. Box 1875
Peoria, IL 61656
(309) 578-6040 ; fax (309) 578-2953; e-mail: Paulson_tom@cat.com

DOE Technology Development Manager: Jerry L. Gibbs
(202) 586-1182; fax: (202) 586-1600; e-mail: Jerry.gibbs@ee.doe.gov
ORNL Technical Advisor: D. Ray Johnson
(865) 576-6832; fax: (865) 574-6098; e-mail: johnsondr@ornl.gov

---

Contractor: Oak Ridge National Laboratory, Oak Ridge, Tennessee
Prime Contract No: DE-AC05-00OR22725
Subcontractor: Caterpillar Inc., Peoria, Illinois

Objectives

- Develop advanced materials applied for diesel engine aftertreatment systems that will comply with future emission regulations.
- Assess impact of phosphorus on oxidation (DOC), catalyzed DPF (CDPF) and urea-SCR catalysts, alone and in combination with sulfur and thermal aging.

Approach

- Assess impact of phosphorous (P) and sulfur (S) on aftertreatment systems by comparing fresh and aged catalyst performance using fuel burner and bench test system
- For DOC: Evaluate P impact on CO and HC oxidation as indicated via lightoff temperature.
- SCR: Evaluate impact of P and sulfur and /or thermal degradation on zeolite-based samples using temperature and NO_2/ NO_x ratio sweeps.
- CDPF: Evaluate P impact on PM filtration efficiency and soot regeneration.

Accomplishments

- Determined the impact of phosphorus (P) exposure on HC and CO lightoff over oxicats to be comparable to the loss of NO_x reduction over SCRs at similar exposure levels.
- The deactivation of zeolite-based SCR catalysts due to combinations of phosphorus, sulfur and thermal exposure was identified.
    - ✓ At low exposure temperatures (210°C), sulfur initially increases the observed deactivation over P alone for both NH_3 and NO conversions; the effect is reversible upon exposure to sulfur free gas.
    - ✓ At higher temperatures (450°C), the effect of sulfur on deactivation is less reversible.
    - ✓ Sulfur initially adversely affects NH_3 conversion more than NO_x. Thermal exposure alone does not significantly affect SCR activity, but does inhibit SCR in combination with sulfur and phosphorus. Phosphorus alone or in combination with sulfur or thermal exposure blocks NH_3 adsorption sites which in turn prevent NO reduction.
    - ✓ Effects from exposure to phosphorus and sulfur can be mitigated by operating at higher NO_2/ NO_x ratios, or by increasing the catalyst substrate volume

- Determined that the main impact of combusted phosphorus on particulate filters is on the regeneration step that occurs over the catalyst.

Future Direction

- Explore 1 or 2 mitigation strategies in more detail for larger catalysts; blank in front; wash catalyst to restore activity.
- Evaluate the impact of non-combusted P on exhaust catalyst and compare it to the effect of combusted P.
- Correlate results from lab aging studies with real world catalyst samples aged on an engine and or in the field. Use correlation to develop rapid aging protocols that accurately predict in-use deactivation modes.
- Continue to identify novel DPFs with improved pressure drop, filtration efficiency, and regeneration capabilities.

Introduction

The objective of this effort is to develop and evaluate materials that will be utilized in aftertreatment systems for diesel engine applications to comply with future government emission regulations. The materials include catalysts for NO_x abatement and filtration media for particulate control in the exhaust system. The project is a part of Caterpillar strategy to meet EPA requirements for regulated diesel emissions in 2007 and beyond. This year's focus is to assess durability of various catalyst technologies in terms of phosphorous, sulfur and thermal degradation, and to identify materials that have high diesel particulate filtration efficiency, low pressure drop, and comply with future emission regulations for heavy-duty diesel engines.

Approach

Catalyst Deactivation: The effort was focused on identifying the impact of phosphorus (P) exposure on diesel particulate filters (DPF) and diesel oxidation catalysts (oxicats) and of P plus sulfur (S) exposure on SCR catalyst formulations. The performance of fresh DPFs and catalysts was tested, and then each DPF or catalyst was exposed to P in a diesel fuel burner using fuel doped with tricresyl phosphate that mimicked the effect of P from combusted lube oil. In the case of the Selective Catalytic Reduction (SCR) catalyst, the diesel fuel was additionally doped with S to expose the sample to SO_2. All aged samples were evaluated and compared to the analogous fresh samples, while the aged SCR catalysts were additionally compared to the activity of SCR samples exposed to P only.

Results

Oxicat durability:
A set of 10g Pt oxidation catalysts (oxicats) were evaluated for CO and HC lightoff performance before and after aging via P exposure using a diesel fuel burner. The P had only a mild effect on the oxicat activity, with the worst impact being a 20°C increase in CO lightoff after an exposure of 19g/L P. The lightoff curves shifted toward higher temperature with increasing P exposure without changing shape, which is typical of a decline in activity due to physical blockage of active sites. The results were compared to previous tests that measured the P effect on NO_x reduction over Lean NO_x Traps (LNTs) and SCR catalysts. CO and HC oxidation over the tested catalysts are affected by P to

about the same extent as NO_x reduction over SCR catalysts. P impacts LNT performance more than either oxicats or SCRs.

Results in Figures 1a and 1b respectively show the effect of P exposure on the CO and HC lightoff performance of a Pt catalyst. The lightoff temperature (T_{50}, the temperature at which 50% conversion is obtained) of the catalyst increased by about 8°C for HC and 15°C for CO when exposed to 5.5g/L P. The lightoff temperatures increase with increasing exposure levels of P. A second catalyst core was exposed to 3.6g/L P, and results are in line with those from the first core. All of the samples, which were aged in the lab on the diesel fuel burner, have lightoff curves that are similar in shape to the fresh benchmark. The shift in the curves with increasing P is typical of a decline in activity due to physical blockage of active sites. Most likely, the accumulated P blocks some of the sites where HC or CO is adsorbed. The actual P concentration that a catalyst will see is a function of the catalyst volume, the concentration of P in the oil, and the engine oil consumption rate.

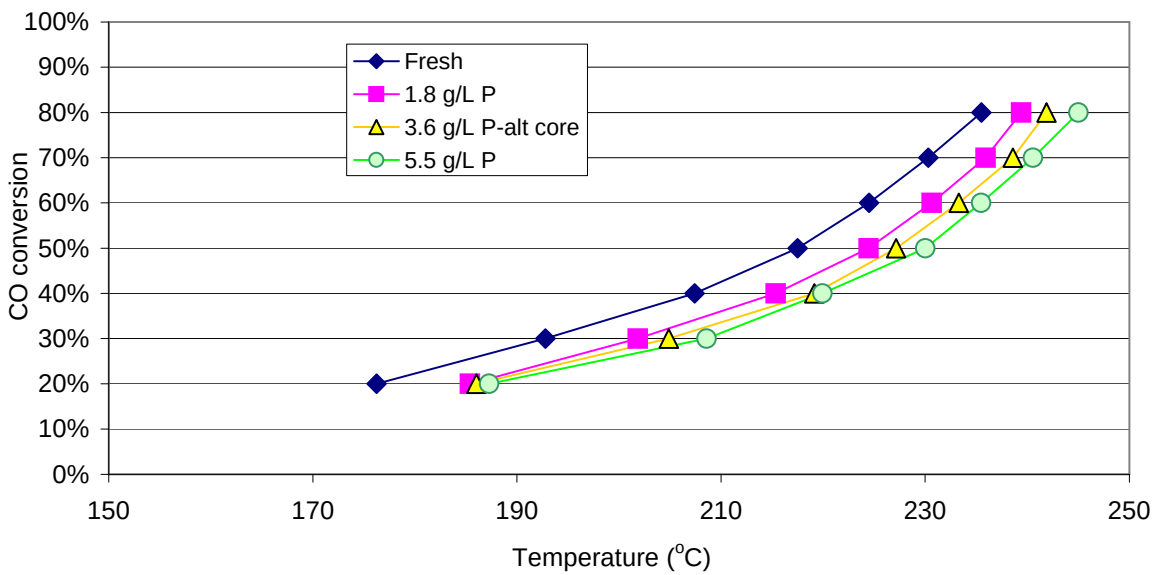

FIGURE 1a. Effect of P exposure level on CO lightoff over a Pt oxicat

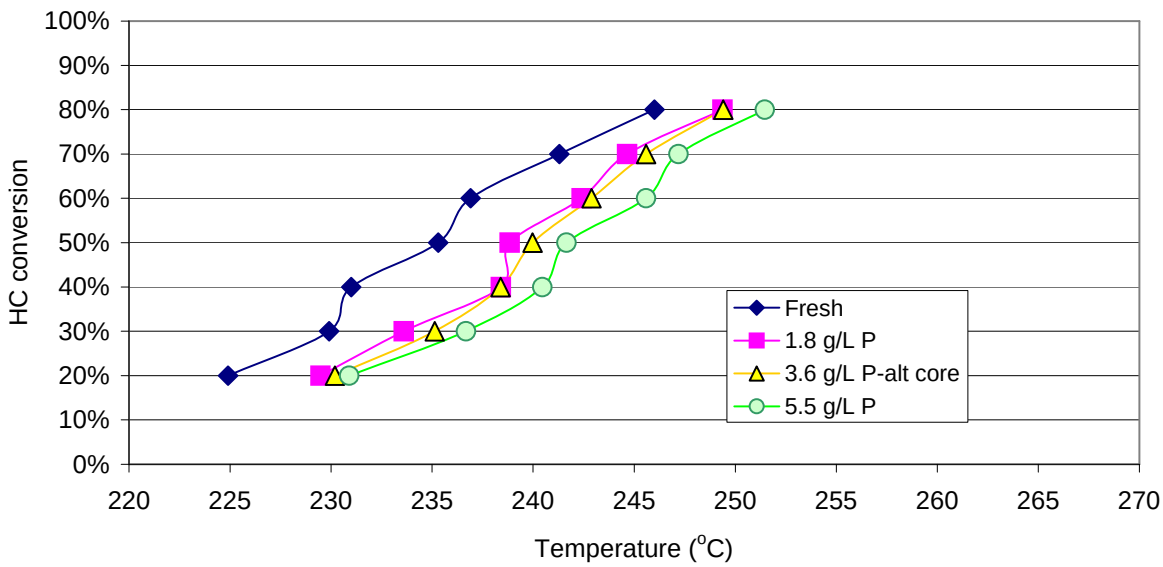

FIGURE 1b. Effect of P exposure level on HC lightoff over a Pt oxicat

The impact of P on oxicats was compared to its effect on LNTs and SCR. First the temperature for 90% CO conversion over the fresh catalyst was obtained, then amount of CO converted at that same temperature for a P aged catalyst was determined. The procedure was repeated for each level of P exposure, and then again for the HC. Results for LNT and SCR catalysts were determined based on fresh vs. aged NO_x reduction. Oxicat conversion of CO and HC is affected by P to about the same extent as NO_x reduction over vanadia based, or zeolite based, SCR catalysts. The impact of P on LNTs is greater than that for oxicats or SCRs. In all cases, P is physically blocking adsorption sites.

<u>SCR Catalyst durability :</u>
Zeolite based urea SCR catalysts provided by Umicore Catalyst Company were previously mildly aged with P alone. Using a diesel fuel burner, additional core samples were taken from this catalyst and exposed to P plus significant levels of SO_2, such that the resulting S weight exposure was equal to the P exposure. The activity of these aged samples was characterized by doing a temperature sweep, an NH_3/ NO_x ratio sweep, and a NO_2/NO_x ratio sweep over the aged catalyst. These results indicate the addition of S into the aging mix initially accelerates the degradation of zeolite SCR performance.

Results in Figure 2 show the effect of exposure to 5g/L P and 5g/L S on the NO_x and NH_3 conversions, calculated by dividing the aged catalyst activity by its previously tested fresh performance under the same conditions. In this plot 100% means the aged sample has activity equal to a fresh sample, not complete conversion. The relative performance of the sample aged using P only is also plotted in this figure. Results from mild aging with P showed little or no loss of NH_3 and NO_x conversion activity. The addition of S to the aging mix drops the relative performance by about 10 % for both the NO_x and the NH_3. The relative NO_x conversions from both agings appear to be slightly lower at low temperatures, and then

increase with temperature. This seems to indicate that active sites for low temperature NO_x reaction are more strongly impacted by P and S. An analysis of NO and NO_2 conversions from these agings indicates that NO conversion is lost at low temperature. The decline in activity is due to a decrease in NO oxidation to NO_2. In contrast, the activity loss for NH_3 conversion due to exposure to P, or P and S, does not seem to correlate with increasing temperature.

The effect of core size was also investigated. A 1-inch diameter by 3-inch long core from a zeolite SCR catalyst was exposed to the same level of S and P as a 1 inch by 6-inch long core. The results are shown in Figure 3 and indicate the longer core has better low temperature NO_x conversion, both fresh and after aging. In fact, the aged 6-inch core has a NO_x lightoff temperature similar to the fresh 3-inch core. At high temperature, the activity of the 6-inch core drops below the performance of the 3-inch core. This may be due to the longer residence time of NH_3 in the 6-inch core, which allows NH_3 oxidation to occur earlier. The results suggest one method of reducing the impact of S and P exposure may be to increase the volume of the SCR catalyst.

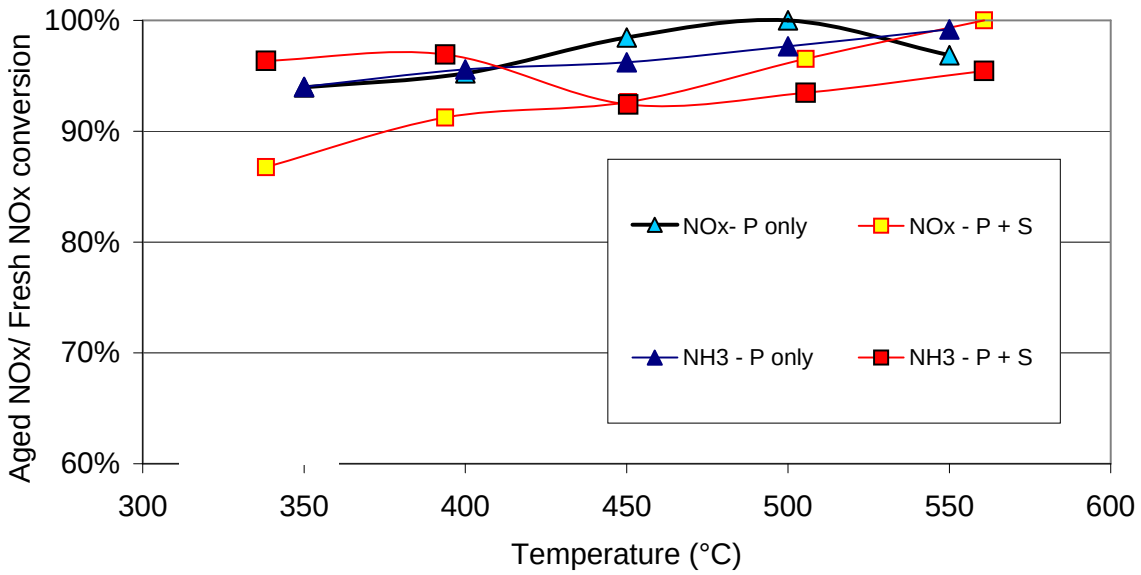

FIGURE 2. Relative performance of SCR catalysts after exposure to 5g/L P plus S or P only.

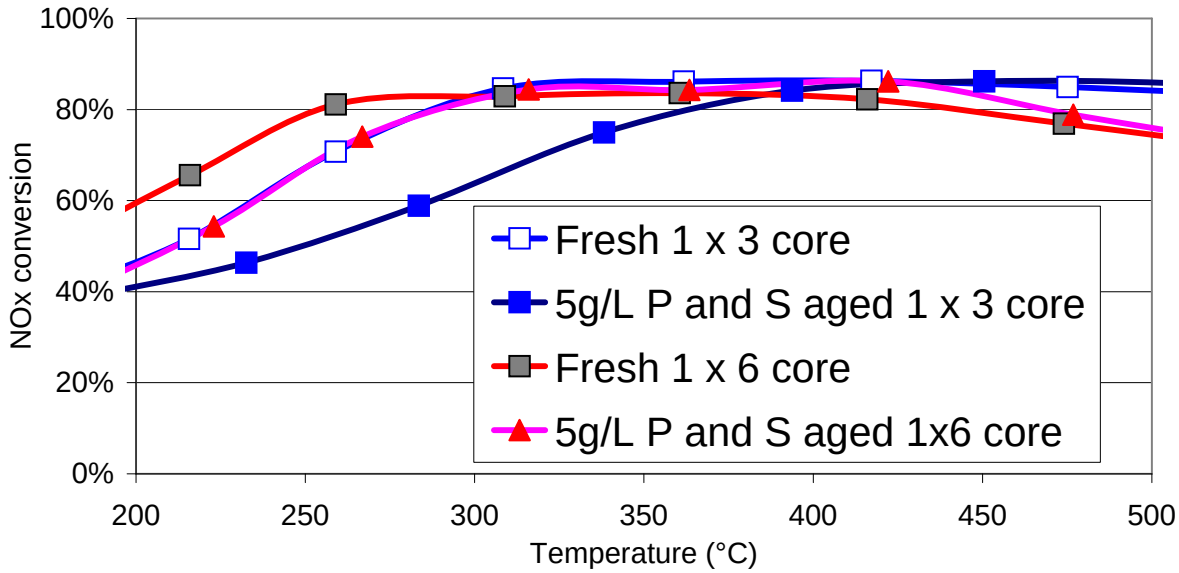

FIGURE 3. Comparison of NO_x conversion as a function of space velocity, before and after exposure to 5g/L P and S.

The relative activity of zeolite based urea SCR NO_x reduction catalyst after exposure to higher levels of P and S is shown in Figure 4. As seen also in Figure 2, catalysts that were exposed to 5g/L P and S at 210°C showed a slight degradation in NO_x conversion relative to the degreened activity. Increasing the exposure level at that temperature to a total of 10g/L P and S resulted in an initial apparent loss of 70% of the degreened activity at 300°C. A repeat of the activity test showed a significant recovery in NO_x conversion, such that the activity loss at 300°C was just 20%. For comparison, this amount of activity was lost from exposure to 10g/L P only. Activity testing was performed in the absence of S and P, so it appears that exposing the catalyst to S-free gas removes most of the S that was responsible for the initial activity loss. The resulting "cleaned" catalyst performs similar to a sample that was just exposed to 10g/L P. The cleaning effect can even be observed during the first activity test, where there is significant recovery in activity as the sample is ramped up in temperature.

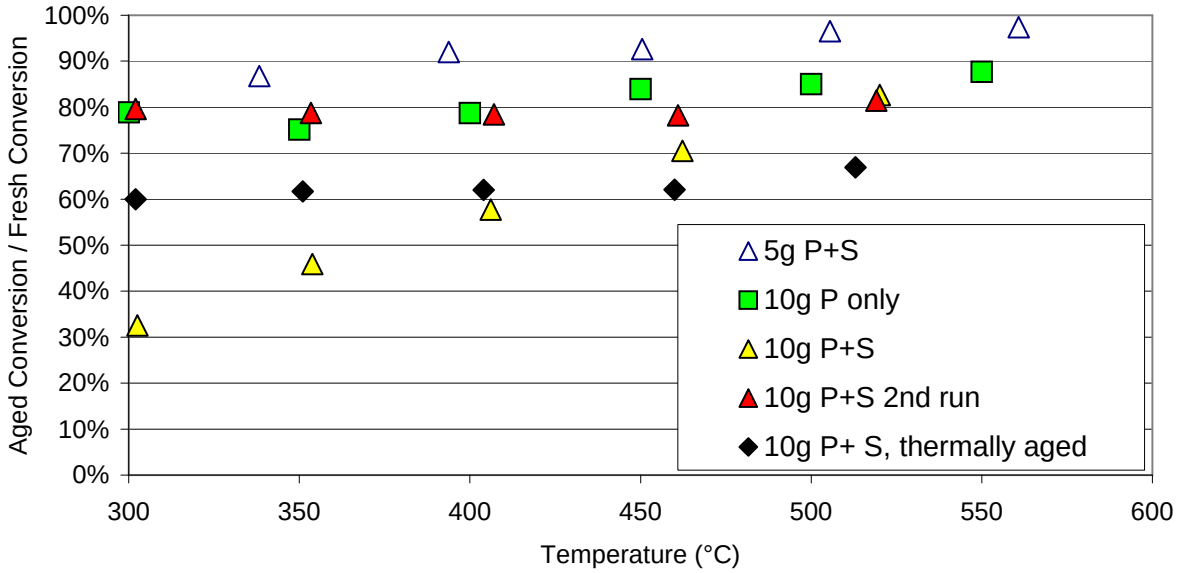

FIGURE 4. Relative NO_x performance of SCR catalysts after exposure to 10g/L P, 5g/L and 10g/L P and S and after 10g/L P and S plus thermal aging for 24h at 650°C.

A drop in initial SCR NO_x conversion activity at 175°C and 400°C as a function of exposure level to P and S can be seen in Figure 5. The results in this figure show the decline in activity accelerates with increasing exposure amounts. It may be that the Fe-zeolite catalysts have a buffering capacity for up to about 5g/L P and S exposure, but after that the active sites become overwhelmed. The figure also indicates the difference between the initial activity loss due to exposure to 10g/L P and S is about 10 to 15% greater than that due to exposure to a similar amount of P alone. If the NO_x activity measured in the second and subsequent runs are plotted instead of the initial decline in activity due to P and S, the resulting curve is much flatter and the data point at 10 g/L exposure falls on top of the P only data point. However, even if the data from the repeat runs are utilized, the decline in NO_x activity between 0 and 5g/L is less than the decline in going from 5 to 10g/L P and S exposure.

Similar relative performance results for ammonia conversion are observed in Figure 6. Typically NH_3 is converted either by reacting with NO_x or with O_2 under SCR reaction conditions. Just as with NO_x in Figure 4, the initial NH_3 conversion drops significantly when the P and S exposure level is increased from 5g/L to 10g/L. In this case, sweeping the catalyst with S free gas recovers 90% of the initial activity, or results in a loss of just 10% of degreened NH_3 conversion. The recovered activity also corresponds to the effect of a P-only exposure of 10g/L.

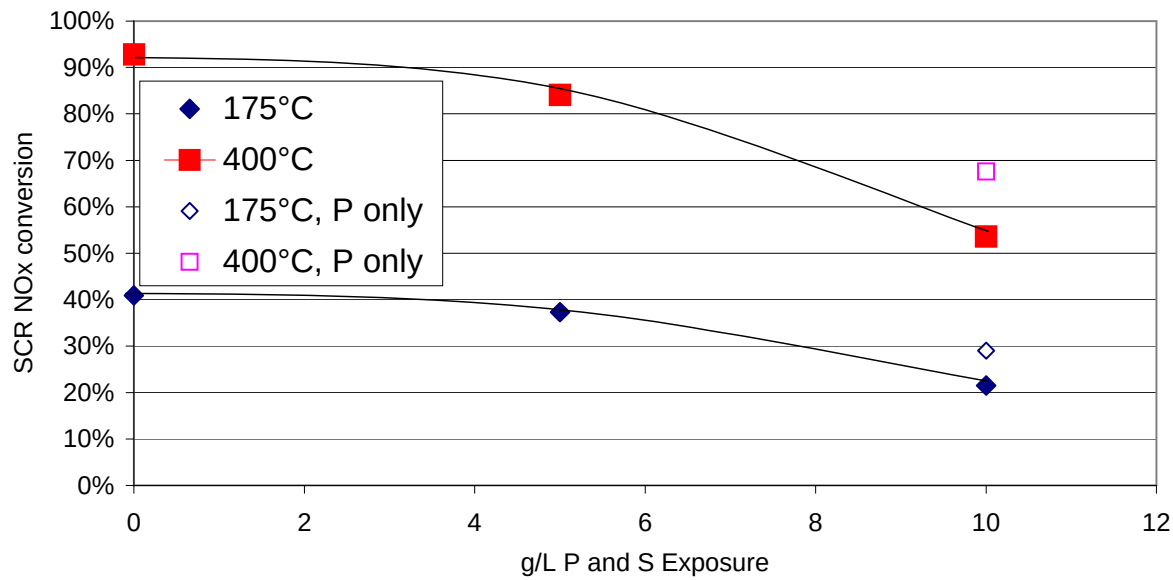

FIGURE 5. Impact of exposure level on initial NO_x activity at 175°C and 400°C

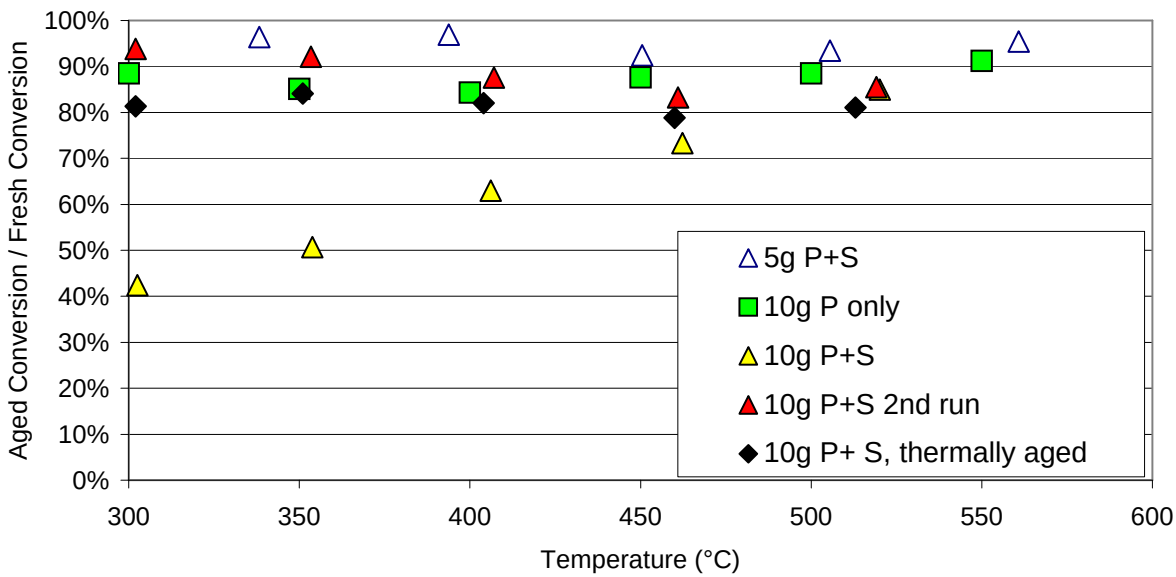

FIGURE 6. Relative NH_3 conversion of SCR catalysts after exposure to 10g/L P, 5g/L and 10g/L P and S and after 10g/L P and S plus thermal aging for 24h at 650°C

The 10g/L P and S exposed catalyst was then thermally aged at 650°C for 24 hours in a mixture of 10% steam and air. The resulting loss of NO_x conversion, shown in Figure 4, was about 40% of the degreened performance or about the same effect as that of the P and S exposure. This loss of activity did not appear to be recoverable by exposing the sample to S free gas, or by repeated testing. The effect of the thermal aging on NH_3 conversion (shown in Figure 6) is less dramatic, resulting in a total decline of just 20% of degreened activity. This level is not much different than the effect of P and S exposure alone. The difference in temperature effect may be due to sintering of the

active metal (e.g. iron or copper) due to the hydrothermal aging. The active metal seems to play an important role in activating the NO_x, but may not be as critical in converting NH_3.

Comparing Figures 4 and 6, the relative NO_x performance loss appears to be slightly higher than the NH_3 conversion loss for any given P and S exposure. This may indicate that the catalyst oxidation of NO to NO_2 is more susceptible to activity loss due to thermal aging or P and S exposure than is the De NO_x reaction, which converts equal molar amounts of both NH_3 and NO_x

Figure 7 shows the NO_x activity as a function of temperature after thermally aging a fresh sample for 24h at 650°C. The results are compared to the repeat test of the sample exposed to P and S, which was then thermally aged. The catalyst that was only thermally aged shows very similar activity to the fresh sample, indicating little or no loss of performance. In contrast, there is about a 15% performance decline after the P and S exposed sample is thermally aged under the same conditions. This suggests that exposing the P and S contaminants to an elevated temperature can cause them to adversely interact with other elements of the catalyst surface, resulting in an increased loss of activity.

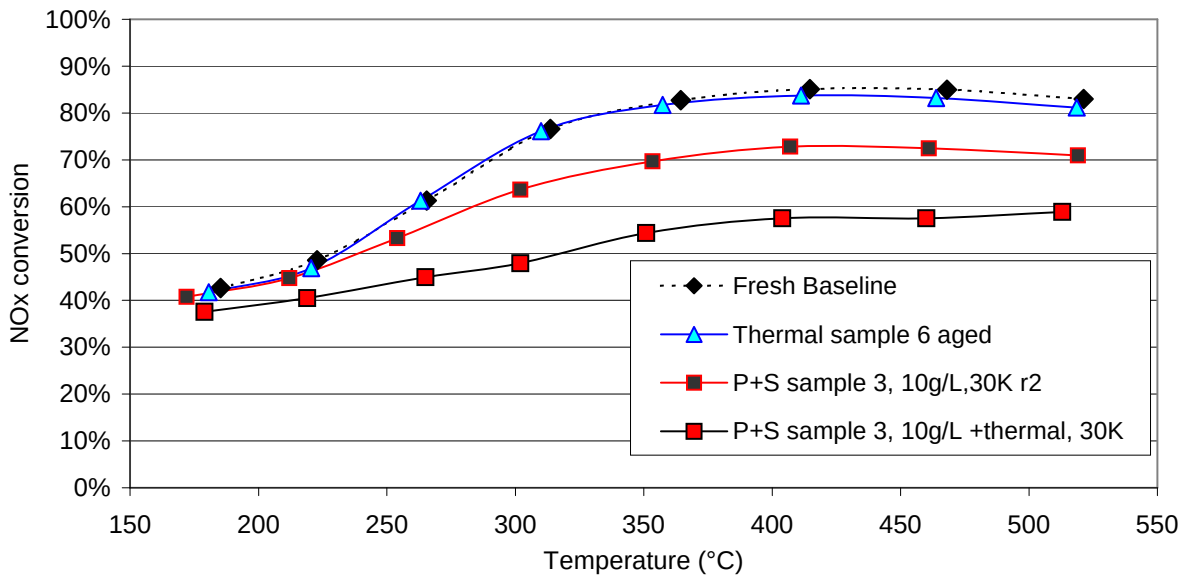

FIGURE 7. Effect of thermal aging on fresh and P + S exposed catalyst.

The relative activity (aged conversion/ fresh conversion) of these same catalysts at 190°C and an NH_3/ NO_x ratio of 1.1was plotted versus a varying NO_2/ NO_x ratio in Figure 8. In this case, the sample that was only thermally aged retains >95% of the fresh catalyst's performance. The sample exposed to 10g/L P and S saw a decline of more than 50% off the baseline at low NO_2 / NO_x ratios, but performance improved to 90% of the fresh sample when the NO_2 / NO_x ratio increased to between 0.25 and 0.65. A similar improvement in activity was seen over the thermally aged, P and S exposed sample, which was 65% less than the baseline at low NO_2 / NO_x ratios but improved to 90% of the fresh performance at a ratio of 0.5. At a NO_2 / NO_x ratio of 0.5, the NO_2 level is equal to

the amount of NO, and is the condition where "fast SCR" can occur. The fact that there is only a minor decline in activity at this point, and despite the temperature being just 190°C, indicates the P and S primarily impact NO oxidation or its interaction with NH_3. The relatively uniform decline after thermally aging the P and S exposed sample suggests that some NH_3 adsorption might be adversely affected by heating these contaminants, possibly by physically blocking more of the NH_3 adsorption sites. The relatively mild decline in activity at 0.5 NO_2 / NO_x ratio even after significant aging also suggests another mitigation strategy may be to try to run closer to this condition as the system ages.

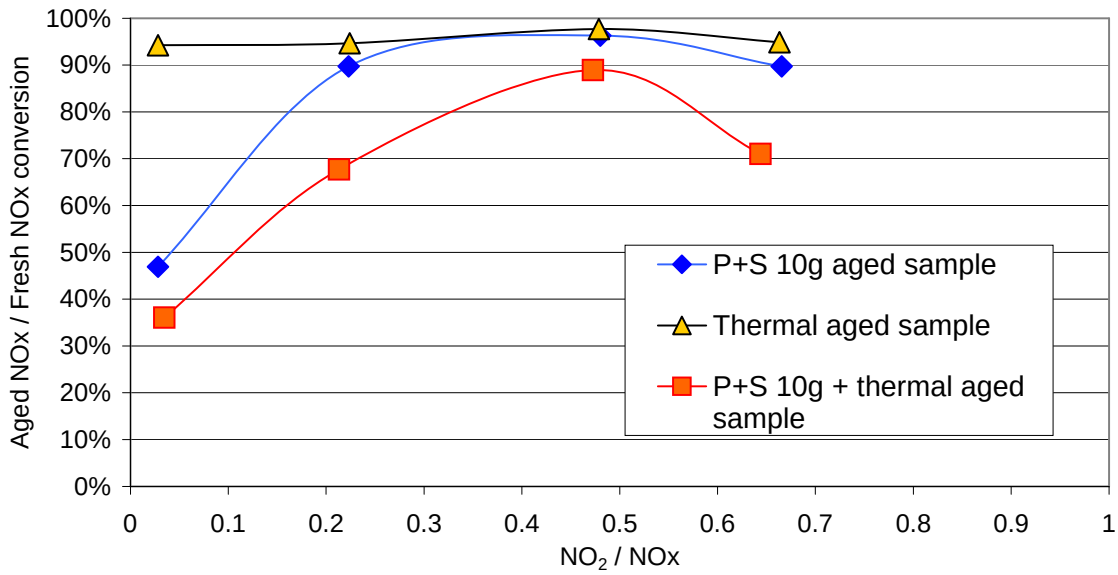

FIGURE 8. Relative NO_x performance of SCR catalysts after exposure to P plus S and after exposure to thermal aging only.

Figure 9 compares the effect of aging the catalyst with 5g/L P and S at 450°C versus aging at 210°C, in order to see the impact of exposure temperature. Increasing the exposure temperature appears to decrease the relative activity by about 8% across the range of the temperature sweep. The other effect seems to be that the activity loss due to sulfur after the higher temperature exposure is not as readily reversible as it is when the temperature is lower. It is also seen that relative NH_3 performance is better than NO_x in most cases. However, the gap between the high and low temperature exposure activity loss seems slightly higher for NH_3 than it does for NO_x. Again, this may be due to the higher exposure temperature leading to more significant interference of the P and S with NH_3 adsorption.

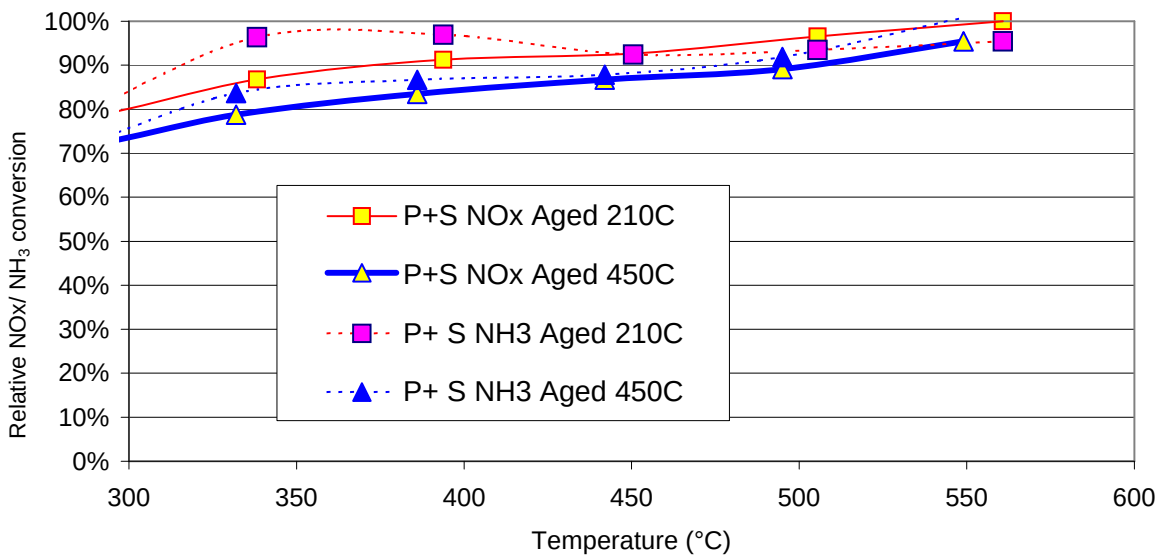

FIGURE 9. Effect of P and S exposure temperature on NO_x and NH_3 relative conversion.

Diesel Particulate Filter (DPF)

Catalyzed and uncatalyzed diesel particulate filters (DPF) obtained from suppliers were loaded with particulate matter on a diesel fuel-burner bench and regenerated. This process was repeated after 100 hours and after 200 total hours of hydrothermal aging. In all cases, the filtration efficiency did not change significantly. One trend found in this study was that the pressure drop during the tests decreased slightly on catalyzed samples (Figures 10 and 11). However, it could be due to extended degreening. Several projects have been executed to improve the performance and efficiency of the diesel fuel burner on which the 1-inch diameter DPF cores are tested. One such project was a 6-sigma "lean" event. A team composed of primary users and customers of the test bench examined the entire process of loading particulate matter onto a DPF. This team was able to suggest changes to the procedure as well as physical changes on the bench itself. Many safety issues were also resolved. Another 6 sigma-like project was carried out and determined the reproducibility of the measurements acquired from the fuel burner bench. This project ascertained that the filtration efficiency of a DPF can be measured with less than 2% error

.

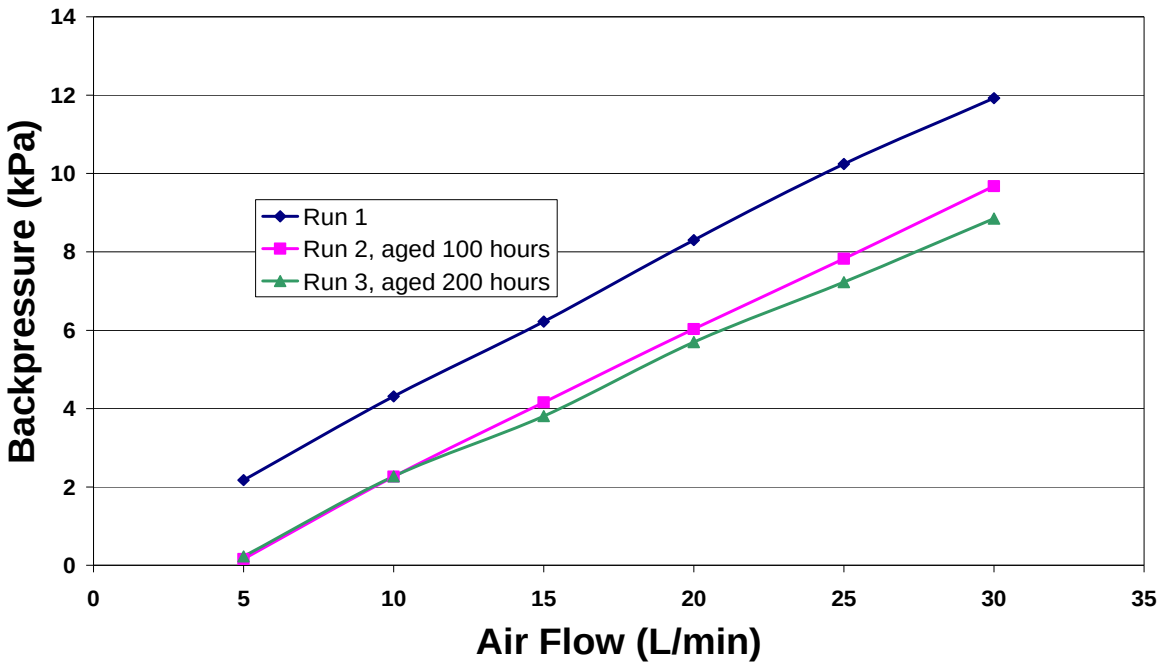

FIGURE 10. Pressure drop versus flow rate for catalyzed cordierite before and after hydrothermal aging for 100 h and 200 h.

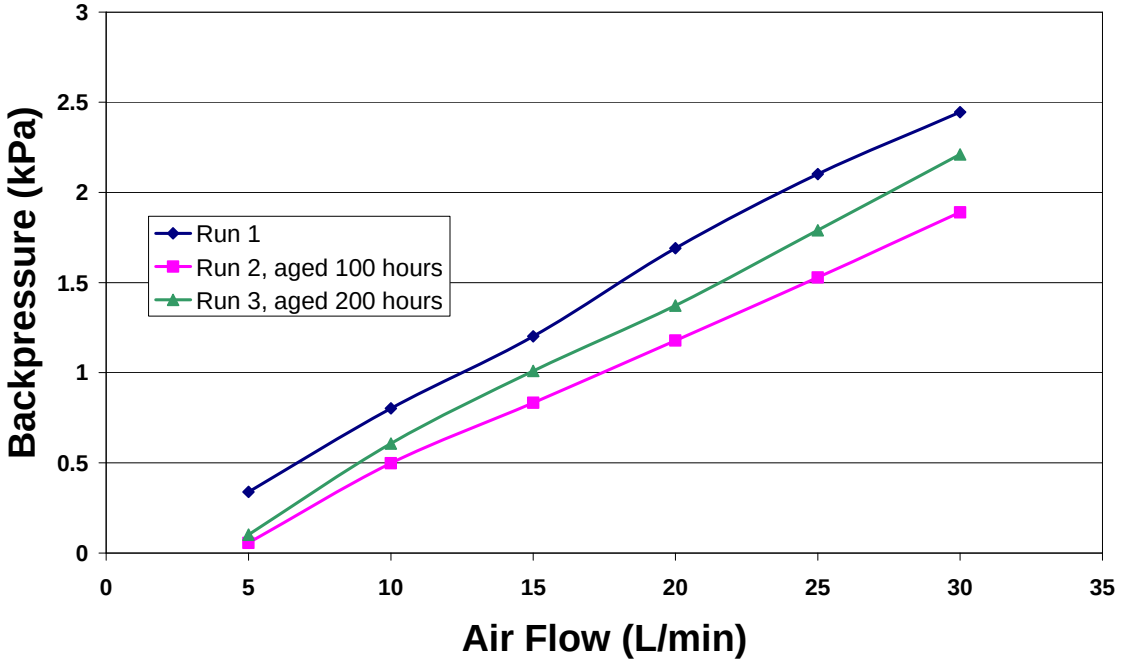

FIGURE 11. Pressure drop versus flow rate for catalyzed alternative DPF, before and after hydrothermal aging for 100 h and 200 h.

DPF P durability

A P deactivation study on catalyzed cordierite and the catalyzed alternative DPF was done. The catalyzed alternative DPFs were exposed to P for 200 and 400 minutes, corresponding to 8g/L and 16g/L of P exposure. Figure 12 presents results for the effect of P exposure on the filtration efficiency of blank cordierite, catalyzed cordierite, and catalyzed alternative substrate. The results showed that the largest decline in efficiency occurred over the blank cordierite. The two catalyzed samples had similar losses up to about 7g/L P exposure, but the catalyzed alternative substrate declined more slowly than the catalyzed cordierite at P levels above that.

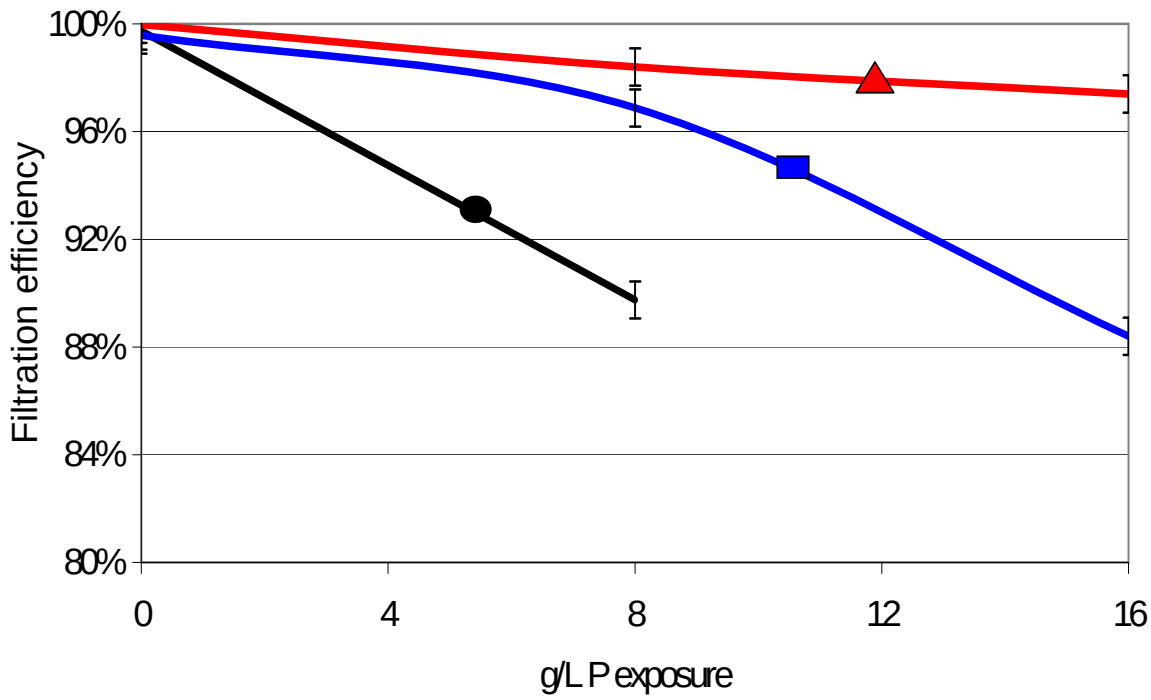

FIGURE 12. The effect of P exposure level on filtration efficiency over blank cordierite (#), catalyzed cordierite (!) and catalyzed alternative substrate (%). Error bars are shown at 8 g / L P exposure.

P exposure slightly affected the filtration efficiency but had no significant effect on pressure drop. The largest impact of the P exposure was on soot regeneration. Figure 13 shows the concentration of CO + CO_2 released during soot regeneration as a function of temperature at different levels of P exposure for catalyzed cordierite. Figure 14 shows similar results for the catalyzed alternative substrate and includes additional results for hydrothermal aging. . The fresh samples each show two peaks, with the lower temperature peak being larger than the high temperature peak for the alternative substrate and the opposite result obtained over the cordierite. The lower temperature peak is thought to be

associated with passive regeneration of soot, and the higher temperature peak is likely associated with active regeneration. As the samples are exposed to increasing levels of P, at first the passive regeneration peak declines in area and the CO + CO_2 emissions shift toward the high temperature peak. As P levels continue to increase up to 16g/L, the regeneration peak shifts all the way to the point where it is the same as the peak temperature found over blank cordierite, suggesting the P has completely deactivated the catalyst activity for soot regeneration.

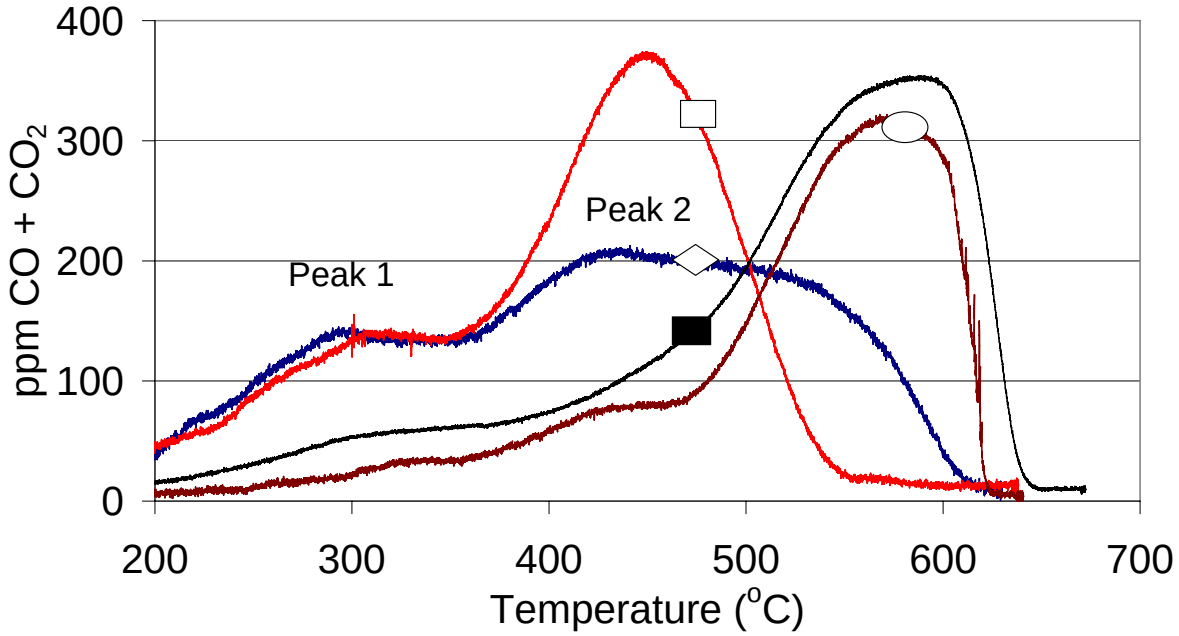

FIGURE 13. Concentration of CO + CO_2 from soot regeneration over catalyzed cordierite DPF as a function temperature for different levels of P exposure: ( )) Fresh, uncatalyzed; (') Fresh catalyzed; (( ) 8 g / L P aged catalyzed; (!) 16 g / L P aged catalyzed.

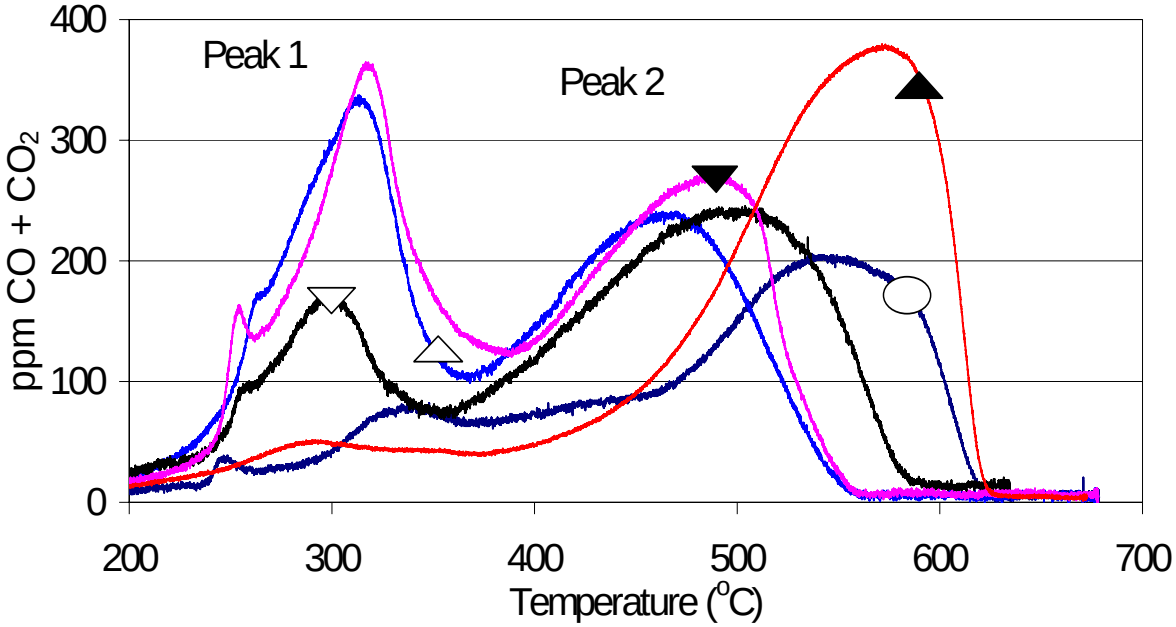

FIGURE 14. Concentration of CO + CO_2 from soot regeneration over alternative DPF substrate material as a function temperature for different aging protocols: ( )) Fresh, uncatalyzed ; (+) Fresh catalyzed; (&) Thermally aged catalyzed; (,) 8 g / L P aged catalyzed; (%) 16 g / L P aged catalyzed.

Conclusions

Results from the catalyst deactivation study over oxidation catalysts showed that exposure to 5g/L P reduces conversion of CO and HC over these samples by about 10%, which is about the same extent as it reduces NO_x reduction over SCR catalysts. The impact of P on LNTs is greater than that for oxicats or SCRs. In the case where P exposure is combined with S, the initial loss of activity proved to be reversible simply by repeating the evaluation test in S-free gas, suggesting that at an exposure temperature of 210°C the sulfur is a reversible contaminant. The addition of mild thermal aging was shown to be detrimental only when P and S were already on the surface. Exposing the catalyst to P and S at higher temperatures also increased the loss of performance. Based on previous work and work cited in the literature, it is thought that P impacts these catalysts by physically blocking adsorption sites.

Regarding DPFs, thermal aging had a minor effect on the filtration efficiency and pressure drop, while P aging drastically affected the regeneration capability of the filters.

Travel

1. Ron Silver traveled to Detroit, MI, to attend the 2006 SAE World Congress.
2. Herbert DaCosta traveled to Detroit, MI, to attend the 2006 DEER meeting.
3. Herbert DaCosta traveled to Boston, MA, to attend the 2006 COMSOL meeting.

Presentations/Publications

H. DaCosta C. Shannon, and R. Silver, "Thermal and Chemical Aging of Diesel Particulate Filters," submitted to the 2007 SAE World Congress.

H. DaCosta, C. Shannon and R.G. Silver, "DPF Durability – Bench Studies on Cordierite Filters," oral presentation at the 2006 DEER meeting, Chicago, IL (2005)

B. Ultra-High Resolution Electron Microscopy for Characterization of Catalyst Microstructures and Deactivation Mechanisms

*L. F. Allard, D. A. Blom, C. K. Narula, S. A. Bradley*and M. Jose-Yacaman***
Oak Ridge National Laboratory
P.O. Box 2008, MS-6064
Oak Ridge, TN 37831-6064

**UOP LLC, Des Plaines, IL 60017*
*** University of Texas-Austin, Austin, TX 78712*

DOE Technology Development Manager: Jerry L. Gibbs
(202) 586-1182; fax: (202) 586-1600; e-mail: Jerry.gibbs@ee.doe.gov
ORNL Technical Advisor: D. Ray Johnson
(865) 576-6832; fax: (865) 574-6098; e-mail: johnsondr@ornl.gov

Contractor: Oak Ridge National Laboratory, Oak Ridge, Tennessee
Contract No.: DE-AC05-00OR22725

Objectives

- Develop and utilize new capabilities and techniques for ultra-high resolution transmission electron microscopy (UHR-TEM) to characterize the microstructures of catalytic materials of interest for reduction of NO_X emissions in diesel and automotive exhaust systems.
- Relate the effects of reaction conditions on the changes in morphology of heavy metal species on "real" catalyst support materials (typically oxides).
- Develop capability to experimentally study the effects of experimental reaction treatments on TEM samples of NO_X trap catalyst materials before and after reactions, using the High-Temperature Materials Laboratory (HTML) "ex-situ" catalyst reactor with a specimen holder designed for use in the aberration-corrected electron microscope (ACEM).

Approach

- Utilize Oak Ridge National Laboratory ACEM to characterize the atomic morphology and behavior of heavy-metal species such as platinum and rhenium on oxide support materials (alumina, silica and titania) via techniques of annular dark-field (ADF) or "Z-contrast" imaging.
- Utilize ACEM ADF imaging and techniques of spectrum imaging to characterize the structure and chemistry of a series of model bimetallic nanoparticle comprising controlled compositions in the platinum/gold system.

Accomplishments

- Characterized the nature of platinum catalyst structures on alumina, silica and titania support materials, including the imaging of platinum species dispersed as single atoms and in precrystalline clusters known as "rafts." In particular, the different behavior of the Pt atoms, clusters and rafts on the support materials was characterized, as a function of electron beam excitation.
- Demonstrated the potential for the Z-contrast atomic imaging process to allow determination of the precise shapes of nanoparticles and clusters.
- Tested and demonstrated the functionality of a new catalyst reactor specimen rod for before-after studies of catalyst reactions.

Future Direction

- Focus on the use of the ACEM to characterize the location of sulfur species on NO_X reduction catalyst materials, to enable characterization of the mechanisms of sulfur poisoning of these materials. This will involve not only imaging of the catalysts at the single-atom level, but also the use of the electron spectroscopy capabilities on the ACEM to obtain chemical information at the atomic level.
- Continue to work on the critical problem of determination of precise shapes of catalyst nanoparticles to determine the most important characteristics for control of catalytic performance.
- Perform precisely controlled thermal experiments using ex-situ catalyst reactor to understanding the interaction of Pt atoms with catalyst supports, which is critical for the development of new and improved catalysts.

Technical Progress

Imaging of ultrafine atomic clusters of heavy metals on low atomic number supports has been demonstrated to provide a new level of capability for characterizing catalytic materials. The advent of research on the HTML's new aberration-corrected electron microscope (JEOL 2200FS-AC "ACEM"), has given us the ability to image the locations of heavy metal atomic species at the single-atom level, and to observe the different behaviors of, for example, Pt atoms and clusters dependent on the nature of the support materials, under the influence of the incident electron beam. Using the technique of high-angle annular dark-field imaging (HA-ADF) to image the heavy atoms in high contrast also allows the characterization of the structures of nanoparticles in the 1-3 nm size range, which represent structures found on typical "real" catalyst materials such as those used in commercial automotive systems. In this report, we show examples of the structures and behaviors of Pt species on alumina, silica and titania supports, which gives information on the different metal-support interactions of these systems. The analysis of the structure of discrete bimetallic Au/Pd particles suggesting the nature of "active sites" on the particles surfaces is also illustrated. The latter samples are part of a specimen suite provided by Prof. M. Jose-Yacaman of the University of Texas at Austin. The former samples, discussed first, represent work with colleagues S. A. Bradley and W. Sinkler of UOP Co. Pt on titania samples were provided originally by colleague C.K. Narula, in prior work when Dr. Narula was working at Ford Research Laboratory.

Imaging Pt on oxide supports: Although the preparation and properties of heterogeneous catalysts have been studied for decades, it is not well understood how fine dispersions of heavy metal species in "as-prepared" catalysts are arranged on common supports such as γ-alumina, titania, or amorphous silica. Aging or calcining treatments typically cause atomic level dispersions to coalesce into discrete particles of sizes >2 nm, which have crystal lattices that can be imaged using conventional high-resolution bright field imaging techniques. The present study, however, illustrates the advanced capability of aberration-corrected imaging to characterize catalysts comprising Pt on γ-Al_2O_3 and amorphous SiO_2; systems which have different metal-support interactions. To study the effect of the supports on metal cluster behavior, catalysts were prepared by impregnating the support materials with 0.35 wt. % Pt, and oxidizing the material at 525ºC. The Pt on γ-Al_2O_3 was then reduced at 500ºC in H_2. Samples were examined in ORNL's JEOL 2200FS FEG ACEM, fitted with a hexapole aberration-corrector (CEOS GmbH, Heidelberg, Germany) for the probe forming optics, which provides a nominal probe diameter of 0.07 nm (0.7Ångström) [1]. Goals of the investigation were to determine the number of atoms in a cluster and the structure of the cluster (or raft), investigate metal-support interactions, and by using an *ex-situ* reactor, to understand the formation of discrete metal clusters as a result of reduction of the oxidized catalyst.

Figure 1 shows an example of oxidized Pt on γ-Al_2O_3 at increasing magnification. The majority of the Pt species are in the form of single atoms, dimers and some small clusters. These are seen in greater detail in Fig. 2. No discrete particles or rafts were seen on this sample. However, after a hydrogen reduction treatment at 500°C in the ex-situ reactor, the Pt was observed to form rafts of 1-2 layers in

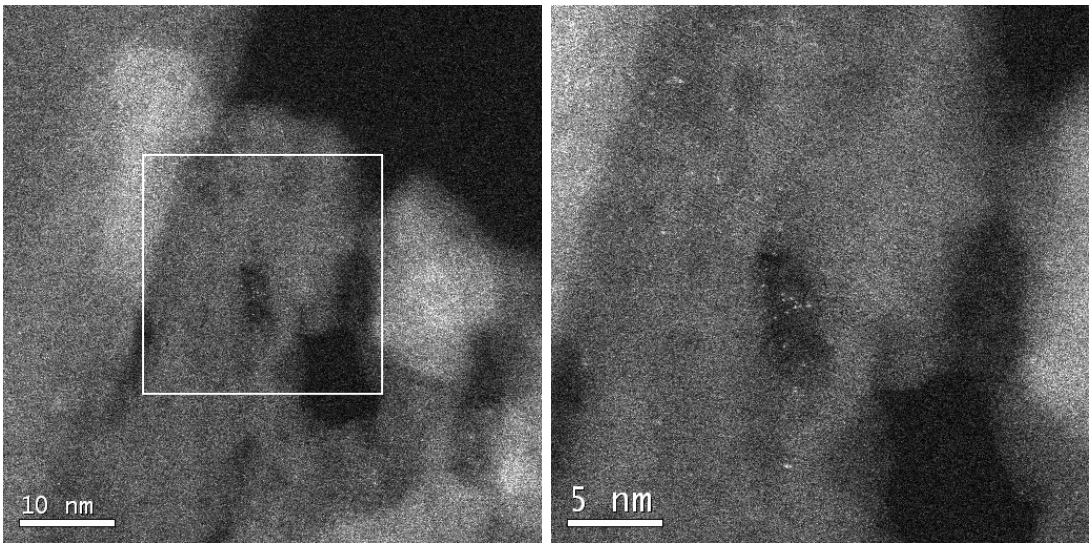

Figure 1. (a) Oxidized platinum species on γ- Al_2O_3; no large discrete particles are seen. b) higher magnification shows Pt dispersed in single atoms or dimers.

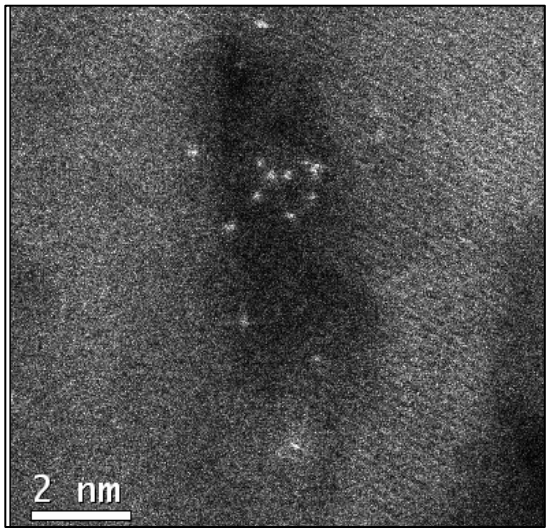

Figure 2. Detail of the central area on Fig. 1b. Only single atoms or dimers are present.

thickness, with some single atoms still present. It was interesting to note that, under the influence of the electron beam (which can be argued as representing effects similar to direct heating of the sample), the rafts tended to re-arrange their structures, but single atoms remained pinned to the support. Figure 3 shows a pair of images of the reduced sample, taken from a sequential series of images of the same area, several scans apart. The raft of atoms shows some changes in structure (but no dramatic change in size or structural rearrangements), while 3 single atoms remain clearly pinned in position. The oxidized Pt on silica sample was different from the equivalent Pt on γ-Al_2O_3 sample, in that it showed rafts similar to the reduced Pt on alumina, but also numerous single atoms, dimers and small clusters, as seen in Fig. 4. These rafts were very mobile under observation, and showed a tendency to sinter together into larger agglomerates under beam conditions similar to those used for the Pt/alumina sample. This suggests a stronger metal-support interaction in the Pt/alumina system compared to the Pt/silica system.

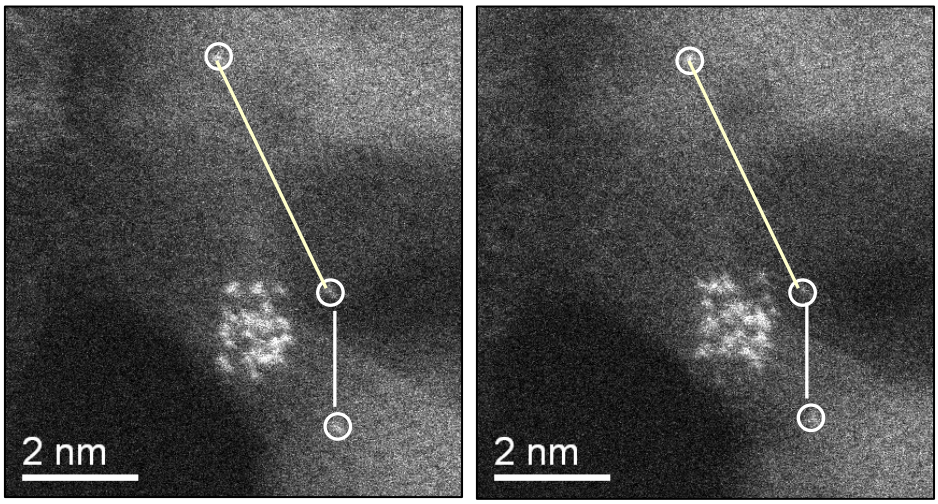

Figure 3. HA-ADF image pair from separate scans of Pt species on g alumina, after a reduction at 500°C in H2-Ar mixture. The raft represents a collection of 25-30 atoms, but 3 isolated atoms are also seen (circled). While the atoms in the raft are somewhat mobile under incident beam irradiation, the single atoms remain pinned to sites on the alumina surface.

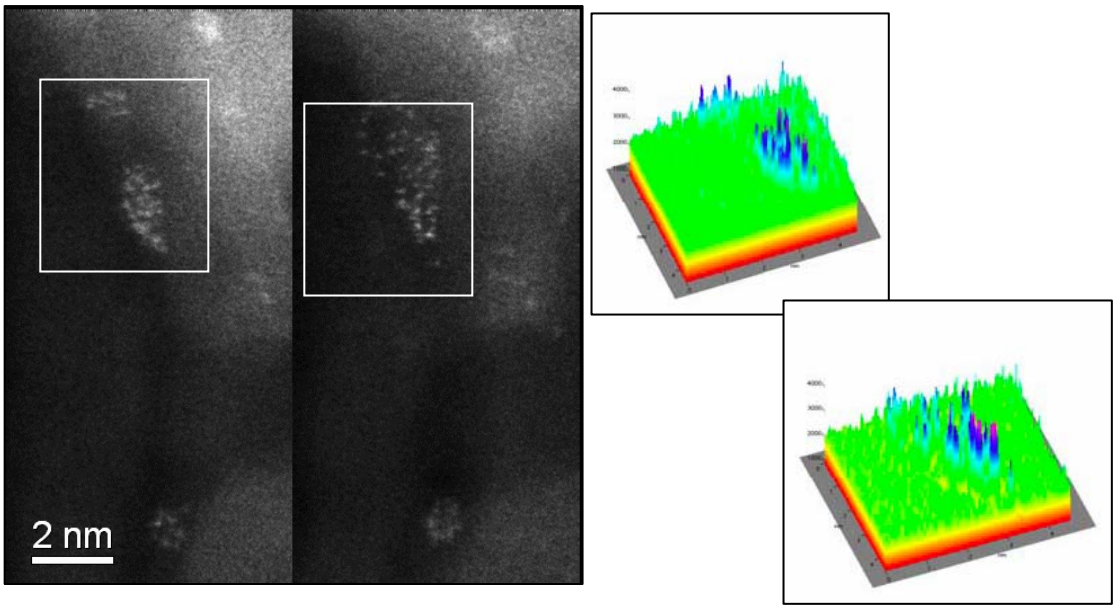

Figure 4. HA-ADF image pair from separate scans over rafts of Pt on amorphous silica. Insets show areas from which respective colorized intensity perspective views were taken. The mobility of the Pt species on the surface of the silica results in the conjoining of separate reafts into one larger aggregate of Pt atoms.

In the Pt/TiO2 (rutile) system, for a sample of 1% Pt reduced under conditions similar to the alumina and silica samples, the Pt species were observed to form small clusters with some rafts on the order of 1 nm in size, with also a significant fraction of individual atoms present. The Pt rafts tended to show alignment of atoms within the raft, and in line with the underlying rutile structure. Figure 5 is an example of the analyis of a Pt raft. The intensity profile over a line of Pt atoms suggests that the brighter atoms represent 2 atoms aligned directly atop one another, in comparison to an adjacent single atom at ½ the intensity.

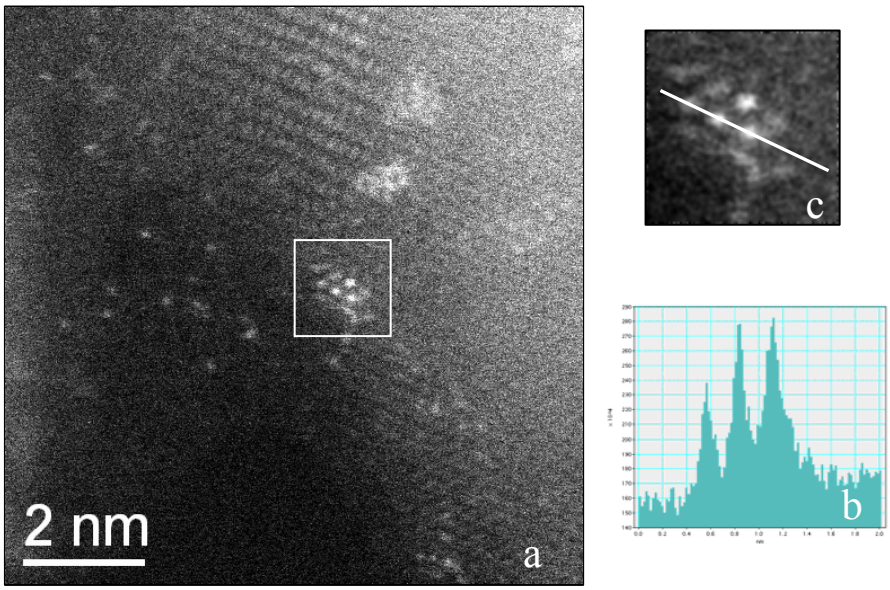

Figure 5. (a) Pt species deposited onto TiO2 (rutile) support material. Note regular underlying lattice image contrast from the rutile structure. Inset (b) shows one raft with atoms aligned along rutile planes. An intensity profile (c) as indicated in (b) suggests the bright triangle of atoms results from an essentially perfect alignment of atoms on a second layer, directly above the first layer atoms, giving twice the intensity in the HA-ADF image.

A final example of our capability to study the behavior of these catalyst systems before and after reaction treatments is shown in Fig. 6. This image pair shows the same sample area of Pt on γ-Al_2O_3 at medium magnification, before and after a reduction treatment. There is almost a single-atom level dispersion of Pt species prior to reduction, and these atoms have agglomerated into rafts about 1 nm in size after reduction. There are small changes in the underlying alumina structure, but it is easy to recognize that the areas are essentially equivalent. This remarkable capability will be used routinely in further work on these catalyst systems.

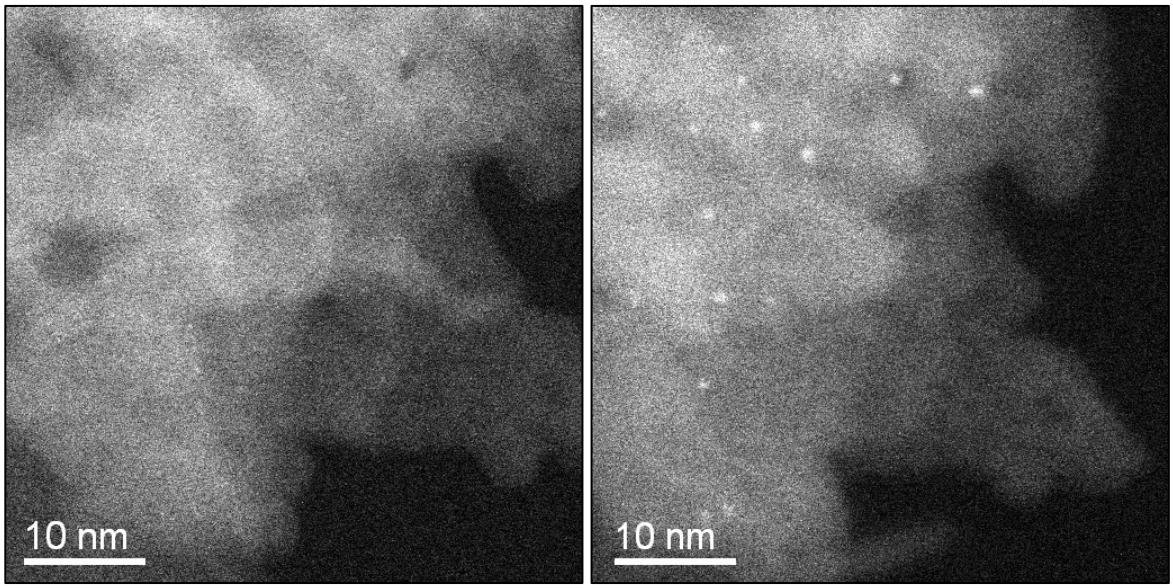

Figure 6. a) "Before" HA-ADF image of oxidized Pt species on γ- Al_2O_3, showing high dispersion of Pt. b) Identical area "After" reduction treatment in ex-situ reactor. Pt aggregates into small clusters and rafts 0.5-1.0 nm in size.

Imaging Au/Pd nanocrystals: It has been known for several years that the addition of a second metal into monometallic nanoparticles significantly changes some of their properties, e.g. optical properties, catalytic properties, electronic properties, etc. [2,3]. When two or more different elements compose one nanoparticle, the differences in atomic radii are going to influence the way the atoms accommodate. However, very little is known about the crystal structure of bimetallic nanoparticles in the size regime from 0.5 to 2 nm [4]. For bimetallic nanoparticles composed of a noble metal and a transition metal, recent experimental results indicate that an icosahedral phase structure is preferred over the others [5]. In the present work we are conducting a complete study of the structure, size, shape, optical response and catalytic properties of single, bimetallic and multimetallic nanoparticles.

Figure 7 shows an aggregate of minimal Au1Pd5 nanoparticles which show significant variations in intensity in atomic columns, e.g. as indicated in the inset. The particle is near a <100> projection. Intensity profiles over several single atoms on the adjacent thin carbon film indicated intensity levels of ~900 and ~500 units, suggesting that these represented Au and Pd atoms, respectively. The profile over the row in the inset suggests that the column with the highest intensity must contain one or more Au atoms. The observed intensity, if considering only Pd atoms in the column, would indicate a column thickness at least 3 atoms greater than surrounding columns, an energetically unfavorable situation. Results such at these are at the leading edge for analysis of the structures of bimetallic nanoparticles, but correlation to ADF image and DFT structure calculations will provide more reliable interpretation as we continue to develop our imaging expertise with the sub-Ångström resolution of the ACEM.

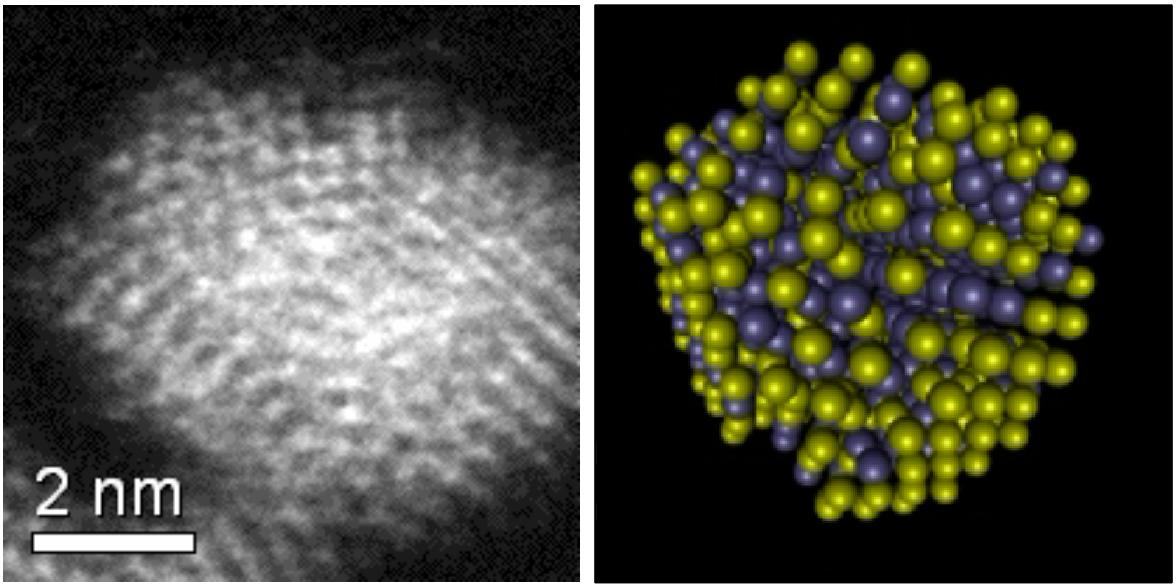

Figure 7. a) HA-ADF image of particle with nominal Au1-Pd1 composition. B) Density Functional Theory computation of Au1Pd1 nanoparticle, originally created as a perfectly ordered multiply-twinned particle, then heated to 1000K and cooled to RT. The latter disordered configuration is a reasonable match to the observed particle, with numerous irregular surface sites.

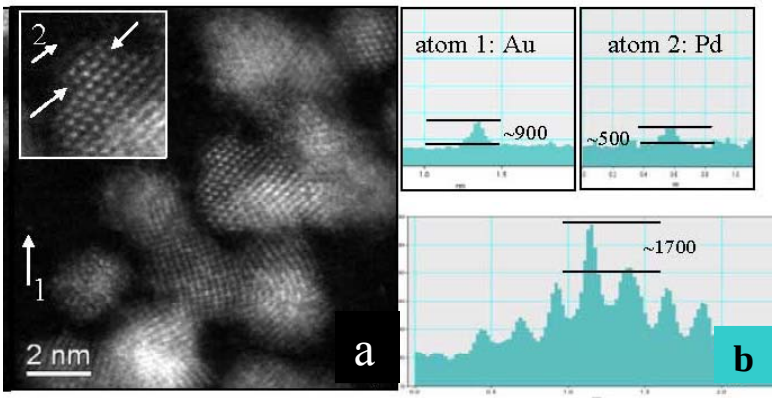

Figure 8. (a) Aggregate of Au1Pd5 nanoparticles in 2-4 nm size range. Inset shows variation in intensity of atomic columns; b) intensity profile over atom row arrowed in inset. Profiles of individual atoms labeled 1 and 2 suggest the intensity associated with Au and Pd respectively. Central column intensity in (b) is too great to represent only Pd atoms; therefore one or more Au atoms must be present.

References

1. M. A. O'Keefe, L. F. Allard, S. J. Pennycook and D. A. Blom, "Transcending the One-Ångström Atomic Resolution Barrier in the TEM," *Microsc Microanal* 12(Supp 2), Cambridge University Press, p. 162-163 (2006)
2. A.M. Venezia, V. La Parola, V. Nicolì and G. Deganello, J. Catalysis 212, 56-62 (2002)
3. L. Guczi, et al., *Surface and Interface Analysis*, **34**(1) 72-75 (2002)
4. J.L. Rodriguez-Lopez J.L., et al., *Physical Review Letters* **92**(19) 2004
5. M. Jose-Yacaman, et al., *J.Vac. Sci. & Tech. B*, **19**(4) 1091-1103 2001

Presentations and Publications

D. A. Blom, S. A. Bradley, W. Sinkler and L. F. Allard, "Observation of Pt Atoms, Clusters and Rafts on Oxide Supports, by SubÅngström Z-Contrast Imaging in an Aberration-Corrected STEM/TEM," *Microsc Microanal* 12(Supp 2), Cambridge University Press, p. 50-51 (2006)

M. José-Yacamán, S. Mejía-Rosales, E. Pérez-Tijerina, D.A. Blom and L.F. Allard, "Imaging Au-Pd Nanoparticles with the Aberration-Corrected STEM/TEM," *Microsc Microanal* 12(Supp 2), Cambridge University Press, p. 772CD (2006)

D. A. Blom, L. F. Allard, S. Mishina and M. A. O'Keefe, "Early Results from an Aberration-Corrected JEOL 2200FS STEM/TEM at Oak Ridge National Laboratory," Microsc Microanal 12, Cambridge University Press, p. 483-491 (2006)

M. José-Yacamán, S. Mejía-Rosales, E. Pérez-Tijerina, D. A. Blom and L. F. Allard, "Catalyst Characterization Coupling Cs-Corrected High-Angle Annular Dark-Field Imaging with Molecular Dynamics Calculations," ICM16, Sapporo, Japan, p. 1554 (2006)

C. K. Narula, M. J. Moses and L. F. Allard "Analysis of Microstructural Changes in Lean NO_x Trap Materials Isolates Parameters Responsible for Activity Deterioration," SAE 2006-01-3420, Dearborn, MI (2006).

C. Development of NO_x Sensors for Heavy Vehicle Applications

David L. West, Fred C. Montgomery, Timothy R. Armstrong, Jaco H. Visser, and David J. Kubinski**
Oak Ridge National Laboratory
P.O. Box 2008, Mail Stop 6054
Oak Ridge, TN 37831-6054
(865) 576-2264; fax: (865) 574-1249; e-mail: westdl@ornl.gov

**Scientific Research Laboratory, Ford Motor Co.*

DOE Technology Development Manager: Jerry L. Gibbs
(202) 586-1182; fax: (202) 586-1600; e-mail: Jerry.gibbs@ee.doe.gov
ORNL Technical Advisor: D. Ray Johnson
(865) 576-6832; fax: (865) 574-6098; e-mail: johnsondr@ornl.gov

Contractor: Oak Ridge National Laboratory, Oak Ridge, Tennessee
Prime DOE Contract No.: DE-AC05-00OR22725
Subcontractor: Ford Motor Company, Detroit, Michigan

Objectives

- Develop NO_x sensors for remediation and monitoring of diesel engines.
- Develop sensors that have an operating temperature of 500–700°C and are able to measure NO_x concentrations from ~10–200 ppm at oxygen levels from 5 to 20 vol %.
- Ensure that sensors are selective for either NO (insensitive to NO_2), or able to measure "total NO_x" (combined NO + NO_2).

Approach

- Fabricate prototype sensing elements by screen printing electrode layers onto oxygen-ion conducting [typically yttria stabilized zirconia (YSZ)] substrates.
- Operated elements either in a "non-Nernstian" mode (where the output is a voltage) or under direct current electrical bias.
- Characterize sensor in bench setting for NO_x sensor response, sensitivity to varying [O_2] and the interferents propylene (C_3H_6), CO, and stability under long-term operation.

Accomplishments

- Developed sensing elements with improved long-term stability by modifying electrode architecture.
- Sensing elements displayed near "total NO_x" behavior.
- Sensitivity to C_3H_6 and CO was observed, indicating an oxidation catalyst will be required in the sensor.

Future Direction

- Dynometer testing at Ford Motor Co.

Introduction

Environmental stewardship is placing increasing demands on emission control of vehicle exhausts. For spark ignited, direct injection (SIDI) engine exhausts, these demands are largely being met with the use of a "three-way catalyst" (TWC), capable of simultaneously removing carbon monoxide (CO), hydrocarbons (C_yH_z), and oxides of nitrogen (NO_x). Unfortunately, the current generation TWC is only effective for all three of these pollutants within a narrow range of oxygen concentrations ([O_2]), losing its effectiveness for NO_x reduction in the presence of excess O_2 (Fig. 1). Thus existing TWCs cannot be used for NO_x remediation of the O_2-rich exhausts from diesel engines.

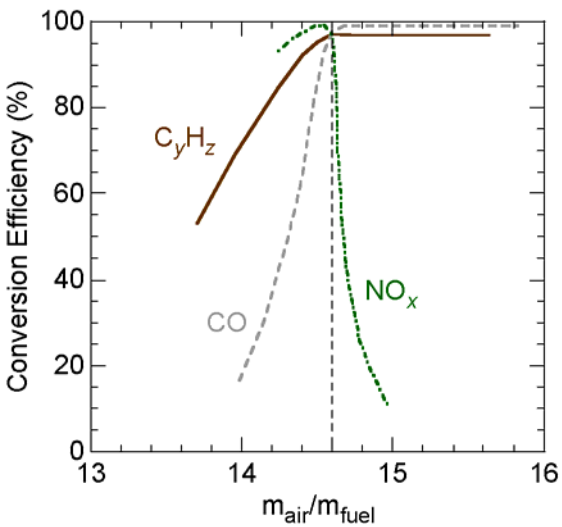

Figure 1. Three-way catalyst (TWC) efficiency.[1] As m_{air}/m_{fuel} is increased through ~14.6 ("stoichiometry") the O_2 content of the exhaust will increase by several orders of magnitude. This increased O_2 content strongly inhibits reduction of NO_x to N_2 and O_2.

Two technologies proposed for NO_x remediation of diesel exhausts are the lean-NO_x trap (LNT), and selective catalytic reduction (SCR). Both of these approaches require on-board NO*x* sensors, to control trap regeneration in the case of LNT or reagent injection in the case of SCR.

The "NO_x" in combustion exhausts is typically a mixture of nitric oxide (NO) and nitrogen dioxide (NO_2), with NO predicted to be the dominant equilibrium species above ~500 ^oC[2]. However, equilibrium conditions cannot be assumed for the exhaust and the relative abundances of NO and NO_2 in the exhaust rarely are known with certainty. In such a situation it will be useful to have a "total NO_x" sensor that possesses equal response characteristics to either NO or NO_2. Such a sensor would measure [NO] + [NO_2].

In this project ORNL is developing "total NO_x" sensing elements that can be used in diesel engine exhausts. The *minimum* requirement for this application is an operating temperature of 600–700°C and the ability to measure 10–200 ppm NO_X. The project is a cooperative research and development agreement (CRADA) with Ford Motor Company.

Approach

The approach selected is to build a sensing platform on yttria-stabilized zirconia (YSZ). YSZ, an oxygen-ion conducting material, is widely used in oxygen sensors for gasoline engines. Two other NO_X sensors based on YSZ are also near commercialization but these two designs have shortfalls; either poor sensitivity at low NO_x or reliance on conversion of the NO_x to NO_2 before sensing. In addition, both are relatively complex with multicavity constructions. This construction is required because in the first design[3] preliminary O_2 removal from the sampled exhaust is required before the NO_X is measured amperometrically. In the second design[4] the sampled exhaust must pass over a conversion electrode in order to convert the NO_X into NO_2 before detection in the sensing cavity.

Most of the work at ORNL has focused on the sensing *element* portion of the sensor (the portion of the sensor that responds to the presence of NO_x), the CRADA partner (Ford) has been focusing on the packaging and electronics required to make a working sensor. ORNL fabricates sensing elements by screen-printing electrodes onto YSZ substrates and subsequently firing. The elements are then tested for sensing performance using a furnace to simulate elevated temperature service and a commercial gas mixing unit to deliver blends of N_2, O_2, NO_X (either NO or NO_2), and other species as required.

Results

During FY 05 "all-oxide" total NO_x sensing elements were developed and characterized. As indicated in the previous year's report two main challenges in bench-top testing remained. First, the

long-term stability of the elements had to be improved (the "background" signal drifted) and the response to potential interferents such as CO and hydrocarbons needed to be characterized.

In order to improve the long-term stability of the sensing elements the electrode architecture was altered to improve the electronic conductivity. This alteration involves partially overcoating the electrodes with a noble metal. This will cause small increase in materials and manufacturing cost, but the CRADA partner felt that reduction/elimination of sensor drift could readily justify a small cost increase in the sensing element.

Figure 2 illustrates the stability of a sensing element with the improved electrode architecture. Over approximately one day of continuous operation, the output from the sensor only changes by about 1%. This is much smaller than the changes induced by ~100 ppm NO_2 (also shown in Fig. 2) and shows that the drift has been reduced to a more manageable level.

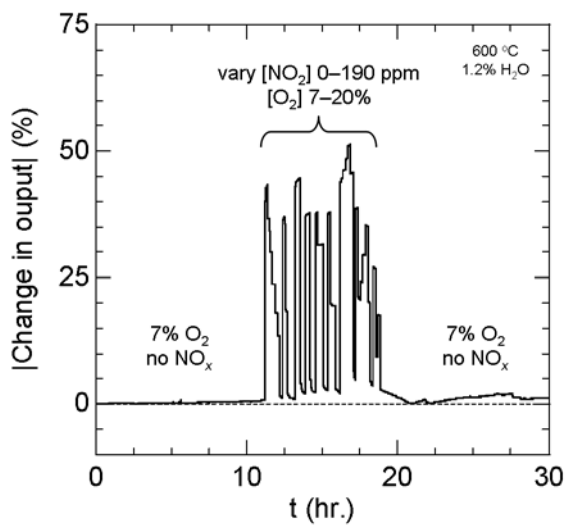

Figure 2. Drift of signal with time for sensing element with improved electrode architecture

As mentioned previously, the NO_x in diesel exhaust is a mixture of NO and NO_2, with the relative amount of each typically unknown. Therefore it is important that the sensing element yield approximately the same response irrespective of the [NO]:[NO_2] ratio present. Some data verifying this important characteristic appears in Fig. 3, which shows the sensor output as [NO]:[NO_2] is varied under conditions of 100 ppm NO_x. Varying the NO_2 content from ~50 to 0%* induced an approximately 6% change in the output signal. This shows that the sensing element is fairly insensitive to the relative abundance of the two NO_x species.

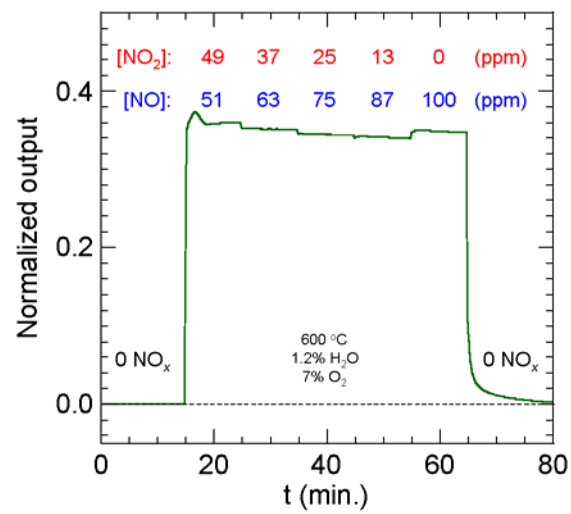

Figure 3. Response trace showing how the sensing element output changes with [NO]:[NO_2].

The final two characteristics evaluated for these sensing elements with improved electrode architecture were their response to changing [O_2] and the effect of the potential interferents CO and hydrocarbons. The effect of changing O_2 is particularly important as diesel exhaust will typically contain between 10 and 15% O_2.[5]

The effect of changing [O_2] under conditions of fixed [NO] and [NO_2] is illustrated in Fig. 4. Changing [O_2] does affect the sensing element output, indicating that an independent assessment of [O_2] will be required during operation of the sensor. However, the CRADA partner indicated that this may be preferable to the O_2 pumping step required with the current amperometric NO_x sensor[3].

Figure 5 shows how the potential interferents CO and C_3H_6 (propylene, a "representative" hydrocarbon) affected the sensor output. It can be seen these species do affect the sensor output when present at concentration levels around 100 ppm. Fortunately, these species are easily eliminated with an oxidation catalyst in the O_2-rich diesel exhaust environment (as Fig. 1 suggests). One of the

*Increasing the NO_2 content from 50 to 100% also caused an approximate 6% change in the signal relative to its value at [NO]:[NO_2] = 1:1.

commercial sensors mentioned earlier[4] incorporates such an oxidation catalyst, so the need for a similar catalyst with the sensing elements described herein does not represent a substantial disadvantage.

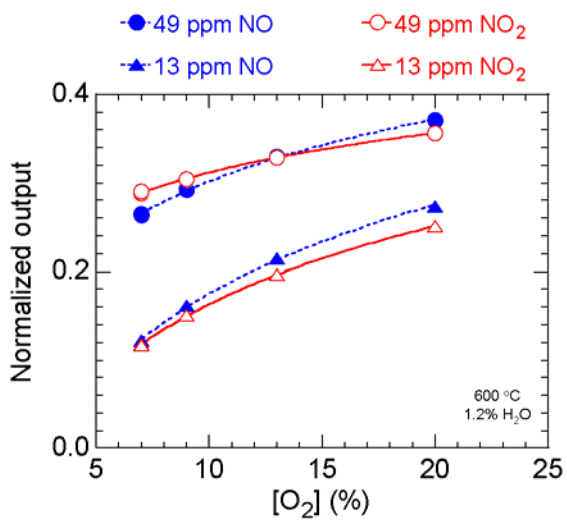

Figure 4. Change in sensor output with oxygen content.

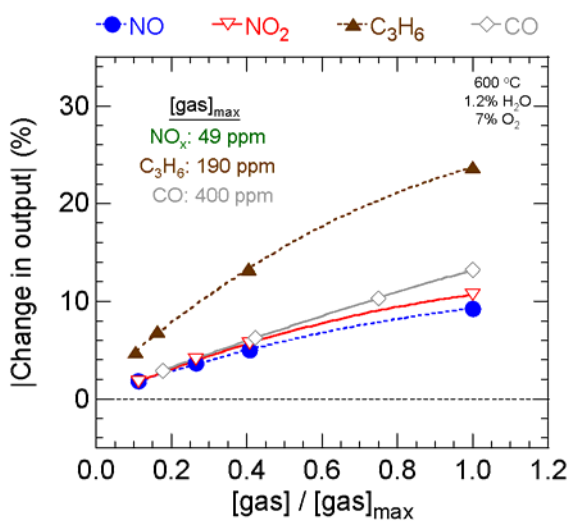

Figure 5. Comparative response to NO_x, C_3H_6, and CO.

Conclusions

Sensing elements that are capable of "total NO_X" sensing behavior have been further improved during FY 06. The drift of these sensing elements was dramatically reduced by altering the electrode architecture. The sensing elements are sensitive to changing $[O_2]$ and the potential interferents CO and propylene (C_3H_6). Therefore an independent assessment of $[O_2]$ as well as an upstream oxidation catalyst will be required.

References

1. J. Woestmann and E. Logothetis, "Controlling automotive emissions," *The Industrial Physicist*, **1**, 21, 1995.
2. K. Schnell and C. Browne, "NO_X control," in *Air pollution control technology handbook*, CRC Press, 2001, pp. 241–255.
3. N. Kato, H. Kurachi, and Y. Hamada, "Thick film ZrO_2 sensor for the measurement of low NO_X concentration," SAE Technical Paper 980170, 1998.
4. A. Kunimoto, M. Hasei, Y. Yan, Y. Gao, T. Ono, and Y. Nakanouchi, "New total-NO_X sensor based on mixed potential for automobiles," SAE Technical Paper 1999-01-1280, 1999.
5. J. Kaspar, P. Fornasiero, and N. Hickey, "Automotive catalytic converters: Current status and some perspectives," *Catalysis Today*, **77**, 419, 2003.

Patents

1. F. C. Montgomery, D. L. West, and T. R. Armstrong, "NO_X sensing devices having conductive oxide electrodes," U.S. Patent App. 20060073070 (2006).
2. F. C. Montgomery, D. L. West, and T. R. Armstrong, "NO_X sensing devices having conductive oxide electrodes," Int. Pat. App. PCT/US2005/034279, 2006.

Presentations and Publications

1. D. L. West, F. C. Montgomery, and T. R. Armstrong, "Total NO_X sensing elements with compositionally identical oxide electrodes," *Journal of the Electrochemical Society*, **153**, H23–8, 2006.

D. Development of Materials Analysis Tools for Studying NO_x Adsorber Catalysts (CRADA No. ORNL-02-0659 with Cummins, Inc.)

Thomas Watkins, Larry Allard, Doug Blom, Michael Lance, and Harry Meyer
Oak Ridge National Laboratory
P.O. Box 2008
Oak Ridge, TN 37831-6064
(865) 574-2046; fax: (865) 574-3940; e-mail: watkinstr@ornl.gov

DOE Technology Development Manager: Jerry L. Gibbs
(202) 586-1182; fax: (202) 586-1600; e-mail: jerry.gibbs@ee.doe.gov
ORNL Technical Advisor: D. Ray Johnson
(865) 576-6832; fax: (865) 574-6098; e-mail: johnsondr@ornl.gov

---

Contractor: Oak Ridge National Laboratory, Oak Ridge, Tennessee
Contract No.: DE-AC05-00OR22725

Objective

- The objective of this effort is to produce a quantitative understanding of the processing and in-service effects on NO_x adsorber catalyst technology leading to an exhaust aftertreatment system with improved catalyst performance capable of meeting the 2007 Environmental Protection Agency (EPA) emission requirements in the United States.

Approach

- Characterize lab-engine tested samples with X-ray diffraction (XRD), spectroscopy, and microscopy. Correlate findings with Cummins data and experience.

Accomplishments

- Supported continued characterizations of new materials from various stages of the catalyst's life cycle.
- X-ray diffraction, X-ray photoelectron Spectroscopy and Scanning Transmission Electron Microscopy were used to evaluate the thermal degradation of a NO_x storage and reduction (NSR) catalyst within the catalyst support brick as a function of macroscopic position, catalyst history and operating conditions.
- Completed two studies characterizing a new catalyst system and a diesel oxidation catalyst in the unused and aged states.

Future Direction

- Assist Cummins to competitively produce engines which attain the required emission levels for 2010 and beyond while maintaining the advantage of the diesel's inherent energy efficiency.
- Evaluation of hydrothermal aging of a SCR catalyst.
- Continue to characterize the soot, coke and ash formed on the catalyst from different fuels, including biodiesel.

Introduction

In order to meet the 2007 US Environmental Protection Agency (EPA) emission requirements for diesel exhaust, aftertreatment in diesel engines may be necessary. The technology necessary for 2007 will need to integrate aftertreatment with engine control systems. Currently, no commercial off-the-shelf technologies are available to meet these standards. Consequently, Cummins Inc. is working to understand the basic science necessary to effectively utilize these catalyst systems. ORNL is assisting with the materials characterization effort. Prior reports and presentations have covered the accomplishments related to the NO_x adsorber catalyst technology, this report will focus on the diesel oxidation catalyst (DOC) study.

A diesel oxidation catalyst (DOC) is a flow through device composed of a porous honeycomb structure within which a high surface area ceramic washcoat is situated. Small amounts of precious metal are dispersed within the washcoat and provide the catalytic activity necessary to oxidize carbon monoxide, gaseous hydrocarbons and liquid hydrocarbon particles (unburned fuel and oil).[1] Regulated emissions are thus controlled.

Base metal oxides (BMOs) and precious metals are major and critical components in current DOCs, respectively, that Cummins seeks to use. The microstuctural, chemical and phase changes of these components are of great interest as DOCs experience aging/normal operating conditions. Ultimately, it is desired to prevent/control these changes such that this technology becomes commercially viable.

Approach

In general, the crystal structure, morphology, phase distribution, particle size, and surface species of catalytically active materials supplied by Cummins will be characterized using transmission electron microscopy (TEM), X-ray diffraction (XRD), X-ray photoelectron spectroscopy (XPS), and Raman Spectroscopy. These materials will come from all stages of the catalyst's life cycle: raw materials, as-calcined, sulfated, regenerated, etc. Both ORNL and Cummins personnel have participated in this work.

Samples

Briefly, Cummins provided various series of "core" samples taken from cordierite "bricks" containing and an aluminosilicate support. The general features of each series will be given below in the text as needed. The brick/core samples consisted of a new/never-been-used DOC and an aged DOC. Here, the aged DOC originate from the same unused DOC. Aging was accomplished in a retort oven at 700°C for 24 hours, with 10% water added.

Results

The above samples were examined with XPS, Raman, XRD and TEM from October 2005 to September 2006, which is summarized below.

Spectroscopy

Spectroscopic techniques provide important information about the chemical state of and identification of adsorbed surface species. Two complementary spectroscopic techniques are X-ray Photoelectron Spectroscopy (XPS) and Raman Spectroscopy which provide low frequency vibrational and molecular vibrational information, respectively.

X-ray photoelectron spectroscopy (XPS) was used to examine compositional variations along the length (~5 cm) of individual "troughs" or channels of the new and aged samples The average surface compositions are shown in Table I. Single-trough samples were prepared by sectioning out a layer containing 8-10 troughs from the interior of the honeycomb core. Equidistant positions along 2 separate troughs were defined; two sets of data were taken within each trough (15 points/trough), analyzed and averaged. For the new sample, a third trough was examined 5 months after the first two, confirming the reproducibility of the data (i.e. no significant change with time). The compositional variation along the troughs is demonstrated in Figures 1 and 2 for the new and aged DOCs, respectively. Each shows two graphs, one for the major elements (O, Al, Si, and C) and one for the minor elements (N, Pt, and F) identified. Presently, the origin of F is unknown. The figures show a small decrease in the amount of O within in the probe depth and a slight increase in the amounts of Pt, Al and C in the aged relative to the new DOC.

The amount of Si seems unchanged, and the variability of N and F is inconclusive. Examination of the individual runs (not shown), made prior to adding/averaging, show the O, C, and Al data were more scattered, which could be due to the atmospheric contamination for O and C. The origin of the changes in Al is unclear, as absence of magnesium indicates that the signal originates from

Table I. Surface composition (atom %) of new and aged DOC samples averaged from data taken along the length of a single trough using XPS.

Average Composition per Trough

New

	O	Al	Si	C	N	F	Pt
T-1+2	58.5	25.1	11.0	4.6	0.33	0.34	**0.13**
T-3	61.4	24.6	10.4	2.6	0.60	0.25	**0.12**

Aged

	O	Al	Si	C	N	F	Pt
T-1	56.4	28.4	11.2	3.2	0.40	0.22	**0.20**
T-2	56.8	26.2	10.3	5.5	0.62	0.43	**0.23**

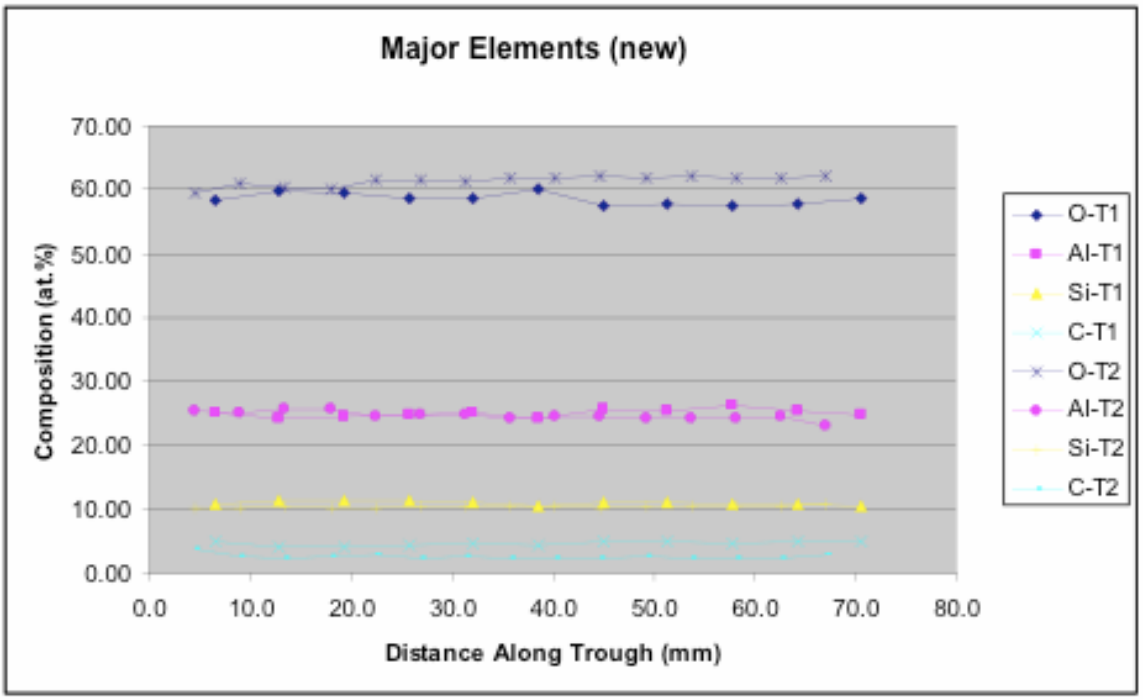

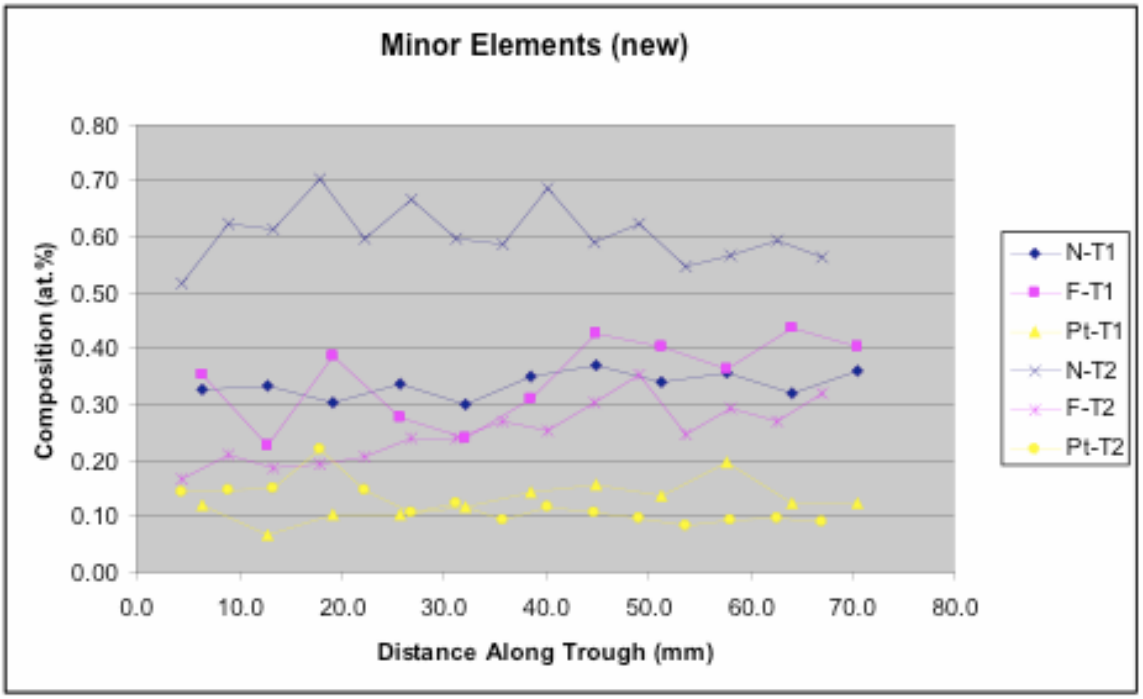

Figure 1. Typical XPS results showing the major and minor elements in the new/unused DOC sample along two troughs (1&2) of the cordierite honeycomb.

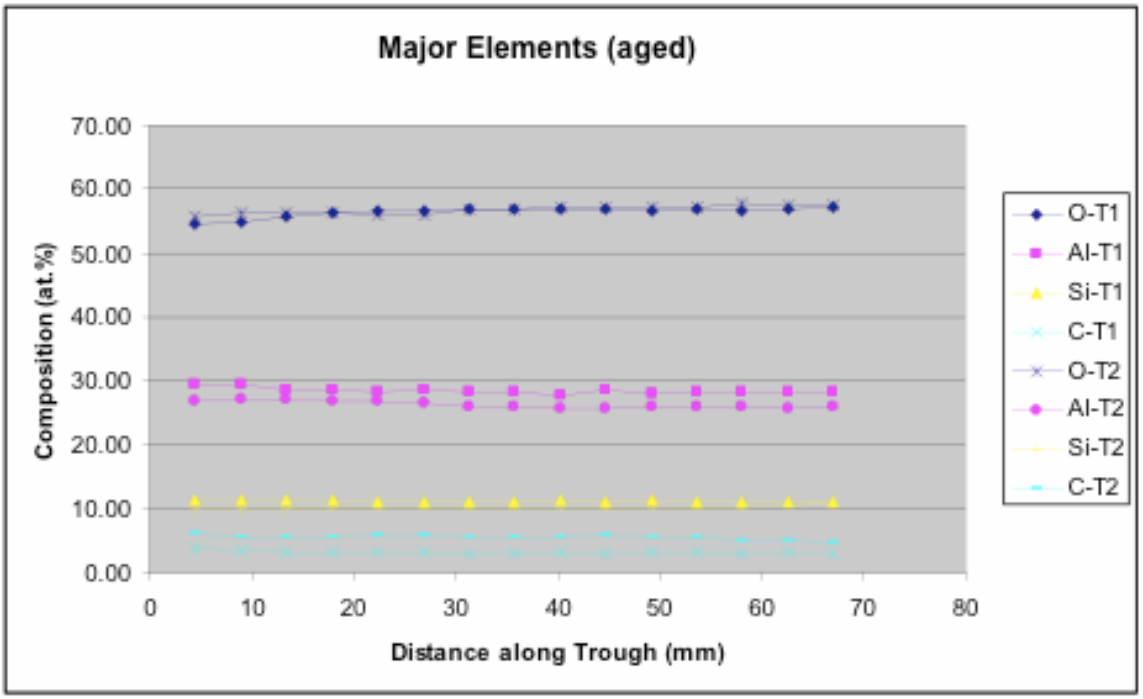

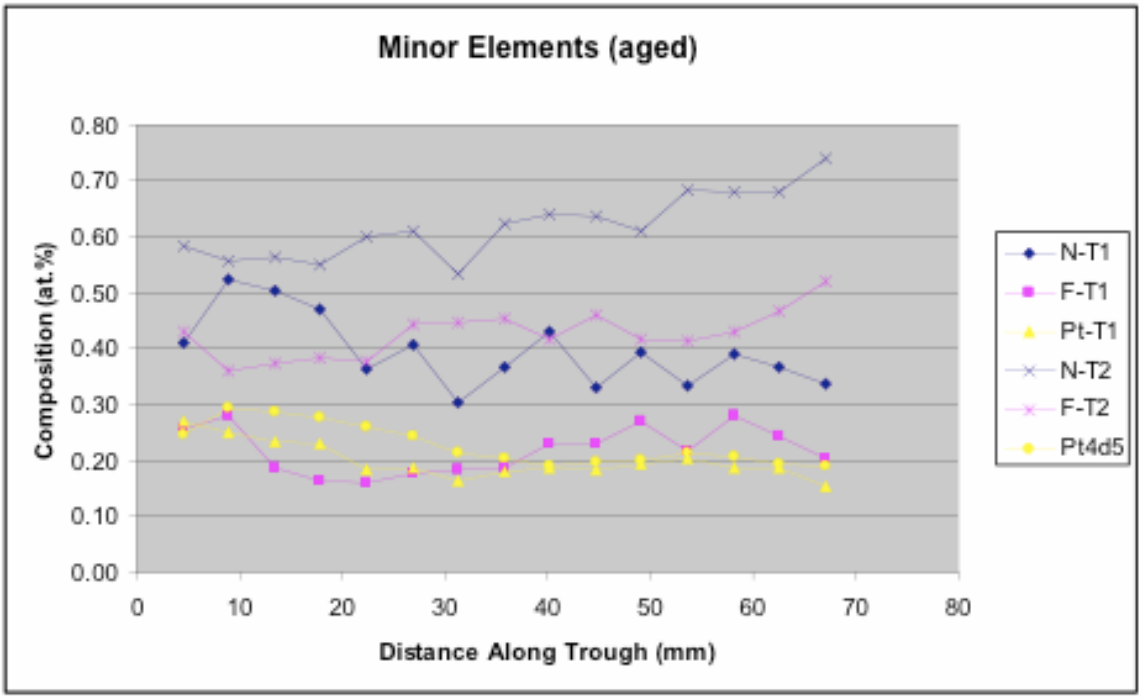

Figure 2. Typical XPS results showing the major and minor elements in the aged DOC sample along two troughs (1&2) of the cordierite honeycomb.

the washcoat only. The washcoat likely contains some sort of alumino-silicate, based on the majority elements. In contrast, the Pt scans were more consistent, trough-to-trough and run-to-run. Based on this, two major conclusions can be drawn from these data. First, the aging process does not influence the nominal composition of the *major* elements or change the uniform distribution along the trough. Second, the Pt signal is nearly doubled for the aged sample and implies that Pt atoms have migrated/redistributed to the near surface region (~5-10 nm, i.e. the probe depth for XPS).

Raman spectroscopy measures the characteristic vibrational energy levels of molecules and crystals and so is very sensitive to any changes in bonding, stoichiometry and phase/symmetry. Raman spectroscopy confirmed the presence of γ-alumina in the washcoat (see Figure 3). There is evidence to suggest a small a mount of θ-alumina *may* also be present.

X-ray

X-ray diffraction (XRD) was employed to understand the crystalline nature of the samples. For the unfamiliar, the following analogy can be applied: As a fingerprint identifies a person, so a diffraction pattern identifies a crystalline material.

In Figure 4, XRD indicates that the sample contains orthorhombic cordierite ($2MgO•5SiO_2•2Al_2O_3$) and platinum. The broad peak at low angle at ~20° 2Θ is due to an amorphous phase, possibly part of the washcoat. Previously, γ-alumina was tentatively identified within the washcoat of the new DOC. Figure 5 compares the XRD patterns of the new/unused and aged DOC samples showing the marked crystallite size growth of the Pt (<1, i.e., not observable, to ~30 nm).

Microscopy

Scanning Transmission Electron Microscopy (STEM) techniques were used to characterization of the microstructure of the on both the new and aged DOCs. In the new sample, a majority of the washcoat/support is found to be amorphous (see above), and energy dispersive spectroscopy (EDS) indicates the presence of Si, Al and O (perhaps alumina and silica). The washcoat contains Pt metal crystals, which are 1 - 4 nm in size (see Figure 6). Much of the Pt is atomically dispersed as seen with Aberration-corrected STEM. This is the first time such a non-ideal sample has been examined in this fashion. Small clusters of Pt (1-3 atoms thick) are also observed. For thicker areas, the more limited depth of field in aberration-corrected STEM provides richer, 3D data to be extracted by using a focusing/defocusing technique over ~5nm. Again, this is the first time that this has been applied to large cluster. The *aged* sample demonstrated evidence of massive Pt sintering (see Figure 7), which is consistent with the XRD results above. Small nanocrystals, atomic clusters, and single atoms are also still present (see Figure 8). In Figure 9, the moderately sized nanocrystals are surrounded by "cloud" of Pt clusters, which suggests a redispersion of Pt, supporting the XPS result above The mechanism is presently unknown but the electron beam from the STEM has been eliminated as a potential cause due to lack of change with time. Finally, the Pt atoms are observed to preferentially attach to alumina planes in the support.

References

[1] Washington State University Extension Energy Program, Diesel Oxidation Catalyst, http://www.energy.wsu.edu/pubs/.

Acronyms

BMOs	Base metal oxides
DOC	diesel oxidation catalyst
EDS	Energy dispersive spectroscopy
EPA	Environmental Protection Agency
NO_x	Nitrogen and Oxygen containing compounds
ORNL	Oak Ridge National Laboratory
SCR	selective catalytic reduction
STEM	Scanning Transmission Electron Microscopy
XPS	X-ray photoelectron spectroscopy
XRD	X-Ray Diffraction

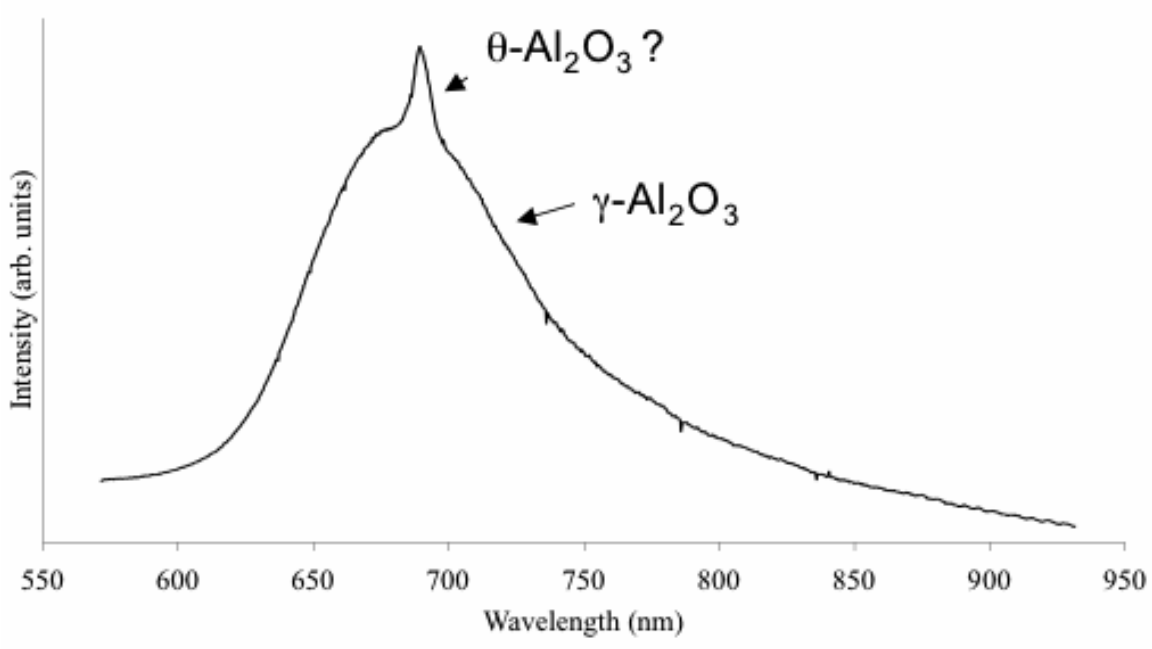

Figure 3. Raman spectrum of the DOC washcoat.

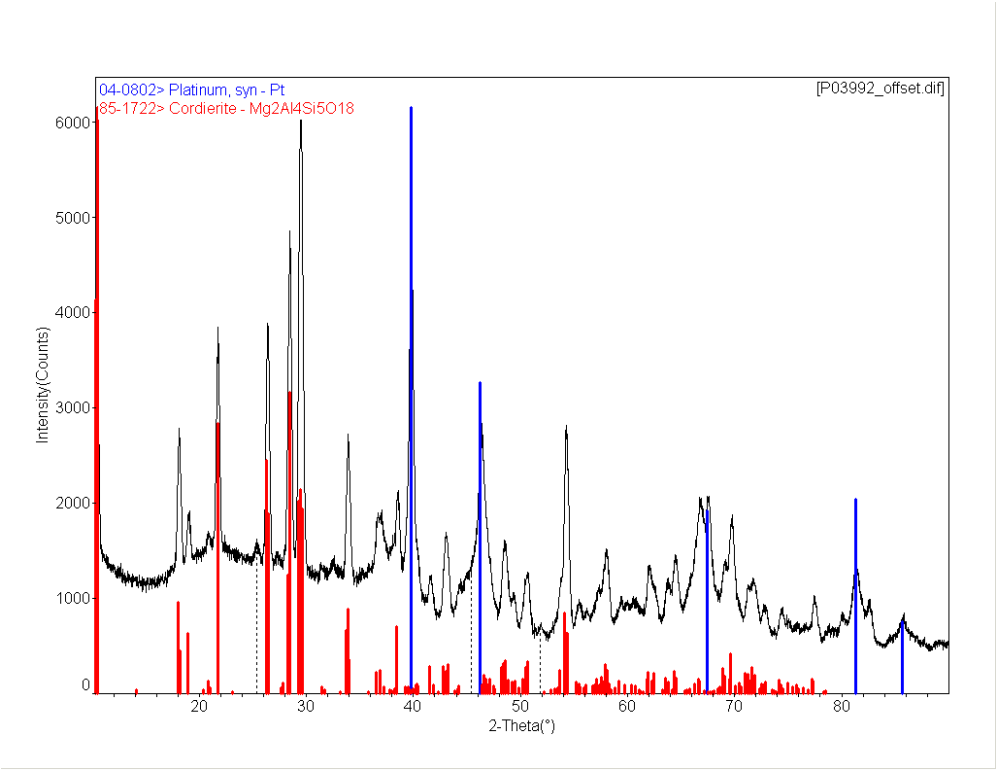

Figure 4. XRD pattern of the aged DOC sample.

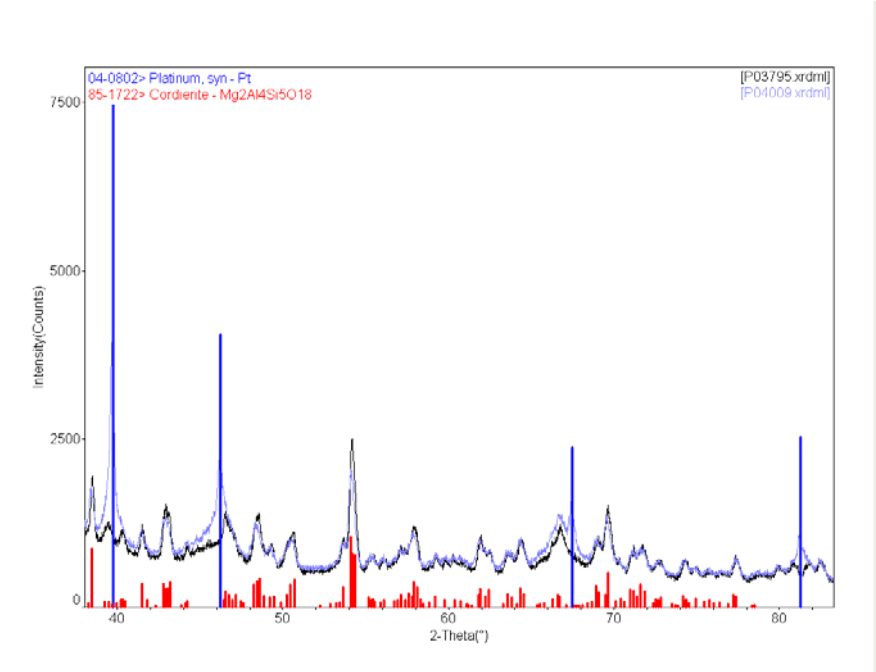

Figure 5. XRD patterns of the new (black curve) and aged (blue curve) DOC samples and highlights the large Pt peaks present in the aged relative to the new DOC.

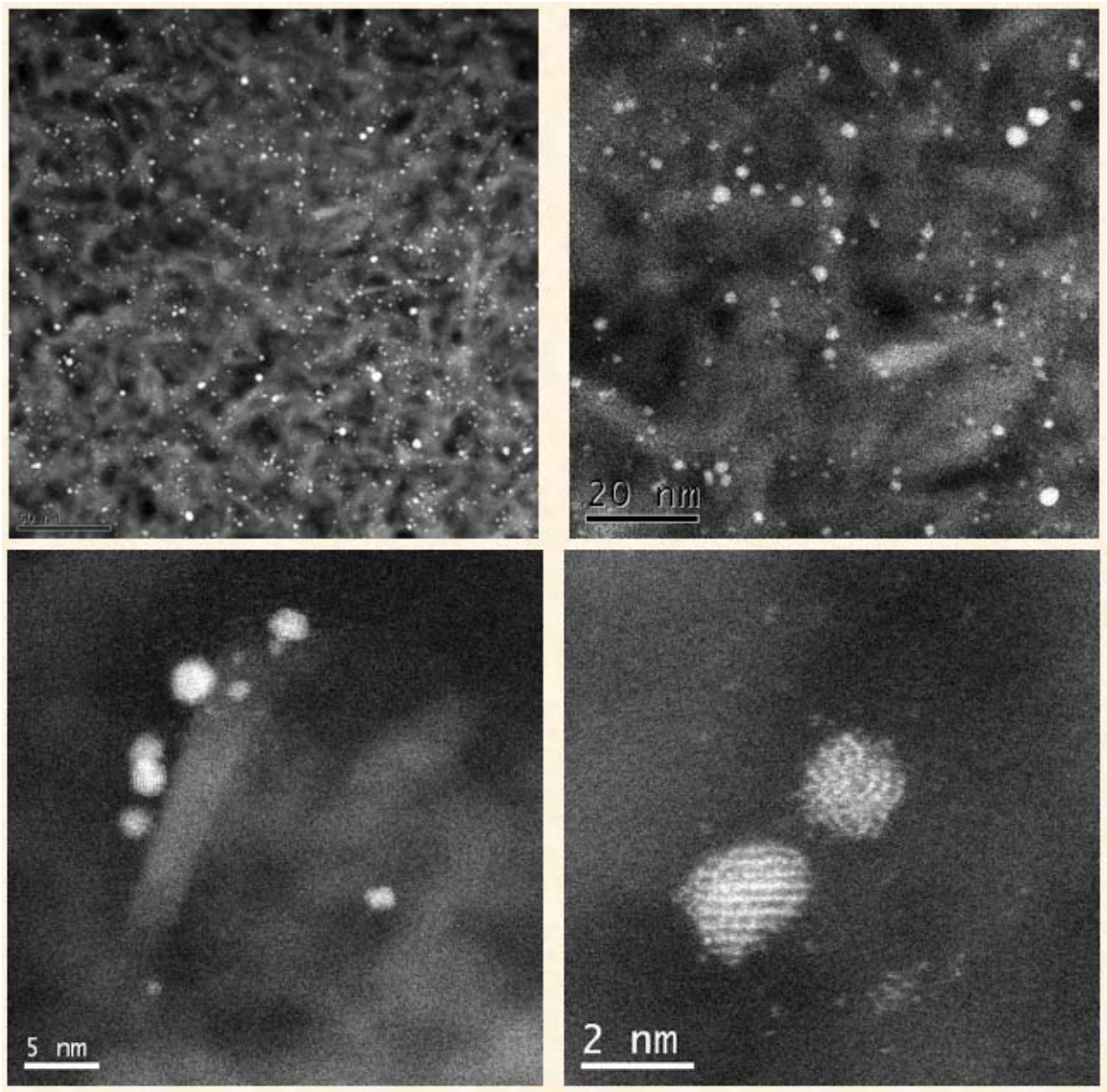

Figure 6. Images show the near atomically dispersed Pt particles and clusters in the new DOC taken with Aberration-corrected STEM.

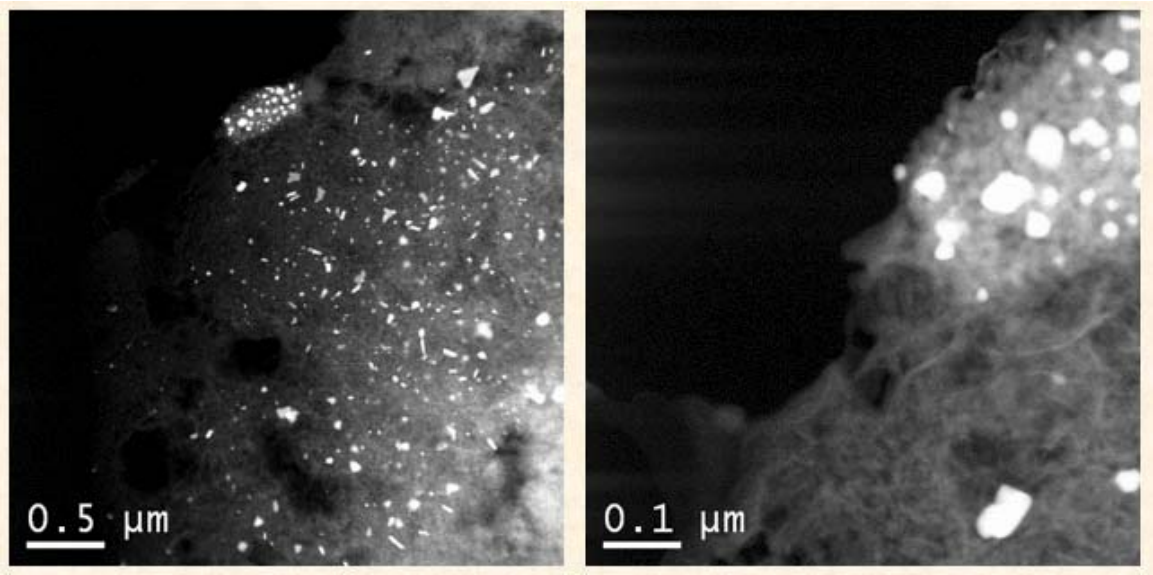

Figure 7. STEM images showing the large Pt crystals in the aged DOC.

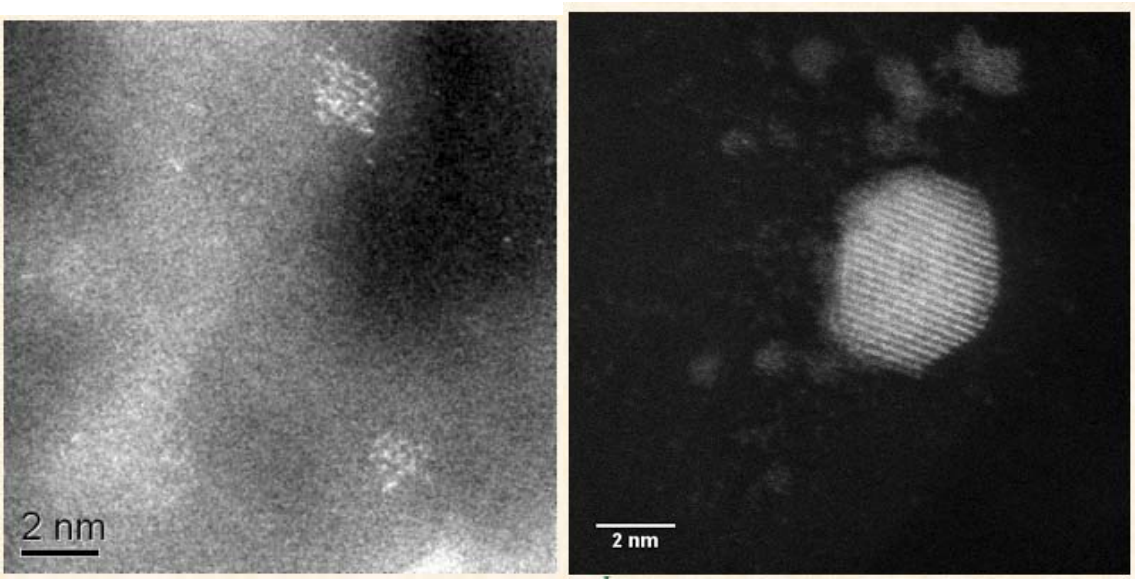

Figure 8. STEM images showing the near atomically dispersed Pt cluster and particles still present within the aged DOC.

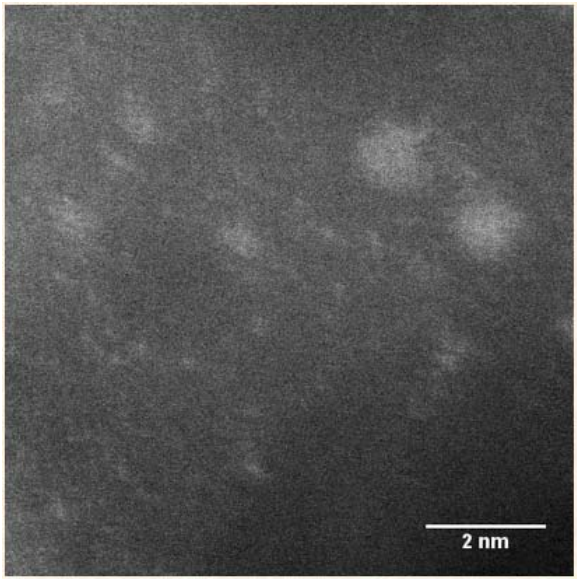

Figure 9. STEM images showing nanocrystals (white arrows) surrounded by "cloud" (hazy "milky-way") of Pt clusters within the aged DOC.

E. Catalysis by First Principles

C. K. Narula, L.F. Allard, M. Moses, W. Schneider, W. Shelton, Y. Xu
Oak Ridge National Laboratory
P.O. Box 2008, MS 6116
(865)574-8445, narulack@ornl.govl

DOE Technology Development Manager: Jerry L. Gibbs
(202) 586-1182; fax: (202) 586-1600; e-mail: Jerry.gibbs@ee.doe.gov
ORNL Technical Advisor: D. Ray Johnson
(865) 576-6832; fax: (865) 574-6098; e-mail: johnsondr@ornl.gov

---

Contractor: Oak Ridge National Laboratory, Oak Ridge, Tennessee
Contract No.: DE-AC05-00OR22725

Objective

The objective of this work is to search for durable emission treatment catalysts (LNT, TWC, OC) from a protocol based on

- an integrated approach between computational modeling and experimental development,
- design and testing of new catalyst materials to rapidly identify the key physiochemical parameters necessary for improving the catalytic efficiency of these materials.

Approach

- Theoretical Modeling
  - Density functional theory-based first-principles calculations
  - Optimization of Pt clusters supported on alumina
  - Interaction of CO, NO_x, and HC with Pt clusters supported on alumina
- Experimental System
  - Synthesize Pt Nanoclusters on morphologically diverse alumina supports
  - Evaluate systems for CO, NO_x, HC oxidation
  - We are employing *Ex-situ reactor* to expose Pt cluster in 2%Pt//γ-Al_2O_3 (1nm Pt) catalyst to CO oxidation conditions in order to monitor microstructural changes by atomic resolution electron microscopy. This approach permits us to repeatedly image the exact same areas of the fresh supported Pt catalyst and after multiple CO oxidation reaction conditions.
  - We carried out *In-situ* FTIR studies to determine the CO absorption modes on fresh 2%/γ-Al_2O_3 and after CO oxidation testing. Catalysts with 1 nm and 25 nm Pt clusters/particles were compared at various stages of exposure to CO oxidation conditions to understand the effect of Pt microstructure on CO absorption.

Accomplishments

- We completed the synthesis of a series of supported Pt catalysts [2%Pt/MgO, 2%Pt/γ-Al_2O_3 (1nm and 25nm Pt), 2%Pt/θ-Al_2O_3 (1nm Pt)] and evaluated them for CO oxidation.
  - We have established that the nanostructure of 2%Pt/γ-Al_2O_3 is quite different form that reported in literature and found that it undergoes changes even on exposure to CO oxidation initiation conditions.
  - We monitored the light-off temperatures of these catalysts on a bench reactor (%CO oxidation) and initiated the efforts to correlate the activity with catalysts' microstructure.

  - The preliminary studies on 1nm 2%Pt/θ-Al_2O_3 suggest that the structure of substrate has a significant impact on CO oxidation initiation and light-off. The efforts to determine the impact of substrate structure on nano-structure of catalysts are in progress.
- We have used DFT methods to investigate formation and adsorption energies as well as reaction energy profiles.
  - Formation energies $Pt_{1-3}O_y$ on MgO(100)
  - Adsorption energies of O and CO on Pt_xO_x and Pt_xO_{2x}
  - Adsorption energies of O, O_2, CO, CO_2, NO, and NO_2 on Pt_x
  - Reaction energy profiles for $CO+1/2O_2 \rightarrow CO_2$ and $NO+1/2O_2 \rightarrow NO_2$

Future Direction

- Understanding of the structures of nano-clusters on support. Our results show that nano-clusters are 10-15 atoms
  - Theoretical models to understand cluster oxidation state (oxidized, reduced, in equilibrium), dependence on cluster size, and the kinetics of oxidation
  - Experimental studies on the structures of these systems using EXAFS, XANES
- Support interaction with clusters and its impact on the structure and reactivity
  - Cationic or zero-valent metals or both
  - Cationic metals at the metal–support interface
- Reactivity of the clusters
  - Theoretical and experimental studies on structure-reactivity correlation towards NO_x, and HC oxidation studies
  - The impact of cluster size on catalytic activity
- Translate these results into design of durable supported catalysts for lean NO_x traps (and other systems such as TWC, OC for diesel etc.)

Introduction

This research focuses on an integrated approach between computational modeling and experimental development, design and testing of new catalyst materials, that we believe will rapidly identify the key physiochemical parameters necessary for improving the catalytic efficiency of these materials.

The typical solid catalyst consists of nano-particles on porous supports. The development of new catalytic materials is still dominated by trial and error methods, even though the experimental and theoretical bases for their characterization have improved dramatically in recent years. Although it has been successful, the empirical development of catalytic materials is time consuming and expensive and brings no guarantees of success. Part of the difficulty is that most catalytic materials are highly non-uniform and complex, and most characterization methods provide only average structural data. Now, with improved capabilities for synthesis of nearly uniform catalysts, which offer the prospects of high selectivity as well as susceptibility to incisive characterization combined with state-of-the science characterization methods, including those that allow imaging of individual catalytic sites, we have compelling opportunity to markedly accelerate the advancement of the science and technology of catalysis.

Computational approaches, on the other hand, have been limited to examining processes and phenomena using models that had been much simplified in comparison to real materials. This limitation was mainly a consequence of limitations in computer hardware and in the development of sophisticated algorithms that are computationally efficient. In particular, experimental catalysis has not benefited from the recent advances in high performance computing that enables more realistic simulations (empirical and first-principles) of large ensemble atoms including the local environment of a catalyst site in heterogeneous

catalysis. These types of simulations, when combined with incisive microscopic and spectroscopic characterization of catalysts, can lead to a much deeper understanding of the reaction chemistry that is difficult to decipher from experimental work alone.

Thus, a protocol to systematically find the optimum catalyst can be developed that combines the power of theory and experiment for atomistic design of catalytically active sites and can translate the fundamental insights gained directly to a complete catalyst system that can be technically deployed.

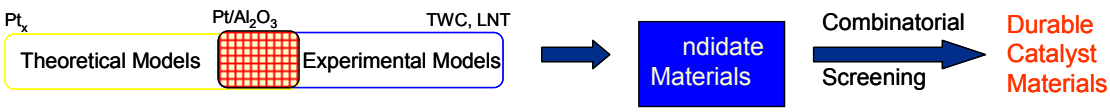

Although it is beyond doubt computationally challenging, the study of surface, nanometer-sized, metal clusters may be accomplished by merging state-of-the-art, density-functional-based, electronic-structure techniques and molecular-dynamic techniques. These techniques provide accurate energetics, force, and electronic information. Theoretical work must be based on electronic-structure methods, as opposed to more empirical-based techniques, so as to provide realistic energetics and direct electronic information.

A computationally complex system, in principle, will be a model of a simple catalyst that can be synthesized and evaluated in the laboratory. It is important to point out that such a system for experimentalist will be an idealized simple model catalyst system that will probably model a "real-world" catalyst.

Thus it is conceivable that "computationally complex but experimentally simple" system can be examined by both theoretical models and experimental work to forecast improvements to obtain optimum catalyst systems.

Approach

The theoretical modeling is based on DFT studies of Pt clusters to understand the relationship between cluster size, structure, composition, and reactivity. This coupled with first-principles thermodynamics provides insights into the effects of oxidizing atmosphere (O_2) – finite (T, p_{O_2}), structure, composition, redox potential on particle size. The results provide guidance for investigations of larger / supported clusters. The next steps of this work will model supported clusters, based on input from experimental results, and their interactions with CO, NO_x, and HC.

Experimentally, we have synthesized a series of Pt clusters and particles supported on morphologically different aluminas. The microstructural characterization reveals the presence of 1-3 atom and 10-20 atom clusters. We have carried our CO oxidation studies on these catalysts and we plan to study NO_x and HC oxidation activity.

Guided by the theoretical models and experimental results of our study, we will synthesize new set of catalyst materials with higher durability under operating conditions.

Results

Over the last year, we have carried out theoretical studies and experimental studies of Pt nanoclusters and nanoparticles and their CO oxidation activity employing a bench-top reactor connected to Agilent GC for gas analysis. We monitored CO adsorption and desorption on catalysts by in-situ FTIR studies using a 1%CO gas flow (He balance) at 25 mL/min across a pressed wafer of the catalyst. We employed our ex-situ reactor[6] and ACEM to study the nanostructural changes in catalysts upon exposure to various reaction condition of CO oxidation. It is important to note that the ex-situ reactor permits duplication of CO oxidation conditions of bench-top reactor.

The results show the correlation between nanostructural changes and their impact on the catalytic activity and are summarized in the following subsections:

OXIDATION CATALYSTS - Pt/MgO

Magnesia (MgO) is a model basic oxide surface that is relatively inert toward many adsorbates and its (100) facet is thermodynamically the most stable. Our DFT investigation for Pt clusters supported on MgO(100) is on-going. Preliminary results are summarized in Figure 1.

The oxides of the Pt dimer and trimer exhibit very similar formation energies on MgO(100) compared to those of the free Pt_2 and Pt_3 clusters, while Pt_1O_y clusters have markedly lower formation energies. Furthermore, the morphologies of the various Pt oxide clusters on MgO(100) closely resemble their gas-phase counterparts. These results support our hypothesis that the oxidation energetics and morphologies of the free Pt nanoclusters should by and large be preserved on a relatively inert surface and therefore our approach of investigating the isolated Pt nanoclusters first.

While efforts to experimentally synthesize Pt nanoclusters supported on MgO are in progress to validate theoretical models, we have synthesized Pt/MgO with Pt particle size predominately in the 15-20 nm range supported on single crystal MgO particles. The results of CO oxidation studies are shown in Figure 2. The CO oxidation gradually reaches ~10% in 170-230ºC range but rapidly becomes quantitative just above 230ºC.

OXIDATION CATALYSTS - Pt/γ-Al_2O_3

1 nm 2%Pt/γ-Al_2O_3: We synthesized 1 nm 2%Pt/γ-Al_2O_3 by impregnation of γ-Al_2O_3 with $H_2PtCl_6 \bullet 6H_2O$ followed by calcination in air at 450°C. STEM analysis shows that platinum particle size ranges from 0.6-1.4 nm and the distribution is centered at 1.1 nm (Figure 3). In general, the models for such nanoclusters assume perfect spherical shape to calculate number of particles in such cluster. Atomic resolution of the particles by Aberration Corrected Electron Microscopy (ACEM) in the HAADF-STEM mode clearly shows that such models are incorrect and the atomic make-up of these platinum nano-clusters involves on average between 10-20 atoms (Figure 4). In addition, single atoms and 2-3 atom clusters can also be observed that are not visible in TEM images obtained from non-aberration correct STEM. Structurally, such clusters can be expected to be quite different from bulk platinum and our previously reported theoretical studies also suggest that these clusters could incorporate oxygen.

We tested the 1 nm 2%Pt/γ-Al_2O_3 catalyst for CO oxidation activity on a bench-top reactor. The conversion of CO to CO_2 was monitored by the analysis of the off gases by gas chromatography (GC) as a function of temperature. The reaction was stopped after CO oxidation had initiated (4.4% CO conversion) at 210 °C (Figure 5) and the sample was collected for analysis. A fresh sample was placed in the reactor and the temperature was increased till CO conversion became quantitative. The reaction was stopped and the reactor was allowed to attain room temperature. The CO oxidation reaction was repeated 2 more times (Figure 6). In the first cycle, CO oxidation began at 210 °C while the third cycle required only 180 °C for the CO oxidation initiation. Analysis of these test samples by X-ray diffraction (XRD) gave broad or unobservable Pt diffraction patterns due to the small Pt particle sizes. The images obtained on an electron microscope suggest that Pt nanoparticle have increase in size to some degree.

The fresh 1nm 2%Pt/γ-Al_2O_3 catalyst showed no CO adsorption at 25°C during in-situ IR studies. However, at 85°C, one CO peak was seen by IR at 2116 cm^{-1} which has a small shoulder (ca. 2094 cm^{-1}). When the adsorbed sample was subject to desorption by flowing only helium the peak shifted to 2114 cm^{-1} but did not desorb (Figure 7). The 1 nm 2%Pt/γ-Al_2O_3 catalyst was also studied by the in-situ FTIR process after it was tested for 100% CO oxidation 3 times. This catalyst had three CO vibrations at 25°C (2175, 2117, 2063 cm^{-1}) under adsorption conditions

(Figure 7). The two lower energy vibrations desorbed in the absence of CO while the higher energy vibration shifted to 2058 cm^{-1}. When the sample was tested at 85°C three similar CO vibrations were seen but the high and the low energy vibrations were shifted (2177, 2116, 2069 cm^{-1}). While the two lower energy vibrations mostly desorbed, vibrations were still discernable with the lowest shifting in comparison to the adsorption data (2248 and 2116 cm^{-1}). The major vibration seen under desorption conditions was the highest energy vibration which was shifted (2050 cm^{-1}). Interestingly, the vibration around 2116 cm^{-1} is present in all spectra and is most intense in the fresh sample. Furthermore, it does not change after exposing fresh sample to desorbing conditions. This suggests that this vibration is caused by CO adsorption on monatomic Pt.

Thus TEM and IR studies suggest that even exposure to CO oxidation initiation conditions results in changes in nanostructure of 1nm 2%Pt/γ-Al_2O_3 catalyst. In order to ascertain the extent of nanostructure changes, we have initiated the study of nanostructural changes in 1nm 2%Pt/γ-Al_2O_3 catalyst on our unique *ex-situ* reactor at ORNL in conjunction with microscopy using the ACEM. This study allows us to monitor changes in selected areas repeatedly after exposure to various reaction conditions such as (1)fresh samples, (2)CO oxidation initiation conditions, (3) degreening process (100% conversion 2x), and (4)100% CO conversion after sample degreening. The fresh sample shows small Pt clusters and single Pt atoms (Figures 8a, 9a and 10a). After exposure to CO oxidation initiation conditions, large clusters (Figure 8b and 9b) and small Pt particles (2nm) (Figure 10) can also be seen. The ex-situ reactor study confirms our observations that nanostructural changes in 1nm 2%Pt/γ-Al_2O_3 catalyst occur even on exposure to CO oxidation initiation conditions (4.4% CO oxidation). This study is continuing and will be completed in the next quarter.

These results are also supported by theoretical modeling. Preliminary DFT calculations of the oxidation of CO and NO on Pt clusters indicate that the reaction energetics are strongly dependent on the size of the clusters as well as the extent of oxidation on the clusters. We first look at the adsorption of the relevant atomic and molecular species on Pt nanoclusters, including O, O_2, CO, CO_2, NO, and NO_2. Figure 11 shows the lowest adsorption energies (i.e., strongest adsorption) for the six species on Pt_x. Adsorption geometry, including adsorbate and the cluster, are fully relaxed. Overall, the adsorption of all six species is highly size-dependent in the angstrom regime and substantially stronger than on the bulk Pt surface (Pt(111)). As particle size increases, the adsorption energies trend toward the Pt(111) level ("∞" in Figure 11). That the adsorption of these species is enhanced compared to Pt(111) means that the energy profiles of CO and NO oxidation on Pt_x also differ from their bulk-surface counterparts (Figure 12). CO oxidation on the bulk Pt surface is exothermic every step along the reaction path, but because of the enhanced adsorption of CO, there is a minimum in energy when CO adsorbs on the clusters. The same phenomenon can be seen in NO oxidation. This indicates that the ability of the Pt clusters to catalyze CO and NO oxidation may be inhibited by the strong adsorption of CO and NO.

Our latest results indicate that the adsorption of O, CO (Figure 13) and NO (not shown) are weakened on the Pt_xO_x and Pt_xO_{2x} clusters, which suggests that the energetics of CO and NO oxidation may be more favorable on the small oxidized Pt clusters than on the original, metallic clusters.

25 nm 2%Pt/γ-Al_2O_3: The sintering of 1 nm 2%Pt/γ-Al_2O_3 at 650C for 4h led to the formation of 25 nm 2%Pt/γ-Al_2O_3 with Pt particles of an average size of 25 nm (Figure 14) as calculated from analyzing Pt diffraction peaks in XRD pattern using Scherrer's formula. The CO oxidation studies mirrored the CO oxidation protocol described for 1 nm 2%Pt/γ-Al_2O_3 catalyst (Figures 5 & 6). 100% CO oxidation occurred at a lower temperature for the 25 nm Pt catalysts than that seen for the 1 nm Pt catalysts. The larger Pt particles also exhibit a shift in the temperature required to achieve 100% oxidation between the 2nd and 3rd cycle (from 250 to 242 °C). Pt particle growth was

noted by XRD analysis after both the initiation test and the 100% oxidation 3 times, see Figure 14. The analysis of diffraction peaks in XRD by Scherrer formula showed that Pt particles grew from 25 nm to 28 nm after initiation which was stopped at 8.1% conversion and to 34 nm after cycling to 100% conversion 3 times (Figure 14). No significant difference in CO oxidation activity was observed when 30 nm instead of 25 nm Pt particles were tested.

The in-situ FTIR studies of CO adsorption-desorption on fresh 25 nm 2%Pt/γ-Al_2O_3 catalyst at 25 and 85°C showed bands at 2170, 2117, 2069 cm^{-1} and 2179, 2116, 2060 cm^{-1} respectively (Figure 15). At both temperatures, only the high energy vibration remained during desorption conditions and were shifted to 5 cm^{-1} higher energy. The catalyst, after going through three CO oxidation cycle, exhibits bands at 2173, 2116, 2073 cm^{-1} and 2173, 2117, 2063 cm^{-1} in its IR spectra at 25 and 85°C respectively. It is important to note that the CO adsorption behavior does not significantly change for this catalyst after exposure to CO oxidation conditions. Desorption, on the other hand, results in a strong band at 2075 and 2056 cm^{-1} and weak band at 2173 and 2139 cm^{-1} at 25 and 85°C respectively (Figure 15). All samples also exhibit a weak vibration at 2116 cm^{-1} also.

OXIDATION CATALYSTS - Pt/θ-Al_2O_3

The θ–alumina is the first structurally diverse alumina that we selected to understand the impact of surface properties and structure of substrate on the behavior of nanocatalysts. Compared with γ–alumina, θ-alumina (BET surface area ~100 m^2/g) has a simple structure and its surface properties while less attractive than sol-gel derived γ–alumina (BET surface are ~200m^2/g) are still comparable to commercial γ-alumina (BET surface are ~ 100m^2/g). It can be easily synthesized by sintering sol-gel derived γ-Al_2O_3 at 900°C for 34 hours. The Pt was loaded by impregnating it with $H_2PtCl_6 \bullet 6H_2O$ and subsequent calcination in air at 450°C. The electron microscopic analysis shows that the Pt clusters sizes ranges from 0.6-1.3 nm and are centered at 1.1 nm (Figure 16). Thus, the Pt particles distribution is similar to that for fresh 2%Pt/γ-Al_2O_3, prepared from commercial γ-alumina. The nanostructure analysis of this sample by ACEM is in progress and will be reported in a future report.

We subjected this catalyst to the test protocol described for 1 nm 2%Pt/γ-Al_2O_3 and the results and comparison with 1 nm 2%Pt/γ-Al_2O_3 are presented in Figure 17 and Figure 18. The 2%Pt/θ-alumina samples show lower CO oxidation initiation and light-off temperatures. Further nanostructural studies will reveal the differences between Pt/θ-alumina and Pt/γ-Al_2O_3 catalyst that could explain their CO oxidation behavior.

Conclusions

The most important result of this study is that the nanostructure of Pt supported on alumina is quite different from that reported in several literature studies. Furthermore, we have shown that even exposure to CO oxidation initiation conditions results in dramatic changes in the nano-structure of Pt. The increase in Pt size from 1 to 25 nm results in lower CO oxidation initiation and completion temperatures. We have also shown the changes in CO absorption supported Pt catalysts after exposure to various CO oxidation conditions by FTIR. Computational calculations and simulation have shown that the stronger adsorption of reactants on small Pt clusters may inhibit there oxidation. Adsorption of oxidation reactants on oxidized Pt clusters is weaker, suggesting that CO and NO oxidation may be more favorable than on non-oxidized Pt clusters.

The impact of support on the nanostructure of supported Pt is not fully understood. Experimentally, we have observed that Pt supported on θ-Al_2O_3 exhibits lower CO oxidation initiation and light-off temperatures as compared with Pt supported on commercial γ-Al_2O_3. Our next goals are to complete microstructural studies of the 2%Pt/γ-Al_2O_3 catalysts used for CO oxidation by microscopy and start to initiate the study of NO oxidation on these catalysts.

Presentations and Publications

C.K. Narula presented this work at DEER conference. M. Moses presented a paper at SAE Powertrain and Fluid Systems Meeting.

1. Narula, C.K.; Blom, D,A,; Allard, L.F.; Moses, M.J.; Xu, Y.; Shelton, W.A.; Schneider, W.F.; "Catalysis by Design – Theoretical and Experimental studies of model catalysts for Lean NOx Treatment." DEER 2006, Marriott, Detroit, Aug. 21-25, 2006.
2. Narula, C. K., Moses, M.J., Allard, L.F. "Analysis of Microstructural Changes In Lean NO_x Trap Materials Isolates Parameters Responsible for Activity Deterioration" *SAE no. 2006-01-3420*, 2006.
3. C.K. Narula, M. Moses(speaker), L.F. Allard, SAE Powertrain and Fluid Systems Meeting 2006, Toronto, Ontario, October 18-20, 2006.
4. Narula, C. K., Moses, M.J., Xu, Y., Blom, D.A., Allard, L.F., Shelton, W.A. "Catalysis by Design – Theoretical and Experimental Studies of Model Catalysts." *SAE no. 2007M-418*, 2007, abstract accepted-invited.
5. Y. Xu, W. A. Shelton, W. F. Schneider, Theoretical Aspects of Oxide Particle Stability and Chemical Reactivity, in *Synthesis and Application of Oxide Nanoparticles and Nanostructures*; Wiley, in press.
6. Y. Xu (speaker), W. A. Shelton, and W. F. Schneider, "Nano-scale effects in the oxidation and the reactivity of platinum clusters," AIChE Annual Meeting, San Francisco, CA, 11/2006, abstract accepted.
7. Y. Xu (speaker), W. A. Shelton, and W. F. Schneider, "Platinum clusters for oxidation catalysis: Nano-scale effects in thermodynamics and reactivity," 232nd ACS National Meeting, San Francisco, CA, 231st ACS National Meeting, Atlanta, GA, 3/2006.
8. Y. Xu, W.A. Shelton, and W.F. Schneider, "The thermodynamic equilibrium compositions, structures, and reaction energies of Pt_xO_y (x = 1-3) clusters predicted from first principles," in press, *Journal of Physical Chemistry B*, 110 (2006) 16591.
9. Y. Xu, W. A. Shelton, and W. F. Schneider, "Effect of particle size on the oxidizability of platinum clusters," *Journal of Physical Chemistry A*, 110 (2006) 5839.

References

1. Deng, W.; Toepke, M.W., Shanks, B.H., *Adv. Func. Mater.*, 2003, 13, 61.
2. Gates, B.C., *Chem. Rev.*, 1995, 95, 511
3. Narula, C.K.; Nakouzi, S.R., Wu, R., Goralski, C.T., Allard, L.F., *AIChE Journal,* 2001, 47, 744.
4. Andrews, M. A., Kirtley, S. W., Kaesz, H. D., *Inorg. Synth.* **1977**, 17, 16.
5. Fung, A. S., Tooley, P. A., Kelley, M. J., Koningsberger, D. C., Gates, B. C. *J. Phys. Chem.* **1991**, 95, 225.
6. Narula, C.K., Moses, M.J., Allard, L.F. *SAE no. 2006-01-3420*, 2006.

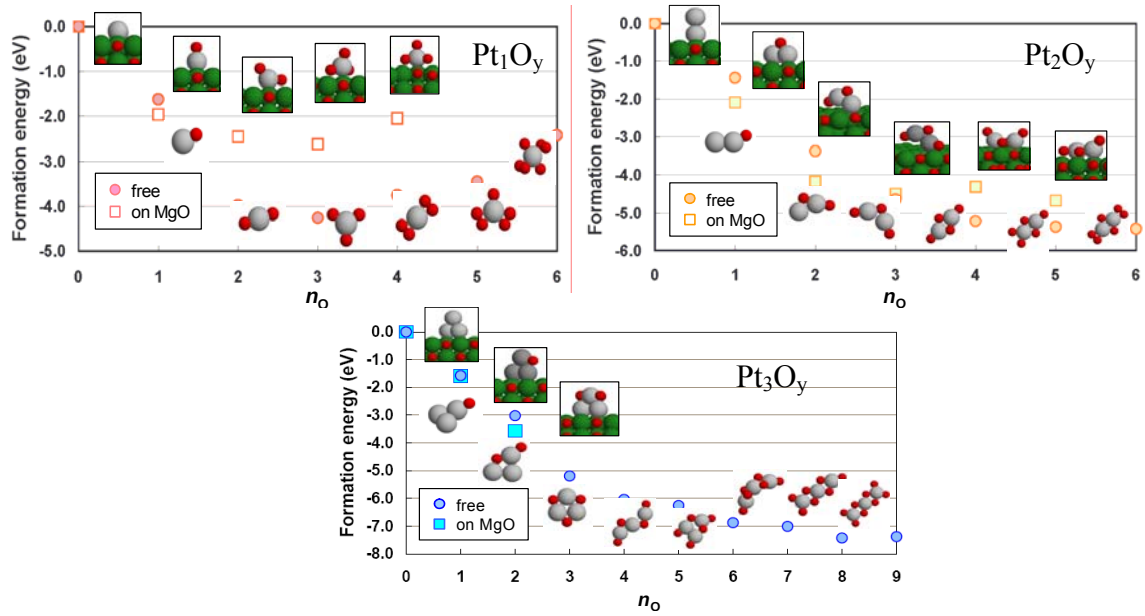

Figure 1. The formation energies of $Pt_{1\text{-}3}O_y$ on MgO(100).

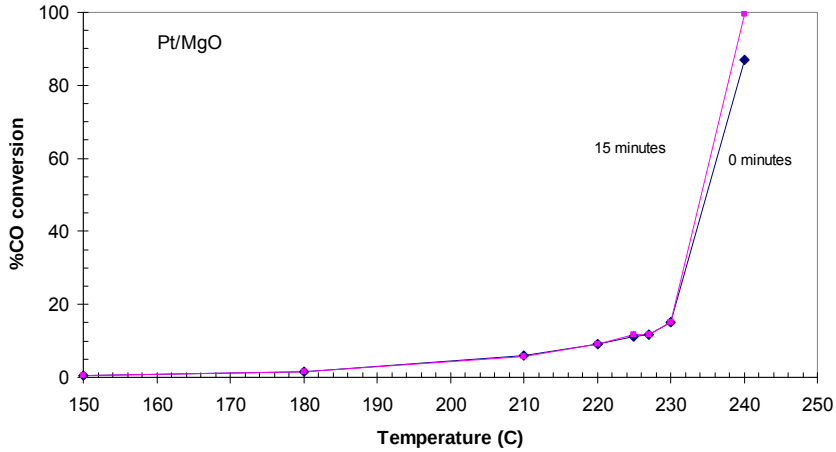

Figure 2. Complete catalytic conversion of CO on 2% Pt/MgO as a function of temperature, with initial sampling and after 15 min. at the given temperature.

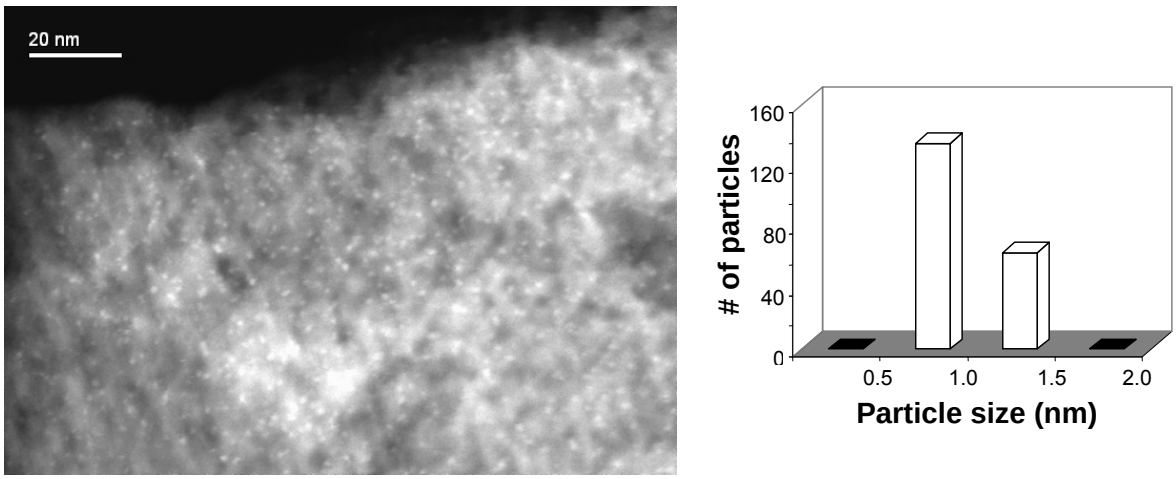

Figure 3. STEM image of fresh 2%Pt/γ-Al_2O_3 (Left), the Pt particles size distribution for this area (Right).

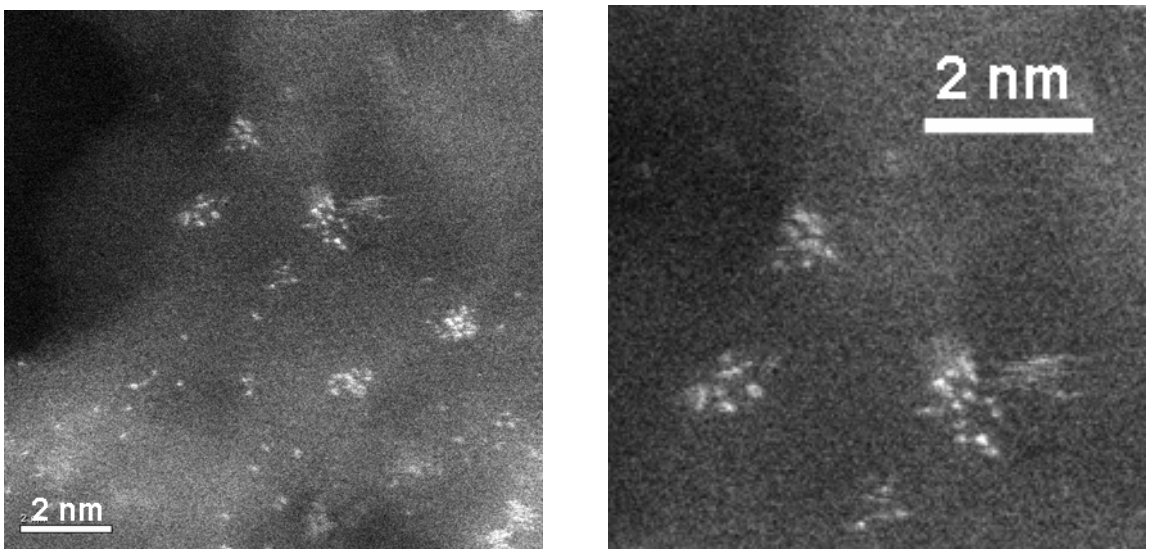

Figure 4. ACEM HAADF-STEM images of 2%Ptγ-Al_2O_3. Bright white dot are Pt atoms, grayish are is alumina support.

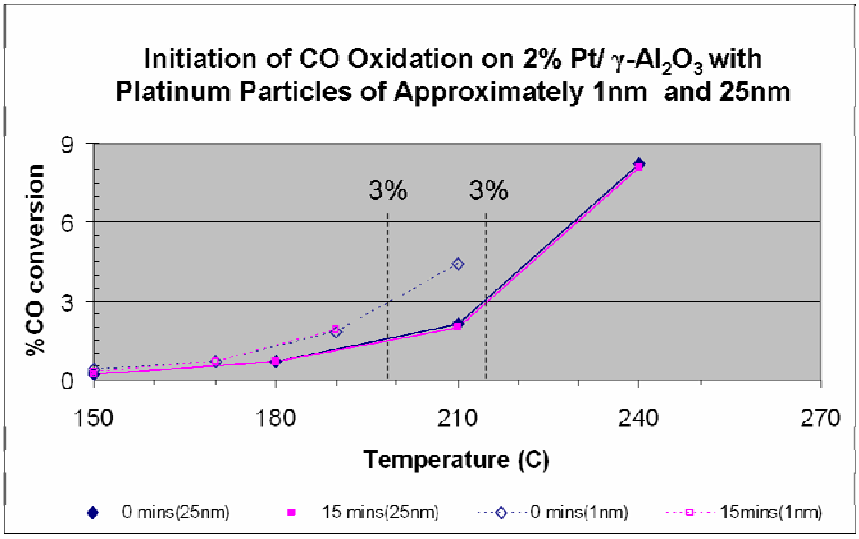

Figure 5. Initiation of catalyst conversion as a function of temperature with sampling at 0 (blue) and 15 (pink) minutes at the indicated temperatures. The solid lines are results for the 2% Pt/ γ-Al_2O_3 annealed at 650°C (ca. 25 nm Pt) and the dotted lines are results for 2% Pt/ γ-Al_2O_3 (ca. 1 nm Pt).

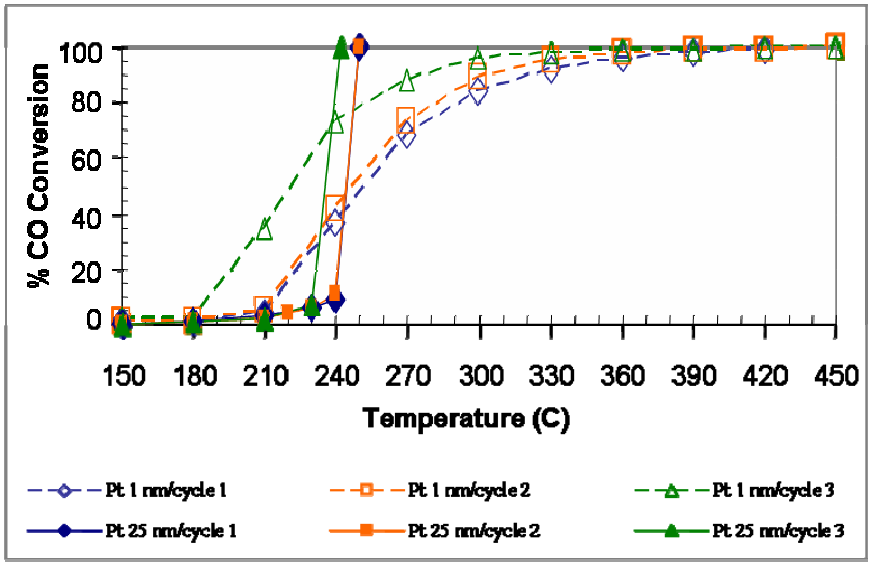

Figure 6. Complete catalyst conversion of CO to CO_2 as a function of temperature with sampling after 15mins at the given temperature. The solid lines are results for the 2% Pt/ γ-Al_2O_3 annealed at 650°C (ca. 25 nm Pt) and the dotted lines are results for 2% Pt/ γ-Al_2O_3 (ca. 1 nm Pt) catalysts.

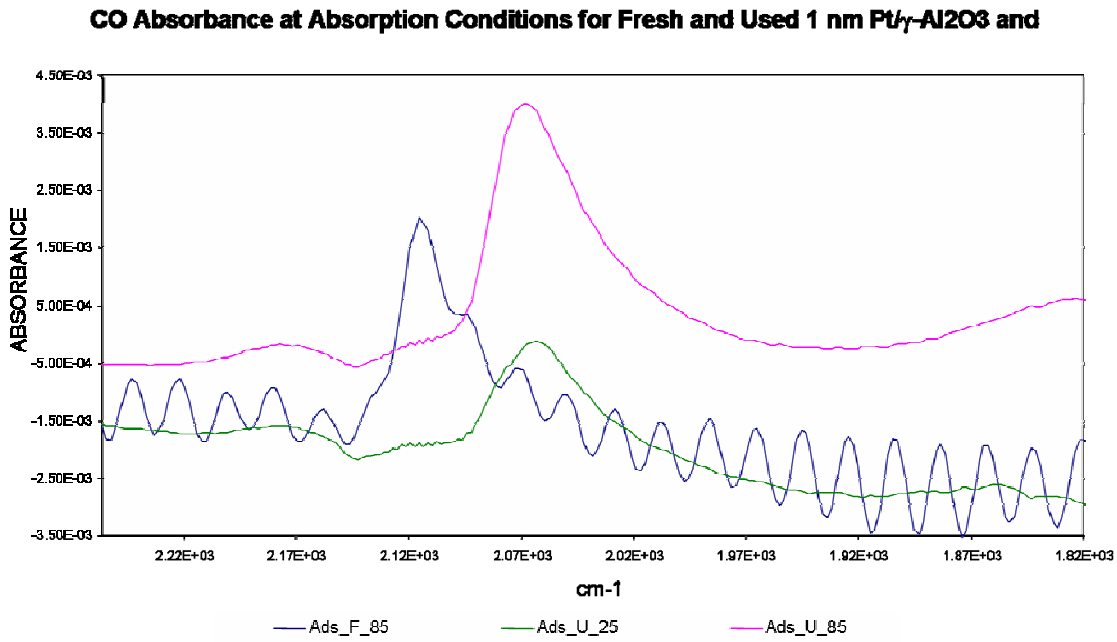

Figure 7. In-situ FTIR CO adsorption data for fresh (1 nm Pt) 2%Pt/γ-Al_2O_3 at 85°C (Ads_F_85) and adsorption data at 25 and 85°C for the catalyst used for 100% CO oxidation tests 3 times (Ads_U_25 and Ads_U_85).

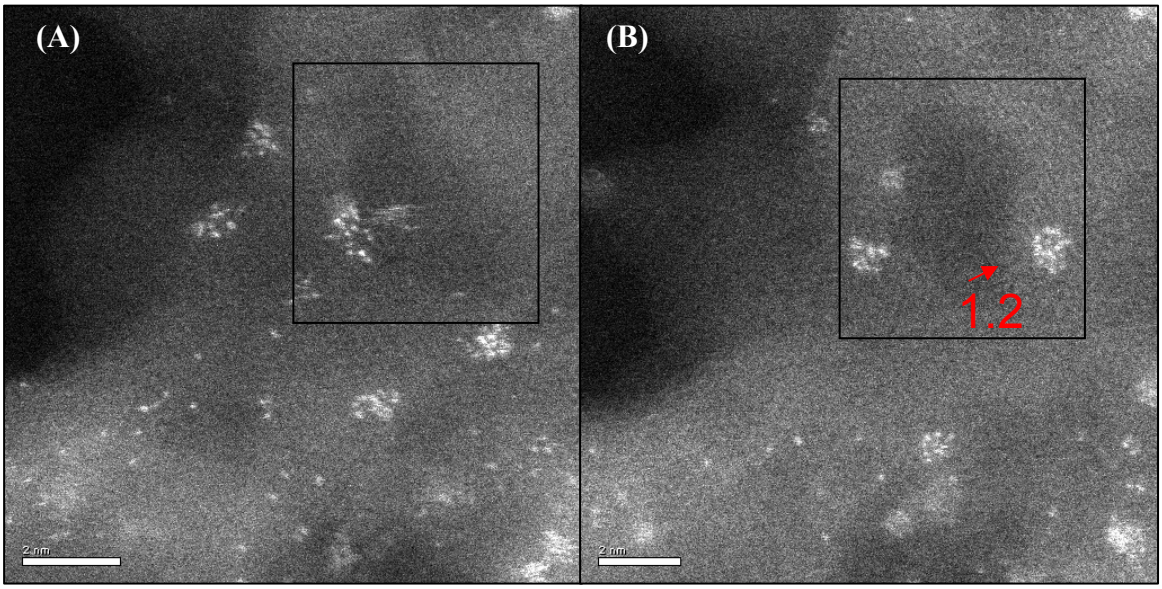

Figure 8. ACEM HAADF-STEM images where the white dots are Pt atoms and grey area is the alumina support. (A) Image of fresh 2%Pt/γ-Al_2O_3 showing both single Pt atoms and small Pt cluster. (B) Image of the exact same spot (for reference squares indicate same area) after exposure to CO oxidation initiation conditions.

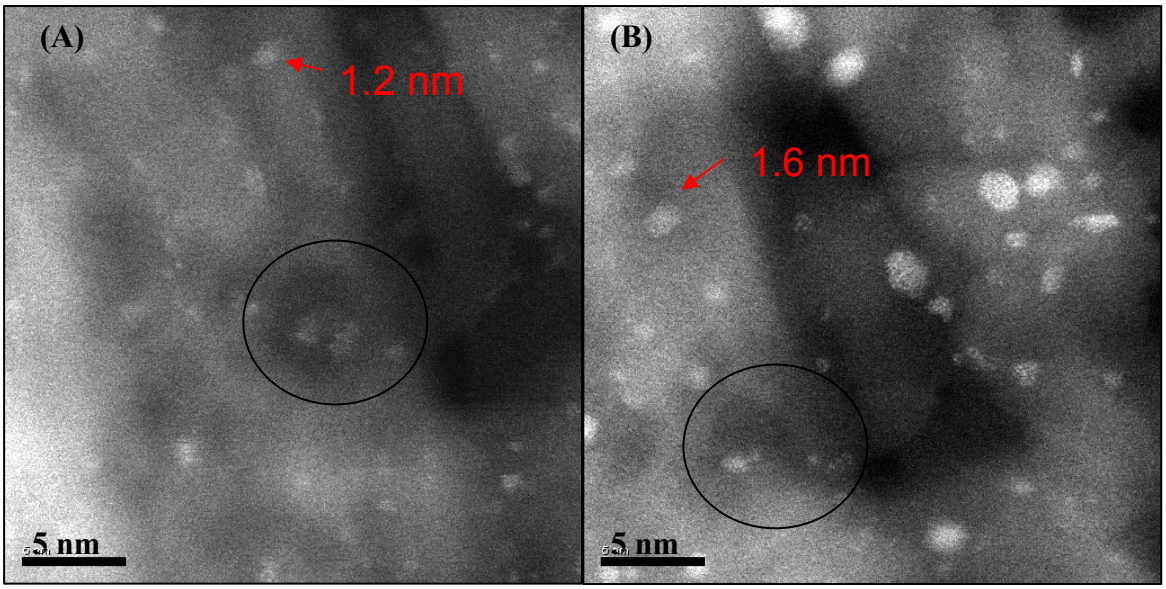

Figure 9. ACEM HAADF-STEM images where the white dots are Pt atoms and grey area is the alumina support. (A) Image of fresh 2%Pt/γ-Al_2O_3 showing mostly small Pt clusters of uniform size. (B) Image of the exact same spot (for reference circles indicate same area) after exposure to CO oxidation initiation conditions shows a small increase in some of the Pt clusters.

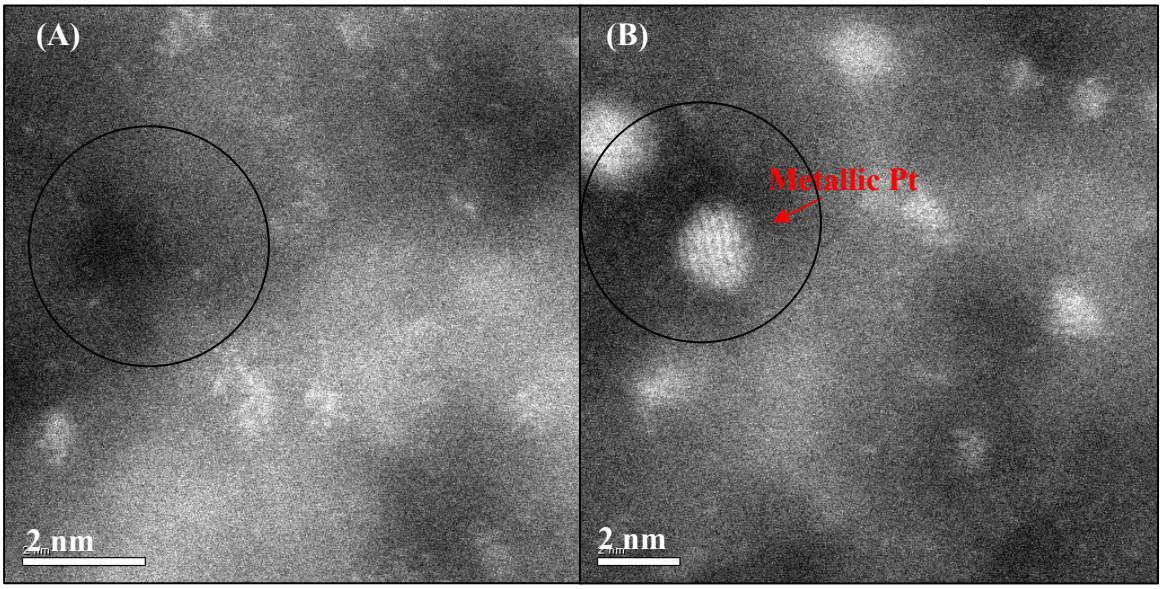

Figure 10. ACEM HAADF-STEM images where the white dots are Pt atoms which form clusters and the grey area is the alumina support. (A) Image of fresh 2%Pt/γ-Al_2O_3 showing both single Pt atoms and small Pt cluster. (B) Image of the exact same spot (for reference circles indicate same area), after exposure to CO oxidation initiation conditions, shows an increase in some of the Pt clusters to metallic Pt particles about 2 nm in size.

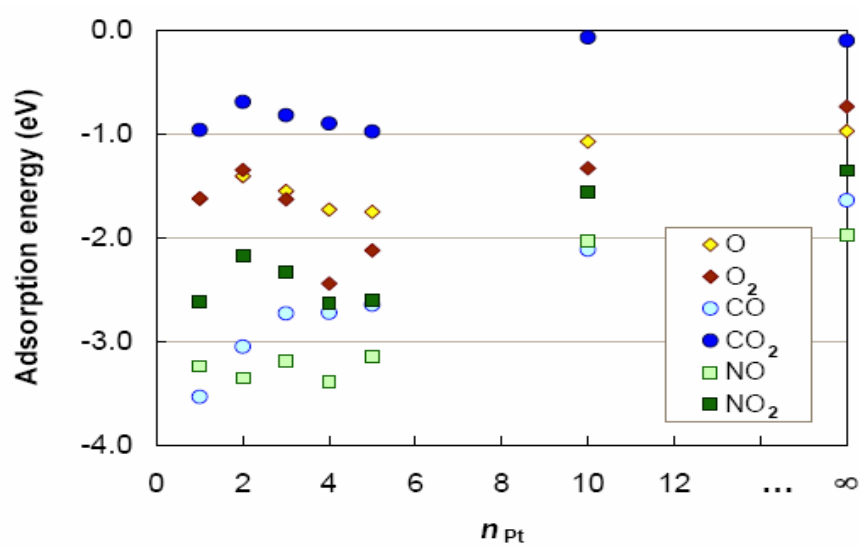

Figure 11. The adsorption energies of O, O_2, CO, CO_2, NO, and NO_2 on Pt_x nanoclusters plotted against the number of Pt atoms in the Pt_x clusters.

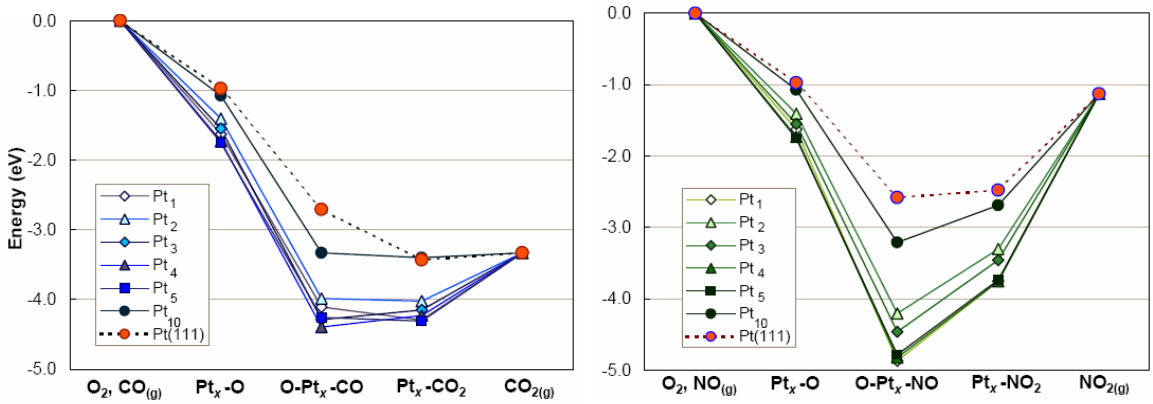

Figure 12. The reaction energy profiles for CO + ½O_2 → CO_2 and NO + ½O_2 → NO_2 on Pt_x (x = 1-5 and 10). The profiles on the bulk Pt surface (represented by the Pt(111) surface) are included**.**

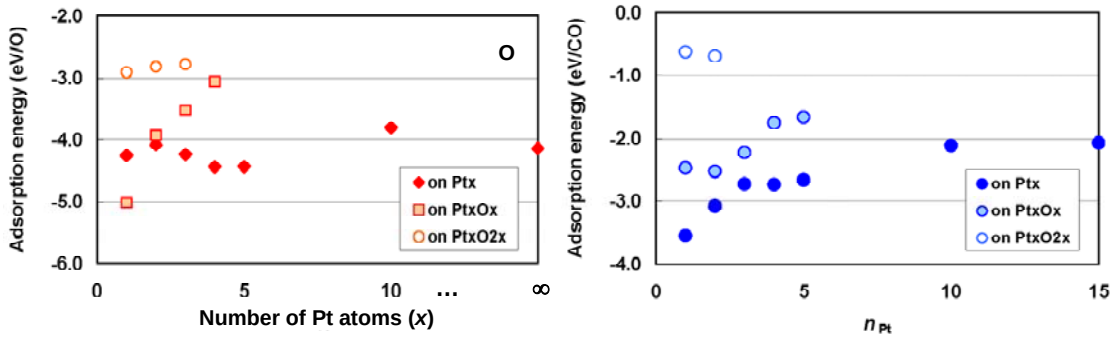

Figure 13. The adsorption energies of O and CO on Pt (Pt_x) and Pt oxide (Pt_xO_x and Pt_xO_{2x}) clusters, plotted against the number of Pt atoms in the clusters.

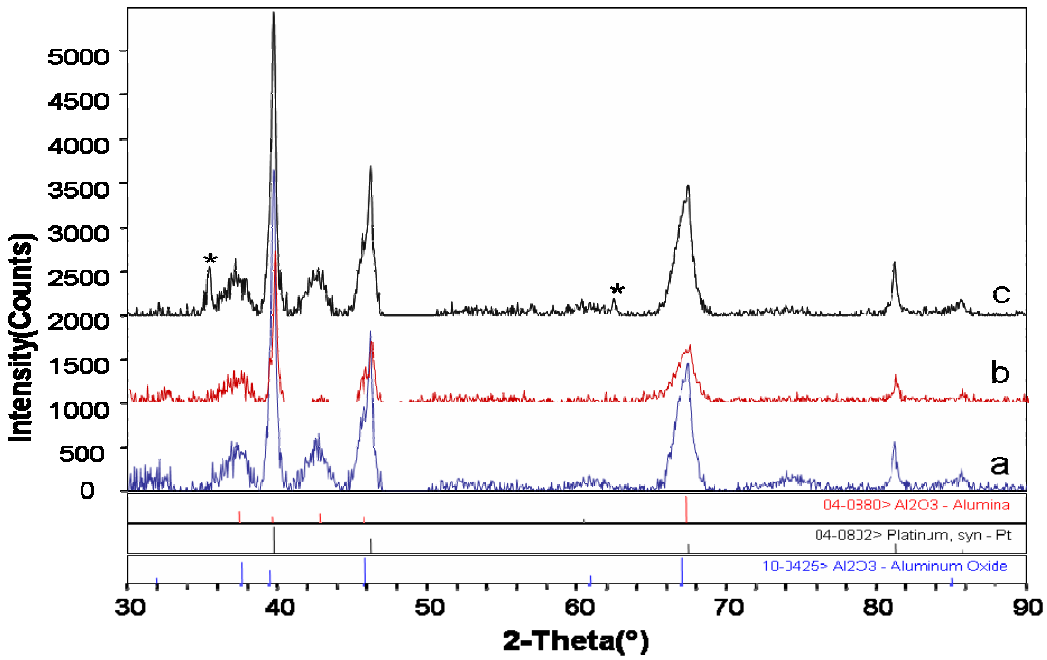

Figure 14. X-ray diffraction pattern of fresh 2% Pt/γ-A_2O_3 annealed at 650 °C (a) fresh and after CO oxidation tests: CO conversion (b) initiation (8.1%) (c) full range (3 cycles at 100%).* denotes a sample holder impurity.

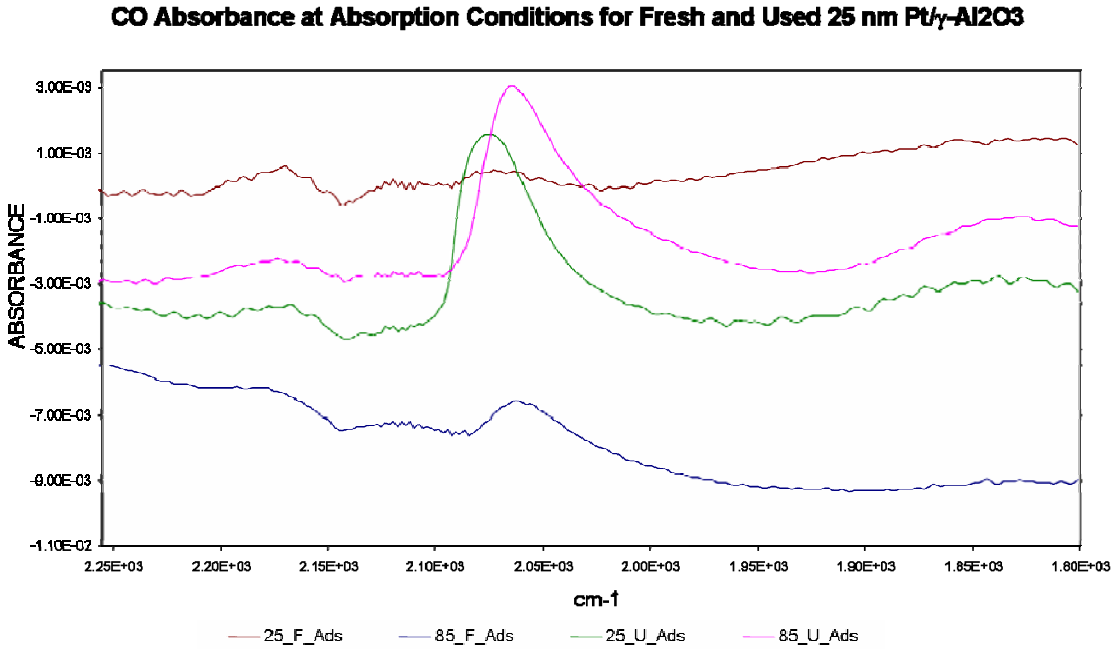

Figure 15. In-situ FTIR CO adsorption data for fresh (25 nm Pt) 2%Pt/γ-Al_2O_3 at 85°C (Ads_F_25 and Ads_F_85) and adsorption data at 25 and 85°C for the catalyst used for 100% CO oxidation tests 3 times (Ads_U_25 and Ads_U_85).

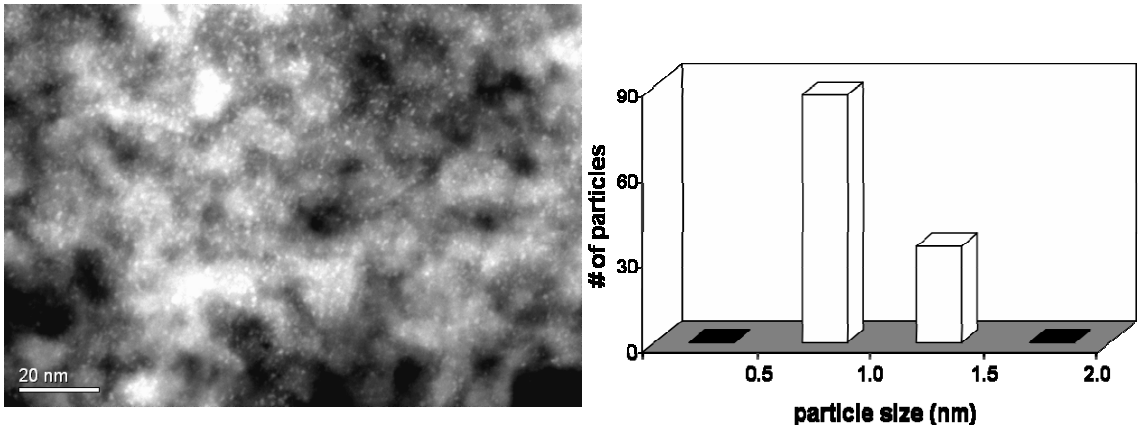

Figure 16. STEM image of fresh 2%Pt/θ-Al_2O_3 (Left), the Pt particles size distribution for this area (Right).

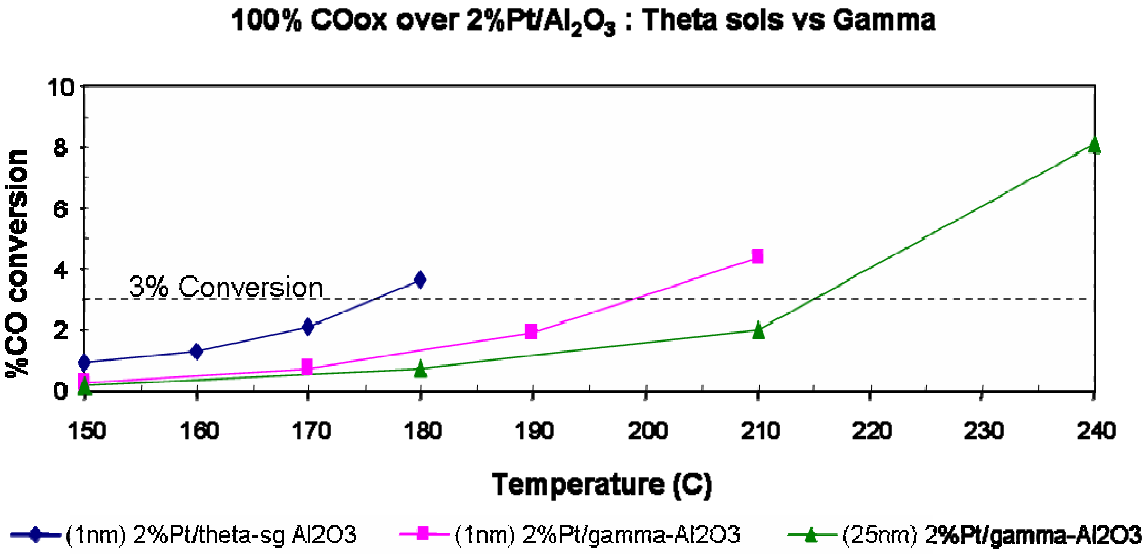

Figure 17. Initiation of catalyst conversion as a function of temperature comparing the different initiation temperature required for 1 nm Pt on θ-Al_2O_3, 1 nm Pt on γ-Al_2O_3 and 25 nm Pt on γ-Al_2O_3.

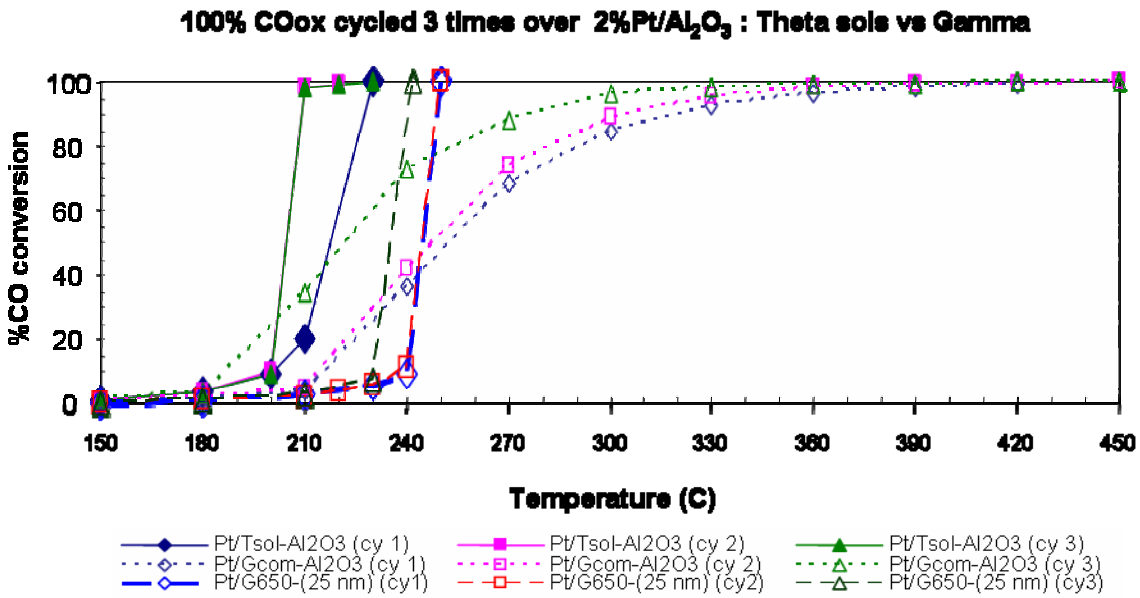

Figure 18. 100% CO oxidation cycled 3 times presented as a function of temperature comparing the different temperature ramps required for 1 nm Pt on θ-Al_2O_3, 1 nm Pt on γ-Al_2O_3 and 25 nm Pt on γ-Al_2O_3.

F. Durability of Diesel Particulate Filters (CRADA with Cummins, Inc.)

Edgar Lara-Curzio, Amit Shyam and Thomas R. Watkins
Oak Ridge National Laboratory
P.O. Box 2008, MS-6069
Oak Ridge, TN 37831-6069
(865) 574-1749; fax: (865) 574-6098; e-mail: laracurzioe@ornl.gov

DOE Technology Development Manager: Jerry L. Gibbs
(202) 586-1182; fax: (202) 586-1600; e-mail: Jerry.gibbs@ee.doe.gov
ORNL Technical Advisor: D. Ray Johnson
(865) 576-6832; fax: (865) 574-6098; e-mail: johnsondr@ornl.gov

Contractor: Oak Ridge National Laboratory, Oak Ridge, Tennessee
Contract No.: DE-AC05-00OR22725

Objective

- Implement test techniques to characterize the physical and mechanical properties of ceramic diesel particulate filters (DPFs) and develop analysis and inspection tools for assessing their reliability and durability.

Approach

- Implement test techniques to determine the physical and mechanical properties of DPF ceramic substrates.
- Application of probabilistic design tools to DPF ceramic substrates.

Accomplishments

- Characterized the fracture mechanical behavior of diesel particulate filter substrates in relevant conditions.
- Carried out physical and mechanical property measurements to better understand the time dependant and fracture mechanical behavior of DPF substrates.

Future Direction

- Implementation of characterization techniques to assess the integrity of DPF ceramic substrates. Inspection schedules would be determined based on the developed probabilistic analysis tools.

Introduction

The pollution emitted by diesel engines contributes greatly to the nation's air quality problems. Even with more stringent environmental regulations set to take effect in 2007, existing trucks and buses will continue to emit nitrogen oxides (NO_x) and particulate matter (PM), both of which contribute to serious public health problems[1]. There are several technologies designed to reduce pollution from existing trucks and buses; prominent among these technologies are DPFs. A DPF is a ceramic device that collects PM in the exhaust stream. The high temperature of the exhaust heats the ceramic structure and allows the particles inside to break down (or oxidize) into less harmful components. DPFs reduce emissions of PM, hydrocarbons, and CO by 60 to 90%.

Most DPFs consist of a ceramic honeycomb with hundreds of cell passages partitioned by walls (Figure 1). Each cell passage has a square cell

opening at one end and is closed at the other end so that the cell passages are alternately closed at each end. This structure forces the exhaust gases through the porous, thin ceramic honeycomb walls. When the gases carrying the carbon particles flow through the fine pores of the walls, the carbon particles are filtered out. High porosity values, in the range of 60%, heighten filtration efficiency to more than 90% while reducing gas-flow resistance to avoid affecting the engine performance.

The process of diesel PM collection continues while the engine is operating. Carbon particles are collected on the ceramic walls and as a result, the backpressure of the system increases. This problem is alleviated by burning the trapped PM, through a catalytic reaction using exhaust gas heat at 400°C or more, into CO_2 and water vapor. This process, called regeneration, results in a cleaner filter. The regeneration process is dependent upon exhaust temperature, oxygen, NO_x content, time, and PM levels.

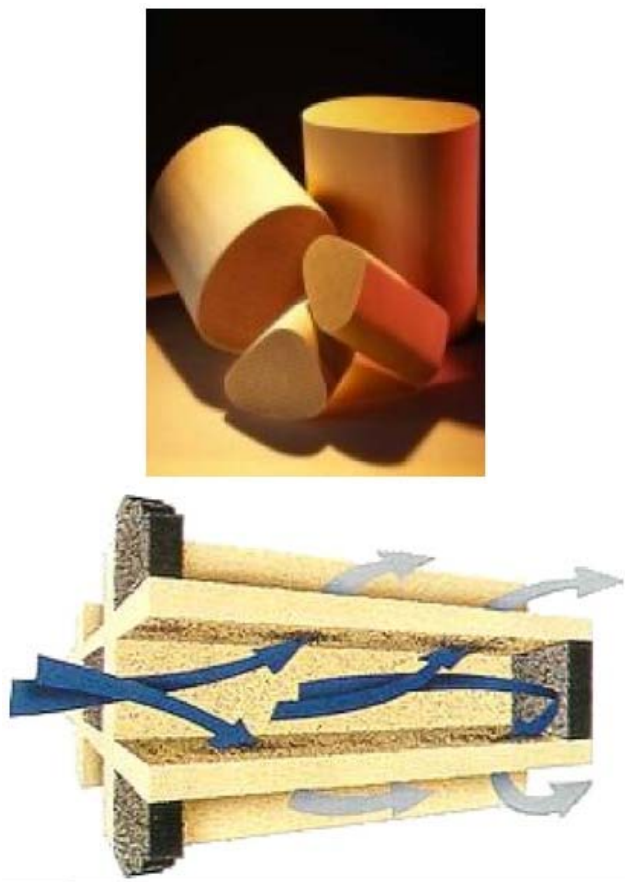

Figure 1. Corning's cordierite-based DPFs.

The key to the successful application of DPFs is to reliably regenerate the filter (e.g., to burn the PM that the filter continues to trap or collect). Traditionally, combustion of soot is done in an oxygen atmosphere (air). In air, soot will burn at about 500°C. However, this is not a typical operating temperature for diesel engine exhaust. Therefore, to burn soot in air, an active system—i.e., one that increases the temperature of the exhaust using some external heat source—is required. But if an active system is not carefully controlled, or if too much PM collects on the filter walls, the filters can experience an "uncontrolled burn" where the temperature increases to 600°C or more, resulting in damage to the filter element.

The objective of this project is to develop and implement methodologies to predict the reliability of DPFs. A useful conceptual model for this purpose is the reliability bathtub curve, which describes reliability-related phenomena of a component over its life cycle.[2] A schematic of the reliability bathtub curve is depicted in Figure 2. It consists of three stages: the infant mortality phase is characterized by premature failures due to improper manufacturing or assembly, poor workmanship, or defects introduced during processing. The second stage of the curve corresponds to the useful life of the component and is characterized by a constant failure rate. In this regime, failures are typically associated with random, excessive loads. If sufficiently high safety factors are used during the design process, the magnitude of this failure rate should be negligible. The third stage of the bathtub curve is known as the wear-out phase, where the failure rate increases with time as a result of aging phenomena. Aging phenomena include thermal and mechanical fatigue,

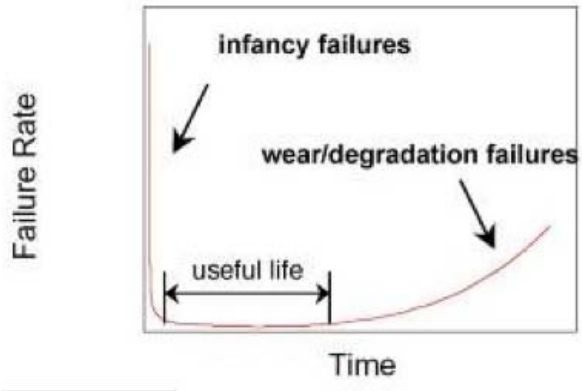

Figure 2. Reliability bathtub curves.

corrosion, creep deformation and environmentally assisted crack growth. The time at the onset of wear-out is often regarded as the useful life of the component.

The reliability bathtub curve can be used as a descriptor of how the failure rate of DPFs evolves over time. Infancy failures of DPFs could be related to manufacturing or process defects (large pores, inclusions, cracking) or defects introduced during assembly. Failures of DPFs during their useful life will be dictated by the intersection between the spectrum of thermomechanical loads and the distribution of DPF strengths. Such failures could result from excessive vibration, for example, or unwanted thermal excursions during transients associated with regeneration. Wear-out and degradation failures of DPFs could be associated with the growth of micro-cracks assisted by thermal fatigue, and/or by the chemistry of the environment, and/or by chemical and microstructural changes in the material due to long-term exposure to elevated temperatures in the exhaust environment.

The objective of this project is to implement test techniques to characterize the physical and mechanical properties of ceramic DPF substrates and to develop analysis and inspection tools for assessing the reliability and durability of DPFs. The developed tools and methods would allow the design of durable and reliable DPFs.

Approach

Designing DPFs that are durable and reliable poses significant challenges. For example, the porosity of DPFs, which allows them to remove PM from the exhaust gas stream, has a deleterious effect on their mechanical strength and stiffness. Designing mechanically reliable DPFs is important because these components will experience demanding thermomechanical conditions during service. These include, for example, thermal shock resulting from rapid heating/cooling and thermal stresses that arise from temperature gradients. The approach that will be followed in this project includes identifying and implementing test techniques for the evaluation of ceramic substrates to assess their integrity. Their physical and mechanical properties and the mechanisms responsible for their degradation in the various stages of the bathtub curve will also be determined and identified. These properties include thermal expansion, thermal conductivity, heat capacity, density, porosity, elastic properties, strength, fracture toughness, and resistance to crack growth at ambient and elevated temperatures, in air and in relevant environments.

The information generated will be used in turn to implement probabilistic design tools. In particular, the applicability of the CARES code[3] to predict the reliability of DPF ceramic substrates will be investigated. Such probabilistic design methodologies are based on a combination of experimentally determined strength data, stress analyses of the component using a finite-element analysis, and selection of appropriate failure criteria. The durability (service life) of the component can also be predicted using this framework by considering the mechanisms that are responsible for the degradation of material strength, such as slow crack growth or creep.

Results

During FY 2006, the procedure to prepare double-torsion (DT) test specimens was further developed and this testing technique was applied determine the fracture toughness and slow-crack-growth behavior of porous cordierite. The double-torsion test configuration is particularly attractive for determination of the fracture mechanical properties of porous cordierite used for fabrication of DPFs. This is due to the following reasons (a) crack length measurements are difficult in porous cordierite and DT characterization does not require crack length measurements, (b) the DT specimen geometry is ideally suitable for plate-like specimens that can be fabricated from DPF walls and (c) the DT configuration is also attractive for slow-crack-growth studies because of the relative stability of crack extension, in contrast to other testing configurations (e.g., SENB, CT).

The preparation of double-torsion test specimens of porous cordierite has been reported earlier.[4] The sample preparation technique was improved further by development of a vacuum fixture to grip specimens while grinding and notching. The fixture increased the parallelism of the prepared double torsion test specimens to 5 μm. The mean thickness of the DT test specimens was equal to 0.375 mm and reproducible to within 10 μm. The consistency of the thickness (and hence volume) of the double-torsion specimens allowed the measurement of the

porosity via high precision mass measurements prior to notching the specimens. The porosity of the specimens determined by this means was 50.00±0.34%. Resonant ultrasound spectroscopy (RUS) of the rectangular plates was also performed prior to notching, in order to obtain an elastic property signature of all the test specimens. Two independent parameter elastic constant fits led to an average elastic modulus of 12.33±0.26 GPa and an average Poisson's ratio of 0.24±0.04.

The fracture toughness of porous cordierite test specimens was determined by loading pre-cracked test specimens to failure at a constant crosshead displacement rate of 0.01 mm/s. The fracture toughness was calculated from the peak load using Equation 1:

$$K_{IC} = PS_m \left[\frac{3(1+\nu)}{St^4 \xi} \right]^{1/2} , \qquad (1)$$

where P is the peak load, S is the width of the test specimens, S_m is the moment arm, t is the specimen thickness, ν is Poisson's ratio, and ξ is a finite beam thickness correction factor given by

$$\xi = 1 - 1.26\left(\frac{t}{S}\right) + 2.4\left(\frac{t}{S}\right) e^{\left(-\frac{\pi S}{2t}\right)} . \qquad (2)$$

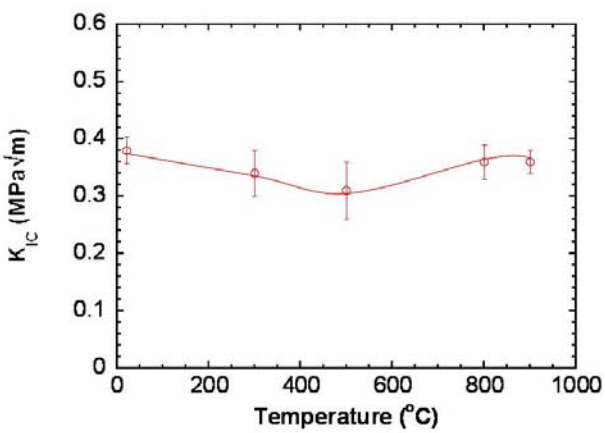

Figure 3. Fracture toughness of porous cordierite as a function of temperature.

In addition, the slow crack growth curves and the slow crack growth exponent were determined by application of the double-torsion load-relaxation method. The fracture toughness and the slow crack growth behavior were determined at temperatures up to 900°C in ambient, water-vapor and simulated diesel engine exhaust environments. The effect of temperature on the fracture toughness of porous cordierite is illustrated in Figure 3. The fracture toughness versus temperature variation of porous cordierite is unusual, in that the fracture toughness decreases from 0.38 ± 0.02 MPa $\sqrt{m}$ at 20°C to 0.30 ± 0.06 MPa $\sqrt{m}$ at 500°C and subsequently increases with temperature to 0.37 ± 0.03 MPa $\sqrt{m}$ at 800°C. The fracture toughness value at 900°C was obtained as 0.35 ± 0.03 MPa $\sqrt{m}$. As expected, porosity plays an important role in determination of the fracture toughness. Cracks extend by joining pores that are favorably oriented with respect to the loading direction. The increase of fracture toughness with temperature above 500°C was attributed to the presence of a glassy phase at the grain boundary. Figure 4 compares the fracture surface of double-torsion specimens tested at 20 and 900°C, respectively. At temperatures above 500°C, periodic undulations of the fracture surface such as that shown in Figure 4(b) were observed. These features are formed due to the activation of viscoplastic processes at elevated temperatures, possibly due to the presence of a glassy phase.

Direct evidence of the amorphous phase at the grain boundary is illustrated in the high resolution transmission electron micrograph (HRTEM) shown in Figure 5 (region between arrows). The thickness of the grain boundary phase varied between 5-20 nm. Electron dispersive spectroscopy (EDS) revealed that the amorphous grain boundary phase was rich in silica when compared to the crystalline cordierite phase. The amorphous phase is beneficial for the elevated temperature fracture resistance due to the softening of the grain-boundary phase. It is, however, well known that the amorphous phase decreases the slow crack growth resistance of silicate ceramics. The grain boundary phase characteristics, therefore, need to be carefully tailored in order to obtain optimum fracture resistance over the range of operating conditions.

The double-torsion test specimens in Figure 3 came from the same region of the filter. It is not necessary that the characteristics of the substrate will remain unchanged in different locations of the filter. During FY2006, studies were conducted that determined the properties of diesel particulate filter substrates as a function of location in the filter.

Figure 6 contains a series of micrographs that illustrate the influence of the location of the filter on the porosity of the walls. The porosity of the

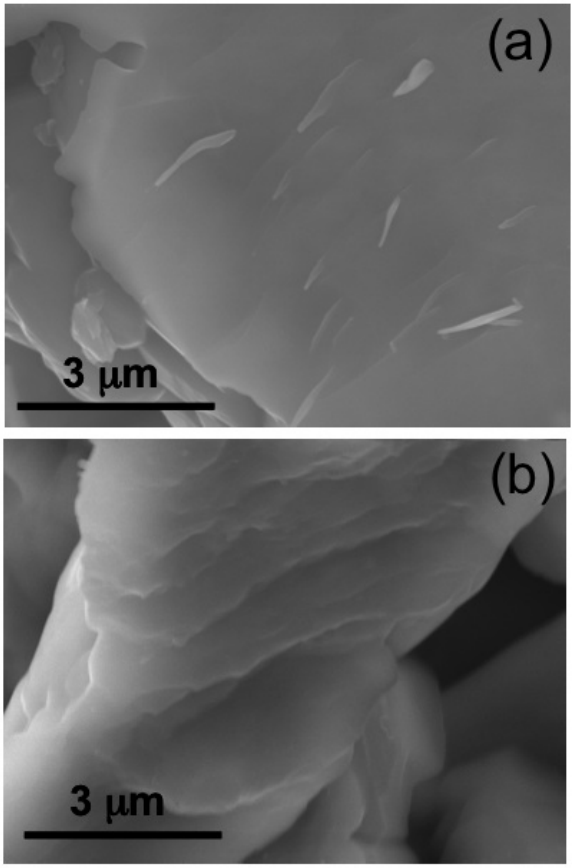

Figure 4. High resolution SEM images comparing the fracture surfaces of failed DT specimens at (a) 20 and (b) 900°C.

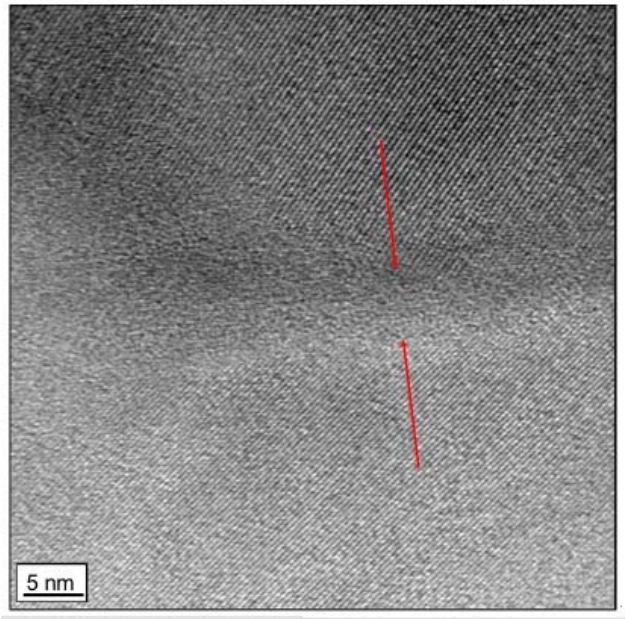

Figure 5. HRTEM image of the silica-rich amorphous phase at the grain boundary of cordierite.

specimens was determined by image analysis and helium pycnometry. The porosity remained close to 50% in all cases, except for tangential specimens close to the edge of the filter (number 13 in Figure 6) where the porosity dropped to about 36%. Both image analysis on SEM micrographs and helium pycnometry showed similar trends except that the helium density measurements yielded slightly lower porosity (by 3-4%) values. This could be due to the fact that the closed, unconnected pores are not accounted for in the helium density measurements.

During FY2006, the effect of thermal cycling on the elastic and thermal properties was characterized. The effect of thermal cycling on the elastic properties of 2x2 cordierite rectangular bars is presented in Figure 7. The modulus measurements were performed in three-point bending in a dynamic mechanical analyzer (DMA). The results indicate that the elastic properties degradation is strongly related to the maximum temperature in the cycle.

Figure 7 demonstrates that damage in the specimen is higher for a maximum temperature of 1000°C compared to 800°C. Moreover, at the thermal loading rate (approximately 40°C/min) applied, most of the damage occurs in the first few cycles and subsequent degradation in elastic properties is minimal. Thermal conductivity was also measured for the same specimens with the hot disk method and it showed a similar variation with thermal cycling.

The thermal expansion and phase composition of the porous cordierite was characterized during FY2006. The thermal expansion behavior of porous cordierite, parallel to the extrusion direction, is illustrated in Figure 8. It can be seen that cordierite has a negative thermal expansion coefficient at lower temperatures and above 300°C; the thermal expansion coefficient becomes positive. The net thermal expansion coefficient is low and this results in excellent resistance to thermal cycling as illustrated in Figure 7.

Cordierite exists in more than one allotropic form. The phase composition cannot be resolved with typical laboratory X-ray diffraction (XRD) due to the low peak resolution and to the fact that the closely spaced overlapping XRD peaks of the orthorhombic crystal structure, making it indistinguishable from the hexagonal structure cordierite. During FY2006, synchrotron XRD

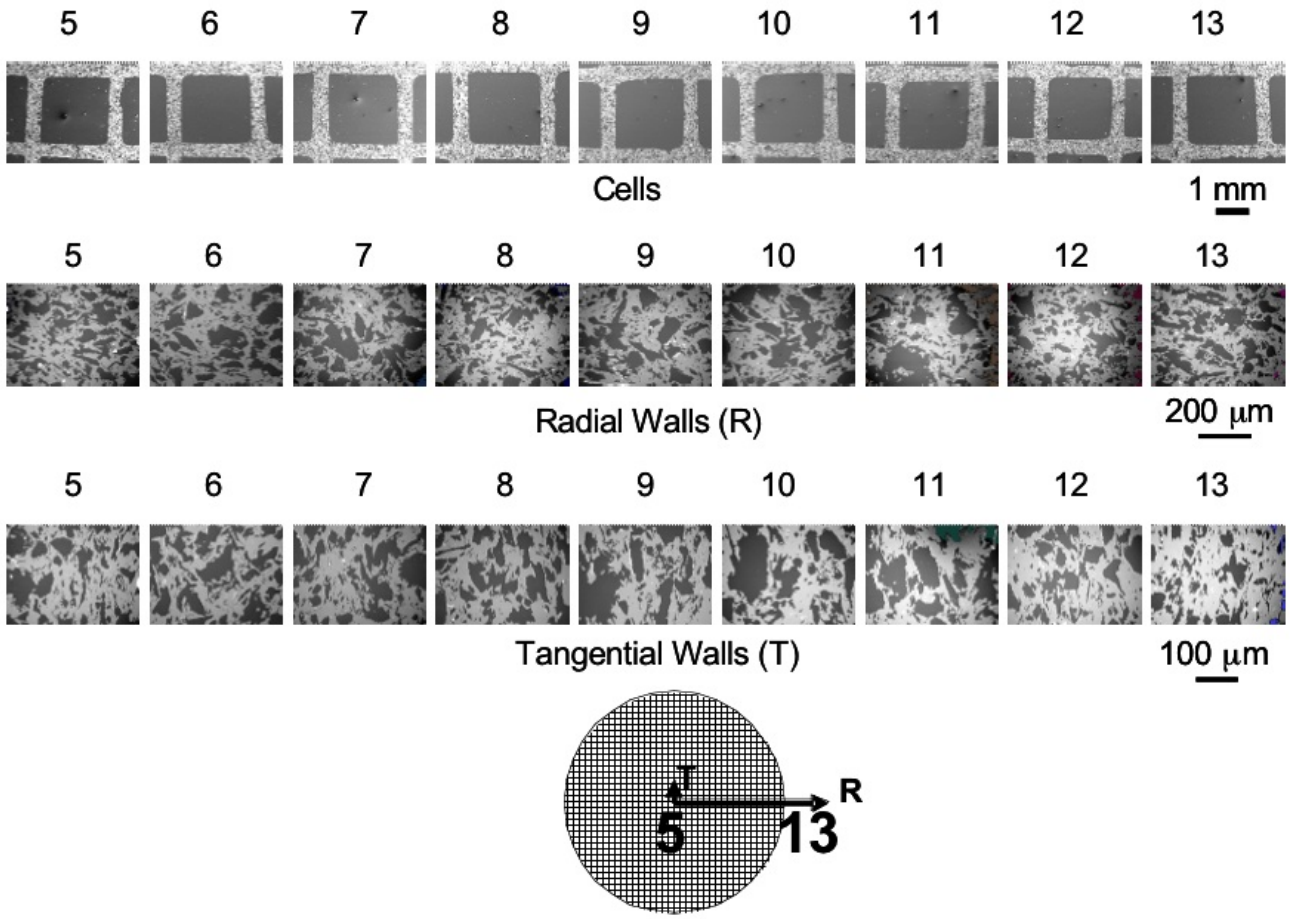

Figure 6. Scanning electron micrographs illustrating the variation of porosity with location in the filter. 5 represents the center of the filter and 13 represents the edge. R and T stand for radial and tangential locations, respectively.

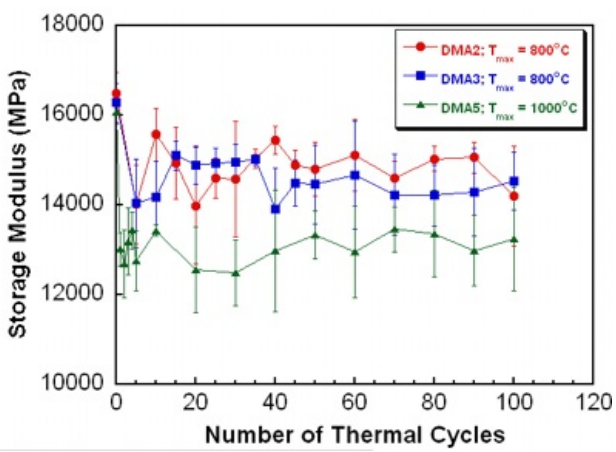

Figure 7. Effect of thermal cycles on elastic property degradation in porous cordierite.

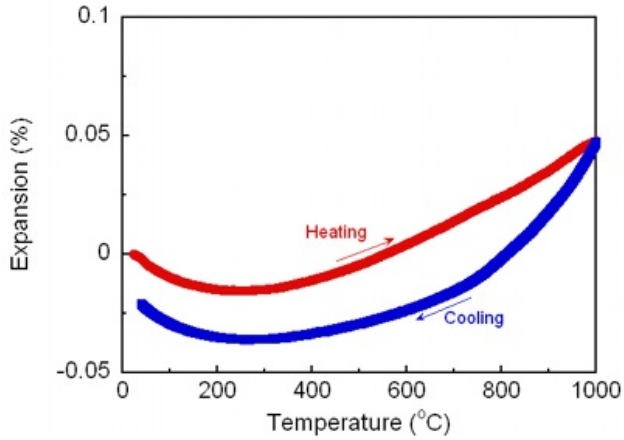

Figure 8. The thermal expansion behavior of porous cordierite for a test specimen parallel to the extrusion direction.

revealed that the porous cordierite material studied has the orthorhombic (ordered) crystal structure. The existence of porous cordierite in the ordered orthorhombic form under ambient conditions rules out the possibility that the mechanical property variations (e.g., Figure 3) are due to phase transitions in the crystal structure. The orthorhombic phase is thermodynamically stable up to temperatures much higher than the operating service temperatures of DPFs.

Summary

The fracture mechanical behavior of porous cordierite was characterized in relevant conditions. It was observed that the fracture toughness variation with temperature was unusual, in that the fracture toughness values increased with temperature above 500°C. The amorphous phase at the grain boundary was characterized and found to increase the fracture toughness of porous cordierite at elevated temperature. Additional physical and mechanical property measurements were carried out to better understand the time dependant, spatial and fracture mechanical behavior of DPF substrates.

References

1. United States Environmental Protection Agency, Office of Transportation and Air Quality EPA420-F-03-017, June 2003. "Questions and Answers on Using a Diesel Particulate Matter Filter in Heavy-Duty Trucks and Buses."
2. G. S. Wasserman, *Reliability Verification, Testing and Analysis in Engineering Design*, Marcel Dekker, New York, 2003.
3. N. N. Nemeth, L. P. Powers, L. A. Janosik, and J. P. Gyekenyesi, "Ceramics Analysis and Reliability Evaluation of Structures Life Prediction Program: Users and Programmers Manual," NASA-GRC, Life Prediction Branch (1993).
4. A. Shyam, E. Lara-Curzio, H.-T. Lin, and R.J. Parten, "Fracture Toughness of Porous Cordierite," in Proceedings of 30th International Symposium on Advanced Ceramics and Composites, Cocoa Beach, 2006 (to be published).

Collaborators

H-T. Lin, Randy Parten, and Claire Luttrell.

Presentations and Publications

A. Shyam and E. Lara-Curzio, "The double-torsion testing technique for determination of fracture toughness and slow crack growth behavior of materials: a review," Journal of Materials Science, vol. 41, no. 13, pp. 4093-4104, July 2006.

A. Shyam, E. Lara-Curzio, H.-T. Lin and R. J. Parten, "Fracture toughness of porous cordierite," to be published in the proceedings of the Cocoa Beach Meeting of the American Ceramic Society, 2006.

4. MATERIALS FOR AIR HANDLING AND THERMAL MANAGEMENT

A. Austenitic Stainless Steels Alloys for Exhaust Manifold

P. J. Maziasz, J. P. Shingledecker, and N. D. Evans
Materials Science and Technology Division
Oak Ridge National Laboratory
P.O. Box 2008, MS-6115
Oak Ridge, TN 37831-6115
(865) 574-5082; fax: (865) 754-7659; e-mail: maziaszpj@ornl.gov

M. J. Pollard
Advanced Materials Technology
Caterpillar Technical Center
14009 Old Galena Rd.
Mossville, IL 61552
(309) 578-6133; fax: (309) 578-2953; e-mail: pollard_michael_j@cat.com

DOE Technology Development Manager: Jerry L. Gibbs
(202) 586-1182; fax: (202) 586-1600; e-mail: Jerry.gibbs@ee.doe.gov
ORNL Technical Advisor: D. Ray Johnson
(865) 576-6832; fax: (865) 574-6098; e-mail: johnsondr@ornl.gov

Contractor: Oak Ridge National Laboratory, Oak Ridge, Tennessee
Contract No.: DE-AC05-00OR22725

Objectives

- Commercialize new CF8C-Plus cast austenitic stainless steel.
- Complete the high-temperature properties database for test specimens from new commercial heats of CF8C-Plus Cu/W and determine the properties of prototype components of both CF8C-Plus and CF8C-Plus Cu/W.

Approach

- Support Caterpillar (CAT) evaluation efforts to upgrade turbochargers from cast iron to cast austenitic stainless steel.
- Perform and evaluate direct comparisons between commercial CF8C-Plus steel and other alloys used by component suppliers/end-users to establish performance benefits at 700–850°C.

Accomplishments

- Provided creep-rupture resistance data on CF8C-Plus Cu/W and CF8C-Plus to further the interest of major diesel turbocharger OEMs to upgrade housings.
- Contracted trial-licensee Stainless Foundry & Engineering to produce ASTM weldability data, and to cast thin-walled step castings of CF8C-Plus and CF8C-Plus Cu/W in support of exhaust component applications.

Future Direction

- Finish all necessary properties measurements and microcharacterization before CRADA ends in July, 2006.
- Support commercial licensing for diesel turbocharger housings, and other applications.

Introduction

Advanced heavy truck diesel engines are increasingly required to have higher fuel efficiency and reduced exhaust emissions without sacrificing durability and reliability. The most demanding normal duty cycles require exhaust manifolds and turbocharger housing materials to withstand temperatures ranging from 70 to nearly 800°C. Such materials must withstand prolonged, steady high-temperature exposure (which requires tensile strength and creep and oxidation resistance) as well as more rapid and severe thermal cycling (which requires resistance to aging and thermal fatigue). New emissions reduction technology and transient power excursions can push temperatures in these critical components even higher.

Higher diesel engine exhaust temperatures push components made from SiMo ductile cast iron well beyond their current strength and corrosion limits. The first Oak Ridge National Laboratory (ORNL)/CAT cooperative research and development agreement (CRADA) (3y) developed a new, modified CF8C cast austenitic stainless steel (CF8C-Plus) as an upgrade alternative to SiMo cast iron and performed the initial mechanical properties testing on a lab-scale heat. The new CF8C-Plus steel was found to have outstanding creep resistance at 850°C. The second ORNL/CAT CRADA project (3y) capitalized on the initial success and began commercial scale-up of the new CF8C-Plus. The new material was found to have good castability, as well as much better mechanical properties at 600–850°C than standard CF8C steel, including resistance to aging, creep, and fatigue/thermal fatigue. The new CF8C-Plus cast steel won a 2003 R&D 100 Award, and in 2004 testing continued of different commercial casting process effects (static, centrifugal, and larger heats).

In 2005, efforts to commercialize CF8C-Plus expanded dramatically, so this CRADA project was extended for 2 more years. Commercial interest to upgrade diesel turbocharger housing intensified in 2006. In 2005, successful casting trials of CF8C-Plus were carried out for components ranging from exhaust manifolds to industrial turbine casing. In addition, the first commercial heats of CF8C-Plus Cu/W were made in 2005 to boost strength and creep resistance at 750–850°C, and were tested in 2006. Three companies have taken trial licenses and, to date, over 31,000 lb of the new steel has been produced commercially.

Approach

Three U.S. foundries obtained trial licenses for CF8C-Plus steel in 2005: MetalTek International, Wollaston, and Stainless Foundry and Engineering. CAT and ORNL both ordered additional heats of CF8C-Plus and CF8C-Plus Cu/W steels in 2005, and cast the pieces in various sizes, using both static casting in sand molds and centrifugal casting of rings of varying thickness, to enable more comprehensive mechanical properties testing. Creep evaluate for further improvements in strength and creep-resistance in the CF8C-Plus Cu/W steel at 750°C and above began in 2006. Finally, in 2006, interest in CF8C-Plus steel as an upgrade replacement for SiMo cast iron for turbocharger housing intensified by the turbocharger OEMs. Upgrading various critical exhaust components to stainless steel should enable the increased durability at the increased engine temperatures needed to allow a 3% decrease in fuel consumption for on-highway trucks. Both CAT and ORNL are performing specific mechanical properties testing and microcharacterization in support of these various applications or efforts.

Technical Progress

Caterpillar

The Caterpillar Technical Center completed characterization and properties measurements on a large industrial turbine end-cover casting of CF8C-Plus steel (8000-lb heat to yield 6700-lb finished component), made by MetalTek International for Solar Turbines (a Caterpillar Company). No defects were obvious visually, and sectioning revealed no cracking or hot tearing at the side flange. This is significant because fully austenitic alloys such as CF8C-Plus are usually more susceptible to hot tearing than similar steel with a much higher δ-ferrite content (standard CF8C steel has 15–25% such phase content). Mechanical properties testing revealed properties generally consistent with other data on CF8C-Plus. This particular demonstration of good properties and castability in making thick-section components (slow cooling rates) compared with smaller test castings (faster cooling rates) is

stimulating commercial interest for larger gas-turbine and advanced steam turbine components.

Caterpillar Regeneration System (CRS) Housing

Figure 1. The first commercial application of CF8C-Plus is the Caterpillar Regeneration System (CRS) housing, announced in July, 2006. This combustor ignites exhaust gas and injected diesel fuel to clean filters, and must withstand high temperatures and rapid thermal cycling.

The 21st Century Truck Partnership technical goal of developing emission-compliant engine systems for Class 7–8 highway trucks is an improvement in engine efficiency from 42 to 50% by 2010. CAT has determined that replacing various SiMo cast iron exhaust components with CF8C-Plus cast stainless steels allows a 90°C increase in exhaust gas temperatures, which translates directly into a 3% increase in fuel economy while also significantly improving performance and durability. CF8C-Plus stainless steel was chosen for Caterpillar Regeneration System (CRS) housing in July, 2006. This component is showing in Fig.1. The CSR will be standard equipment on all heavy-duty highway truck diesel engines starting in 2007.

Efforts also continued at CAT to support and advance CF8C-Plus steel upgrades for other exhaust components. Interest by the turbocharger OEMs intensified in 2006 for upgrading turbocharger housings from SiMo cast iron to CF8C-Plus steel, and CAT and ORNL continue their technical efforts to support such new applications.

ORNL

In 2005, ORNL began the longer term creep testing to prove the overwhelming advantage of CF8C-Plus steel over other stainless steels and alloys at 700-850°C, which continued during 2006. ORNL also began similar creep-testing of the new CF8C-Plus Cu/W alloy. The creep-rupture strength advantage of CF8C-Plus over standard CF8C steel and Ni-resist austenitic cast-iron (an upgrade for some applications relative to SiMo cast-iron) is shown in the Larson-Miller parameter (LMP) plot in Figure 2. CF8C-Plus cast steel is much stronger than either SiMo or Ni-resist cast-irons, and it is almost twice as strong as standard CF8C steel. Figure 3 shows the new creep-rupture data on CF8C-Plus Cu/W at 750°C and 100 MPa. The CF8C-Plus Cu/W has an even larger improvement in creep-rutpure resistance compared to standard CF8C steel, and has about 8 times longer rupture life, but almost 20 times longer secondary creep regime to about 2% strain. Despite the increased creep strength, the CF8C-Plus Cu/W also still has good rupture ductility.

Finally, comparison of CF8C-Plus and CF8C-Plus Cu/W cast stainless steels on an LMP plot (Figure 4) with alloy 617 shows that these new cast stainless steels come close to the creep-strength of alloy 617, a Ni-Cr-Co superalloy (which is about 10 times more expensive than the cast stainless steel), particularly at the highest temperatures. Such properties comparisons are very important to considering CF8C-Plus for potential gas- and steam-turbine applications, as well as many other chemical/petrochemical, energy, or metals processing applications

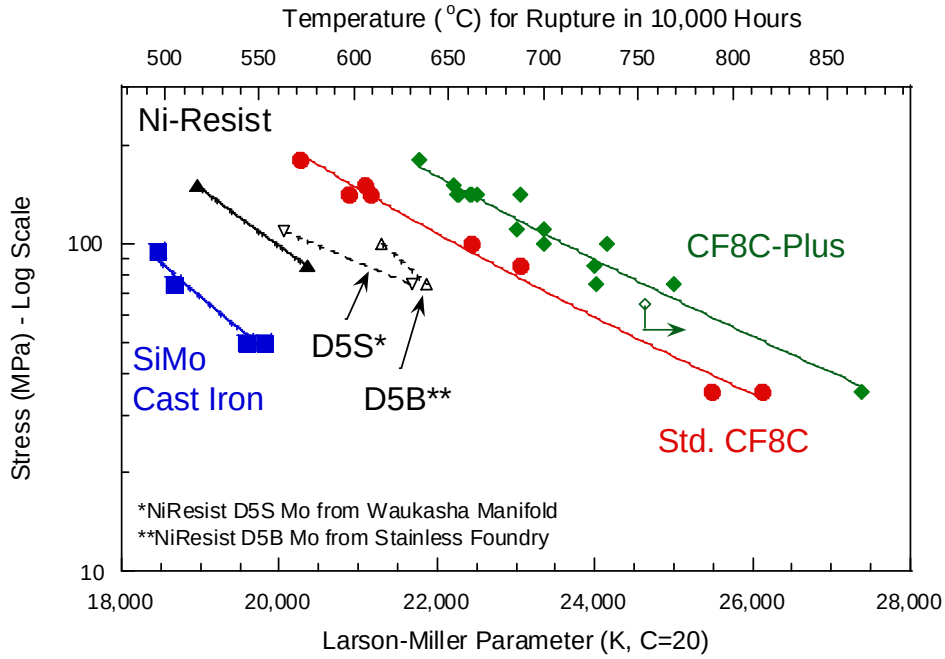

Figure 2. Creep-rupture stress plotted vs LMP for various ORNL creep-rupture tests at 500–850°C in air of various commercial heats of SiMo ductile and Ni-resist austenitic cast irons and standard CF8C and CF8C-Plus. CF8C-Plus shows significant creep-strength advantage over the standard steel or the cast irons.

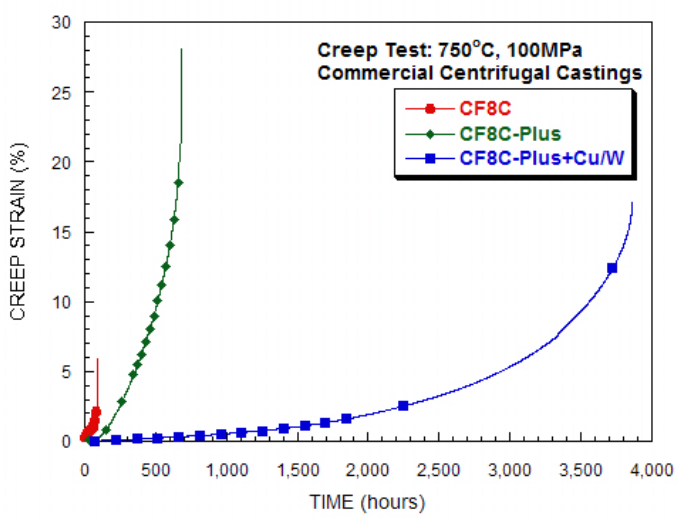

Figure 3. Plots of creep-strain vs time for heats of standard CF8C, CF8C-Plus and the new CF8C-Plus Cu/W, all tested in air at 750°C. Clearly the CF8C-Plus Cu/W has much more creep-resistance, with an extended secondary creep-regime and a very low steady-state creep rate.

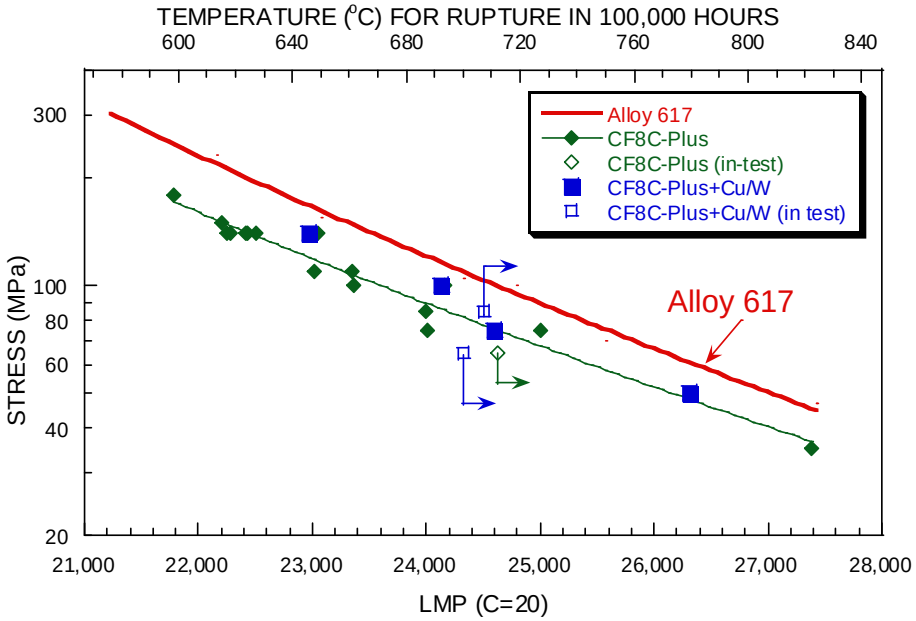

Figure 4. Creep-rupture stress plotted vs LMP for various ORNL creep-rupture tests at 700–850°C in air of CF8C-Plus and CF8C-Plus Cu/W. CF8C-Plus has better creep-strength than most wrought heat-resistant austenitic stainless steels and alloys and compares well with alloy 617, a Ni-Cr-Co superalloy.

In FY 2006, ORNL completed some initial testing of the new CF8C-Plus steel with the Diado KN2 cast stainless steel and other steels and alloys that are being considered as turbocharger housing upgrades relative to SiMo cast iron. The high-temperature creep-strength, fatigue and thermal fatigue properties of CF8C-Plus steel has stimulated considerable interest from several different turbocharger OEMs. At the end of FY2006, ORNL had Stainless Foundry & Engineering make step-casting of various thicknesses to provide thin-walled test material of both CF8C-Plus and CF8C-Plus Cu/W to provide data to support the diesel turbocharger housing application. Testing will begin next year.

Conclusions

ORNL and CAT in 2006 supported and expanded commercialization of the CF8C-Plus cast stainless steel. To date, more than 31,000 lb of commercial CF8C-Plus stainless steel has been cast for various applications, and all prototype component castings have been successful on the first trial, as a result of good castability. Caterpillar chose CF8C-Plus steel as the new CRS housing material in July, 2006. CRS components will be standard equipment on heavy-duty highway truck diesels beginning in 2007. In 2006, interest intensified by several turbocharger OEMs in CF8C-Plus stainless steel as an upgrade to SiMo cast iron for the housing. Testing of CF8C-Plus for diesel exhaust manifold applications also continues.

In 2006, creep-rupture testing of a new commercial heat of CF8C-Plus Cu/W produced by MetalTek International showed significant improvement compared to CF8C-Plus steel. In 2006 thin-walled castings of CF8C-Plus and CF8C-Plus Cu/W were made by Stainless Foundry & Engineering, and will be tested year in support of the turbocharger housing applications.

Publications/Presentations

J.P. Shingledecker, P.J. Maziasz, N.D. Evans, M.L. Santella, and M.J. Pollard, "CF8C-Plus: A New High Temperature Austenitic Casting Alloy for Advanced Power Systems," *Energy Materials* **1** (2006) 25-32.

J.P. Shingledecker, P.J. Maziasz, N.D. Evans, and M.J. Pollard, "Creep Behavior of a New Cast Austenitic Alloy," to be published in *International Journal of Pressure Vessels and Piping* (Special issue on New Steels) in 2006.

Special Recognitions and Awards/Patents Issued

A new, second U.S. Patent Application was filed in July 31, 2006 by Caterpillar, Inc. for 11/495,671 "Heat and Corrosion Resistant Cast Austenitic Stainless Steel Alloy With Improved High Temperature Strength," by P.J. Maziasz, M.J. Pollard and J.P. Shingledecker.

B. Friction and Wear Reduction in Diesel Engine Valve Trains

Peter J. Blau with Jun Qu
Oak Ridge National Laboratory, P. O. Box 2008, Mail Stop 6063
Oak Ridge, TN 37831-6063
(865) 574-5377; fax (865) 574-6918; e-mail: blaupj@ornl.gov

DOE Technology Development Manager: Jerry L. Gibbs
(202) 586-1182; fax: (202) 586-1600; e-mail: Jerry.gibbs@ee.doe.gov
ORNL Technical Advisor: D. Ray Johnson
(865) 576-6832; fax: (865) 574-6098; e-mail: johnsondr@ornl.gov

---

Contractor: Oak Ridge National Laboratory, Oak Ridge, TN
Prime DOE Contract Number DE-AC05-00OR22725

Objectives

- To enable the application of next-generation diesel engine materials by developing test methods which simulate the mechanical, thermal, and chemical environments of wear-prone engine parts, like exhaust valves and exhaust gas recirculation (EGR) systems.

- To conduct friction and wear characterizations of promising new engine component materials, surface treatments, composites, and coatings with a goal of understanding the scientific basis for their performance in severe environments.

Approach

- Identify diesel engine components that require durability and low friction in order to improve propulsion system energy-efficiency and reduce emissions. These include wastegate bushings for exhaust gas recirculation (EGR) components, fuel injector plungers, and valve and valve seat materials.

- Develop test methods, data analysis methodology, and models to evaluate and quantify the performance of candidate materials under simulated use conditions.

- Investigate and understand the characteristics of friction and wear transitions that affect the lifetimes of materials in wear-critical applications like valve trains.

Accomplishments

- Designed, built, and used a high-temperature oscillatory scuffing test system that operates at wastegate bushing temperatures (~ 600 – 700°C).

- Published results of tests on a range of metallic alloys, ceramics, and coatings to determine which of these had the best durability under high-temperature conditions.

- Developed a novel, 'pin-on-twin' scuffing test to evaluate fuel injector materials in diesel fuel and low sulfur fuel environments.

- Developed criteria for the on-set of scuffing damage and evaluated traditional steel fuel injector materials as well as ceramics, advanced cermets, and hard coatings in diesel fuel and low sulfur fuel. Represented results in terms of 'scuffing maps' and transition diagrams.

- Developed and published a model for scuffing tendency that considers both lubricant characteristics and solid material characteristics.

- Designed a high-temperature, controlled environment exhaust valve wear testing system to investigate the combined influences of repetitive impacts, elevated temperatures, and gaseous environments on the durability of candidate valve and seat materials.

Future Directions

- Use the test data from the new instrument to assess implications of material and surface treatment selection for maintaining engine efficiency and reducing diesel engine emissions.

Introduction

The diesel engine industry faces the important challenge of improving fuel efficiency while meeting increasingly strict emissions regulations. These challenges are being addressed by modifying engine designs, introducing homogeneous combustion, designing advanced control systems, and using exhaust gas after-treatments. Such modifications affect the mechanical, thermal and chemical environments in which the engine materials must operate, and currently-used materials may fall short of meeting these needs. New materials or engineered surfaces are needed to enable new technological goals.

The objective of this effort is to enable the selection and use of durable, lower-friction moving parts in diesel engines for heavy vehicle propulsion systems through the systematic evaluation of promising new materials, surface treatments, composites, and coating technologies. The underlying approach involves developing simulative test methods, analyzing microstructures of candidate materials, developing design maps with variables like surface finish and frictional behavior, and modeling the damage process itself.

In prior years, the focus of this effort was on wastegate bushings for exhaust gas recirculation (EGR) systems and fuel injector plungers that must operate in low sulfur fuels. A variety of materials was evaluated using specially-designed tests to simulate the operating environment of the components, and data that compared traditional materials with potential replacement materials was analyzed and shared with industry. For example, computer-based techniques for measuring the onset of scuffing damage were developed, as was a model to describe the progression of surface damage under boundary-lubricated sliding. This work resulted in seven journal publications and reports.

In FY 2006, the focus of this effort was redirected to address the selection and use of materials for the demanding environment of diesel engine exhaust valves, where temperatures can reach over 850° C and materials are subjected to both contact fatigue and deformation in the presence of gaseous environments. The challenge was to investigate candidate materials under

operating conditions that provided a reasonable simulation of their performance in engines but without the high cost and complications of full-scale engine tests.

Approach

The four-pronged approach involves (a) defining the tribosystem operating environment, (b) designing and building an exhaust valve testing system, (c) conducting tests to compare current valve materials with candidate alternative materials and surface treatments, and (d) providing an assessment of the candidate materials' response to engine manufacturers and designers. This annual report describes background considerations and recent progress in designing a high-temperature, controlled-atmosphere, repetitive impact testing apparatus with which to study valve materials. It considers issues such as contact geometry, motion control, thermal and environmental considerations, and it indicates the progress to-date.

When designing a high-temperature, repetitive impact (HTRI) testing system, it was necessary to consider the damage modes that exhaust valves and valve seats experience. Valve face abrasion is caused by fine particles from residual deposits. Adhesive wear and micro-welding can occur to produce pitting and localized pull-out of material. Oxidation and sulfidization can attack the mating surfaces, introducing a tribochemical aspect into the HTRI design.

The ratio of the normal force on a valve seat (N) to the closing force collinear with the stem (P) was discussed in a paper by Giles [N. Giles (1966) "Fundamentals of Valve Design and Material Selection," SAE Paper 660471]. From the contact geometry,

$$(N/P) = 1 / (\cos\theta + \mu \sin\theta) \qquad (1)$$

where θ is the seat angle and μ is the friction coefficient between the valve and valve seat. Figure 1 depicts the relationship expressed in Equation (1) for three common valve seat angles.

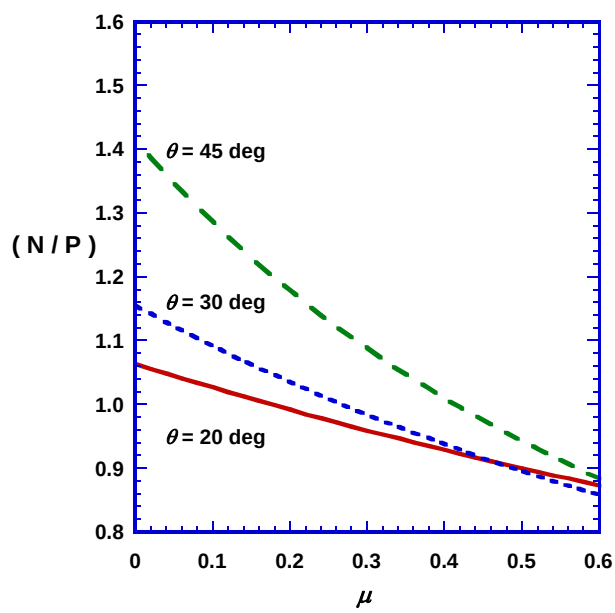

Figure 1. Relationship between the normal force on the seat (N) and the axial force (P) as a function of friction coefficient.

Larger seat angles and lower friction coefficients cause higher normal forces and more wedging between the valve face and insert. While higher normal forces tend to

crush deposits that could otherwise build-up on the mating surfaces, but they also generate more wear. In cases of low-sulfur fuel where the friction coefficients are somewhat higher, higher normal force can be problematical.
On the other hand, shallower seat angles reduce the shear stress and wear, but they allow deposits to form more readily.

In designing the HTRI apparatus, it was desirable to be able to test not only simple test coupons, but also actual diesel engine valves. Therefore, the design included a measure of flexibility. High-temperature alloys were used for all fixtures in the hot zone and the use of screws was minimized to avoid corrosion that could cause binding of the threads. Figure 2 shows the holder arrangement. A selection of production diesel engine exhaust valves was provided by Caterpillar Corporation to aid in the design of the holders, and the holder was made large enough to accommodate a range of valve diameters and bevel sizes.

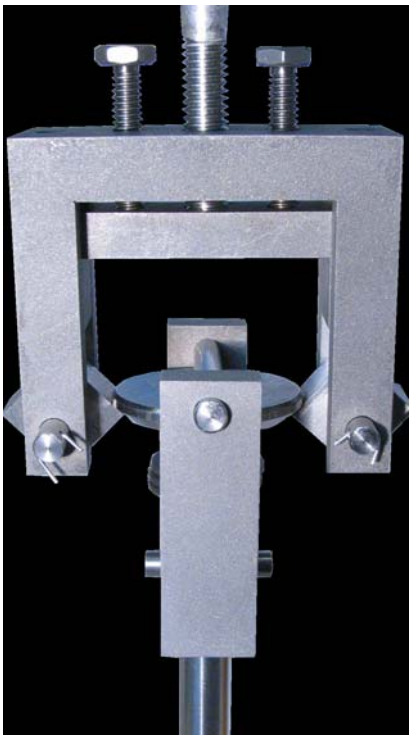

Figure 2. Close-up view of a diesel exhaust valve mounted (inverted) in the holder. When in operation, the valve will repetitively impact the two test blocks that can be fabricated from a variety of candidate seat materials.

One of the challenges in the design of the HTRI apparatus was to enable specimens to be installed and replaced with minimum difficulty. This was accomplished by incorporating a specimen rotation feature into the seat specimens (Figure 2). After the valve specimen is installed, a small displacement of the upper holder causes the two 'seat specimens' to rotate into place below the valve tulip. Additional features were engineered into the fixtures to make the apparatus 'user-friendly'.

In order to reduce the mechanical forces that had to be supplied by the vertical drive shaft, it was decided to support the load only at two locations on the valve seat and use a

non-conformal contact, rather than seating around the entire circumference. This load concentrating design also had the advantage of enabling several tests to be run on the same valve simply by rotating it to a new location. The typical compression pressure for a diesel engine is about 2800 psi. If the valve head is 40 mm in diameter and the angle on the seat is 30 degrees, then the contact pressure is 61 MPa. To achieve this contact stress, based on the Hertz equations of elastic contact, a down force of approximately 22.8 kg-f would be required. If the seat angle were increased to 45 degree, the required down force is 33 kg-f. We will attempt to achieve contact stresses of this level.

The main features of the complete HTRI system are schematically shown in Figure 3. Certain details, like the loading system, have been omitted for clarity. Symbol "A" represents the location of the test specimen holder inside an environmental chamber "B", which is surrounded by a custom-built tube furnace "C." The lower specimen is actuated by a cam drive "D" and a variable-speed motor "E." Gas feed-throughs, labeled "F" and "G," control the environment in the test chamber. Water cooling is supplied to critical components at the top and bottom of the furnace chamber.

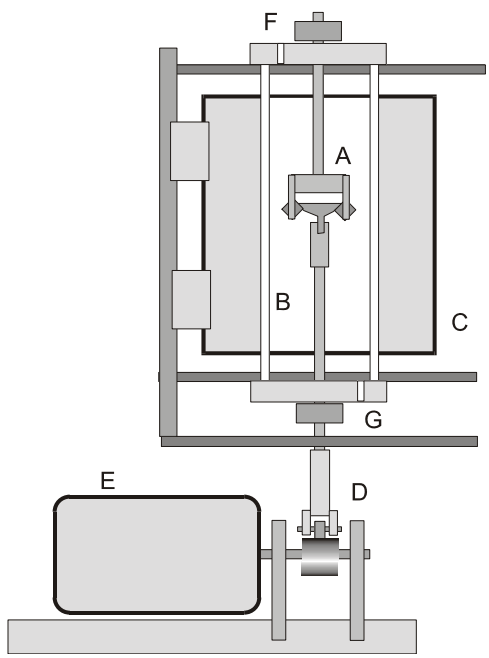

Figure 3. Schematic representation of the HTRI system.

Completion of the HTRI system is expected by the end of calendar year 2006. The system will then be calibrated, and the test specimen wear modes for baseline material combinations will be compared to those on worn valves from actual fired diesel engines to ensure that the test system adequately simulates the mechanical, thermal, and chemical attributes of engine use.

Summary and Conclusions

- Design and construction in under way for a repetitive-impact valve material testing system that operates at temperatures in excess of 800° C in controlled environments. .

- Once baseline tests are concluded, it will be possible to test a wide variety of candidate exhaust valve materials, including novel coatings and surface treatments.

Publications/Presentations

None this period.

5. MATERIALS FOR STRUCTURAL COMPONENTS

A. Cost-Effective Machining of Titanium and HCCI Fuel Systems Spray Hole Drilling

Albert J. Shih
Mechanical Engineering
University of Michigan
Ann Arbor, Michigan 48109-9739
(734) 647-176; fax: (734) 936-0363; e-mail: shiha@umich.edu

DOE Technology Development Manager: Jerry L. Gibbs
(202) 586-1182; fax: (202) 586-1600; e-mail: Jerry.gibbs@ee.doe.gov
ORNL Technical Advisor: D. Ray Johnson
(865) 576-6832; fax: (865) 574-6098; e-mail: johnsondr@ornl.gov

Contractor: Oak Ridge National Laboratory, Oak Ridge, Tennessee
Contract No.: DE-AC05-00OR22725
Subcontractor: University of Michigan, Ann Arbor, Michigan

Objective

- Investigate new technologies for cost-effective machining of titanium alloys with particular emphasis on high-throughput drilling technology
- Evaluate the microstructure and mechanical properties of the workpiece and chip in high-throughput drilling of titanium alloys
- Provide accurate prediction of temperature and stress of cutting tool in high-throughput machining
- Explore the needs and conduct joint research with Caterpillar on the advanced material and manufacturing issues for the future homogeneous charge compression ignition (HCCI) fuel systems

Approach

- Conduct high-throughput drilling test and 3D finite-element modeling using various process parameters.
- Study the Ti-6Al-4V machined surface and the chips using the metallurgical analyses, including Scanning Electron Microscopy (SEM), X-Ray Diffraction (XRD), electron microprobe, and nanoindentation.
- Investigate the spray hole and reverse taper generation for HCCI fuel systems.

Accomplishments

- Achieved 156 mm^3/s material removal rate in titanium drilling using 4 mm diameter tool.
- Analyzed the phase transformation and hardness change in high-throughput drilling of Ti-6Al-4V.
- Predicted drilling process behavior including cutting forces, tool and workpiece temperatures, stresses, etc.

Future Direction

- Explore new manufacturing technologies to enable advanced materials in HCCI fuel systems.
- Finish the 3D finite element modeling of high-throughput drilling and advance the thermal analysis and management of the cutting tool.

Introduction

This report presents the research work to on cost-effective machining of Ti and the exploratory work in spray hole drilling for HCCI fuel systems.

Ti has two crystal structures: the hexagonal closed-pack (HCP) α phase, and body centered cubic (BCC) β phase[1]. Pure Ti is 100% α at room temperature. The allotropic transformation from α to β phase takes place at the β transus temperature 883°C. For Ti-6Al-4V, Vanadium is added to pure Ti to stabilize the β phase by lowering the β transus temperature[1]. Aluminum is added to increase the β transus temperature[1]. With 6 wt% of Al and 4 wt% V, the β transus temperature of Ti-6Al-4V is 980°C. An example of the microstructure of the Ti-6Al-4V used in this study is shown in Figure 1. The dark region is α phase and the light region is β phase.

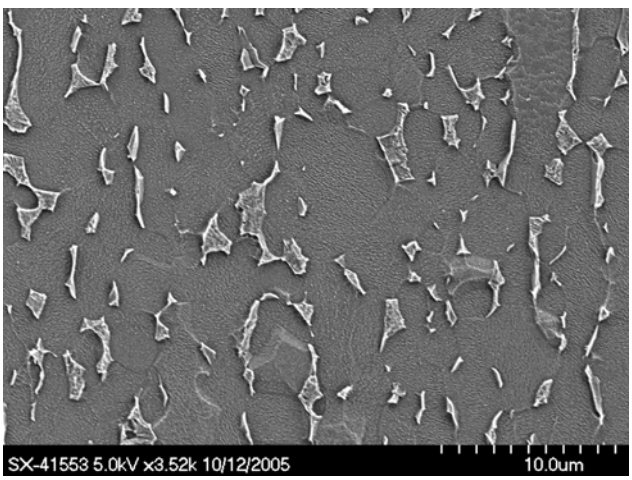

Figure 1. SEM micrograph of an etched microstructure of Ti-6Al-4V with dark region for HCP α phase and light region for BCC β phase.

Drilling is a widely used machining process and has considerable economical importance because it is usually among final steps in the fabrication of mechanical components. In drilling, high material removal rate (MRR) and long drill life are essential to increase productivity and reduce cost. To achieve the desired MRR, high cutting speed and feed per revolution of drill are required[2]. The drilling of Ti-6Al-4V at high cutting speed has been reported in 2005 Annual Report. In this report, the drill life and metallurgical analysis, including SEM, XRD, electron microprobe, and nanoindentation tests, of workpiece and chip in high-throughput drilling of Ti-6Al-4V are studied extensively. The Ti workpiece and chips undergo large strain and high strain rate deformation and subject to high temperature, which are expected to alter the microstructure and material properties. The balance of cutting speed and feed in high throughput drilling to achieve long drill life and good hole surface roughness is investigated.

To achieve the cost-effective machining of Ti, a better understanding of the underlying mechanism through better modeling is necessary[3]. In this report, the 3D FEM modeling of Ti drilling is conducted. The model includes fully adaptive unstructured mesh generation, thermo-mechanically coupling, deformable tool-chip-workpiece contact, interfacial heat transfer across the tool-chip boundary, momentum effects at high speeds and constitutive models appropriate for high strain rate, large deformation analyses.

The geometry of injector spray hole is important for the fuel efficiency and emission of the HCCI fuel systems. To produce consistent quality and control the shape of spray holes, the monitoring and control of electrical discharge machining (EDM) drilling process and the measurement of geometrical features of spray holes are performed.

Approach

High Throughput Drilling of Ti-6Al-4V

High throughput drilling test was conducted at High Temperature Materials Lab at ORNL using a Cincinnati Saber machine with a 4 mm diameter Kennametal K285A01563 WC-Co spiral point drill (WC-Co Spiral). The workpiece was a 6.35 mm thick Ti-6Al-4V plate. This machine has the high speed spindle and through-the-spindle high pressure coolant system. The cutting fluid was 5% CIMTECH 500, a synthetic metalworking fluid.

Table 1 summarizes the cutting fluid supply, peripheral cutting speed, and feed ub four sets of experiments, marked as Exps. I-VI. Exp. I was dry drilling at 183 m/min peripheral cutting speed and 0.051 mm/rev feed. Exp. II was conducted with external cutting fluid supply. Exp. III-IV was conducted with cutting fluid supplied internally through the drill body. The feed was gradually increased from 0.051 to 0.076, 0.102, and 0.152 mm/rev at corresponding drill rotational speed to maintain the same 0.75 m/min feed rate and 156 mm^3/s MRR.

The holes were cut in half to measure the roughness of hole surface using the Taylor Hobson Talysurf model 120 stylus surface profilometer with 0.8 mm cutoff length and 100:1 bandwidth ratio. For each drilling test, the first three holes were measured.

Table 1. Experimental conditions for high throughput drilling tests.

Exp.	Cutting fluid	Cutting speed (m/min)	Feed (mm/rev)
I	No	183	0.051
II	Ext.	183	0.051
III	Int.	183	0.051
IV	Int.	122	0.076
V	Int.	91	0.102
VI	Int.	61	0.152

Metallurgical Analysis

After drilling, one of the sectioned specimens was metallographically mounted in epoxy potting and then polished with fine diamond compound for nanoindentation testing and chemical composition analysis. After nanoindentation, the specimens were etched with a solution containing 6 ml HNO_3 and 3 ml HF in 100 ml H_2O to distinguish the α and β phase structure of Ti-6Al-4V in the SEM. The other sectioned specimen was used for XRD. An original Ti-6Al-4V bulk material was also polished and etched to extract the initial α–β phase information in SEM and XRD testing. The chips were cleaned by acetone, metallographically mounted in epoxy, and sectioned and polished for nanoindentation testing and SEM work.

The polished and etched hole and chip cross sections were examined by a Hitachi S-4700 SEM machine to identify the changes in the microstructure. The phase transformation of α–β phase was examined by a PANalytical XPERT-PRO MPD X-ray diffractometer with Cu tube (generator setting: 40 mA, 45 kV). The chemical composition was investigated by a JEOL 8200 electron microprobe. The nanoindentation tests were conducted on the subsurface adjacent to the hole surface by using a Hysitron triboindenter™ with 2 mN applied load. A MTS Nano-indenter™ II was used for the nanoindentation of drilling chips.

3D FEM Drilling Modeling

The AdvantEdge™ 3D machining simulation software by Third Wave Systems with updated-Lagrangian finite element method, continuous remeshing, and adaptive meshing techniques[4] was used to model Ti machining process. The work-material model contains the power-law strain hardening, thermal softening and rate sensitivity[4]. Figure 2 shows the 3D finite element mesh using a conventional twist drill. The workpiece is modeled with a predrilled cone-shape blind hole to enable the early full-engagement of the whole drill point region to reduce the simulation time.

The model is validated by comparison with experimentally measured thrust force and torque. The drilling test was conducted on a Mori Seiki computer numerical control machining center using a M2 high speed steel twist drill with 3.97 mm diameter, 0.77 mm web thickness, 118° point angle, and 30° helix angle. Workpiece is a 6.35 mm thick Ti-6Al-4V plate. Drilling tests were conducted at three drill rotational speeds, 734, 1100, and 1468 rpm, which corresponds to 9.1, 13.7, and 18.3 m/min drill peripheral cutting speed, respectively. A constant feed of 0.051 mm/rev was used.

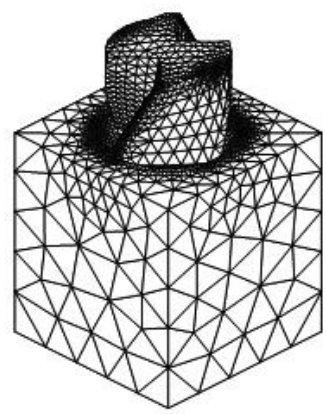

Figure 2. Finite element mesh for 3D drilling model.

Spray Hole EDM

An Agilent Infiniium 54833A digital oscilloscope with 2 GHz sampling rate was used for sub-ns real-time measurement of the gap voltage and current in spray hole EDM. The roundness, straightness, and taper of 0.15 mm diameter fuel injector spray hole was measured using a Werth VideoCheck HA 400 coordinate measurement machine (CMM) using a glass-fiber probe with a

ball end tip and a charge coupling device (CCD) optical sensor to measure the ball contact position.

Results

High Throughput Drilling of Ti-6Al-4V

Supplying the cutting fluid via through-the-drill holes is essential to drill life in high throughput drilling. At 183 m/min cutting speed and 0.051 mm/rev feed, the internal cutting fluid supply (Exp. III) significantly increased the drilling life to 101 holes from 10 holes in dry drilling (Exp. I).

Adjusting the feed also has a significant impact on drill life. Feed is a process parameter which has been overlooked by drilling researchers in the past. Advanced spiral point drill geometry design and new tool material enable the drill to take a higher cutting force and the use of larger feed, which corresponds to lower cutting speed. As shown in Figure 3, at 0.076 mm/rev feed (Exp. IV), the thrust force was at about 200 N and the drill life was 153 holes. Increasing the feed to 0.102 mm/rev (Exp. V) only raised the thrust force to about 260 N for the new drill and 330 N at the end of drill life (204 holes). The lower cutting speed at higher feed helps to reduce the drill temperature, which is beneficial to the drill life. There was a limit of drill life associated with the increase of feed. As the feed increased to 0.152 mm/rev (Exp. VI), the drill life (164 holes) started to deteriorate.

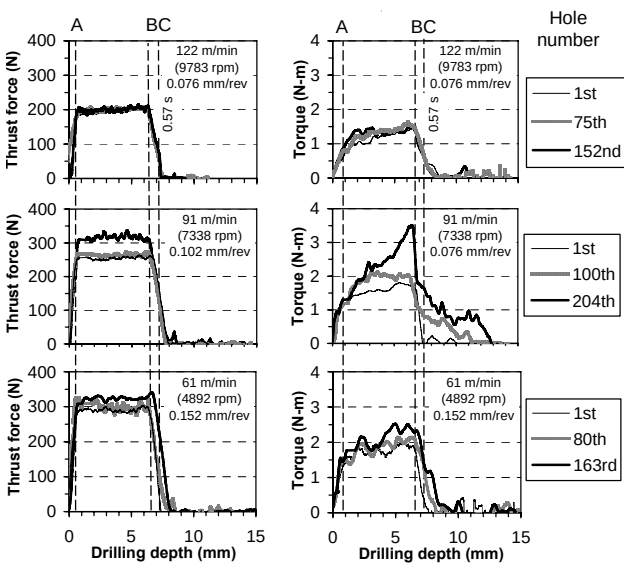

Figure 3. Thrust force and torque of WC-Co Spiral drill for high throughput drilling at 0.75 m/min feed rate and 156 mm^3/s material removal rate with internal cutting fluid supply.

The drill which had good drill life also produced holes with lower surface roughness. Figure 4 shows the hole surface roughness vs. drill life (number of holes) for high throughput drilling tests. All tests have the same MRR, 156 mm^3/s. The range of upper and lower surface roughness of the first three holes is presented. In Exp. IV, the internal cutting fluid supply helps to improve the surface finish. The long drill life positively correlates to the good initial hole surface finish.

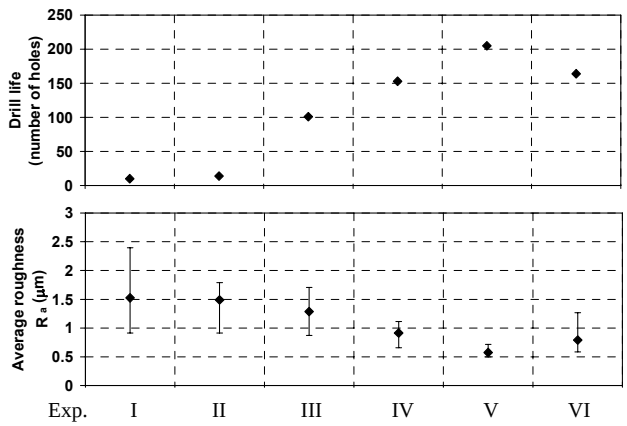

Figure 4. Hole surface roughness under high throughput drilling with the same material removal rate (156 mm^3/s) using WC-Co Spiral drill.

Metallurgical Analysis

Figure 5 shows the SEM micrographs of the hole cross-sections of Exps. I and III, which have the same drilling peripheral cutting speed and feed per revoluation. In Exp. I (dry drilling), the hole surface is rough with many debris welded on the hole surface and 10-15 μm thick subsurface layer. In this layer, there is a gradation of distinct grain boundaries between α and β phases to indiscernable ones from the bulk toward the hole surface. The high magnification micograph of the subsurface layer shows some tiny acicular or elongated grains. This phenomenon is likely due to two factors: one is the phase transformtion from β to α as a result of high temperature and the other is the decrease of grain size due to large plastic deformation.

In Exp. III, the β structure is obseravable at regions very close to the hole surface, suggesting that the extent of the $\beta \rightarrow \alpha$ phase transformation is significantly reduced due to the cutting fluid cooling effect. The subsurface layer is about only 3 μm. As shown in the high magnification micograph, the

grain structure within the subsurface layer is elongated parallel with the hole edge, indicating the severe plastic deformation. The micrographs of Exps. V and VI showed similar features and dimensions of the features as those in Exp. III.

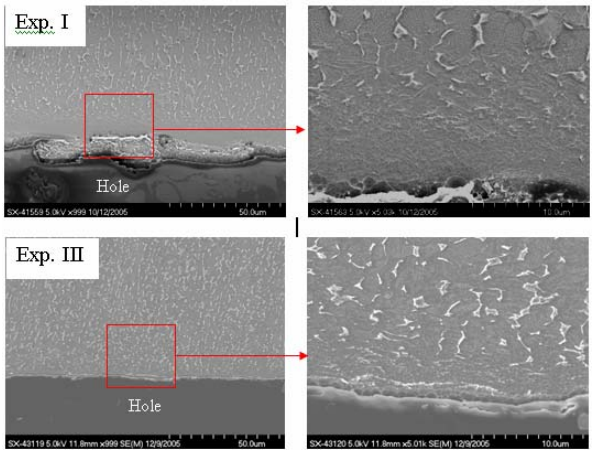

Figure 5. SEM micrographs of the polished and etched cross-sections of drilled holes.

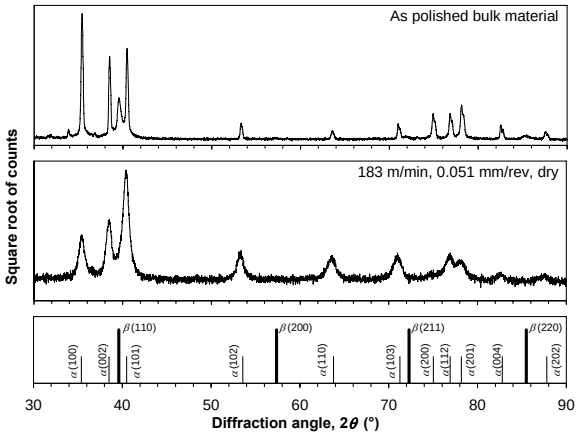

Figure 6. X-ray diffraction patterns of the as-polished bulk material and hole surface of Exp. I.

Quantitative analysis by Rietveld method shows 7.3% β in the bulk material. In Exp. I, the β is reduced to 0%. The X-ray penetration depth is estimated to vary from 4 to 12 μm at 30 to 90° 2θ, respectively, assuming 95% of the total diffraction intensity. According to the micrographs in Figure 1, small amount of β grains still exists in the subsurface layer very close to the hole edge. This is slightly different with the XRD observation. There are two possible causes for the disappearance of β peaks. The main cause is the transformation of a large portion of the β to α phase. The other cause is that the residual β peaks are submerged by broadened neighboring α peaks and become indiscernible. The amount of β phase increases to 13.6, 7.8, and 11.4% for Exps. III, V, and VI, respectively, with the introduction of cutting fluid.

Figure 7 compares the nanoindentation hardness vs. distance from the hole surface in Exps. I and III. The layer of high hardness exists in all conditions, but the extent and the depth of high hardness layer are different from one condtion to another. The highest hardness exists under the dry drilling condition with 183 m/min cutting speed and 0.051 mm/rev feed (Exp. I). At the reigon less than 5 μm from the hole surface, the hardness is over 9 GPa, which is about twice the hardness measured away from the hole surface. The high hardness layer is about 15-20 μm wide. The existence of this hardened layer is the result of severe plastic deformation outweighing the thermal softening effect. The phase transformation from β to α due to high temperature may also contributes to the formation of this layer [5,6]. Beyond this layer, the hardness is stablized around 4.1-5 GPa. When the cutting fluid is supplied at the same cutting speed and feed (Exp. III), the peak hardness is 5-5.5 GPa in the subsurface layer close to the hole edge, which is just slightly higher than the hardness of bulk material. The thickness of hardened layer is reduced to between 5-15 μm.

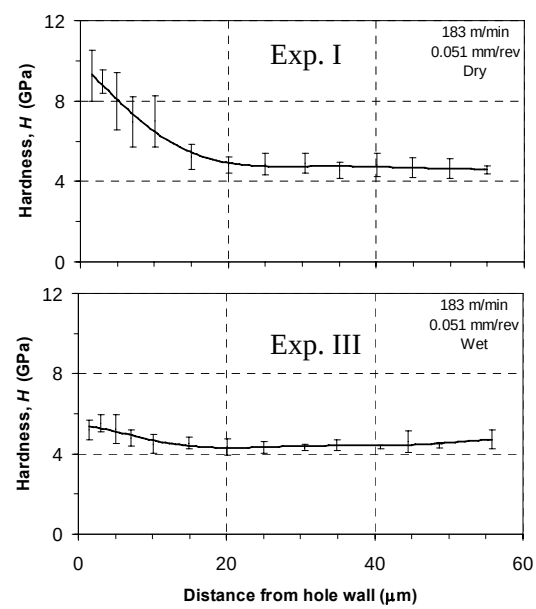

Figure 7. Nanoindentation profile of hole subsurface hardness.

For Ti chip in drilling, the saw tooth chip formation is not a common feature. Both saw teeth and small lamellae were observed in the drilling chips, depending on the locations where cross-sections were taken. Saw teeth are obvious at the outmost edge of the chip which is generated at the outmost point of the drill cutting edge, as shown in the SEM micrographs of chip cross-sections of Exp. I in Figure 8. Even in dry drilling condition, the light β phase can be observed, as well as in the condition with cutting fluid supply. It means the temperature does not reach the β transus temperature across the entire primary shear zone during the drilling process. In chips, shear bands are observed to initiate from the valley of saw-tooth chips. The grain structures are elongated along the both sides of shear bands, clearly identifying the severe plastic shear deformation.

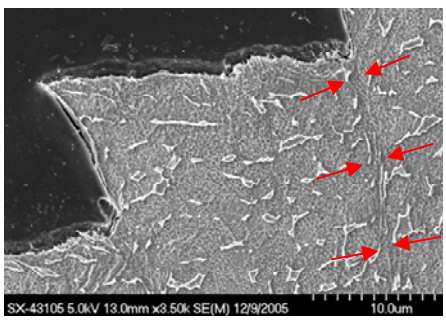

Figure 8. SEM micrograph of chip cross-section in Exp. I.

In the chip formation process at the outmost part of drill cutting edge, high temperature and strain are concentrated in the narrow bands dividing the chips into segments. High temperature tends to soften the material and possibly change the crystal structure, while high strain is expected to increase the hardness. The influence of these competing factors on the mechanical properties was examined by comparing the hardness of shear bands with that of other regions in nanoindentation tests. Figure 9 shows an example of indents on a chip sample. The spacing between each indent is 3-6 μm. No significant difference of hardness can be found between the indents on the shear bands and those on the bulk of chips. Over 140 and 60 indents were made in a similar configuration on saw-tooth chip cross-sections under dry and wet conditions, respectively. The experimental results conclude that the formation of saw tooth feature and shear bands does not change the mechanical properties of chips severely.

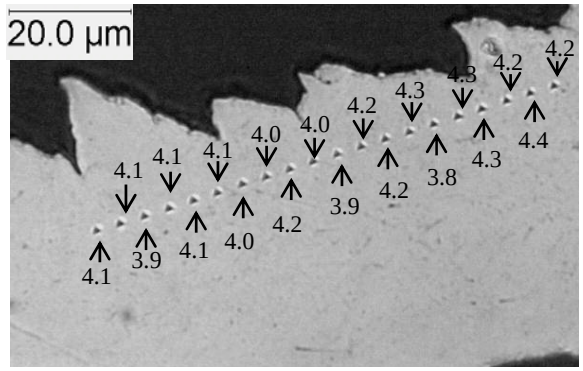

Figure 9. Nanoindentation on the chip cross-section of Exp. I.

3D FEM Drilling Modeling

Figure 10 shows the finite element modeling and averages of experimentally measured thrust forces and torques. The FEM model provides a reasonable estimation of thrust force. The thrust force is less than 20% underestimation, the torque is over-estimated by 50%.

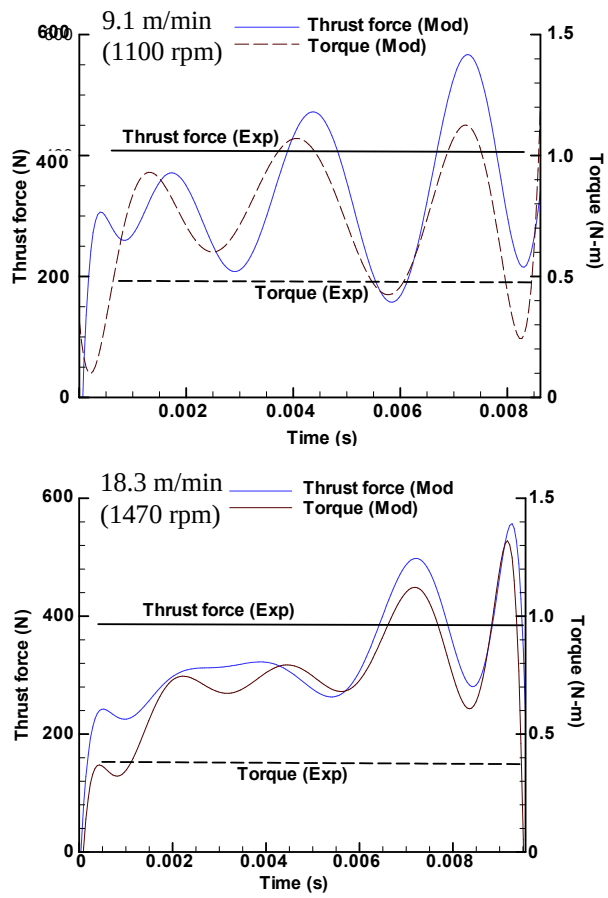

Figure 10. Comparison of modeling and experimental thrust forces and torques.

In experiments, a large amount of heat is generated from the initial contact of the drill and workpiece to the full engagement of drill point region with workpiece. It results in high temperature and softens the workpiece. In comparison, the drill temperature is at room temperature when the cutting edge fully engages the workpiece in FEM. As a result, the workpiece is harder and results in higher torque. Another possible reason for the discrepancy is the inaccuracy of material and friction modeling. A constant coefficient of friction was used.

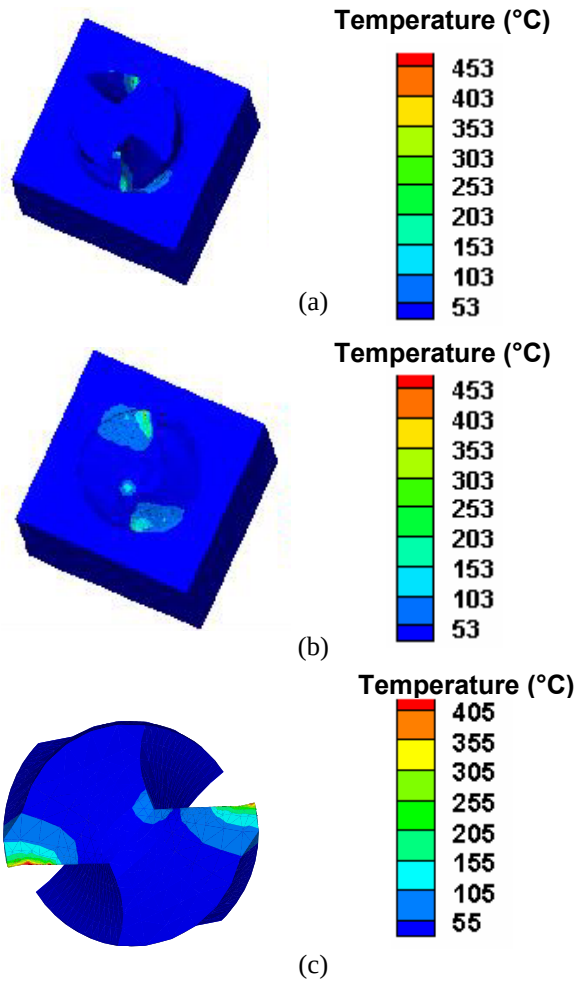

Figure 11. FEM temperature results: (a) drill, chip, and workpiece, (b) chip and workpiece, and (c) drill.

In drilling, the chip formation has a significant influence on the thrust force and torque as well as the temperature and tool performance. An example of the chip formation process is shown in Figure 11. The cutting speed for the selected example is 13.7 m/min. The chip and the engagement of the drill and workpiece are shown in Figure 11(a). Figure 11(b) shows the temperature distribution of the chip and workpiece. The temperature of Ti chip is higher than the cutter surface on the workpiece. The highest temperature, about 453°C, is concentrated in regions contacting the drill cutting edge near the drill margin, where the cutting speed is the highest along the cutting edge. Figure 11(c) shows the temperature distribution on the drill flank face. The peak temperature reaches 405°C. Such high temperature is detrimental to the tool life.

Spray Hole EDM Process Development

Figure 12 shows the gap voltage and current of sample spark and arc pulses and the input and output process parameters in spray hole EDM. The use of thin, 0.075 to 0.15 mm diameter W electrode and short pulse on and off time in spray hole EDM requires the use of sub-ns fast sampling rate to monitor the plasma generation in spark erosion. Figure 13 shows a sample spark using 0.125 mm diameter W wire for EDM AISI 52100. The spark generation events can be divided into six periods, marked as Periods I to IV. A close-up view of the voltage discharge between Period II and III is also show in Figure 13. Applying this monitoring technology, the spark, arc, and short pulses can be identified, the quality of EDM process can be quantified, and the process setup can be adjusted for EDM process optimization.

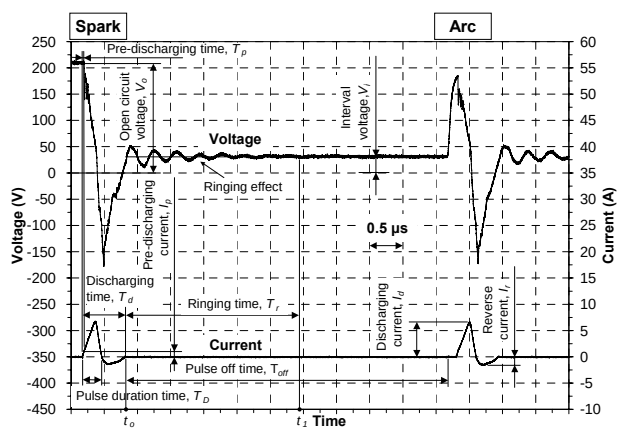

12. EDM process input and output parameters of sample spark and arc pulses.

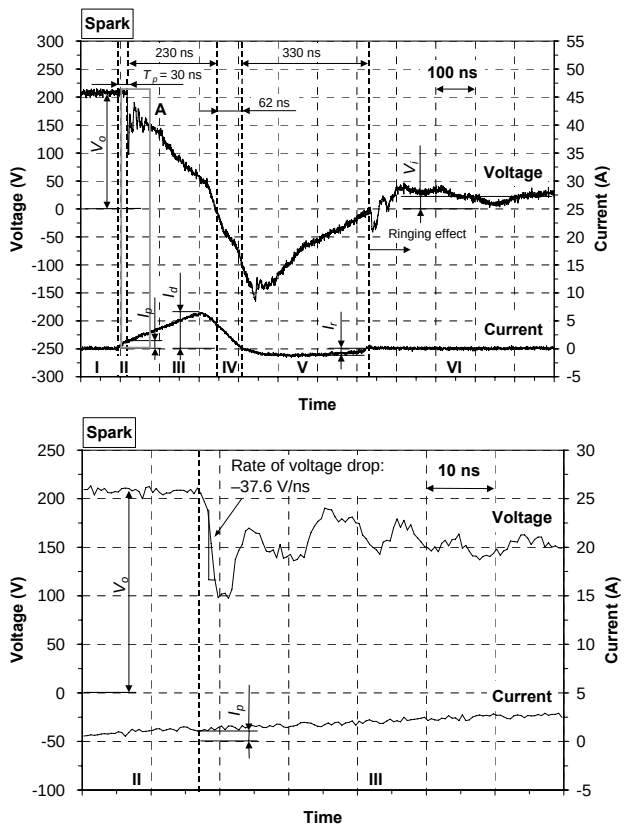

Figure 13. Close up view of the voltage and current change in spark.

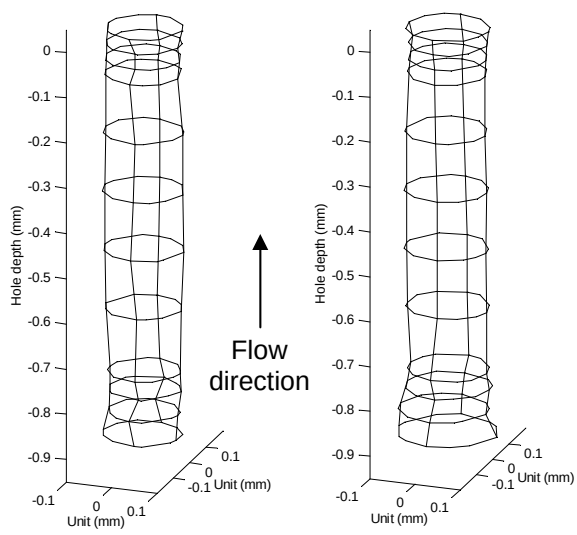

(a) (b)

Figure 14. 3D wireframe representation of a spray hole: (a) before AFM and (b) after AFM.

The geometrical features, including roundness, straightness, and taper, of a 0.15 mm nominal diameter spray hole before and after the abrasive flow machining (AFM) is illustrated in Figure 14 by the 3D wire mesh representation. The effect of AFM to enlarge the size of spray hole on one side on the flow entrance end can be recognized. Using this measurement technology the level of reverse taper and its effect on engine performance can be correlated.

Conclusions

Experiments of high throughput drilling of Ti-6Al-4V with 156 mm^3/s material removal rate using a 4 mm diameter WC-Co spiral point drill demonstrated that supplying the cutting fluid via through-the-drill holes was a critical factor for drill life. The balance of cutting speed and feed is essential to achieve long drill life and good hole surface roughness.

Metallurgical studies, including SEM, XRD, electron microprobe, and nanoindentation tests were conducted on the hole surface and subsurface and the chips in high-throughput drillling of Ti-6Al-4V. In dry drilling, the transformation of BCC β phase into HCP α phase was identified in a 10 to 15 μm wide subsurface layer adjacent to the hole surface by SEM and XRD analysis. High hardness was found in this layer by nanoindentation testing. No obvious $\beta \rightarrow \alpha$ phase transformation occurrd with the supply of cutting fluid. The high hardness layer was also narrower than that of dry drilling. Unlike chips formed in orthogonal cutting, drilling chips had complicated morphology. The saw-tooth feature only formed at the outmost region of the drill cutting edge, mainly due to the variable cutting speed along the cutting edge. Narrrow shear bands could be observed in the cross-sections of chips with distinct saw teeth, but no significant change of mechanical properties along the chips was found using nanoindentation tests.

A 3D Finite Element Drilling Modeling was validated by comparing the experimentally measured and modeling thrust force and torque. The model provides good estimation of thrust force but the torque is overestimated by 50%. Further improvement of the FEM drilling model is currently ongoing. This study will be extended to high-throughput drilling of Ti.

The future research will move to the HCCI fuel systems advanced material manufacturing development. Spray hole will remain to be a critical engine technology that will be further developed in this research to achieve the efficiency and quality

control of spray hole size smaller than the current standard size spray hole and the associated process improvement and geometrical measurements.

References

1. M. J. Donachie, Jr., Titanium: A Technical Guide, ASM International, Material Park, OH, 1988.
2. D. A. Stephenson, J. S. Agapiou, *Metal Cutting Theory and Practice*, Marcel Dekker, New York, 2005.
3. X. Yang and C. R. Liu, "Machining Titanium and Its Alloys," *Machining Science and Technology*, **3**(1), 107–139 (1999).
4. T.D. Marusich, M. Ortiz, "Modeling and Simulation of High-Speed Machining," *International Journal for Numerical Methods in Engineering*, **38**(21), 3675-3694 (1995).
5. A.R. Machado, J. Wallbank, "Machining of Titanium and Its Alloys-A Review," *Proceedings of Institution of Mechanical Engineers, Part B: Management and Engineering Manufacture*, **204**(1), 53-60)1990).
6. J. Cantero, M. Tardío, J. Canteli, M. Marcos, M. Miguélez, "Dry Drilling of Alloy Ti-6Al-4V", *International Journal of Machine Tool s and Manufacture*, **45**(11), 1246-1255(2005).
7. C.A. van Luttervelt, T.H.C. Childs, I.S. Jawahir, F. Klocke, P.K. Venuvinod, "Present Situation and Future Trends in Modelling of Machining Operations -- Progress Report of the CIRP Working Group `Modelling of Machining Operations'," CIRP Annals - Manufacturing Technology, **47**, 587-626 (1998).

Presentations and Publications

R. Li, P. Hegde, A.J. Shih, "High Throughput Drilling of Titanium Alloys," *International Journal of Machine Tools and Manufacture*, **43**, 63-74 (2007).

R. Li and A. J. Shih, "Finite Element Modeling of 3D Turning of Titanium," *International Journal of Advanced Manufacturing Technology* **29**(3-4), 253-261 (2006).

T. D. Marusich, S. Usui, R. Aphale, N. Saini, R. Li, A. J. Shih, "Three-Dimensional Finite Element Modeling of Drilling Processes," presented at 2006 ASME International Conference on Manufacturing Science and Engineering, October 8-11, 2006, Ypsilanti, Michigan.

R. Li, A. J. Shih, "High Throughput Drilling of Titanium Alloys," presented at the 2006 International Conference on Frontiers of Design and Manufacturing, Guangzhou, China, June 19-22, 2006.

R. Li and A. J. Shih, "Inverse Heat Transfer Solution of Tool Temperature in Titanium Drilling," *Journal of Manufacturing Science and Engineering* (submitted).

R. Li, L. Riester, T. R. Watkins, P. J. Blau, A. J. Shih, "Metallurgical Analysis and Nanoindentation Characterization of Ti-6Al-4V Workpiece and Chips in High Throughput Drilling," *Materials Science and Engineering: A* (submitted).

B. Synergistic Process-Enhanced Grinding of Advanced Engine Materials

Ronald H. Chand
Oak Ridge National Laboratory
P.O. Box 2008, Mail Stop 6063
Oak Ridge, TN 37831-6063
(865) 574-3123; fax: (865) 574-6918; e-mail: chandrh@ornl.gov

DOE Technology Development Manager: Jerry L. Gibbs
(202) 586-1182; fax: (202) 586-1600; e-mail: Jerry.gibbs@ee.doe.gov
ORNL Technical Advisor: D. Ray Johnson
(865) 576-6832; fax: (865) 574-6098; e-mail: johnsondr@ornl.gov

Contractor: Oak Ridge National Laboratory, Oak Ridge, Tennessee
Contract No.: DE-AC05-00OR22725

Objective

- The objective of this effort is to understand, develop, and apply synergistic process-enhanced grinding (SPEG) to improve the efficiency of grinding advanced materials while ensuring surface quality.

Approach

- Conduct a comprehensive investigation of the current state of the art in SPEG methods. This study is to focus on advanced laser machining and its application to machining of advanced engine components.
- Modify one or more existing machine tools at ORNL to conduct instrumented, SPEG experiments on ceramics, cermets, and/or metal matrix composites that are candidates for diesel engine components.
- Develop a high-speed, instrumented scratch testing system to study the microstructural response of advanced materials like ceramics and composites to the high deformation rates they experience during grinding.

Accomplishments

- A comprehensive search and evaluation of 2000 recent worldwide publications in the area of laser assisted machining, treatment, and structuring was conducted. Water jet guided laser machining was identified as a potential technology for machining automotive injector nozzle.
- Specifically designed laser machining technology was successfully tested on machining 3mm diameter holes in 5mm thick silicon carbide.
- Milling machine was specifically fitted and instrumented to test high speed boring of holes to improve the cycle time of finishing ID of silicon nitride roller followers.
- A new type of grinding wheel with replaceable diamond inserts was designed for a dynamic scratch test.

Future Direction

- Laser machining of small holes shows great promise and will be further developed
- Hole boring technology will be tested on actual silicon nitride roller follower.
- Dynamic scratch test will be performed using the new design replaceable diamond insert wheel.

Introduction

The advanced ceramic manufacturers have continually faced the challenge of making components for the automotive industry at a cost that the industry could afford. Major cost of an advanced ceramic component continues to be the machining cost. This cost can no longer be lowered any further by arbitrary manipulations of the processing variables. Application of lower cost labor is not a solution either for it results in more out sourcing of jobs. New synergistic process-enhanced machining methodologies are needed to meet the goals.

The objective of this effort is to survey and identify technologies that could help lower the cost of machining advanced engine materials through the systematic evaluation and development of new machining technologies. The current approach involves a comprehensive investigation of the current state of the art in SPEG methods, machining tests on specially modified and instrumented machine tool, especially as related to the machining of advanced ceramics for automotive engine components. The approach also includes design of a high-speed, dynamic scratch testing system to study the microstructural response of advanced ceramics to the high deformation rates they experience during grinding. The focus on roller followers and fuel injector nozzles is based on discussions with manufacturers. Laser drilling and diamond boring tests were conducted on silicon carbide material and a new replaceable diamond insert wheel was developed for a dynamic scratch test on advanced ceramic materials.

Approach

A comprehensive search and evaluation of most recent publications in the area of laser assisted machining, treatment, and structuring was conducted. A water jet guided laser technology was identified as a potential machining methodology for advanced ceramics.

Preliminary experiments were successfully conducted with specifically developed laser machining technology to drill small (3mm diameter) holes in 5mm thick silicon carbide.

For cost-effective machining of the inside diameter of roller followers, a unique hole boring approach was studied. A milling machine was instrumented with Kistler dynamometer and modified with a through the tool coolant delivery system and hole boring experiments were conducted.

To study the microstructural response of advanced ceramics to the high deformation rates they experience during grinding, a scratch test that emulates the dynamics of the grinding process is required. As a first step towards developing a dynamic scratch test a wheel with replaceable diamond inserts was designed.

Results

The results presented here are an abbreviated version of more detailed quarterly reports. The comprehensive search of published literature on laser machining resulted in the evaluation of 2000 most recent publications.

The findings are summarized below:

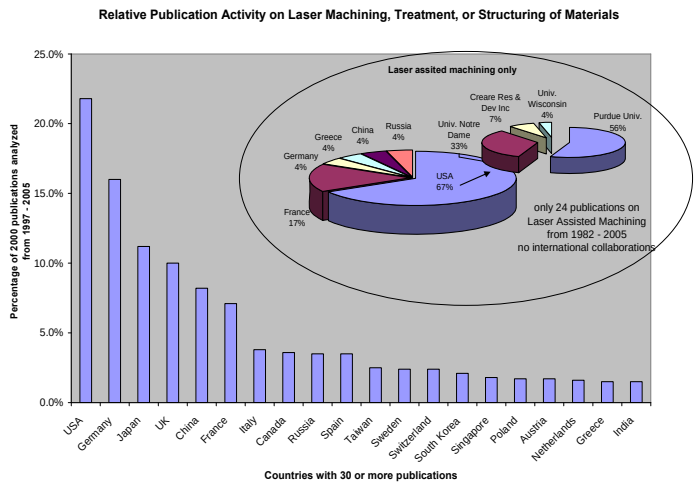

Figure 1 Publication Activity on Laser Machining

Analysis of the literature and trend suggested that

1. Materials' processing with lasers is an active area of research.
2. Laser as a tool is making conventional manufacturing more accurate and cost-effective.
3. Laser technology is also opening up new manufacturing technologies that go beyond conventional methodologies.
4. Laser technology can be arranged in four categories. Namely, Laser Machining, Laser Assisted Machining, Laser Deposition, and Laser Treatment.

As a result of the extensive search and evaluation a ***breakthrough technology*** called the water jet guided laser system (Figure 2) was identified. This system utilizes a water jet to guide the laser beam over a much longer (10 cm) distance as compared to conventional focused laser beam that has a working distance of just a few millimeters. An additional benefit of the water jet is thermal management of the work zone and flushing away of the molten material.

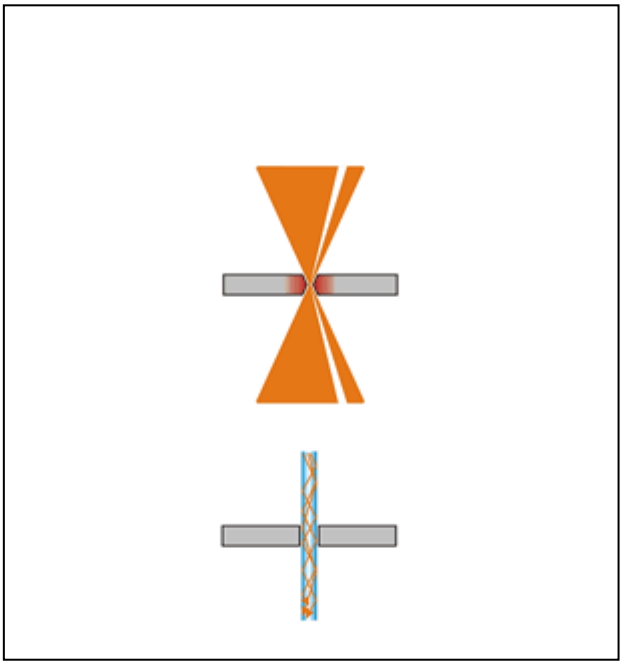

Figure 2 Illustration of Conventional & Water Jet Guided Laser

Preliminary trials of material removal via laser drilling operation in CVD SiC has yielded unprecedented removal rates at an order of magnitude higher than the highest rate obtainable with existing technologies. The experiment was conducted using fiber optic delivered Nd-YAG laser (1.06 µm wavelength) at the operating parameters of 0.5ms pulse duration, 50 Hz pulse frequency and 300W. The high material removal rates and associated high dimensional tolerances of holes (Figure 3) pointed to the possibility of the extension of laser-based machining technique into a hybrid water jet-assisted laser machining technique for rapid and cost effective machining of ceramics. Furthermore, the employment of water jet-assisted laser beam delivery is expected to eliminate generation of the thermal stresses during machining that are often detrimental to the integrity of ceramic component.

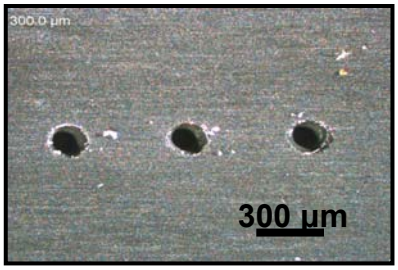

Figure 3 Optical micrograph of photonic drilled holes in silicon carbide.

As a continued effort to test SPEG methodologies a milling machine at HTML was modified (Figure 4) to do test high speed hole finishing of diesel engine roller followers.

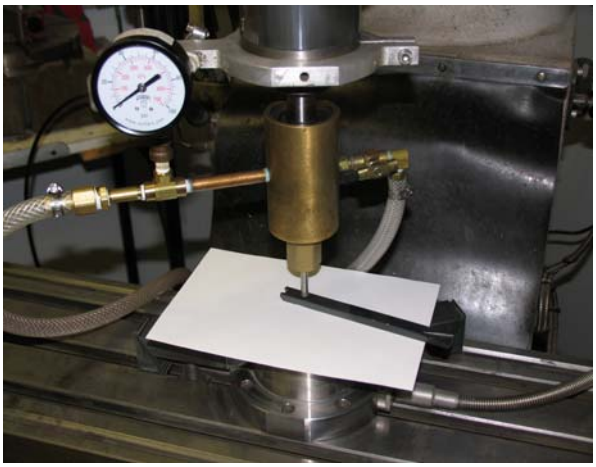

Figure 4 Modified Milling Machine for Hole Boring

Preliminary drilling tests conducted on silicon carbide using the modified machine resulted in 3.5 times the conventional material removal rate.

To study the microstructural response of advanced materials like ceramics and composites to the high deformation rates they experience during grinding a test system comprising of a special wheel with a replaceable diamond insert was developed. The wheel is illustrated in Figure5.

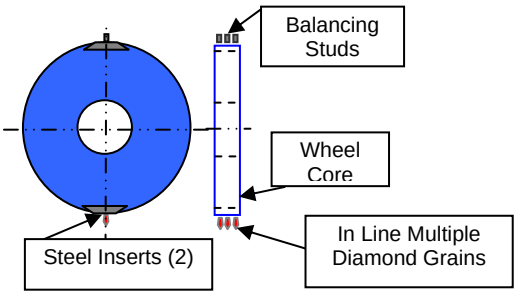

Figure 5 Dynamic Scratch Test Diamond Wheel

Summary and Conclusions

- The comprehensive search and evaluation of SPEG literature resulted in the discovery of water jet guided laser technology. Preliminary results obtained on conventional laser machining of small holes in silicon carbide showed great promise. It is anticipated that water jet guided laser system would enhance laser machining and should be further evaluated as an important tool for machining advanced ceramics.
- Diesel engine roller followers continue to suffer from high cost of machining. The bore finishing test conducted on modified milling machine showed much promise in further developing the high speed bore finishing technology.
- Fundamental understanding of the interaction between the diamond grains and the material during grinding is critical for making the grinding process more efficient. A dynamic scratch test that emulates the grinding process is necessary for studying such interaction. To this end the replaceable diamond insert wheel is a valuable development for it allows the diamond insert to be removed from the wheel for characterization and be inserted back for continuation of the test.

6. MATERIALS FOR HOT SECTION COMPONENTS

A. NDE of Diesel Engine Components

Jiangang Sun
Argonne National Laboratory
9700 South Cass Avenue
Argonne, IL 60439
630-252-5169; fax: 630-252-2785; e-mail: sun@anl.gov

DOE Technology Development Manager: Jerry L. Gibbs
(202) 586-1182; fax: (202) 586-1600; e-mail: Jerry.gibbs@ee.doe.gov
ORNL Technical Advisor: D. Ray Johnson
(865) 576-6832; fax: (865) 574-6098; e-mail: johnsondr@ornl.gov

---

Contractor: Oak Ridge National Laboratory, Oak Ridge, Tennessee
Contract No.: DE-AC05-00OR22725
Subcontractor: Argonne National Laboratory, Argonne, Illinois

---

Objectives

- Develop laser-scattering and other nondestructive evaluation (NDE) methods for detection and characterization of surface and subsurface defect/damage in diesel-engine valve-train components made from advanced materials such as ceramics and intermetallics.
- Develop quantitative NDE analysis tools to identify strength-limiting flaws and failure mechanisms, evaluate damage evolution and growth, and predict mechanical properties for advanced materials.

Approach

- Develop fast and reliable automated laser-scattering NDE systems for surface/subsurface inspection of Si_3N_4 ceramic and TiAl intermetallic valves.
- Inspect valve surfaces using developed NDE methods to determine the level of machining damage and accumulated damages from bench and engine tests.
- Correlate NDE data with microstructure and strength of silicon-nitride specimens for prediction of fracture initiation defects and mechanical properties.

Accomplishments

- Established laser-scatter NDE detection sensitivity for surface damage in TiAl specimens.
- Evaluated 25 SN235P Si_3N_4 and 11 TiAl valves tested by a cyclic-impact bench rig for >20 h. Identified levels of impact damage and verified effectiveness of oxidation treatment for TiAl surface to improve wear resistance.
- Inspected 10 SN235P Si_3N_4 and 4 TiAl valves after 100-h engine test. While minor surface wear was found for Si_3N_4 valves, considerable surface damage was detected for the TiAl valves.
- Developed a high-resolution cross-polarization confocal microscopy technology. For the first time, subsurface C-crack trajectory within translucent Si_3N_4 materials can be directly imaged in 3D.

Future Direction

- Complete NDE evaluation for damage accumulation in SN235P and TiAl valves from 500- and 1000-h engine tests.
- Perform NDE analysis for prediction of strength-limiting defects/damage in engine-tested valves.
- Continue development of the cross-polarization confocal technology to improve detection sensitivity, spatial resolution, and penetration depth for translucent materials.

Introduction

Advanced ceramics and intermetallics are leading candidates for high-temperature engine applications that offer improved fuel efficiency and reduced emissions. Among them, silicon nitrides (Si_3N_4) and titanium aluminide (TiAl) are being evaluated as valve-train materials for diesel and natural gas engines because of their lighter weight, high strength and corrosion resistance at elevated temperatures. However, these materials are brittle so microscopic defect/damage near the surface may significantly degrade their mechanical properties. Material damage in the subsurface may be induced by machining or from service due to impact, wear, and corrosion. For silicon nitrides, material strength may also be limited by inherent defects such as voids and porosities within subsurface. To detect and characterize these defects, Argonne National Laboratory (ANL) developed a laser scattering NDE method to measure detailed surface/subsurface microstructure for these materials. The objective of this research is to demonstrate that this method can be used to assess/evaluate the cost-effectiveness and reliability of valve-train components manufactured from advanced ceramic and intermetallic materials for diesel engines. The primary effort in FY 2006 was to utilize a fast NDE valve-scan system developed in FY2005 to evaluate SN235P Si_3N_4 and TiAl valves after cyclic-impact rig test and 100-hour engine duration test. Another effort was directed on developing a cross-polarization confocal microscopy technology for high-resolution 3D subsurface imaging of translucent materials such as ceramics. This research is collaborated with Caterpillar, Inc.

Approach

The critical region for brittle ceramic and intermetallic components in structural applications is near surface. The common types of defects in this region are mechanical, such as cracks, spalls, inclusions, and voids. The size of the defects that limits the component strength is generally small, say ~100 µm. To detect these defects, a laser-scattering method based on cross-polarization detection of optical scattering originated from surface and subsurface microstructure can be used for noncontact, NDE of these materials. Because ceramics are partially translucent to light, optical penetration can reach the subsurface to directly interact with the subsurface defects. For metallic or intermetallic materials, optical penetration is not possible. However, cross-polarization detection eliminates optical reflection from smooth surface and measures only optical scattering from rough or cracked surface. By scanning the entire surface (flat or curved) of a component and constructing a two-dimensional (2D) scatter image, surface/subsurface defects can be readily identified as they exhibit excessive scattering over the background, and their type and severity may be analyzed. To apply this technology for NDE of Si_3N_4 and TiAl valves, an automated laser-scatter system was developed by ANL for scanning the entire valve surface at high spatial resolutions (5-10 µm). The resulting 2D scattering image data are used to identify the location, size, and relative severity of subsurface defects/damage. Analysis of the NDE data can determine the statistical properties of the component surface, which can be correlated with machining or service conditions. Development of quantitative image-processing methods may lead to automated identification of strength-limiting defect/damage for prediction of mechanical properties.

Results

Evaluation of Cyclic-Impact-Tested Si_3N_4 Valves

Twenty-five SN235P Si_3N_4 valves, consisting of 13 intake and 12 exhaust natural-gas valves finish-machined in FY2005, were proof tested in a cyclic-impact rig at Caterpillar for >20 hours. These valves were evaluated by ANL's automated laser-scatter NDE system. Only valve-head surface was scanned

with a scan pixel size of 10 µm. NDE data were analyzed and compared with photomicrographic surface images to identify damages.

For all 25 SN235P valves, laser-scatter data did not reveal any subsurface damage in the valve head surfaces. This observation is consistent with the results for the 10 NT551 Si_3N_4 valves that exhibited no subsurface damage after testing in the same cyclic-impact rig for up to 1000 hours[1]. A few valves, however, showed apparent circumferential "wear scars" within the contact surface. A "wear scar" is seen in the laser-scatter image (Fig. 1) of exhaust valve #29 after 20-h rig test. The scarred surface displays lower scatter intensity (darker) in the contact surface. Because defect/damage normally generates higher scatter intensities, the reduction of scatter intensity within the scarred area does not indicate damage, but likely due to surface contamination of embedded metal particles from the metal seat insert. This is verified from photomicrograph of the contact surface (in Fig. 1). The higher scatter-intensity spots in the enlarged NDE image represent material inherent defects such as porosities with sizes typically smaller than 50 µm.

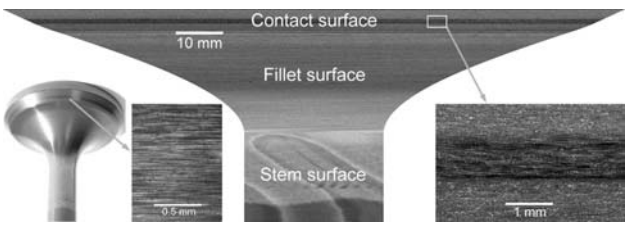

Figure 1. Laser-scatter scan image of head surface of SN235P valve #29 after 20-h rig test.

Evaluation of Cyclic-Impact-Tested TiAl Valves

Eleven TiAl natural-gas exhaust valves were NDE evaluated after cyclic-impact rig test at Caterpillar for >20 hours. Because as-processed TiAl surfaces are susceptible to wear/impact damage, 5 TiAl valves were oxidation treated to improve their surface wear resistance. The treatment caused slight curvature along valve axis which, however, did not significantly affect the NDE scanning. Both head and stem surfaces of these valves were scanned because of apparent damage on these surfaces. NDE data were analyzed and compared with photomicrographic surface images.

For the 6 untreated TiAl valves, significant surface damage from the rig test was observed in the contact and stem surfaces, especially for TiAl valves #1 and #2. The laser-scatter image of the valve-head surface of TiAl valve #1 is shown in Fig. 2. A gross variation of scatter intensity along the axial direction (in fillet surface) is noticeable, which is due to slight angle or focus-distance mismatch during the scan. The impact wear damage within the contact surface is represented by higher scatter intensities (brighter). The photomicrograph and the enlarged NDE image in Fig. 2 show clearly the wear scar. It is evident that the laser-scatter intensity is very sensitivity to the surface condition: surface damage, which may result in higher surface roughness, causes strong laser scatter from the surface. The wear damage in the contact surface of other 4 TiAl valves was less severe than that in TiAl valves #1, as seen in Figs. 3a and 3b.

For the 5 oxidation-treated TiAl valves, very minor surface wear was observed from the NDE data (Fig. 3c). Therefore, NDE data verified that oxidation treatment of the TiAl surface can significantly improve its wear resistance.

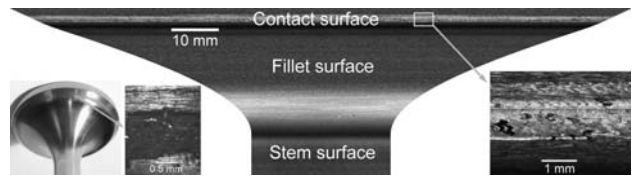

Figure 2. Laser-scatter scan image of head surface of TiAl valve #1 after 20-h cyclic-impact rig test.

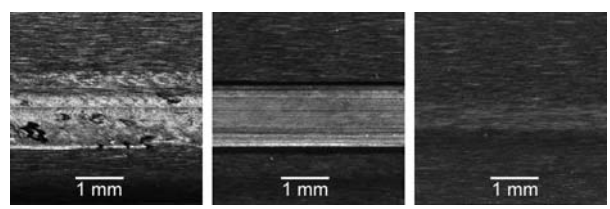

(a) (b) (c)

Figure 3. Detailed laser-scatter images in contact surfaces of TiAl valves (a) #1, (b) #3, and (c) #6 after cyclic-impact rig test.

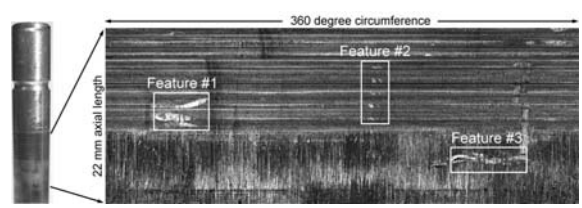

Figure 4. Laser-scatter scan image of stem surface of TiAl valve #1 after 20-h rig test.

NDE scans were also performed for the stem surfaces of all TiAl valves. Figure 4 is the laser-scatter scan image for the stem surface near the keeper groove of TiAl valve #1. In addition to the axial and circumferential wear stripes of higher scatter intensities, three features with distinctly higher scattering intensities are identified. These features were examined under optical microscope, shown in Fig. 5. Correlation of NDE data with photomicrographs concluded that these are surface damages probably induced by scratch or indent.

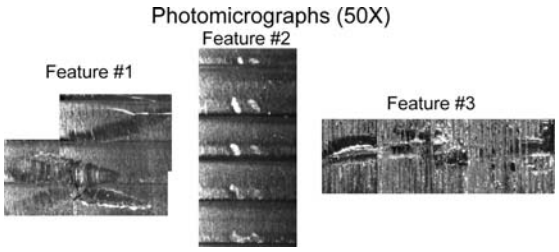

Figure 5. Photomicrographs of features detected in the NDE data in Fig. 4.

Figure 6. Photograph of 100-h engine-tested Si_3N_4 and TiAl valves.

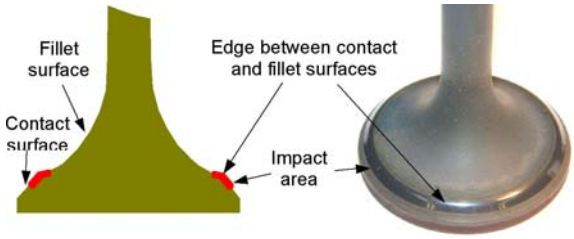

Figure 7. Location of impact area on valve surface.

NDE Characterization of Si_3N_4 and TiAl Valves after 100 Hours of Engine Test

Ten Si_3N_4 and four TiAl valves were run successfully for 100 hours in a Caterpillar natural-gas G3406 generator set at the National Transportation Research Center (NTRC). Figure 6 shows a photograph of these valves. It is seen that all valve-head surfaces were covered by a coat of combustion byproduct[2]. However, the impact area of the valve seat surface is clean without any deposit. The impact area is not entirely within the conical contact surface; it lies around the edge between the contact and fillet surface, as illustrated in Fig. 7.

NDE scans of the valve-head surface for all valves were conducted. Typical results for Si_3N_4 intake, Si_3N_4 exhaust, and TiAl exhaust valves are presented and discussed below. Figure 8 shows the laser-scatter image of the valve-head surface of Si_3N_4 intake valve #20 that was positioned at I2 in the engine. The combustion coating has some effect on scatter intensity in the contact and fillet surfaces. Within the impact area, shown in the enlarged NDE image, the scatter intensity in the conical contact surface is higher that that in the fillet surface (see edge location), which indicates a difference of wear levels in the two surfaces. Nevertheless, no apparent damage was detected within the entire impact region of all Si_3N_4 intake valves.

Figure 9 shows the laser-scatter image of the valve-head surface of Si_3N_4 exhaust valve #11 positioned at E1 in the engine. The combustion coating on this valve is thin, so the valve surface underneath the coating is clearly imaged. The impact region for this valve shows relatively higher scatter intensity than the surrounding surface. The NDE data within the impact region also exhibit multiple bands of scatter-intensity variation; which could be an artifact due to slight laser-incident-angle variation. Despite these NDE indications of surface wear from engine test, no subsurface damage such as cracks was detected for all Si_3N_4 exhaust valves.

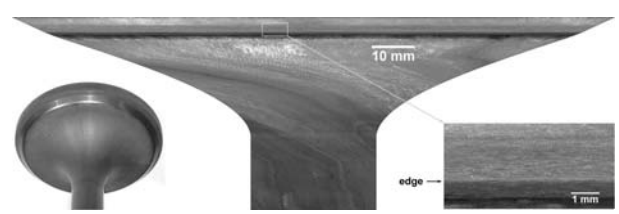

Figure 8. Laser-scatter scan image of Si_3N_4 intake valve #20 (at I2 in engine) after 100-h engine test.

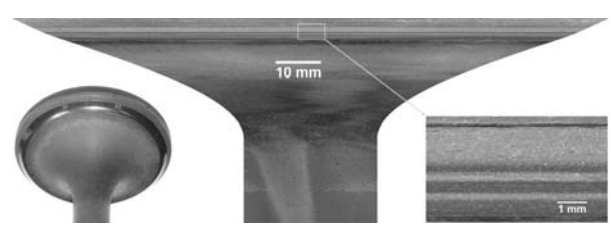

Figure 9. Laser-scatter scan image of Si_3N_4 exhaust valve #11 (at E1 in engine) after 100-h engine test.

Figure 10 shows the laser-scatter image of the valve-head surface of TiAl exhaust valve #8 positioned at E15 in the engine. The combustion coating on this and other TiAl valves caused very high scatter than that from the bare TiAl surface. In order to display scatter image for the entire surface, the scatter intensity is scaled logarithmically in this image (this is a common practice in presenting optical data). For this and other TiAl valves, two types of damage indications were observed. First, several high scatter-intensity spots with sizes up to ~1 mm were detected within the impact region (see enlarged image in Fig. 10). Second, the impact region exhibits considerable wear damage represented by distributed scatter-intensity variations over the entire impact region. These NDE results indicate that the impact damage in TiAl valves appears to be progressing at a faster rate than those observed in the Si_3N_4 valves.

Figure 11 shows photomicrographs of impact surfaces in Si_3N_4 intake valve #20, Si_3N_4 exhaust valve #11, and TiAl exhaust valve #8. For Si_3N_4 intake valve #20, the original machining roughness is still present, with little or no wear is observed. For Si_3N_4 exhaust valve #11, the machining roughness has been worn off, only little remaining along the fillet surface. The worn surface appears smooth, with distributed porosity spots and few subsurface damage marks (bright line) that are probably remnants of the original machining damage. For the TiAl exhaust valve #8, however, a large spot with clear boundary is observed. Material corrosion is suspected within this area, which showed higher scattering in the NDE data (this spot is seen in the enlarged image in Fig. 10). In addition, the impact surface of the TiAl valve becomes very rough, with significant wear damages. In general, the micrographic observations of these valves are consistent with those detected by the laser scatter NDE.

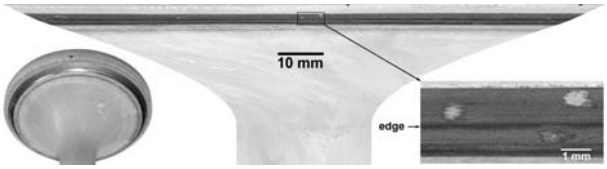

Figure 10. Laser-scatter scan image (in log-intensity scale) of TiAl valve #8 (at E15 in engine) after 100-h engine test.

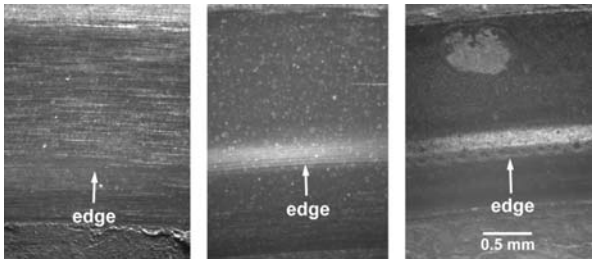

Si_3N_4 intake #20 Si_3N_4 exhaust #11 TiAl exhaust #8

Figure 11. Photomicrographs of impact surfaces of Si_3N_4 and TiAl valves after 100-h engine test.

Cross-Polarization Confocal Microscopy of 3D Subsurface Microstructure in Silicon Nitrides

Measurement of detailed 3D subsurface microstructure is critical in determining material properties. However, the laser-scatter method used for detecting subsurface damage in ceramic valves can only image the 2D microstructure in the subsurface without the depth resolution. To resolve depth and improve spatial resolution, a cross-polarization confocal microscopy technology was developed at ANL. A schematic diagram of the system is shown in Fig. 12. In a typical test, the sample is scanned in the x-y-z directions in a raster fashion, and the resulting 3D scattering data can be viewed as lateral or cross-sectional images representing the subsurface microstructure of the sample. Preliminary tests demonstrated that, with a moderate 40X objective lens at an optical wavelength of 633 nm, the system has an axial (depth) resolution of 2 µm and a lateral resolution of ~0.6 µm, which are significantly higher than other available optical methods used for direct subsurface structure measurement.

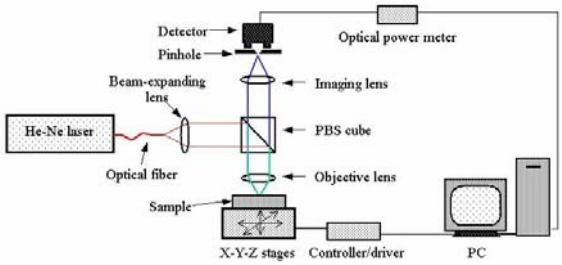

Figure 12. Schematic of cross-polarization confocal microscopy system.

A NT551 silicon nitride specimen with known subsurface damage was tested. The damage is subsurface C cracks induced by indentations with

different loading forces. Figure 13 shows a lateral scan image of a damaged region with two C cracks generated by 2800 and 3000N loads. Strong laser scattering intensity is observed from both C cracks as well as from many individual material defects likely porous spots. Figure 14 is a cross-sectional scan image at Line A marked in Fig. 13, which shows clearly the direction and depth of the C-crack trajectories in the subsurface. The depth of optical penetration is ~40 µm, which can be increased using longer laser wavelengths.

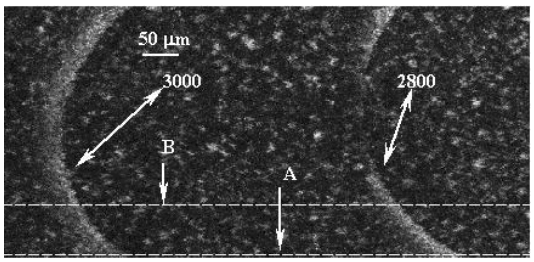

Figure 13. Lateral confocal-scan image of a NT551 silicon nitride specimen with two C cracks.

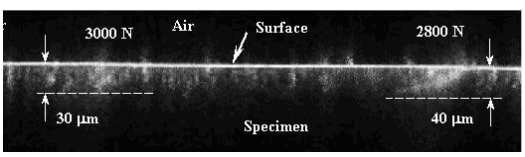

Figure 14. Cross-sectional confocal-scan image along line A as indicated in Fig. 13.

Conclusions

Twenty-five finish-machined SN235P Si_3N_4 valves and eleven as-processed TiAl valves were tested in a cyclic-impact bench at Caterpillar for >20 hours and inspected using the laser-scatter valve-scan system at ANL. The NDE data indicated no detectable damage in SN235P valves. However, surface impact/wear damages ranging from severe to minor were found for TiAl valves. NDE data also verified that oxidation treatment of the TiAl surface can significantly improve its wear resistance.

Ten Si_3N_4 (6 inlet and 4 exhaust) and four TiAl exhaust valves successfully run for 100 hours in a Caterpillar natural-gas G3406 generator set at NTRC were examined by the laser-scatter NDE system. For Si_3N_4 inlet valves, no apparent damage was detected within the entire impact region. For Si_3N_4 exhaust valves, NDE data showed general surface wear within the seat surface; however, no subsurface damage such as cracks was detected. For TiAl exhaust valves, NDE test detected suspected corrosion spots as well as considerable wear damage over the entire impact surface. These results indicate that the impact damage in TiAl valves appears to be progressing at a faster rate than those observed in the Si_3N_4 valves.

A cross-polarization confocal microscopy technology was developed in FY2006. The system resolution was found to be excellent: 2 µm in the axial (depth) direction and 0.6 µm in the lateral direction, which are likely the best resolutions achieved by optical methods. For the first time, subsurface C-crack trajectory within Si_3N_4 materials can be directly imaged in 3D.

References

1. J. G. Sun, "NDE Development for Ceramic Valves for Diesel Engines," *Annual Report for FY 2004, Heavy Vehicle Propulsion Materials Program*.

2. J. S. Trethewey, "High-Temperature Advanced Materials for Lightweight Valve Train Components," *Quarterly Report for April-June 2006, Heavy Vehicle Propulsion Materials Program*.

Presentations and Publications

J. M. Zhang, J. G. Sun, M. J. Andrews, A. Ramesh, J. S. Trethewey, and D. M. Longanbach, "Characterization of Subsurface Defects in Ceramic Rods by Laser Scattering and Fractography," in *Review of Quantitative Nondestructive Evaluation*, Vol. 25, eds. D.O. Thompson and D.E. Chimenti, pp. 1209-1216, 2006.

J. G. Sun, J. M. Zhang, and J. S. Trethewey, "Nondestructive Evaluation of Machining and Engine-Test Damage in Silicon-Nitride Ceramic Valves," paper presented at the 30th International Conference & Exposition on Advanced Ceramics & Composites, Cocoa Beach, FL, Jan. 22-27, 2006.

J. G. Sun presented an invited talk on "Optical NDE Methods for Characterization of Subsurface Microstructure in Silicon Nitride Ceramics" at the 30th Annual Conference on Composites, Materials, and Structures (ITAR Restricted Sessions), Cocoa Beach/Cape Canaveral, FL, Jan. 23-26, 2006.

Patent

J. G. Sun, "Device and Nondestructive Method to Determine Subsurface Micro-Structure in Dense Materials," U.S. Patent No. 7,042,556, issued May 9, 2006.

B. Life Prediction of Diesel Engine Components

H. T. Lin, T. P. Kirkland, A. A. Wereszczak, and H. Wang
Oak Ridge National Laboratory
P.O. Box 2008, MS-6068
Oak Ridge, TN 37831-6068
(865) 576-8857; fax: (865) 475-6098; e-mail: linh@ornl.gov

Jeff Jensen and Nan Yang
Caterpillar, Inc.
Peoria, IL 61656-1875
(309) 578-2969; fax: (309) 578-2953; e-mail: Jensen_Jeff_A@cat.com

DOE Technology Development Manager: Jerry L. Gibbs
(202) 586-1182; fax: (202) 586-1600; e-mail: Jerry.gibbs@ee.doe.gov
ORNL Technical Advisor: D. Ray Johnson
(865) 576-6832; fax: (865) 574-6098; e-mail: johnsondr@ornl.gov

---

Contractor: Oak Ridge National Laboratory, Oak Ridge, Tennessee
Contract No.: DE-AC05-00OR22725
Subcontractor: Caterpillar, Inc., Peoria, Illinois

Objective

- Generate a database and characterize damage mechanisms of candidate advanced ceramics and intermetallic alloys.
- Apply and verify probabilistic life prediction and component design and verification methods for advanced diesel engine components.

Approach

- Evaluate the dynamic fatigue, rotary bending fatigue, and high-temperature fatigue and creep performance of candidate silicon nitride ceramics and TiAl alloys at elevated temperatures in air before and after long-term exposure to simulated engine environments, as well as engine field tests.
- Characterize the evolution and role of damage mechanisms, and changes in microstructure and chemistry, linked to the long-term mechanical performance and reliability of ceramics and intermetallic alloys.
- Predict the failure probability and reliability of complex-shaped diesel engine components subjected to application conditions via the use of life prediction codes.

Accomplishments

- Completed 500-h engine field testing for advanced TiAl and silicon nitride valves using Caterpillar G3406 (in-line 6 cylinders) nature gas engine.
- Completed mechanical reliability evaluation of TiAl turbo wheel component.
- Completed dynamic scratch studies for both Daido and Howmet TiAl alloys.
- Completed initial generation of long-term tensile creep database for Daido and Howmet TiAl alloys.

Future Direction

- Characterize the retained mechanical properties and microstructure of Kyocera SN235P silicon nitride and TiAl valves as a function of engine test time, and verify the probabilistic component design and life prediction.
- Develop a high-temperature tensile creep and step-stress rupture database of commercially available TiAl alloys for probabilistic component design and life prediction for diesel exhaust valve and turbine wheel component application.
- Develop mechanical database for complex-shaped TiAl components for verification of probabilistic component design and life prediction, and also process optimization.

Introduction

There has been considerable interest in the potential for extensive use of advanced ceramics and intermetallic alloys in advanced diesel engine systems because of their superior thermomechanical properties at elevated temperatures. The implementation of components fabricated from these advanced materials would lead to significant improvement in engine efficiency and long-term durability and reduced nitrogen oxides (NO_x) and CO exhaust emissions as required in the 21st Century Truck Program. Interest has focused primarily on research into characterization and design methodology development (life prediction) for advanced silicon nitride ceramics and TiAl alloys to enable the manufacture of consistent, reliable complex-shaped components for diesel engine. The valid prediction of mechanical reliability and service life is a prerequisite for successful use of these materials in internal combustion engine components.

This research project has three primary goals: the generation of a mechanical engineering database, from ambient to high temperatures, of candidate advanced materials before and after exposure to simulated engine environments; the microstructural characterization of failure phenomena in these advanced materials and in components fabricated from them; and the application and verification of probabilistic life prediction methods using diesel engine components as test cases. For all three stages, results will be provided to both material suppliers and component end-users for use in refining and optimizing processing parameters to achieve consistent mechanical reliability, and in validating the probabilistic design and life prediction of engine components made from these advanced materials.

Approach

The biaxial flexure strength [1,2] of TiAl turbo wheel component, as shown in Fig. 1, was measured using a ball-on-ring arrangement. Disk-shaped specimens were machined from both the airfoil surfaces and hub region by first diamond core drilling small cylinders having a nominal diameter of 10.0 mm. Each cylinder was then machined on one face only until the thickness was 0.5 mm. In this way, one face of each specimen always consisted of the as-manufactured surface of the airfoils. Discs machined from hub region were all with machined surfaces. Thus during testing, the as-manufactured surfaces of airfoil discs were always loaded in tension.

The test fixture consisted of a 1-mm-diameter WC ball, which was mounted on a miniature load cell, as shown in Fig. 2. The lower support ring, which was 5.0 mm in diameter, was fabricated from a high-strength polymer. The test fixture itself was mounted on a vertical stepper motor (Z stage), which was affixed to the X-Y stages for positioning in the horizontal plane. A personal computer controlled all three stages using the LabView program (National Instruments, Austin, TX). After placing a specimen on the lower support ring, the X-Y stages were used to position the assembly directly under the upper load ball. A calibration procedure was carried out to ensure the WC ball was centered on the lower support ring prior to the testing. The Z-stage was then lowered at a rate of 0.1 mm/s until the WC ball made a light contact with the specimen. The specimen was subsequently loaded to failure at a displacement rate of 0.01 mm/s. The computer monitored and recorded the displacement, load, and time. The disc strength, S_b, was calculated from the equation

$$S_b = 3P(1+\nu)/(4\nu\, t^2)\bullet[1 + 2\ln(a/b) + ((1-\nu)/(1+\nu))(1 - b^2/2a^2)(a^2/R^2)] \quad (1)$$

where P is the ultimate sustained load, a is the radius of the support ring, b is the effective radius of contact of the loading ball on the specimen, R is the specimen radius, t is the specimen thickness, and ν is Poisson's ratio.

The principle of the experimental scratch-testing technique carried out on TiAl alloys has been described elsewhere [3-5]. The single-grit scratch testing apparatus (developed by Michigan Technological University Houghton, MI) consists of a rigid platform on which the specimen fixture is mounted and that has translation capability for ease of specimen mounting and positioning. A micrometer is mounted on the top of the pendulum such that its shaft is set directly on the top of a diamond tool. Thus, one can measure the tool position with the micrometer, while adjusting the tool in the center of the pendulum. The signals from load cells are outputted to a digitizer (NI5102) via charge amplifiers and acquired by a LabVIEW program. Conical diamond tools used (J & L Industrial Supply, Pittsburgh, PA) had a 90° included angle and shank sizes of 6.35 mm diameter x 50.8 mm length. The conical diamond tips generally had a radius of ~ 5 μm (based on the SEM image analysis).

Results

Characterization of TiAl Components

Studies of biaxial strength of disc specimens machined from TiAl turbo wheel airfoils aimed to provide database directly from component for verification of probabilistic component design and life prediction task, which are critical to end users. Also, the database would provide guidelines to material suppliers for further optimization of component manufacturing processes to achieve consistent mechanical performance and reliability. Figure 3 compares the Weibull strength distribution of TiAl discs machined from airfoils with as-processed and as-machined surface, respectively. Results show that the discs machined from airfoils with as-processed surface exhibit characteristic strength that is 34% lower than those obtained with as-machined surface. Also, these as-processed airfoil discs exhibit relative low Weibull modulus (m ~ 3.5) with respect to the as-machined specimens (m ~ 5.2). Note that huge variation in mechanical properties between as-processed and as-machined airfoils has also been observed in many silicon nitride components; i.e., turbine blade, nozzle, and rotor [6]. The significant difference in Weibull strength distribution as found in previous studies of silicon nitride components was attributed to differences in the microstructure as well as strength-limiting flaws present near the surface region of airfoils. Results suggest that the probabilistic life prediction task that was carried out for TiAl components based on the mechanical data generated from the simple shaped specimen geometry could possibly over-estimate the lifetime performance of turbo wheel under the application conditions. Thus, it is critical to re-verify these tasks by using the database directly generated from complex-shaped components in order to achieve reliable lifetime prediction and performance.

Dynamic Scratch Test of TiAl Alloys

TiAl alloys have also been considered for exhaust/intake valve application of heavy duty vehicles. In general, these exhaust/intake valves are always subject to the high-speed reciprocal movement during services. The responses of TiAl materials in the corresponded application condition need to be properly addressed before they can be successfully implemented in the engine systems. Thus, studies of dynamic scratch test using a single-grit pendulum (rotational) scratch technique were carried out and completed during FY2006. The objective of this study was to provide insight into the dynamic abrasion response of TiAl alloys in sliding contact. This dynamic scratch approach is employed because of its advantages over the traditional sliding scratch technique in characterizing the materials removal mechanisms. TiAl alloys evaluated include Daido HIP and non-HIP TiAl, and Howmet TiAl material, which exhibit differences in grain domain and lamellar size, and thus could lead to differences in mechanical and wear response.

Figure 5 shows the typical scratch surface feature of Daido HIP and Howmet TiAl alloy. The groove surfaces of scratches of two TiAls appeared to have maintained a certain degree of integrity with clear surface contours, which is distinctly different from scratches on brittle materials; i.e., alumina and silicon nitride (where the side ridges were not preserved due to the lateral cracks). The side ridges are developed on banks with appreciable pile-up, especially over the wide middle region of the scratch

that corresponds to the suppressed wear rate. Frequent fractures take place in the transverse direction over the middle region of the scratch, some of which are sizable and run into the bottom of the groove. For the Daido TiAl, no shallow lateral fractures were developed that are observed to occur in pure titanium. However, the lateral fractures were developed for the Howmet TiAl on the sides of the scratch as a result of cleavage; thus the material removal has been enhanced with a predicted high wear rate.

The scratch forces measured by load cells in the time domain were transformed and expressed in terms of the tool position using a linear relationship. The force signals of representative scratches for the two TiAls are given in the top row of Fig. 6. The scratch speeds obtained were ~ 1 m/s, provided that these scratches were generated within 0.003 to 0.004 s with a length of 3 to 4 mm. The normal and tangential forces of the two scratches show a bell shape; they rise as the tool tip penetrates into the specimen, reach the peak in the middle, and then fall as the tool returns to the surface. The force signals are not necessarily symmetrical, especially for the tangential force that usually skews toward the right direction (on upright portion of the stroke). As a result of that, the values of OFC (overall frictional coefficient, defined as the ratio of tangential force to normal force) generally exhibit an ascending trend over the wide middle region of the scratch.

The geometries of the scratch groove section were extracted at every sampling point along the longitudinal axis X. The relevant quantities include the depth of groove, groove section area, plowing section area, and removed section area. Among those parameters, the groove area is the sectional area of the scratch below the original level, the plowing area is the sectional area in contact with the tool face during scratching, and the removed area is the removed groove area (i.e. the groove area minus the total area of two side ridges). Variations of these quantities along the axis X, therefore, result in the derived scratch profiles with respect to the groove depth and the sectional areas. As expected, the profile of the depth of groove shows an arch-shaped curve in response to the imposed circular motion of the tool tip. The derived profiles of sectional areas appear with the similar curves, but they resemble more the shape of scratch forces than the profiles of groove depth. The bottom row of Fig. 6 gives the corresponding profiles of sectional areas of the respective scratches. As expected, the level of the overall groove area is higher than that of the removed area but lower than that of the plowing area. In addition, the profiles of both forces and sectional areas are generally seen with appreciable oscillations whose amplitude increases proportionally with the depth of penetration.

The differences between the defined sectional areas for the shown scratch in Fig. 5 imply the susceptibility of material loss or wear. If looking at the wear rate (defined as the ratio of the removed sectional area to the groove sectional area), then one can find that the wear rates of the tested TiAls vary slightly over the whole scratch process. Over the wide middle region of the scratch, the wear rate profiles illustrate a relatively steady decrease with a moderate suppression around the middle; this becomes pronounced in the case of Daido TiAl HIP. Overall, the wear rate of the Daido TiAl HIP is lower than other TiAl alloy evaluated due to its stronger capability of energy dissipation or resistance against material loss or removal from dynamic scratching.

Characterization of Engine-Tested Si_3N_4 and TiAl Valves

To validate the valve component design and life prediction tasks carried out for advanced heavy duty engines, the engine field tests using Caterpillar G3406 (in-line 6 cylinders), as shown in the top photo of Fig. 7, have been performed during FY2006. The 500-h engine field test for silicon nitride and TiAl exhaust, as well as intake valves, has been successfully accomplished. The metallic valves currently employed in the engine were also included for comparison. The valve position of each material in the engine is also illustrated in the bottom photo of Fig. 7. Following engine testing visual and optical examinations were carried out to inspect the tested valves for any apparent surface damages (chipping and cracking). Figure 8 shows the typical surface features for silicon nitride and TiAl exhaust valve after engine test. Similar features were also observed for the silicon nitride intake valves as well. Results of visual and optical inspection showed that there was not apparent surface damage introduced during the 500-h engine test, except apparent changes in surface morphology (roughness) due to the reciprocating contacts between valve guide and stem region.

A Taylor-Hobson surface profiling system (Model # Form Talysurf 120) was then employed to measurement the surface roughness (and thus degree of wear) of these tested valves. Three sections; i.e., upper valve guide, lower valve guide, and valve seat insert contact region, were evaluated, and three scans at each location were taken at 0, 120, and 240°, respectively. Results showed that there was a significant increase (1.5-5 folds) in roughness (Ra values) in the valve seat region for both silicon nitride and TiAl valves. As for the valve guide region, the Ra values (roughness) of silicon nitride valves decreased after 100-h engine test probably due to the polishing effect, and exhibited a slightly increased roughness after 500-h test, as shown in Fig. 9. Nonetheless, the Ra values of 500-h tested silicon nitride valves are comparable to those measured for the as-received valves. On the other hand, the TiAl exhaust valves showed a much more increase in Ra value (2-10 folds) as compared to the silicon nitride valves, probably due to the loss of oxide layer formed during the heat treatment performed prior to the engine testing. The effect of the surface roughness introduced after 500-h engine test on the mechanical performance will be evaluated via destructive test using half-cylindrical bend bars after the completion of NDA task performed at ANL. Also, 1000-h engine field test will be continued in FY2007 to provide important insight into the long-term effect of engine environment on the mechanical reliability and component durability of TiAl and silicon nitride valves.

References

1. R. Thiruvengadaswamy and R. O. Scattergood, "Biaxial Flexure Testing of Brittle Materials," *Scripta Metall. et Mater.*, Vol 25, 1991, pp2529-2532.

2. D. K. Shetty, A. R. Rosenfield, P. McGuire, B. K. Bansal, and W. H. Duckworth, "Biaxial Flexure Tests for Ceramics," *Ceramic Bulletin*, Vol 59 [12], 1193-97 (1980).

3. H. Wang, G. Subhash, A. Chandra, "Characteristics of Single-grit Rotating Scratch With a Conical Tool on Pure Titanium," *Wear*, 249: 566-581, 2001

4. G. Subhash, J. E. Loukus, S. M. Pandit, "Application of Data Dependent Systems Approach for Evaluation of Fracture Modes During a Single-Grit Scratch," *Mech. Mater*. 34: 25-42, 2002

5. H. Wang, A. A. Wereszczak, M. J. Lance, "Effect of Grain Size on Dynamic Scratch Response in Alumina," *Ceram. Eng. Sci. Proc*. (2006), in print.

6. H. T. Lin and M. K. Ferber, "Characterization of Mechanical reliability of Silicon Nitride Microturbine Rotors," *Key Engineering Materials* Vol. 287 (2005), pp. 393-403.

Presentations and Publications

Presentation

H. Wang, H. T. Lin, A. A. Wereszczak, J. A. Jensen, and N. Yang, "Specific Energy and Scratch Hardness of Gamma Titanium Aluminides Subjected to Single-Grit Pendulum Scratching," presented at ASME Internal Combustion Engine Division 2006 Fall Technical Conference, November 5-8, Sacramento, CA.

Publications

1. H. Wang, H. T. Lin, A. A. Wereszczak, J. A. Jensen, and N. Yang, "Specific Energy and Scratch Hardness of Gamma Titanium Aluminides Subjected to Single-Grit Pendulum Scratching," ICEF2006-1532, published in the Proceedings of ASME Internal Combustion Engine Division 2006 Fall Technical Conference, November 5-8, Sacramento, CA.

2. H. T. Lin, T. P. Kirkland, A. A. Wereszczak, and M. J. Andrews, "Strength Retention of Silicon Nitride After Long-term Oil Immersion Exposure," *J. Mater. Sci.* (in press).

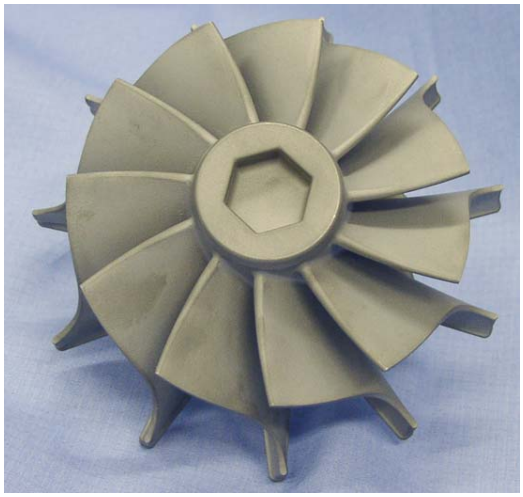

Figure 1. Photo of TiAl turbo wheel acquired from Caterpillar.

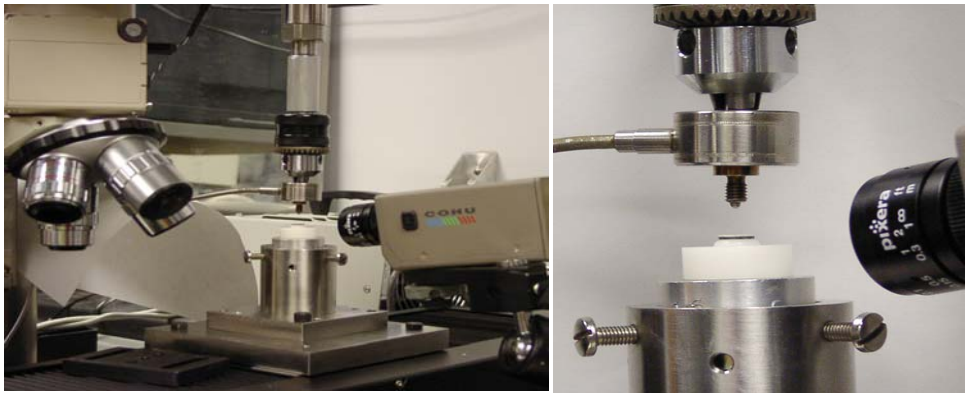

Figure 2. Photos show the biaxial test facility used for testing biaxial discs machined from the TiAl turbo wheel airfoils.

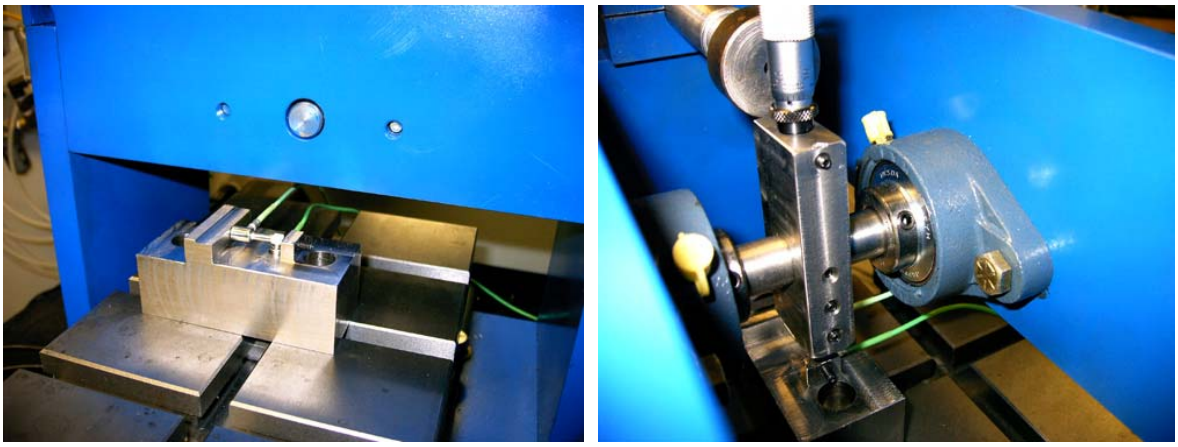

(a) (b)

Fig. 3 Components of the single-grit pendulum scratch tester: (a) specimen fixture mounted on a rigid platform that is operated by a handle (not shown); (b) pendulum, equipped with a positioning micrometer on the top, is driven by a piston that is pneumatically operated by high pressure gas

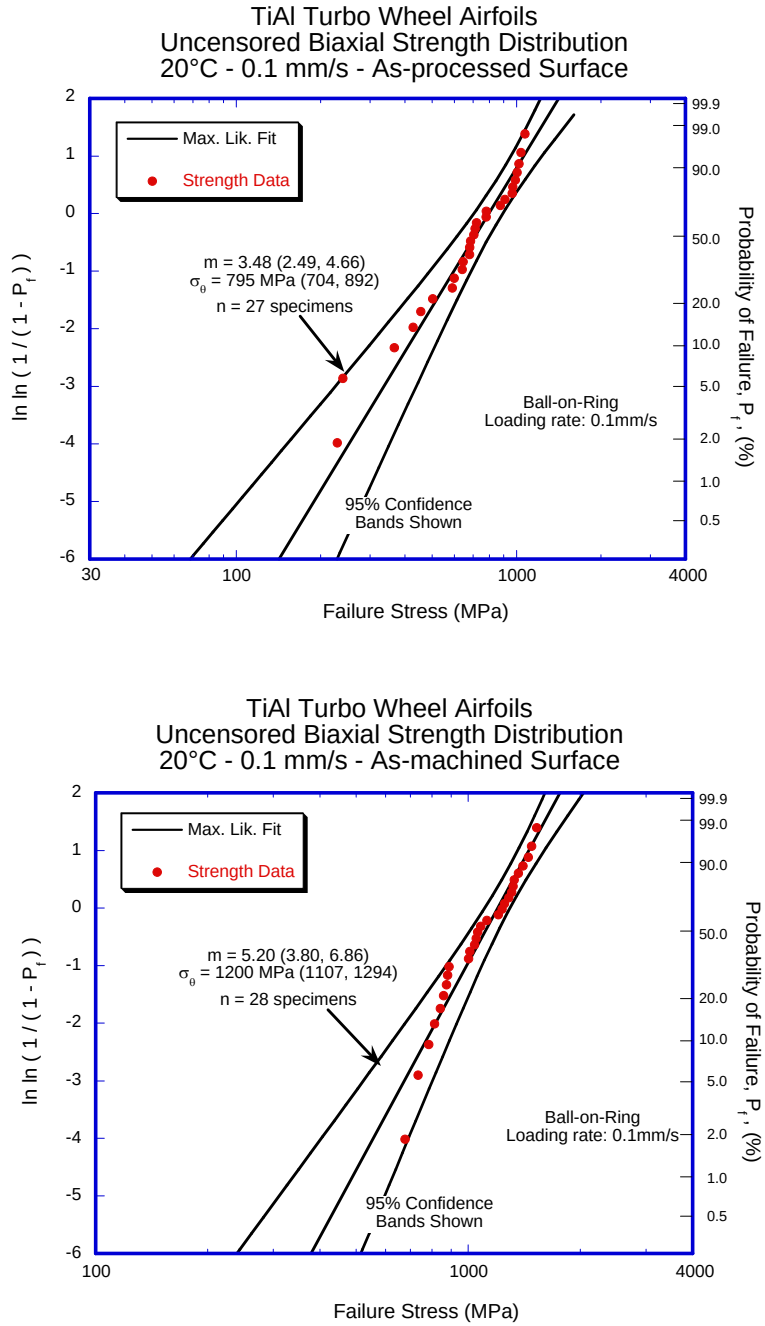

Figure 4. Uncensored Weibull strength distribution of TiAl biaxial discs machined from airfoil with as-processed surface (top) and as-machined surface (bottom).

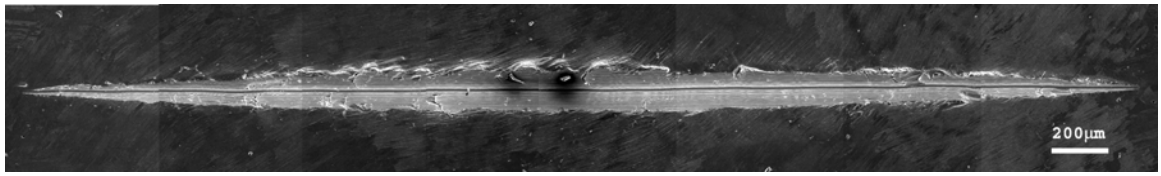

(a)

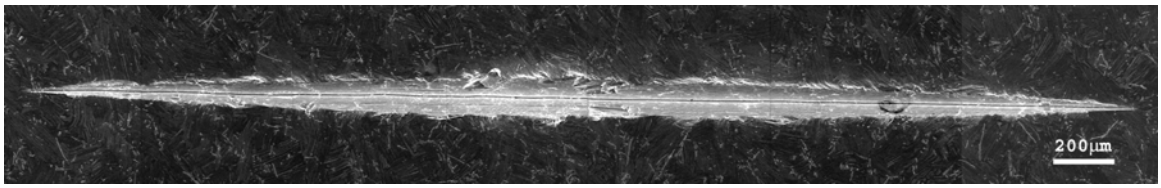

(b)

Fig. 5 SEM micrographs of scratch on: (a) Daido TiAl HIP and (b) HOWMET TiAl. Scratch ran from left to right. The micrographs were taken after chemical etching.

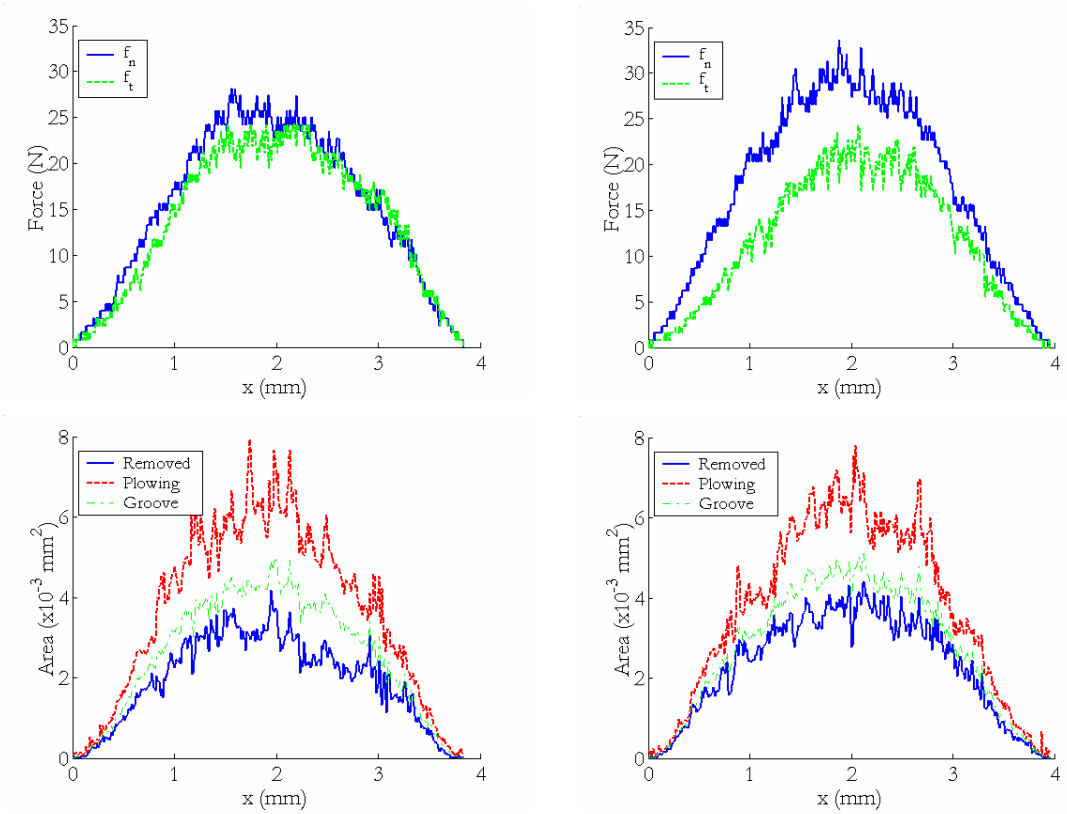

(a) (b)

Fig. 6 Variations of scratch forces (top row) and sectional areas (bottom row) for a typical scratch on (a) Daido TiAl HIP and (b) HOWMET TiAl.

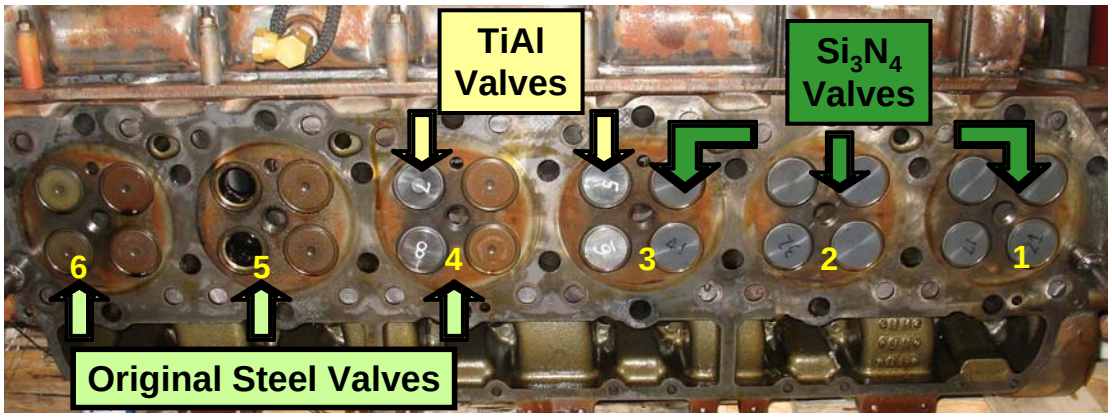

Figure 7. Photos show Caterpillar G3406 (in-line 6 cylinders) nature gas engine (top) and valve position of each material in the engine compartment (bottom).

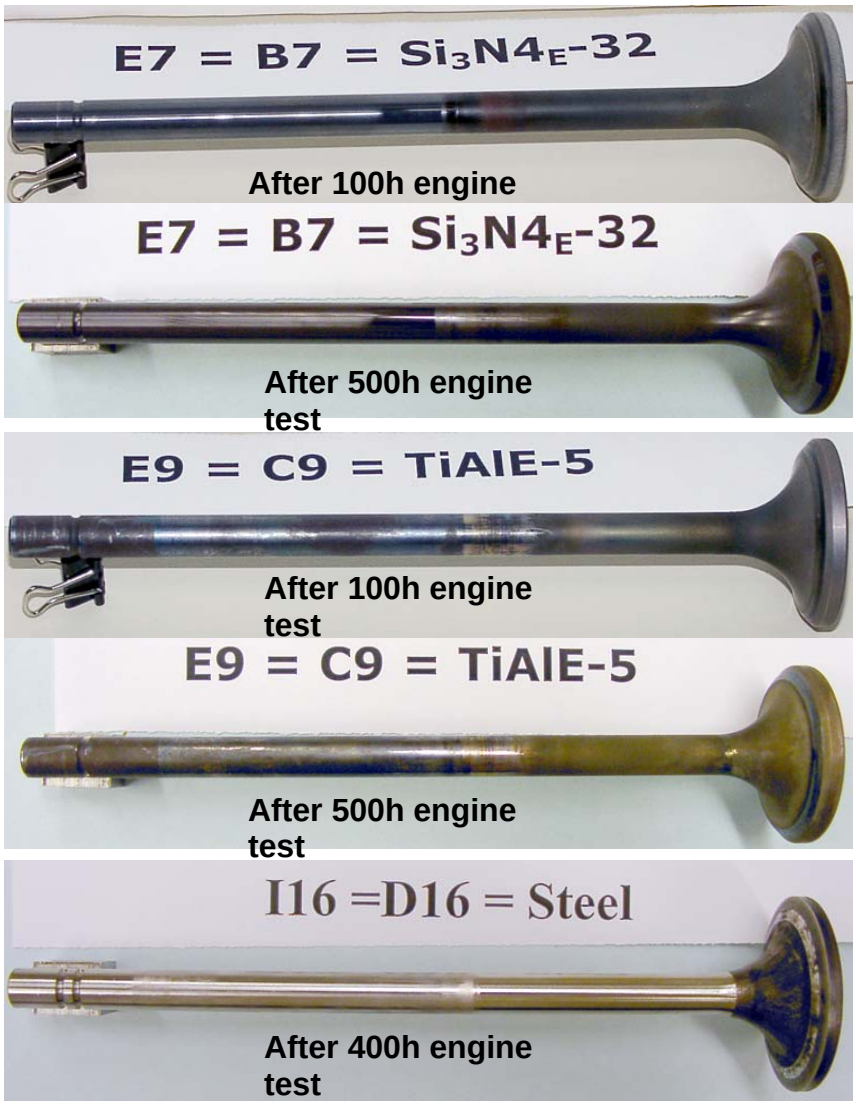

Figure 8. Comparisons of surface features of silicon nitride valve, TiAl valve, and steel valve as a function of engine test time.

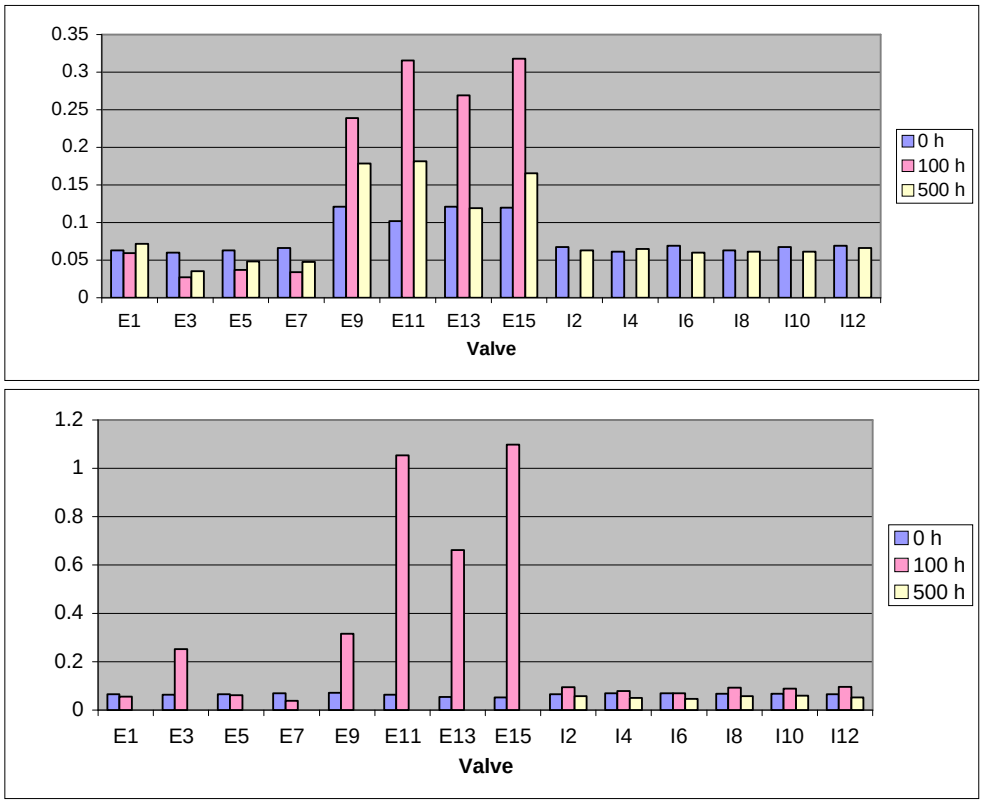

Figure 9. Roughness Ra valves measured for valves in the as-received, 100-h test, and 500-h test condition. Note that B_{top} and C_{top} are two locations above and below the valve guide contact region, respectively.

C. Engineered Surfaces for Diesel Engine Components

M. Brad Beardsley
Caterpillar, Inc.
Technical Center Bldg. E/854
P.O. Box 1875
Peoria, IL 61656-1875
(309) 578-8514; fax: (309) 578-2953; e-mail:Beardsley_M_Brad@cat.com

DOE Technology Development Manager: Jerry L. Gibbs
(202) 586-1182; fax: (202) 586-1600; e-mail: Jerry.gibbs@ee.doe.gov
ORNL Technical Advisor: D. Ray Johnson
(865) 576-6832; fax: (865) 574-6098; e-mail: johnsondr@ornl.gov

Contractor: Oak Ridge National Laboratory, Oak Ridge, Tennessee
Contract No.: DE-AC05-00OR22725
Subcontractor: Caterpillar, Inc., Peoria, Illinois

Objectives

- Develop coating processes to apply amorphous steels and quasicrystal materials to engine pistons and cylinder heads for use as thermal barrier coatings in homogenous charged combustion ignition (HCCI) engine designs.
- Quantify the diffusion stability of new quasicrystalline material at engine operating temperatures.

Approach

- Use high-velocity oxygen fueled (HVOF) processes to apply amorphous and quasicrystalline materials to engine piston and cylinder head.
- Use microprobe analysis of diffusion couples to determine the stability of quasicrystalline and bond coating couples at engine operation temperatures.

Accomplishments

- A HCCI piston coated with amorphous steel demonstrated improved coating durability over ceramic thermal barrier coatings in single cylinder engine tested.
- Thermal conductivity measured for the amorphous steel coating was higher than that reported for this type of material and resulted in higher than desired heat rejection through the piston.

Future Direction

- Develop graded coating structures for the quasicrystalline material based upon the diffusion profiles developed.

Introduction

Two new materials, amorphous steels and quasicrystalline materials, are investigated as thermal barrier coatings. Both materials are capable of being sprayed using high-velocity oxygen fuel (HVOF) processes that produce denser coatings with higher strengths than plasma spraying. The denser coating structure of HVOF coatings eliminates the need for sealing of the coating porosity and the higher strength enhances the coating durability. Amorphous steel coatings are reported to have low thermal conductivity as

well as high hardness and toughness, making them attractive as thermal barrier coatings.[1,2] The quasicrystal being studied, $Al_{71}Co_{13}Cr_8Fe_8$, has been shown to be capable of 1100°C operation in a turbine engine.[3]

Approach

Amorphous Steel Coatings

A piston was coated with the SHS717 amorphous steel produced by The NanoSteel Company, Maitland, Florida. The coating was nominally 3.5 mm in thickness. The piston was run for approximately 24 hours in a single cylinder test during which component temperatures were measured.

Quasicrystalline Materials

Analysis of the chemical mobility of the species in the quasicrystalline coating has continued. Interaction zones of up to 100 micon in thickness at the interface between the quasicrystal and NiCrAlY bond coating are being analyzed.

Results

Amorphous Steel Coatings

The piston temperatures measured were higher than expected for the reported thermal conductivity of the amorphous steel coatings. A measurement of the HVOF produced coating showed that the thermal conductivity was 1.5 to 2 times higher than the 5 W/m-K reported, Figure 1. Lower thermal conductivity amorphous materials will be needed if they are to be of use for applications to diesel engine components.

Conclusions

Amorphous Steel Coatings

The durability of the amorphous steel coating showed significant improvement over plasma sprayed ceramic thermal barrier coatings. However, lower thermal conductivity compositions will need to be identified in order to provide the required thermal resistance needed for diesel engine component applications.

References

1. D. J. Branagan, W. D. Swank, D. C. Haggard, and J. R. Fincke, "Wear Resistant Amorphous and Nanocomposite Steel Coatings," *Met. & Mat. Transactions A*, **32A**, 2615–2621 (2001).

2. D. Shin, F. Gitzhofer, and C. Moreau, "Development of Metal Based Thermal Barrier Coatings (MBTBCs) for Low Heat Rejection Diesel Engines," Proceedings of the 2005 International Thermal Spray Conference, 915–919 (2005).

3. A. Sanchez, F. J. Garcia, J. M. Algaba, J. Alvarez, P. Valles, M. C. Garcia-Poggio, and A. Aguero, "Application of Quasicrystalline Materials as Thermal Barriers in Aeronautics and Future Perspectives of Use for These Materials," *Mat. Res. Soc. Symp. Proc.*, **553**, 447–458 (1999).

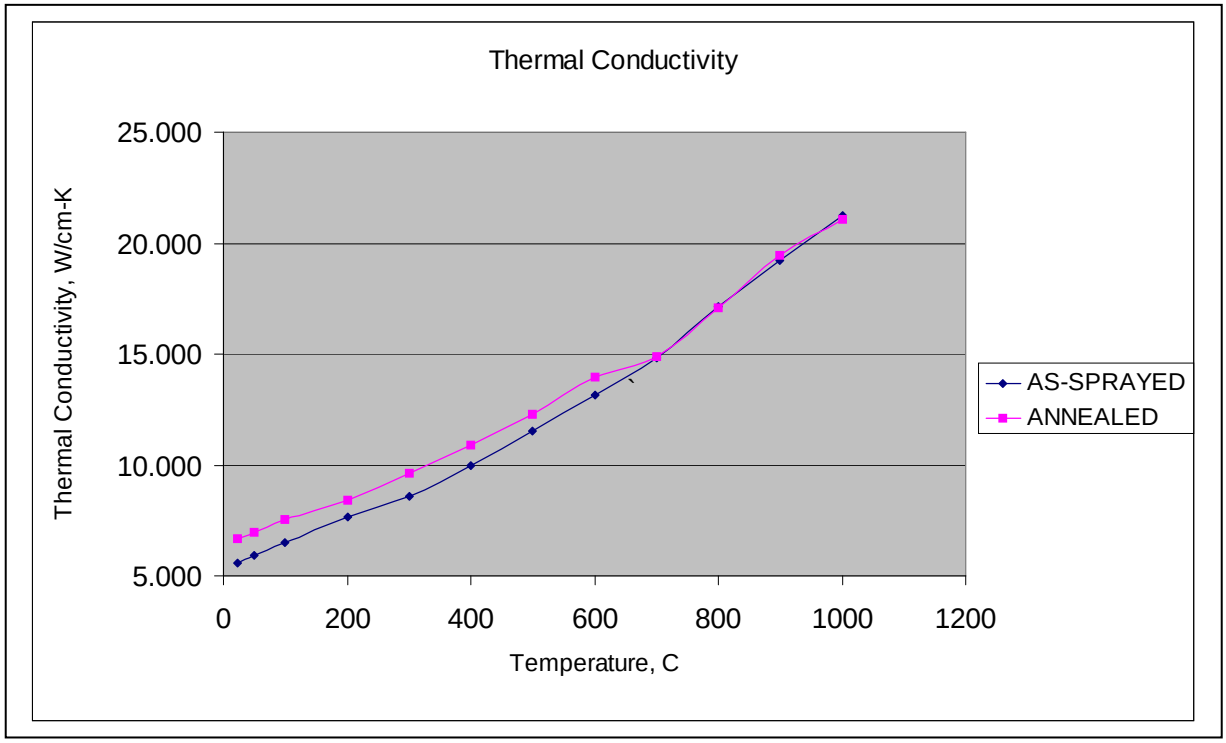

Figure 1. Exposure to temperatures above glass transition temperature (700°C) causes an increase in thermal diffusivity of amorphous steel.

D. High-Temperature Advanced Materials for Lightweight Valve Train Components

Nathaniel S. L. Phillips, Principal Investigator
Jeff Jensen, Jeremy Trethewey, Natalie Vanderspiegel, David Longanbach, and Chad Logan
Caterpillar Inc.
Tech Center 854-22 TC-E
14009 Old Galena Rd.
Mossville IL, 61552
(309) 578- 5788 (voice)
(309) 578-2953 (fax)
E-mail: Phillips_Nate@cat.com

DOE Technology Development Area Specialist: Jerry L. Gibbs
(202) 586-1182; fax: (202) 586-1600; e-mail: jerry.gibbs@ee.doe.gov
ORNL Technical Advisor: D. Ray Johnson
(865) 576-6832; fax: (865) 574-6098; e-mail: johnsondr@ornl.gov

---

Contractor: Oak Ridge National Laboratory, Oak Ridge, Tennessee
Contract Number: DE-AC05-00OR22725
Subcontractor: Caterpillar Inc., Peoria, Illinois

Objective

- Evaluate prospective lightweight valve materials and determine feasibility of implementation in heavy-duty diesel and natural gas applications.

Approach

- Design, procure, and evaluate γ-phase titanium aluminide (TiAl) and silicon nitride (Si_3N_4) heavy-duty engine valves.
- Demonstrate performance and durability advantages by performing 1000-h durability test on valves in a Caterpillar G3406 natural gas engine.
- Develop finite-element analysis (FEA)-based life prediction model (NASA CARES/Life) that will generate life prediction curves for advanced valve materials.
- Evaluate the thermal, chemical and mechanical properties of TiAl and Si_3N_4 that are critical to on-engine valve performance and durability.
- Investigate manufacturing considerations (i.e., machinability and quality inspection technique) of these novel materials.

Accomplishments

- Completed 500 hour engine testing.
- Completed 500-hour post-test non-destructive analysis (NDE).

Future Direction

- 2/3 of the valves will be re-installed in the engine while the remaining 1/3 will be replaced by fresh valves and reserved for destructive testing.
- After the engine has run for another 500 hours, all valves will be removed, inspected, and prepared for destructive testing. By performing fast fracture tests on valves that have accumulated 0, 500, and 1000 hours of engine time, the effect of engine aging on the materials' retained strength will be examined.
- Along with combustion dynamics and fuel consumption measurements, this data will enable the team to quantify performance gains and establish useful life estimates of Si_3N_4 and TiAl valves in a heavy-duty engine environment.

Introduction

Valve train components in heavy-duty engines operate under high stresses, at elevated temperatures, and in severely corrosive environments. Structural ceramics and emerging intermetallic materials are highly corrosion and oxidation resistant and possess high strength and hardness at elevated temperatures. These properties are expected to allow higher engine operating temperatures, lower wear, and enhanced reliability. In addition, the lighter weight of these materials (~50% of production alloys) will lead to lower reciprocating valve train mass that could improve fuel efficiency.

Over the past decade, the automotive engine industry has demonstrated moderate success with TiAl as a valve material. Eylon et al.[1] demonstrated a 2% fuel savings on a Chevrolet Corvette that ran for 25,000 km with TiAl valves. This fuel efficiency increase is attributed to the decrease in valve train parasitic frictional losses. In another study with TiAl valves, Maki et al.[2] demonstrated a 1000-rpm increase in over-speed performance on a Nissan VRT35 engine. This capability would allow more efficient engines to operate in more demanding regimes. The current research and development program at Caterpillar, Inc. extends this body of knowledge from the automotive community and examines TiAl and Si_3N_4 in the context of heavy-duty diesel and natural gas engine environments.

The valve train material development effort will provide the materials, design, manufacturing, and economic information necessary to bring these new materials and technologies to commercial realization. With this information, component designs will be optimized using probabilistic lifetime prediction models, and validated in rig bench tests and short- and long-term engine tests. After establishing proof-of-concept with valves, this design approach will be applied to other components made from high-temperature materials.

Approach

Many perspectives must be considered when evaluating TiAl and Si_3N_4 materials for use in valve applications. As such, there are several facets to this project. Validation of these components begins with the fabrication of TiAl and Si_3N_4 valves and testing them on a Caterpillar G3406 (in-line 6 cylinder) natural gas engine. Previous annual reports documented the design process used to modify the current baseline metallic valve to accommodate the limited ductility of ceramic and intermetallic materials.[3] For example, the head dimensions were changed to reduce the stress concentration

experienced in the fillet radius. Silicon nitride and TiAl valve blanks were formed, rough machined, friction welded to a Ti-6Al-4V shaft (TiAl only), and finish machined.

A parallel effort to develop a design tool for high-strength, brittle materials is also being pursued. A FEA-based life prediction code (NASA CARES/Life) is used to evaluate component design and generate life prediction curves. This approach uses material properties and thermo-mechanical boundary conditions as the primary inputs. A probability-based code then calculates the accumulated damage through the life of the valve and creates a life prediction curve.

A variety of other studies contribute to the understanding of the behavior of TiAl and Si_3N_4 and how they may perform in an engine environment. Several studies examine the fundamental properties of the materials: tensile strength, creep strength, thermo-physical properties, friction coefficient, wear resistance, oxidation resistance, and corrosion resistance. Two other studies examine the manufacturability of the materials: the effect of machining damage on fatigue resistance and a NDE technique to evaluate surface quality.[4]

Results

Pre-engine test valve characterization

Prior to subjecting the TiAl and Si_3N_4 valves to the full-scale engine test, three characterization techniques were used to gather baseline information about the valve dimensions, material surface quality and structural integrity. A coordinate measuring machine (CMM) profile scan was performed along the axis of each valve to verify that they met the dimensional specifications.

In order to establish the pre-engine test surface condition, profilometry scans were performed on 5 key regions: keeper groove, Ti-6-4 stem, TiAl stem, fillet and the seat contact region. Figure 1 shows a series of roughness measurements for a single TiAl valve. It was confirmed that the surface roughness specification (Ra) was met for nearly all of the measured regions on all of the valves.

The most sophisticated set of data collected was the laser scatter scans performed by Dr. JG Sun at Argonne National Laboratory. The fundamental physics and experimental setup are detailed in the "NDE of Diesel Engine Components" quarterly reports. Scans were performed at the fillet and keeper groove locations on all TiAl and Si_3N_4 valves. An additional scan of the weld region was also performed to determine if any cracks formed during the friction welding process. Figure 2 shows two scans of the fillet region of the same Si_3N_4 valve. Figure 2a shows the scan after poor finish machining. During the last year's efforts these valves were re-machined to meet the desired surface quality. Figure 2b shows the same valve after corrective finish machining. Valves with little or no detectable damage were used for the engine test.

Engine testing of Titanium Aluminide, Silicon Nitride and production valves

One of the primary goals of this study is to evaluate the performance of ceramic (Si_3N_4) and intermetallic (TiAl) valves in an engine environment. As outlined in previous quarterly reports (see Oct-Dec 2004), arrangements have been made to perform parallel 1000-hour endurance tests on three valve materials: γ-TiAl, Si_3N_4 and the austenitic steel production valve. These tests were performed at the National Transportation Research Center (NTRC) on a natural gas G3406 genset.

Since the design of these "advanced material" valves was optimized for the less ductile nature of these materials, several additional modifications to the G3406 valve train components had to be

made, including seat inserts, valve guides, keeper locks, and bridges.

Caterpillar and NTRC personnel oversaw the installation of 4 TiAl and 10 Si_3N_4 valves at Stowers Industrial Power, the East Tennessee Regional Caterpillar dealership. During the installation process, it was requested that the mechanic handle the valves with the same degree of care in which he would handle a standard steel valve. Figure 3 shows the valves as they are being installed. It is more realistic to require that the new material is sufficiently robust to survive the current standard installation procedure than to modify the procedure to conform to the limitations of the new material. The fact that all 14 of the "advanced valves" survived installation is an indication of the handling robustness of the materials. Figure 4 shows the valve array immediately after installation. It is worth noting that all of the custom-designed peripheral valve train components (seat inserts, guides, keeper locks, and bridges) were successfully integrated in the "advanced valve" head re-build.

In addition to valve train hardware, instrumentation specific to this engine test was also installed. Calibrated Kistler 6125B pressure pick-ups were installed in each of the six cylinders. Pressure traces from these transducers enabled the evaluation of the valve material's effect on the combustion performance (i.e. heat release rate). Also, a fuel consumption meter was installed to estimate the valves' aggregate effect on fuel efficiency. Finally, as a safety precaution, a fuel line shut-off valve was installed upstream of the genset intake and was calibrated to trigger if abnormal engine vibration occurred.

The table below (Table 1) outlines the progress of this engine durability test.

Engine operating conditions

The valves were installed in the following arrangement (Table 2) to ensure that the performance of the Si_3N_4 and TiAl valves could be isolated during post-test analysis.

Table 1 Engine durability test progress

Phase	Action	Status
Initial Installation	Valve Installation	Completed in March
Phase #1 (0 h – 100 h)	Engine Exposure	Completed in May
	Post-test Analysis	Completed in June
Phase #2 (100 h – 500 h)	Engine Exposure	Completed in July
	Post-test Analysis	Completed in November
Phase #3 (500 h – 1000 h)	Engine Exposure	Not yet started
	Post-test Analysis	Not yet started

Table 2 Valve installation arrangement

Cylinder	Intake	Exhaust
1	Silicon Nitride	Silicon Nitride
2	Silicon Nitride	Silicon Nitride
3	Silicon Nitride	Titanium Aluminide
4	Production Steel	Titanium Aluminide
5	Production Steel	Production Steel
6	Production Steel	Production Steel

Within the first few hours of engine operation, Cylinder 1, outfitted exclusively with Si_3N_4 valves, began to exhibit the signs of knocking. This pre-ignition condition is a symptom of altered combustion dynamics and is most likely caused by the protrusion of the seated valve ~1.5 mm farther into the combustion chamber than originally designed. This protrusion may cause pre-ignition because it changes the compression ratio and provokes autoignition prior to spark-controlled ignition. It is also possible that local hotspots are generated on the valve face due to the increased thermal mass in the hottest region of the combustion chamber. The protruding portion of the valve head exacerbates this hotspot formation, a potential cause of pre-ignition. Because this portion of the valve head does not contact the valve seat, there is no direct path for thermal conductivity and the local material temperature increases. It is important to note that this protrusion is an artifact of the valve geometry re-design and is correctable in future valve design iterations. To circumvent knocking, an exceedingly harsh operating environment, the genset was derated from 235 kW to 125 kW for the remainder of the test.

Valve Inspection –

Visual & Profilometry

In a heavy-duty engine, the first 100 hours of service time is considered the "break-in" period. During this initial phase the valve and seat insert conform to each other by a scuffing wear mechanism. Valve/guide contact may also cause wear on the stem while valve/bridge contact may cause wear on the stem tip. After 100 hours, the Si_3N_4 and TiAl valves showed minimal stem tip wear, acceptable valve/guide wear, and significant seat/insert wear. Figures 5a-c show a representative Si_3N_4 exhaust valve (Si3N4E-32) after the first 100 hours of testing. As expected, there was an even coating of combustion byproduct on the valve's head face, fillet and lower valve stem regions. The stem wear was evident in the discoloration ending halfway up the valve. Figure 5d shows the wear profile of the valve seat region. Figures 6a-d present the same results for a representative TiAl valve (TiAl-5).

In addition to wear scar depth, surface roughness, or R_A, also allows direct comparison of worn contact regions. Table 3 displays the surface roughness of each Si_3N_4 and TiAl valve before and after the first 100 hours of engine exposure.

Several preliminary conclusions may be drawn from these photographs, profilometry scans and surface roughness measurements.

Valve/seat wear: The 2x increase in valve/seat surface roughness for Si3N4E-32 is evidence of break-in scuffing wear on the Si_3N_4 valve. Figure 5d shows a relatively constant wear scar depth of ~2μm. However, the 5x increase in valve/seat surface roughness for TiAl-5 is an indication that wear has exceeded standard break-in levels. This is confirmed by Figure 6d which shows that the valve/seat wear scar depth was ~15μm, a significant magnitude for 100 hours of engine exposure. This accelerated wear in the valve/seat region of the TiAl valve suggests that an optimized wear-resistant surface treatment may be necessary to ensure acceptable wear behavior. When the 500 hour and 1000 hour wear data has been captured firm conclusions will be drawn from these observations.

Table 3. Surface roughness measurement of Si_3N_4 and TiAl valves at 0 hours and 100 hours

	Valve ID #	Valve Location	Time (hrs)	Valve Guide (R_A)		Valve Seat (R_A)
Si3N4 Intake	Si3N4I-20	I2-SI3N4	0	0.067		0.152
			100	0.095		0.226
	Si3N4I-21	I4-SI3N4	0	0.061		0.15
			100	0.079		0.779
	Si3N4I-25	I6-SI3N4	0	0.069		0.143
			100	0.069		0.199
	Si3N4I-28	I8-SI3N4	0	0.063		0.178
			100	0.093		0.435
	Si3N4I-33	I10-SI3N4	0	0.067		0.174
			100	0.089		0.185
	Si3N4I-41	I12-SI3N4	0	0.069		0.174
			100	0.096		0.394
Si3N4 Exhaust	Si3N4E-11	E1-SI3N4	0	0.063		0.232
			100	0.059		0.436
	Si3N4E-17	E3-SI3N4	0	0.06		0.211
			100	0.027		0.888
	Si3N4E-9	E5-SI3N4	0	0.063		0.222
			100	0.037		0.382
	Si3N4E-32	E7-SI3N4	0	0.066		0.206
			100	0.034		0.389
				Ti	TiAl	
TiAl Exhaust	TiAl-5	E9-TiAl	0	0.121	0.121	0.187
			100	0.239	0.316	0.970
	TiAl-6	E11-TiAl	0	0.102	0.102	0.221
			100	0.316	1.054	1.157
	TiAl-7	E13-TiAl	0	0.121	0.121	0.211
			100	0.269	0.661	0.762
	TiAl-8	E15-TiAl	0	0.12	0.12	0.226
			100	0.318	1.097	1.143

Valve/guide wear: The surface roughness data suggests that minor scuffing wear moderately increased the R_A of the Si_3N_4 intake valves. In contrast, the R_A of the Si_3N_4 exhaust valves decreased because the higher stem temperature enabled the stem/guide to undergo a polishing wear mode. The TiAl valves exhibited inferior wear performance compared to the Si_3N_4 valves in the valve/guide region. However, the 2x-3x R_A increase in the Ti-6-4 segment of the stem indicates that the thermal oxidation heat treatment was more effective on the Ti-6-4 than on the TiAl, which showed a 3x-10x R_A increase.

Valve integrity: Although the wear mechanisms and rates must be better understood before Si_3N_4 and TiAl can be successfully implemented into production, the fact that these valves have survived 500 hours of service is an indication that these valve materials may be capable of withstanding a heavy duty engine environment.

Valve Inspection – Laser Scatter NDE

At the end of the first 100 hour "break-in" test phase each valve was scanned with the laser-based NDE (Non-Destructive Evaluation) instrument outlined in the project titled "NDE of Diesel Engine Components." Figure 7 presents the NDE scans for exhaust valves Si3N4E-32 and TiAl-5 (the same valves in Figures 5 and 6). In general, these valves scans are similar to the pre-test scans with a couple of exceptions. The region of interest in these images was the valve seat band, the location of highest accumulated damage. The white stripes above and below the valve seat band were most likely caused by a combustion byproduct and are not significant flaws. The continuous grayscale transition in the Si_3N_4 valve seat band (Figure 7a

insert) confirms that there was no notable surface damage in its valve/seat wear region. However, the valve seat band in the TiAl valve (Figure 7b insert) showed a significant level of surface damage. More detail may be found regarding NDE data interpretation in Dr. JG Sun's Apr-Jun 2006 quarterly report.

Development of a valve life prediction tool using CARES/Life

The ongoing effort to predict the life expectancy of a heavy-duty valve subjected to typical engine loads had made significant progress in this past reporting period. The results of the first generation model were presented in a previous quarterly report (Jan-Mar 2005). Since then, the most significant accomplishment has been the shift from an axisymmetric model to a three-dimensional model. The additional degrees of freedom permit a more accurate representation of the valves deformation modes. In addition to the axisymmetric loads, the valve stem is permitted to bend and the valve head is permitted to deflect in a "pringle" deformation mode. Figure 8 presents the resultant stress field superimposed on a deformed valve. It is interesting to note that the maximum principal stresses observed on the 3D model is a factor of two greater than that observed on the preliminary axisymmetric model.

After applying the thermal and mechanical boundary conditions to the Si_3N_4-based 3D model the NASA/CARES probabilistic code was executed to examine the slow crack growth failure mode as a function of service time. Figure 9 presents the resulting life prediction curve for a Si_3N_4 valve experiencing slow crack growth under continuous G3406 genset operating conditions. Note that two curves are displayed; one represents a safety factor of one (i.e. loads are identical to those specified by the simulation-derived boundary conditions), the other represents a safety factor of two (i.e. applied loads were doubled). This 3D model is considerably more conservative than the preliminary axisymmetric model. The valve's lifetime predicted with this 3D model is substantially shorter than the lifetime predicted by the axisymmetric model (see Jan-Mar 2005 quarterly report). Even so, a probability of failure corresponding to ~0.01 ppm failed valves after one year of *continuous* operation in a heavy-duty engine is exceptional!

A couple of cautionary notes must be presented. This model relies on boundary conditions acquired from FEA simulations. Thus, they may not be exactly representative of field-tested engines. Also, this model only captures the probability of failure as a function of slow crack growth damage. As in any engineering system, several failure modes are acting simultaneously. This model focuses on the slow crack growth failure mode (prominent in ceramics). Other failure modes such as wear, impact resistance, and environmental resistance must be independently considered to gain a full perspective on the life prediction of a valve component.

As discussed in previous reports (FY2005 Annual Report), Jadaan Engineering & Consulting has been developing a probabilistic lifetime prediction model for TiAl and Si_3N_4 valves as they experience engine-like thermo-mechanical loads. Progress in this quarter expands upon the establishment of a three-dimensional FEA model for a Si_3N_4 valve (Oct-Dec 2005) by incorporating TiAl material properties. Also, a sensitivity study using the Probabilistic Design System (PDS) function in ANSYS was performed. Below are three significant conclusions that may be drawn from this set of analyses:

Si_3N_4 Valve Performance: Life prediction estimations for Si_3N_4 valves can be construed as a cautious "vote of confidence" in the material's reliability. For example, after 15,000 hours, a valve will have a probability of failure of 8x10-11. Assuming an engine will contain 12 Si_3N_4 valves, 1 out of one billion engines would experience a catastrophic valve failure. However, doubling the stress field, an exceedingly conservative approach, would increase the probability of failure to 2x10-4 (1 out of 450 engines would experience a catastrophic valve failure).

TiAl Valve Performance: Results for TiAl valves were inconclusive. Two factors suggest that the TiAl valve predictions are of questionable accuracy. First, there was insufficient data to develop reliable statistical material characteristics. Second, the maximum stress, shown in Figure 10, is atypical of valve behavior. This may be an artifact of the insufficient material properties and/or boundary conditions. Caterpillar will review the FEA model for discontinuities. However, if this analysis is an accurate representation of the TiAl/Ti-6-4 stress field, this atypical stress "hot spot" may suggest that a re-design may be required to mitigate the valve's maximum stresses. In other words, it is likely that TiAl may not be regarded as a "drop in" replacement for either the "current steel" or "advanced Si_3N_4" valve design.

PDS Results: The sensitivity study examined the importance of six variables (valve face pressure, Weibull modulus, scale parameter, Young's modulus, coefficient of thermal expansion and thermal conductivity) on the probability of failure and maximum stress of TiAl and Si_3N_4 valves. Figure 11 summarizes these results. Young's modulus, valve face pressure, and coefficient of thermal expansion are found to be the critical variables for defining the maximum stress found in the valve. However, Weibull modulus, Young's modulus, and the scale parameter are the three strongest influences on the ultimate probability of failure. Of course, the accuracy of the PDS analysis is only as good as the accuracy of the FEA model (discussed above). With this in mind, the PDS analysis suggests that controlling the latter set of variables would have the largest impact on improving the valves' durability.

Conclusions

Lightweight, high-strength, high-temperature materials are enablers for advanced combustion concepts and fuel-efficient engine designs. This effort aims to examine two prospective materials, TiAl and Si_3N_4, in the context of heavy-duty diesel and natural gas engine environments. Progress has been made on several fronts this year, including: (1) engine tests on these valve materials, (2) development of a probabilistic life prediction model, and (3) compilation of material properties of TiAl and Si_3N_4 that are critical to implementation of these materials in the extreme environment of a heavy-duty engine.

Twelve TiAl and forty-five Si_3N_4 valves have completed the fabrication process. Their incorrect surface finish provided by the machining supplier was rectified. The valves have been subjected to several pre-engine test characterization assessments: CMM, profilometry and laser-scatter NDE. The first set of valves has accumulated 20 h on an impact rig and has demonstrated acceptable performance. Upon successful completion of the impact rig test, the valves will be tested on a Caterpillar G3406 engine at the NTRC. In addition to fabricating custom components that will enable this engine to accept the new modified valve design,

the engine has been instrumented to capture the performance of each cylinder.

Significant progress was made toward developing a NASA CARES/Life prediction model. A preliminary model was developed, and a life prediction curve was generated. It was speculated that this preliminary curve significantly under predicted the probability of failure due to incomplete representation of the boundary conditions. Model enhancements are currently underway and updated results will be correlated to the engine performance of the valve hardware.

Thermo-physical properties (e.g., coefficient of thermal expansion, thermal conductivity, density) and mechanical properties (e.g., ultimate tensile strength, Young's modulus, ductility) of TiAl and Si_3N_4 have been collected. Properties specific to implementation of these advanced materials in a valve environment are also under investigation (e.g., machinability, frictional coefficients, corrosion resistance).

This diverse effort will help to equip design engineers with the information required to implement advanced lightweight materials in a valve train application. This program has made significant progress toward this goal in FY 2006 and is poised to significantly advance the case for TiAl and/or Si_3N_4 as a future valvetrain material in FY 2007.

References

1. D. Eylon et al., "Development of permanent-mold cast TiAl automotive valves," *Intermetallics*, **6**, 1998.

2. K. Maki et al., "Development of a high-performance TiAl exhaust valve," SAE Paper 960303, Warrendale, Pennsylvania, 1996.

3. M. J. Andrews and J. Chapa-Cabrera, "High-temperature advanced materials for lightweight valve train components," *Heavy Vehicle Propulsion Materials 2003 Annual Progress Report*, Energy Efficiency and Renewable Energy Office of FreedomCAR and Vehicle Technologies, March 2004.

4. J. G. Sun, "NDE development for ceramic valves for diesel engines," *Heavy Vehicle Propulsion Materials 2004 Annual Progress Report*, Energy Efficiency and Renewable Energy Office of FreedomCAR and Vehicle Technologies, May 2005.

5. J. S. Trethewey et al., "High-temperature advanced materials for lightweight valve train components," *Heavy Vehicle Propulsion Materials 2004 Annual Progress Report*, Energy Efficiency and Renewable Energy Office of FreedomCAR and Vehicle Technologies, May 2005.

6. Biery et al., "Use of Weibull statistics to quantify property variability in TiAl alloys," *Metallurgical and Materials Transactions A*, 33A, 3127–3136 (October 2002).

Presentations and Publications

O. Jadaan, J. S. Trethewey "Reliability of high temperature lightweight valve train components in a total probabilistic design environment," paper presented at the American Ceramic Society's 30th Ann. Intl. Cocoa Beach Conf. & Exposition on Advanced Ceramics & Composites, Cocoa Beach, Florida, January 21-26, 2006, and to be published in conference proceedings.

J. G. Sun, J. M. Zhang, J. S. Trethewey "Nondestructive evaluation of machining damage in silicon nitride ceramic valves," paper presented at the American Ceramic Society's 30th Ann. Intl. Cocoa Beach Conf. & Exposition on Advanced Ceramics & Composites, Cocoa Beach, Florida, January 21-26, 2006, and to be published in conference proceedings.

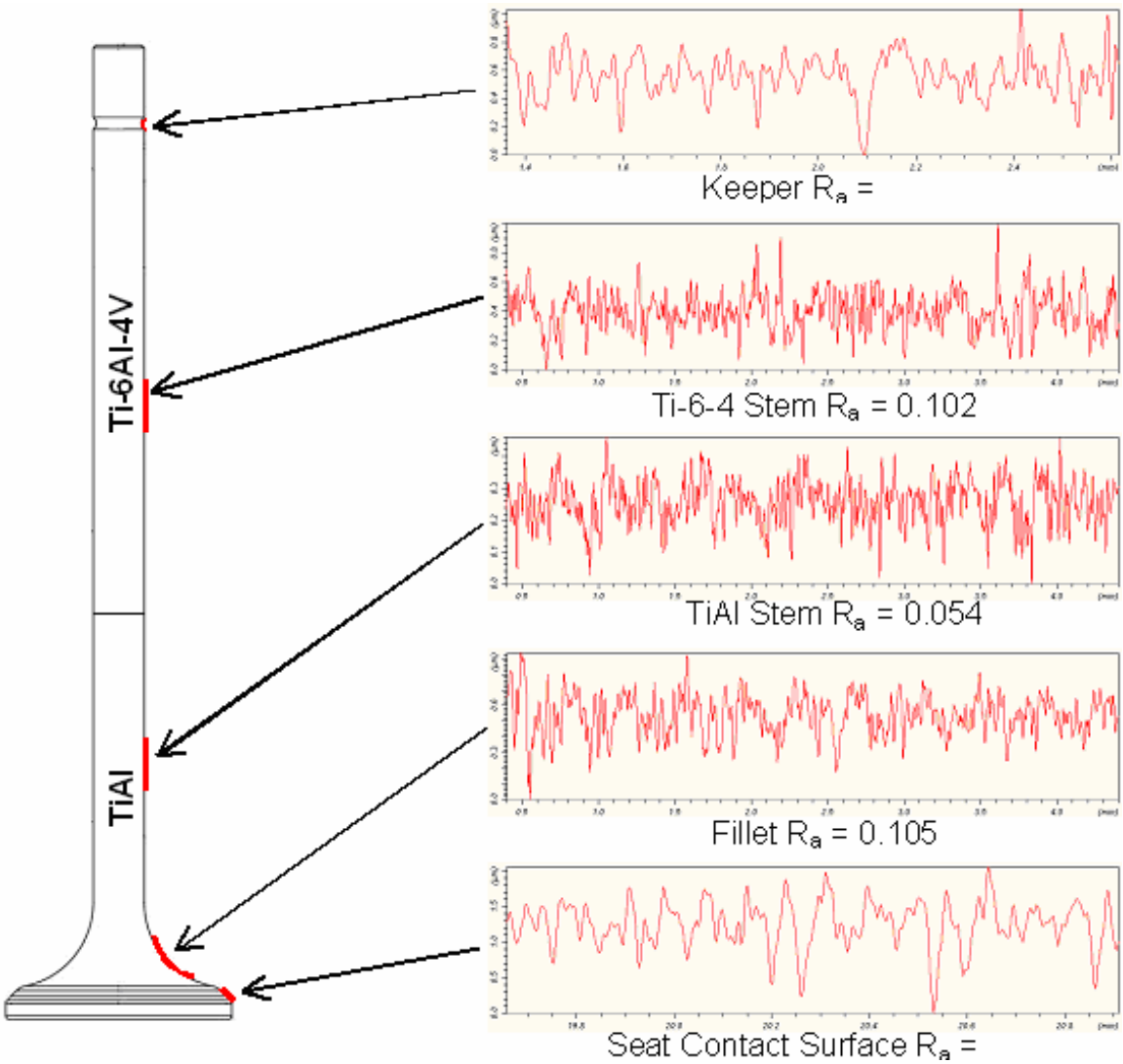

Figure 1 Surface roughness measurements on a TiAl valve. Note that scan fluxuation may not appear to correlate with the stated R_a value – this is because the plotted range for each scan is different

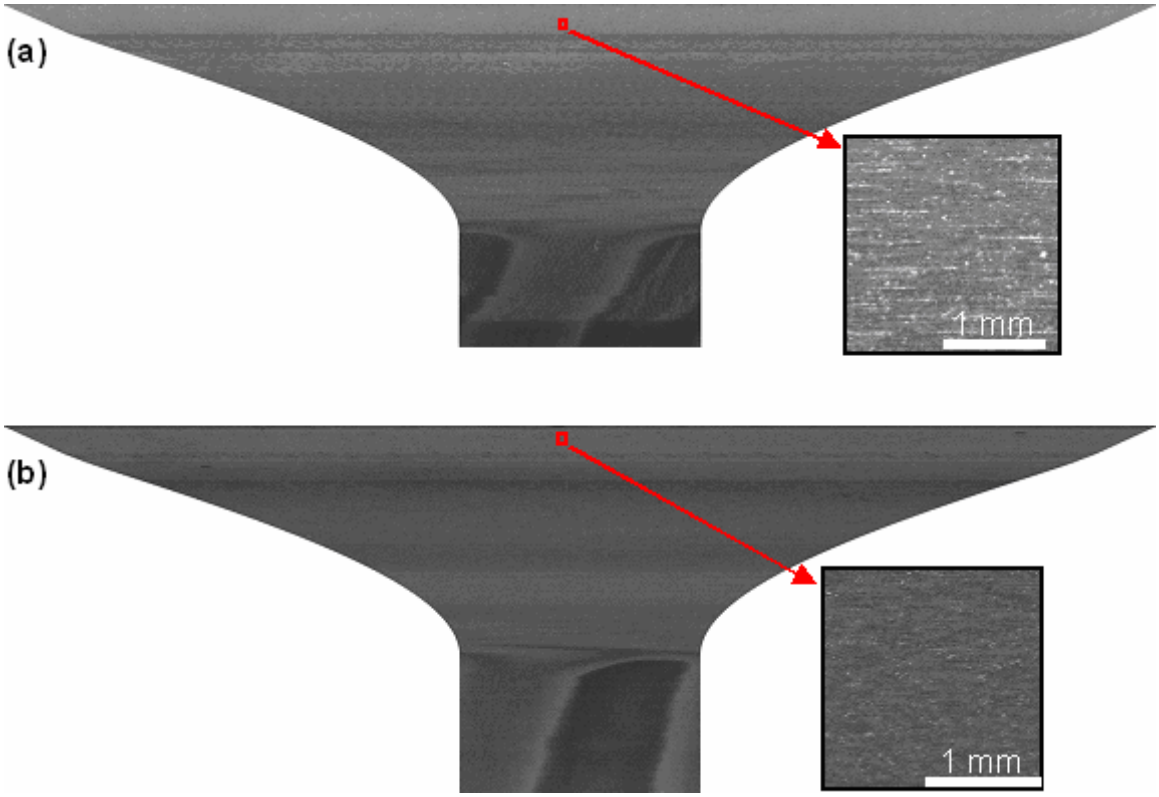

Figure 2 Laser scatter NDE scans of a Si_3N_4 valve (a) after incorrect finish machining and (b) after corrective finish machining. Note that the white streaks in (a-inset) that indicate subsurface damage have been removed by the corrective finish machining (b-inset)

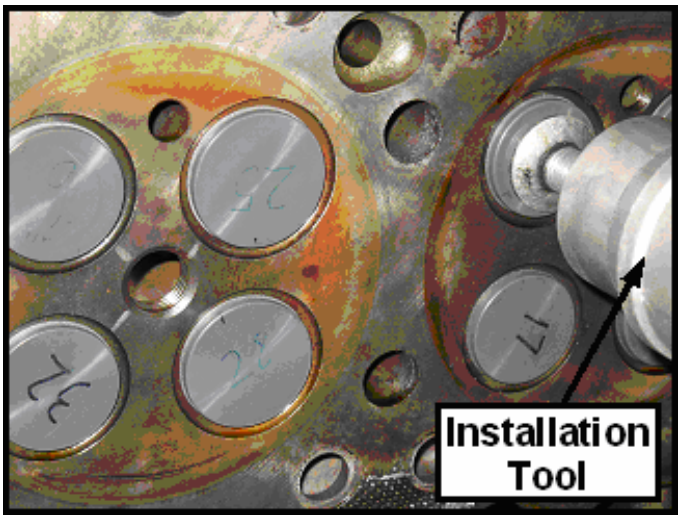

Figure 3 Si_3N_4 valve under compression from an installation tool

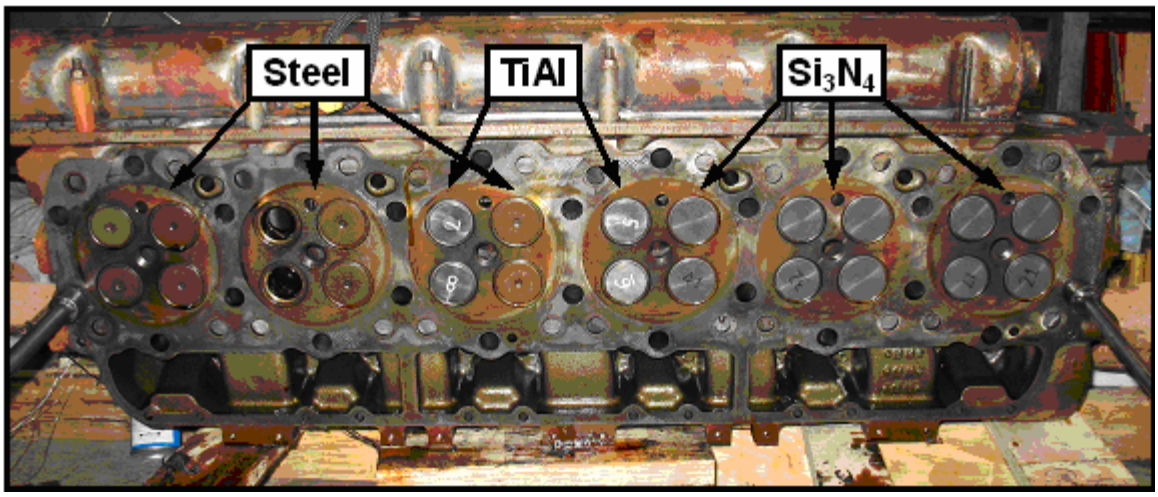

Figure 4 Caterpillar G3406 cylinder head after "advanced valve" installation. From left to right there are 10 production steel valves (2 temporarily removed), 4 TiAl exhaust valves and 10 Si_3N_4 valves

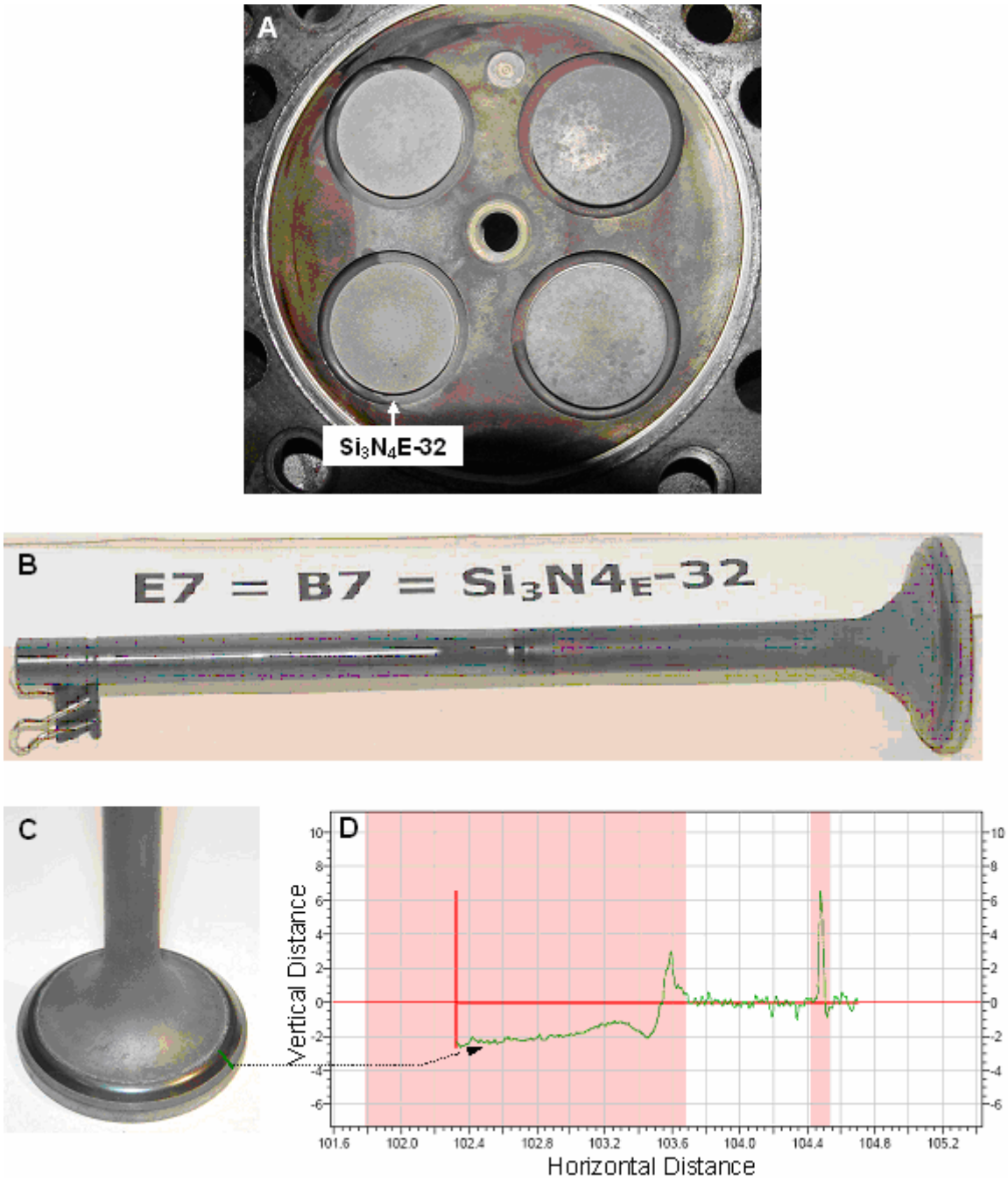

Figure 5 (A) An image of Cylinder 'B' immediately after the completion of the first 100 hour break-in phase. (B,C) Valve Si3N4E-32, a representative Si_3N_4 exhaust valve. (D) Profilometry scan of the valve/seat wear scar showing a wear scar depth of ~2 μm

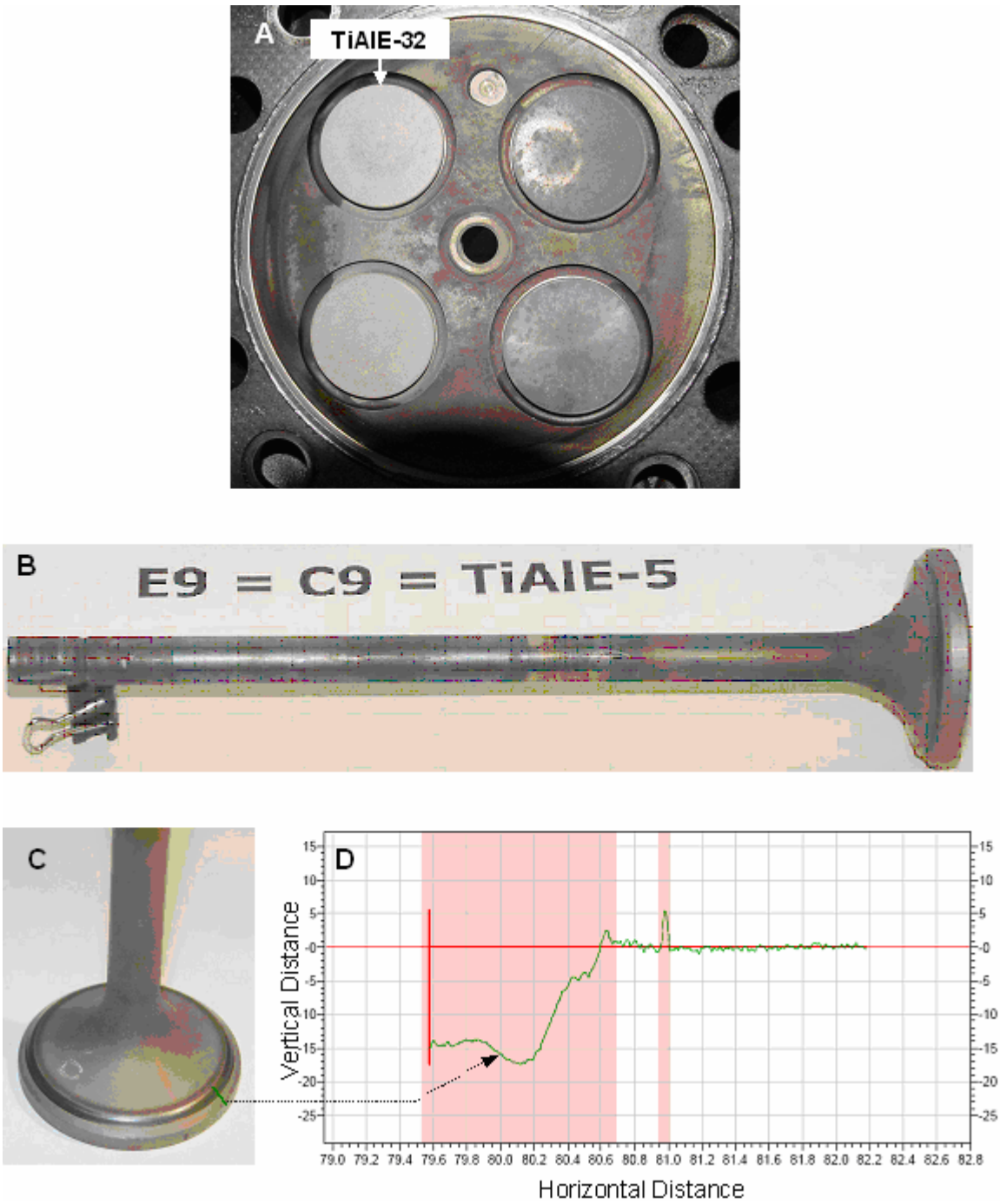

Figure 6 (A) An image of Cylinder 'C' immediately after the completion of the first 100 hour break-in phase. (B,C) Valve TiAl-5, a representative TiAl exhaust valve. (D) Profilometry scan of the valve/seat wear scar showing a wear scar depth of ~15 μm

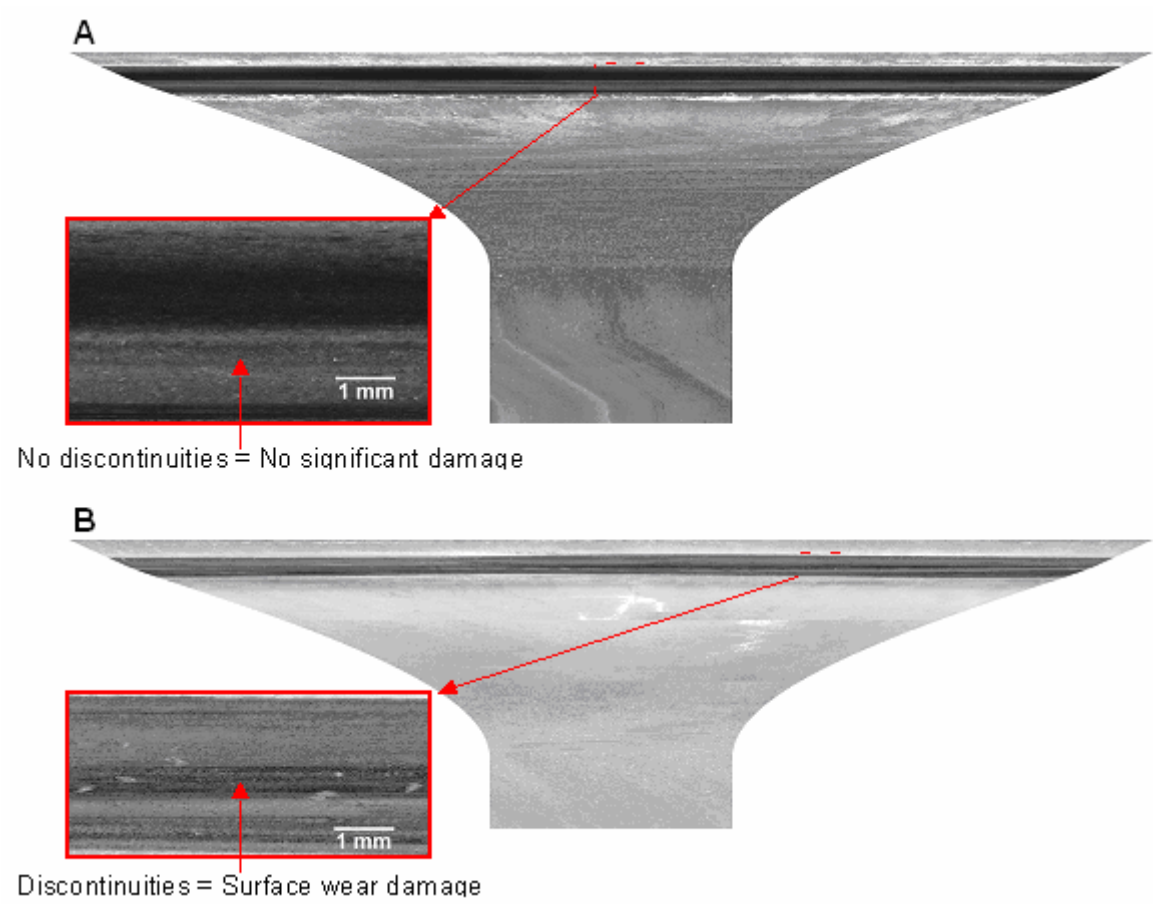

Figure 7 Laser-based NDE scans of (A) Si3N4E-32 and (B) TiAl-5 indicating that the Si_3N_4 valve has not sustained major wear damage, but the TiAl valve is showing signs of significant valve/seat wear

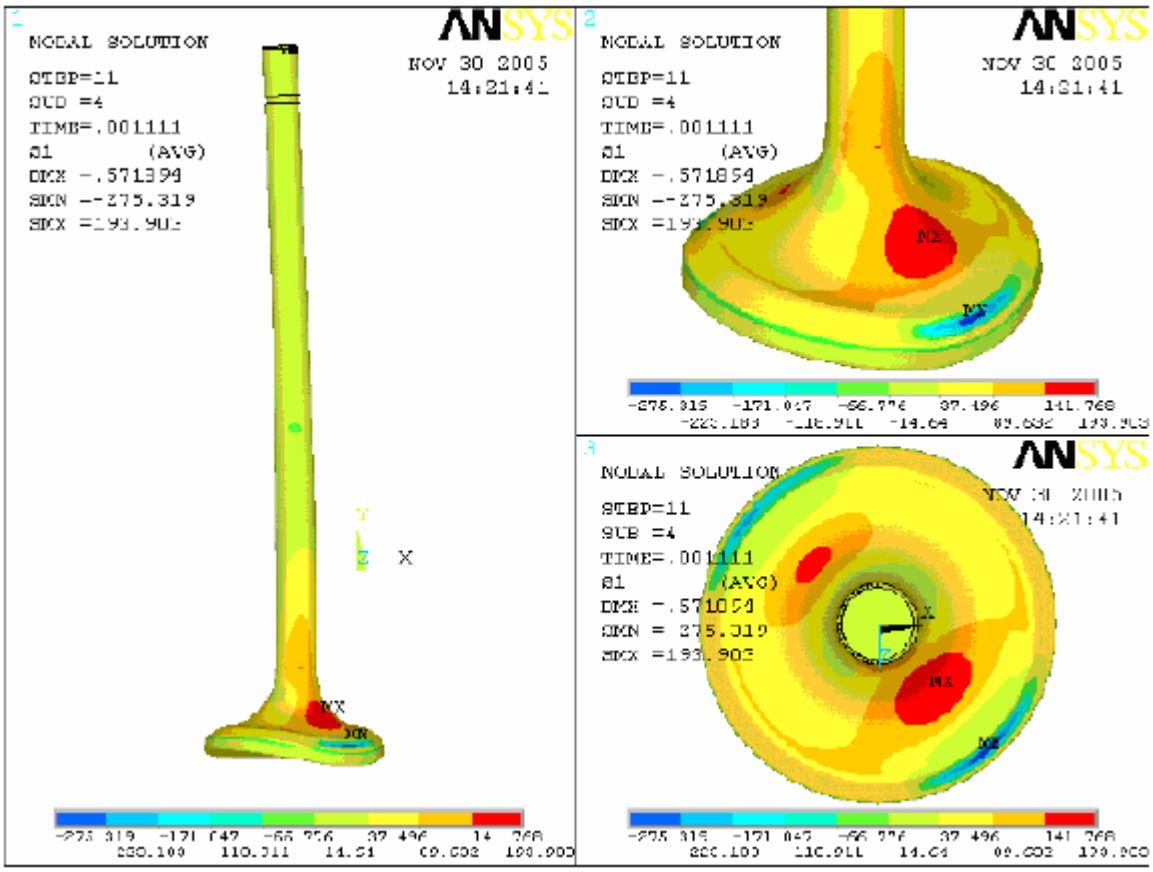

Figure 8 Principal stress field of the three-dimensional valve FEA model. Note the non-axisymmetric stem bending and "pringled" seat warping. The maximum stress observed in this 3D model is approximately a factor of two greater than the maximum stress observed in the axisymmetric model

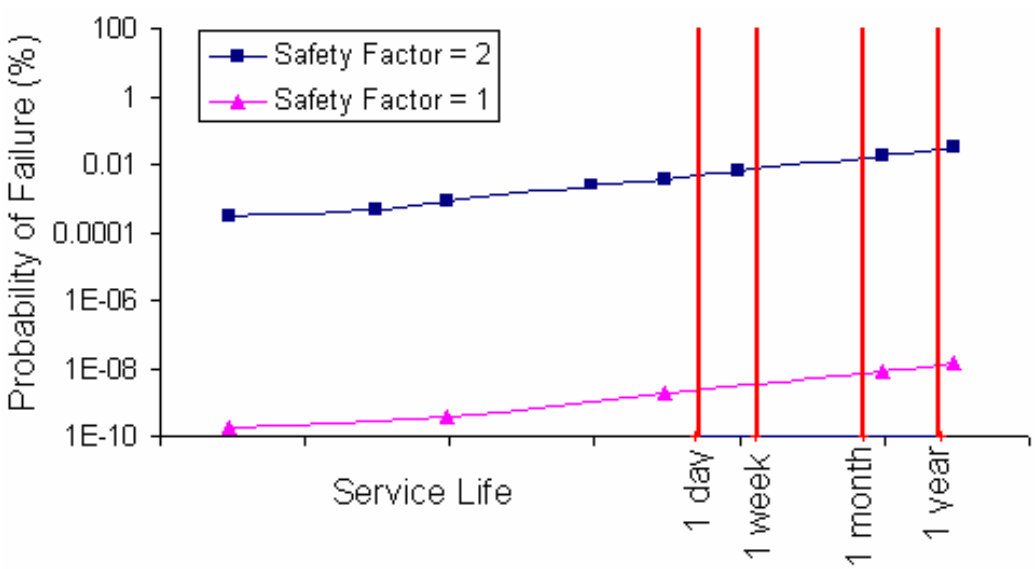

Figure 9 Life prediction curve for Si_3N_4 valve experiencing slow crack growth under *continuous* G3406 genset operating conditions using the 3D model. Note that the safety factor corresponds to a multiplication factor on the applied loads. As such, a load factor of two would generate more severe loading conditions resulting in a higher probability of failure

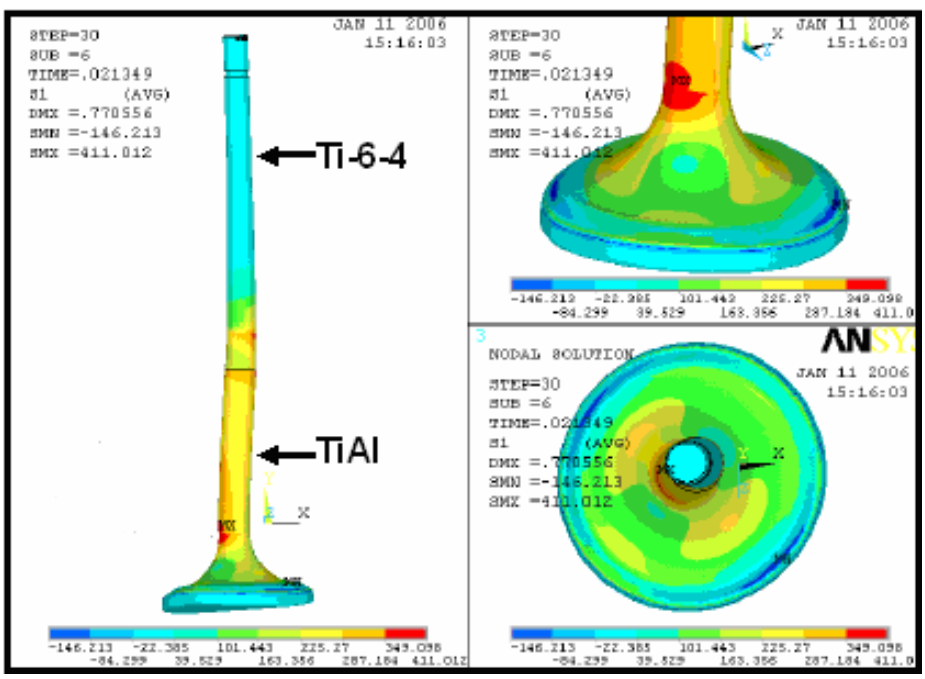

Figure 10 Principal stress field of TiAl/Ti-6-4 valve near peak cylinder pressure. The location of the maximum stress value (431 MPa) is not at the center of the fillet radius, which may indicate that the valve design is not optimized for the TiAl's material properties

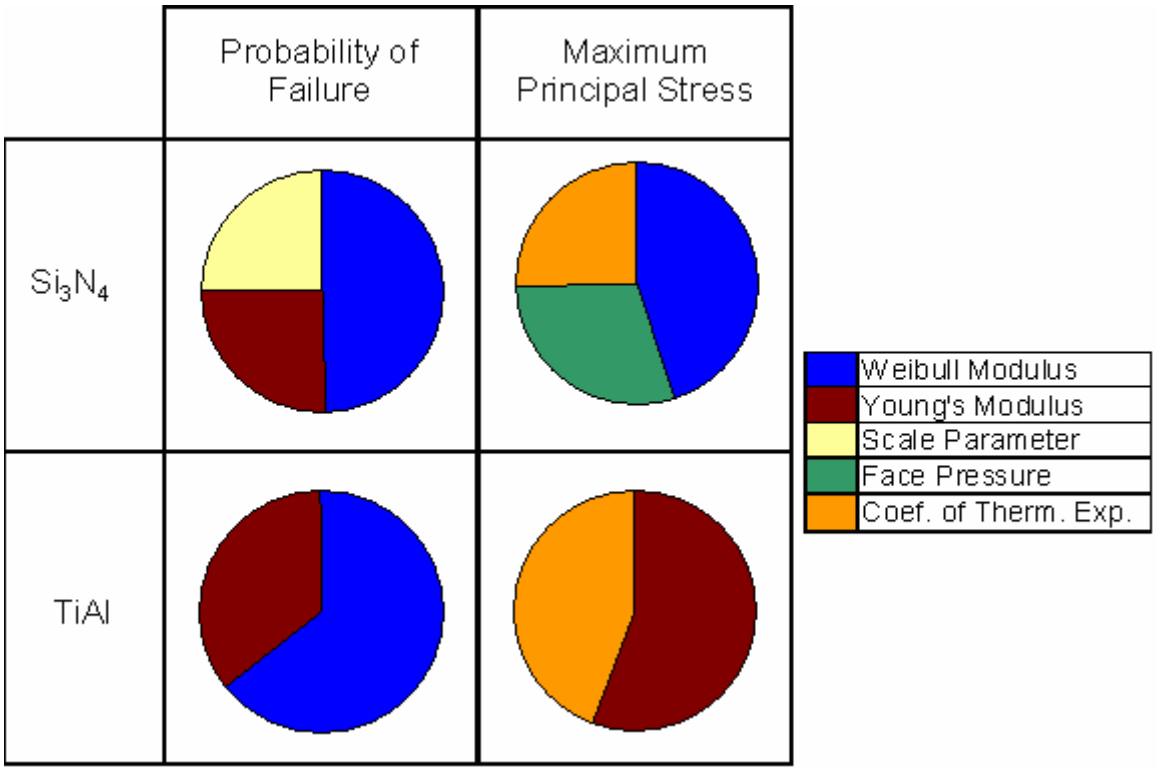

Figure 11 Results of the PDS sensitivity study highlighting the relative effect of the input variables on the probability of failure and maximum principal stress for Si_3N_4 and TiAl valves

7. CHARACTERIZATION OF PHYSICAL AND MECHANICAL PROPERTIES

A. Implementing Agreement for a Programme of Research and Development on Advanced Materials for Transportation Applications

Andrew A. Wereszczak and Mattison K. Ferber
Ceramic Science and Technology Group
Oak Ridge National Laboratory
P.O. Box 2008, MS: 6068
Oak Ridge, TN 37831-6068
(865) 576-1169; fax: (865) 574-6098; e-mail: wereszczakaa@ornl.gov

DOE Technology Development Manager: Jerry L. Gibbs
(202) 586-1182; fax: (202) 586-1600; e-mail: Jerry.gibbs@ee.doe.gov
ORNL Technical Advisor: D. Ray Johnson
(865) 576-6832; fax: (865) 574-6098; e-mail: johnsondr@ornl.gov

---

Contractor: Oak Ridge National Laboratory, Oak Ridge, Tennessee
Prime Contract No.: DE-AC05-00OR22725

Objectives

- Integrate new technologies into the transportation sector by implementing research that improves material properties and performance while maintaining acceptable life-cycle costs.
- Promote commercialization of new materials technologies by developing standard testing and characterization methods with domestic and international standards communities.

Approach

- Define and implement research in conjunction with International Energy Agency's (IEA) Implementing Agreement Advanced Materials For Transportation (IA-AMT) Applications.
- Promote candidate annex on coating performance and evaluation and assess alternative coating test methods.

Accomplishments

- Defended proposed new annex on Coating Performance and Evaluation to IA-AMT Executive Committee.
- Assessed laser spallation and large-scale deflection test methods to characterize coating spallation and bonding adherence.

Future Direction

- Project concluded in FY06.

Introduction

The current mission of the IA-AMT is to investigate promising new technologies for evaluating and ultimately improving the performance of materials for transportation systems. The primary motivation for this activity is new material technologies are required to increase efficiency and reduce harmful emissions in these systems. Examples of these technologies include lightweighting to improve fuel efficiency; surface engineering to improve the resistance to wear and contact damage; development of durable coating systems for thermal, wear, and environmental management; and development of revolutionary materials (structural ceramics and ceramic matrix composites) for operation at much higher temperatures and pressures.

In FY06, the primary effort of this project was to explore and develop innovative test methods to characterize coat performance. Coatings are technologically important to the transportation sector for applications needing improved tribological, thermal, and environmental protection of metallic (substrate) components. However, for coatings to enhance those enhancements, they need to be mechanically robust and remain adherent to the metallic component.

Approach

Three methods were considered this year to test coating adherence and spallation resistance.

The first method involved using a laser-induced shock to cause coating spallation, and collaboration with Laser Shock Peening Technologies, Inc. (Dublin, OH). A schematic of the system is shown in Fig. 1. A high-energy laser is pulsed onto an ablative tape that is adhered to a metal substrate. The coating under evaluation is positioned on the opposite end to where the laser will strike. Water floods the impact side, is transparent to the laser, and serves as an impedance barrier. The laser goes through the water, impacts the ablative tape, and creates a plasma that lasts only up to a couple tens of nanoseconds. The water's impedance causes the resulting shock wave to transmit into the substrate. The wave transmits into the substrate as a compressive wave. It continues into the specimen and reflects off the back surface becoming a tensile wave. The created tensile stress causes a portion of the coating to spall off. The energy of the laser, dimensions and properties of the substrate, and the produced spall are all known or are measurable, so there is the potential to calculate the spall strength of the coating using this technique.

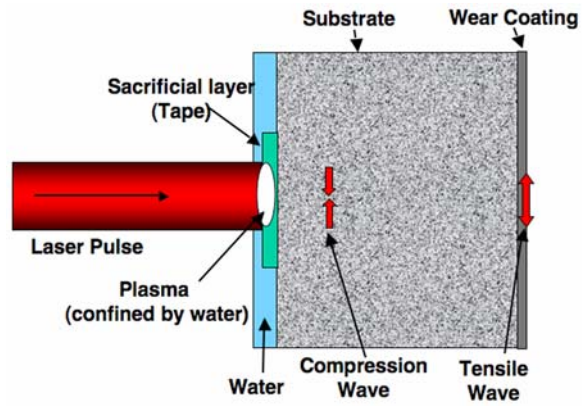

Figure 1. Schematic of the laser shock test that was very effective at inducing coating spallation.

The second method involved using a pendulum-based scratch tester. A picture of the system is shown in Fig. 2. A gas gun pushes on the pendulum horizontally. That event coupled with the pendulum's radius causes high speed scratching with a conical diamond tool that is positioned at the bottom of the pendulum. Two high frequency load cells, positioned to measure normal and tangential forces, continuously capture load as a function of time. Those signals are then combined with postmortem of the produced scratch geometry to interpret scratch resistance. This system has been primarily used with monolithic materials; however, interest existed to assess its viability for characterization coating adhesion properties.

The third considered method involved subjecting a coated metallic substrate to ball-on-ring equibiaxial flexure. Essentially, this is an axisymmetric three-point-bend test. Examples of tested coupons and a side-view schematic are shown in Fig. 3. The coated side of the coupon is loaded against with a ball using a mechanical testing frame. The coated specimen is deflected by several times the thickness of the specimen causing (at least) permanent deformation of the metallic substrate. During that deflection, the coating will spall. Its diameter is then linked to the radius of curvature of

the permanently deformed specimen. That radius of curvature can then be used to calculate the imposed strain at that location, or effectively, the coating strain to failure or spallation. If spallation is more apt to occur in tension or compression, then the coating can simply be placed on the top or bottom to promote. This technique relies on the deformation of the substrate to impose a strain on the coating, and then a critical strain of spallation or cracking can be estimated.

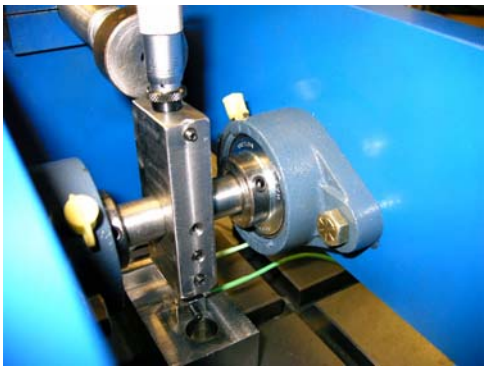

Figure 2. High-speed pendulum scratch tester. The horizontal piston shown at the top strikes the vertical steel bar resulting in a pendulum motion at its bottom where a conical diamond tool is mounted.

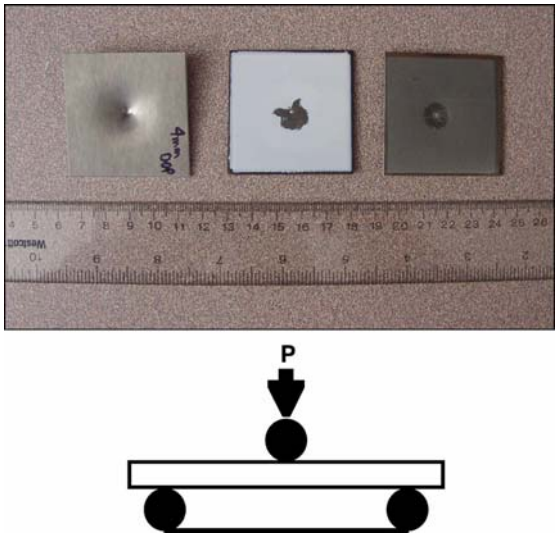

Figure 3. Examples of coated specimens tested in ball-on-ring biaxial flexure (top). Sectional view of ball-on-ring biaxial flexure test configuration.

Results

The laser shock spallation test method was quite effective at producing coating spallation. An example of a test is shown in Fig. 4. Spall diameter is the dependent parameter, whereas laser energy or pressure, pressure waveform, substrate and coating physical properties and dimensions, and coating strength are independent parameters. Modeling of the shock event is needed to link those independent parameters to the produced spall diameter so that coating strength can be back calculated out.

Polished cross-sections of the spall were examined with scanning electron microscopy (SEM). In one example (Fig. 5), the laser shock caused spallation at the interface between a bond coat and topcoat in a thermal barrier coating. Because the laser pressure could be controlled and varied, spallation was able to be initiated at different locations within the substrate - interface - bond coat - interface - top coat system. This is attractive because it enables the adherence characterization of the discrete layers within this multilaminate coating system (and presumably other multilaminate systems too).

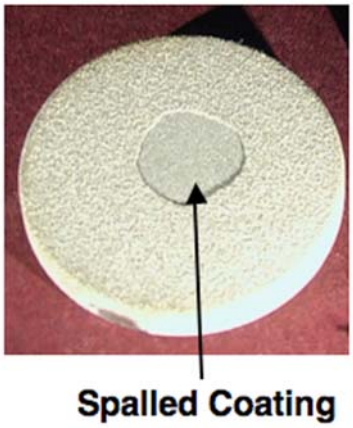

Figure 4. Examples of coating spallation produced by laser shock test system. Diameter of this coated coupon was 1 inch (25.4 mm).

Sponsorship of the project terminated before scratch adhesion testing of coatings could be interrogated using the pendulum tester; however, strong potential for it to be an effective method for such exists. A schematic of the produced groove from the scratch testing is shown in Fig. 6. The height of the swinging pendulum can be adjusted to

produce different depths of plowing or adjusted to best match the depth corresponding to coating thickness. Work is ongoing in other projects to continue to assess the viability of using pendulum-based scratch testing to characterize coating mechanical properties.

Strain to failure is estimated using the spall size (or the location where cracking initiates if no spallation has occurred), radial deflection profile (measured with a profilometer), and finite element analysis (FEA). In one example (Fig. 7), the coating spall diameter was approximately 6 mm; that value on the predicted FEA curve was found to correspond to a strain to failure of ~4%. This method is a simple and inexpensive test to conduct to estimate coating failure strains.

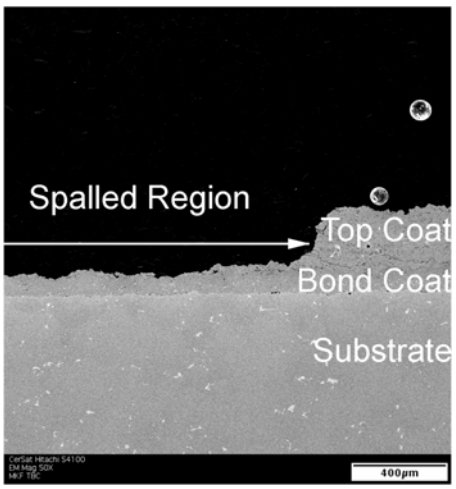

Figure 5. Polished cross-section of spall.

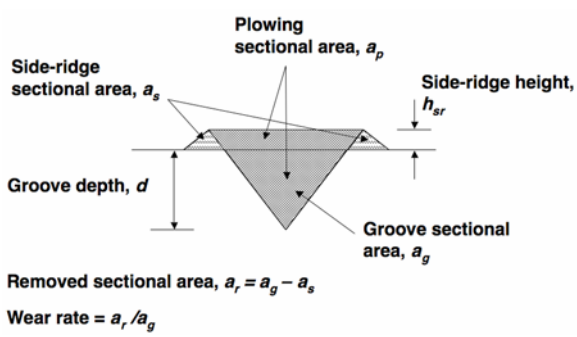

Figure 6. Schematic of groove produced by pendulum scratch tester.

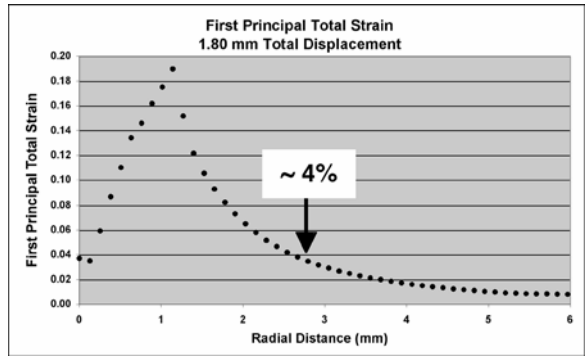

Figure 7. Stress profile predicted by FEA that is used to estimate strain-to-failure.

Conclusions

Three innovated test methods were considered for use to characterize coating strain to failure. The demonstration of two of the techniques (laser spallation and biaxial deflection) is very effective at enabling coating adherence characterization. The third technique (scratch adhesion testing) has potential to also be an effect test in characterizing coating adherence. Coatings (tribological, environmental, and thermal) can enhance or enable the performance of transportation-related components, so developing techniques to understand their adhesion characteristics is very relevant.

Presentations and Publications

M. K. Ferber, "Coating Evaluation: New Annex," IEA IA-AMT Executive Committee Meeting, Porto, Portugal, 11 October 2005.

A. A. Wereszczak, "Coating Evaluation & Performance: New Annex?" IEA IA-AMT Executive Committee Meeting, Calgary, Canada, 07 May 2006.

B. Rolling Contact Fatigue

Andrew A. Wereszczak
Ceramic Science and Technology Group (CerSaT)
Oak Ridge National Laboratory
PO Box 2008, MS 6068
Oak Ridge, TN 37831-6068
(865) 576-1169; fax: (865) 574-6098; e-mail: wereszczakaa@ornl.gov

DOE Technology Development Manager: Jerry L. Gibbs
(202) 586-1182; fax: (202) 586-1600; e-mail: Jerry.gibbs@ee.doe.gov
ORNL Technical Advisor: D. Ray Johnson
(865) 576-6832; fax: (865) 574-6098; e-mail: johnsondr@ornl.gov

---

Contractor: Oak Ridge National Laboratory, Oak Ridge, Tennessee
Prime DOE Contract Number: DE-AC05-00OR22725

Objectives

- Identify and study surface and sub-surface flaws in ceramic balls.
- Summarize rolling contact fatigue (RCF) test methods and result interpretations used in Germany, Japan, United Kingdom, and the United States.

Approach

- Develop a robust test method that enables the exploitation and study of surface and sub-surface flaws in ceramic balls used in bearings.

Accomplishments

- Developed "c-sphere" strength (i.e., hoop tensile strength) test method to characterize ceramic balls.
- Measured and compared c-sphere strength of three commercial grades of silicon nitride ball bearings.
- Published ORNL Technical Report summarizing internationally used RCF test methods.

Future Direction

- Project concluded in FY06.

Introduction

Silicon nitride (Si_3N_4) balls for use in hybrid bearings have been shown to extend rolling contact fatigue (RCF) lifetime, reduce the dynamic loading in high-speed roller element applications because of their lower density, compared to steel balls, and enable bearing use in more corrosive and higher temperature environments. During their development, many parameters such as density, hardness, elastic modulus, fracture toughness, 3- and 4-pt flexure strength and Weibull modulus, crushing strength, grain size and secondary phase morphology, porosity, and surface finish have been extensively studied in an effort to improve or predict RCF performance of Si_3N_4 balls. As an outcome of many of those studies, ASTM F2094 was developed to specify allowable minimums and maximums of many of those properties and finish conditions.

In spite of the above work, little or no study has been devoted to the quantification of sub-surface inhomogeneities and what effect they could have on RCF performance. Sub-surface factors such as damage due to machining and remnants from hot-isostatic-pressing glass encapsulation that are sometimes used in processing are examples of this. Such sub-surface inhomogeneities usually play a dominant role in the performance (strength, fatigue, etc.) of structural ceramics. Their study in structural ceramics is typically facilitated using simple tensile or flexure strength specimen geometries that enable the concurrent measurement of strength and strength-limiting flaw size (latter identified through fractographical practices).

However, for ceramic spheres, two historical barriers to the study of strength-flaw-size relationships within them are the (1) the inherent geometry of the sphere itself, and (2) sphere size which inhibits the size of extractable strength specimens (e.g., bend bars). Regarding the former, it is nearly impossible to mechanically load a ceramic ball in a manner to produce a predictable tensile stress field at the sphere's surface sufficient to cause its fracture. Compressively loading a ceramic sphere diametrally produces two Hertzian contacts where ring- and cone-crack initiation occurs, and ultimate fracture can result if the contact stresses are sufficiently high. Hence, the evolution of ultimate fracture with this test method makes the study of strength limitation from surface- and sub-surface-located intrinsic and extrinsic flaws nearly impossible. The fracture of brittle spheres from diametral compression occurs at such high loads (i.e., a great deal of stored energy exists in the sphere at fracture) that the test coupon disintegrates into fine rubble rendering fractography nearly impossible, and thus, inhibiting the study of the relationship between strength and flaw size. Other complicating issues can result if one opts to crush small ceramic spheres; for example, exorbitantly high contact stresses are created causing the (typically very strong) sphere, in effect, to act as a spherical indenter against the loading platens before it is crushed.

Because the desire exists to identify and study surface-located flaws and sub-surface damage in ceramic spheres, and crush testing was deemed to be impractical, a new test coupon called the "C-sphere" flexure strength specimen was conceived and developed to enable the study of and measurement of a strength and associated linked flaw size. The C-sphere flexure strength specimen fractures at low to modest loads, and fractographical analysis can readily be performed and strength-limiting-flaw studies can ensue in a practical manner because excessive fragmentation is not produced. Enabling the identification of a flaw type and measurement of its size in finished ceramic balls is indeed important for the study of strength, but more importantly, for the study and predictability of RCF performance (a response limited by surface- or near-surface-located flaws or in changes thereof). Hadfield reported that a critical depth of ring cracking in RCF is 5-20 microns below the surface. The C-sphere specimen facilitates the study of flaws that can exist at those depths in ceramic ball bearings and ceramic spheres in general.

Approach

A schematic of the C-sphere specimen is shown in Fig. 1. It is produced through the controlled slotting of a ceramic sphere. It is then diametrally loaded perpendicular to that slot (or flexed) to initiate hoop tensile fracture at the sphere's surface or "outer fiber" as shown in Fig. 2. This specimen is analogous to a "C-ring" flexure specimen, which is produced through controlled slotting of a ceramic ring and enables strength evaluations of tubular components.

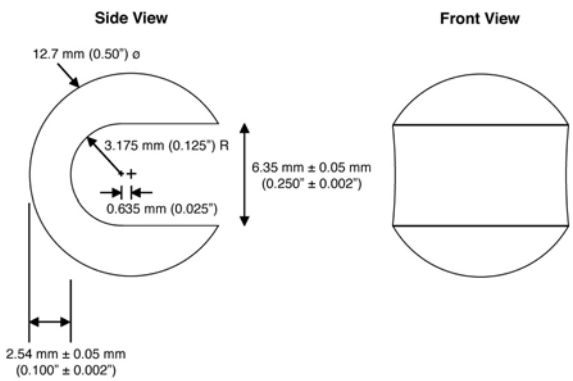

Figure 1. Side and front views of the C-sphere flexure strength specimen.

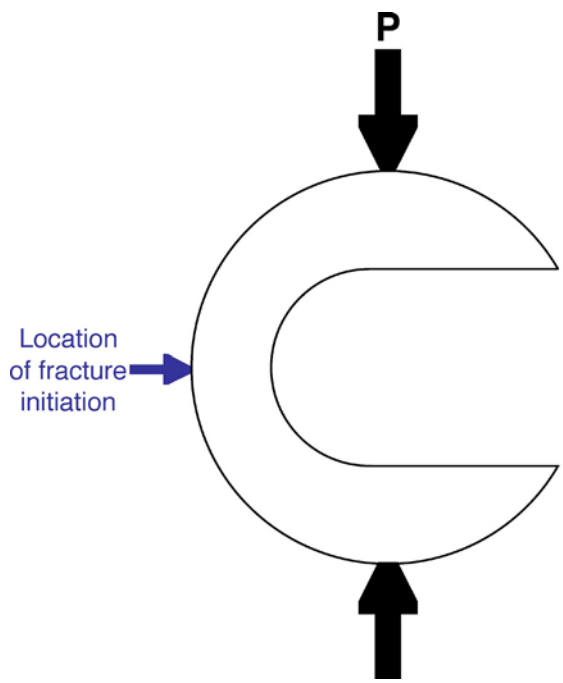

Figure 2. Diametral compression of the C-sphere flexure specimen causes fracture initiation from a hoop stress at the outer fiber.

An important aspect of the geometry is the purposeful non-coincidal positioning of the sphere's center and the center of curvature of the slot's innermost depth. The introduction of this offset acts to increase the outer-fiber tensile stress through the introduction of an applied bending moment; if it were not introduced, then too much tensile stress could develop on the ground surface of the notch and fracture would undesirably initiate there. Slot depth (related to this offset) in the FEA model was varied until a slot-width and slot-depth combination produced at least a 10-times higher outer-fiber surface or hoop tensile stress than any other surface tensile stress located elsewhere on the coupon. The final offset size (0.635 mm) resulted in a C-sphere geometry that, when diametrally compressed, produced an outer-fiber or hoop tensile stress much larger than that on the ground interior and a (desirably) high likelihood that fracture would occur at the outer fiber.

The nodal stress distribution plots for the C-sphere model are shown in Fig. 3 for an applied compressive force of 200N. One observes from these plots how the maximum tensile stress of 132.1 MPa is located at the outer fiber area of the C-sphere. This model shown was used to compute the effective area and effective volume for the C-sphere specimen, and those results are shown in Fig. 4(a).

Area and volume efficiencies were computed by dividing the effective area and volume by the original sphere's total area and volume. Their dependencies as a function of Weibull modulus are shown in Fig. 4(b). The use of the concepts of area and volume efficiencies is useful to consider when evaluating how efficient a particular specimen is in sampling surface-type and volume-type strength-limiting flaws. If a ceramic has a Weibull modulus of 10, then the C-sphere geometry described herein would sample flaw populations on about 3% of the a sphere's surface and in about 0.1% of its volume. As a comparison to an established test configuration, the area efficiency is about 24% for an ASTM C1161B flexure configuration with a 3 x 4 x 50 mm bend bar of a ceramic with a Weibull modulus of 10. While the C-sphere's area efficiency is modestly good, its volume efficiency is not. However, its design was never intended to sample volume flaw populations in ceramic spheres, so its poor volume efficiency is not viewed as a limitation.

The inherent geometry of the C-sphere produces a desirable artifact associated with the stress state at the edges that intersect the original sphere surface and the ground surfaces from the slotting procedure. Additional machining steps (i.e., edge chamfering after C-sphere slotting) are not necessary because significant tensile stresses never develop at the edges during diametral compression. Therefore, rudimentary chipping that can potentially result at

these edges from the slotting procedure will not initiate fracture and not influence measured strength.

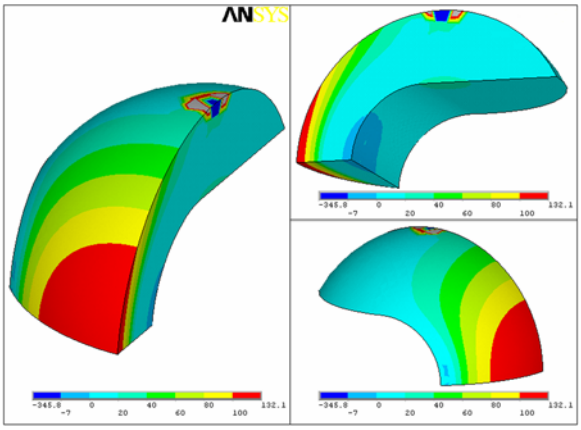

Figure 3. Nodal first principal stress distribution at three different views for an applied compressive force of 200 N. Shown values have units of MPa.

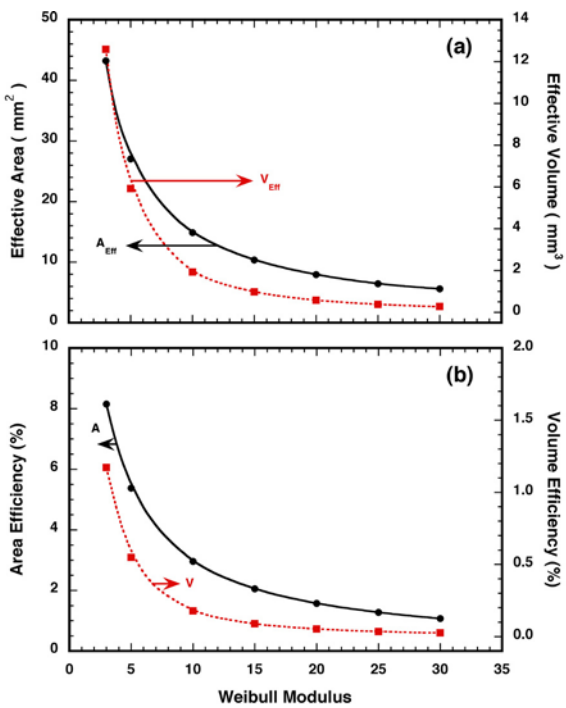

Figure 4. (a) Effective area and effective volume and (b) area and volume efficiency as a function of Weibull modulus for the C-sphere flexure strength specimen. The latter is the effective area and volume divided by the sphere's total surface area and volume, respectively.

NBD200, SN101C, and TSN-03NH balls with 12.7 mm diameter were machined into C-sphere flexure strength specimens. Examples of machined C-spheres are shown in Fig. 5.

After ligament thickness was measured in all C-sphere specimens, they were monotonically loaded in compression to failure using an electromechanical universal testing machine. A special alignment jig was used to horizontally align the C-sphere slot prior to loading (see Fig. 6). A slight compressive preload (~ 25 N) was applied to the jigged C-sphere specimen enabling the jig to be pulled out without disturbing the C-sphere alignment. The specimens were then tested using a constant crosshead displacement rate. Load to fracture was recorded and used to determine C-sphere flexure strength using interpretations of Fig. 3. Approximately 30 C-sphere specimens each of NBD200, SN101C and TSN-03NH were tested. Weibull strength distributions were determined using commercially available software. Optical fractography was conducted on all specimens to identify failure location and the fracture surfaces of a select few specimens were examined with scanning electron microscopy.

Figure 5. Machined Si_3N_4 C-sphere flexure strength specimens.

Results

The C-sphere characteristic strength of SN101C was 27% and 17% larger than the NBD200 and TSN-03NH, respectively. The Weibull moduli of SN101C and NBD200 were equivalent, whereas that of the TSN-03NH was slightly larger. The 95% confidence ratio rings for the two-parameter Weibull distributions of each are illustrated in Fig. 7.

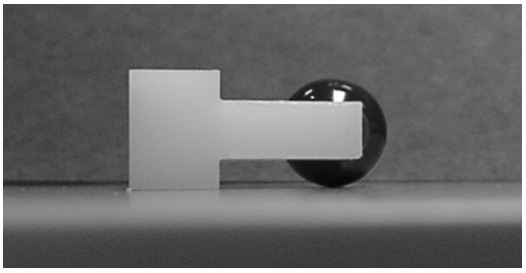

Figure 6. A plastic jig was used to align the C-sphere specimens prior to their diametral compressive loading.

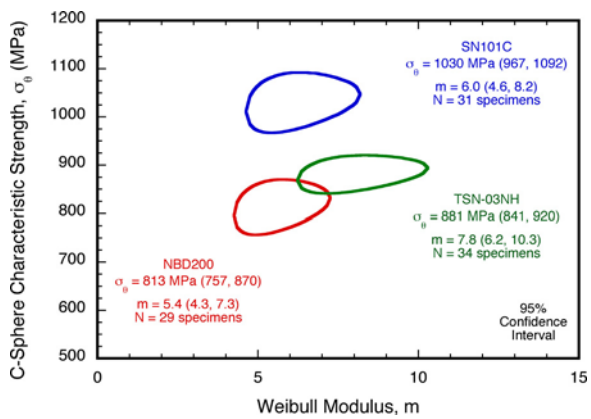

Figure 7. 95% confidence ratio rings for the three tested silicon nitrides.

Optical fractography showed that failure always initiated at the surface but not necessarily always exactly at the apex of the outer fiber. Failure-initiation locations for all the tested C-sphere specimens are mapped in Fig. 8. The scatter in the failure locations matches the region where there is tensile stress on the C-sphere's surface as shown in Fig. 3. No failures initiated at the edges, which is consistent with there being little or no stress in that region during loading.

A representative example of a failure location is shown in Fig. 9. The fracture of all specimens initiated at the C-sphere surface, which is an occurrence that was sought with the design of the C-sphere flexure specimen. For a strength of 770 MPa, a fracture toughness of 6 MPa√m, and a crack geometry factor of 1.5, the estimated Griffith flaw size for the specimen shown in Fig. 9 would be approximately 30 microns. That is of the size scale that Hadfield had indicated to be a critical size for crack penetration during RCF.

Conclusions

A "C-sphere" flexure strength specimen geometry was developed to measure the hoop tensile strength of bearing-grade silicon nitride balls and enable the study of surface-located strength-limiting flaws in these ceramic spheres. The C-sphere has the advantage of possessing a simple geometry that is easy to test. A simple, monotonically increasing uniaxial compressive force produces a hoop tensile stress at the C-sphere's outer surface that ultimately initiates fracture. The C-sphere strength is determined using the combination of measured failure load, geometry, and finite element analysis. Representations of C-sphere effective area, effective volumes, area efficiency, and volume efficiency as a function of Weibull modulus were developed. C-sphere flexure strength distributions were determined for NBD200, SN101C, and TSN-03NH (all commercial grade Si_3N_4 balls). SN101C was found to have the highest characteristic strength and TSN-03NH the highest Weibull modulus. The C-sphere test configuration was successful 100% of the time in causing fracture initiation at the surface, and therefore is effective at enabling the study of surface-located strength-limiting flaws.

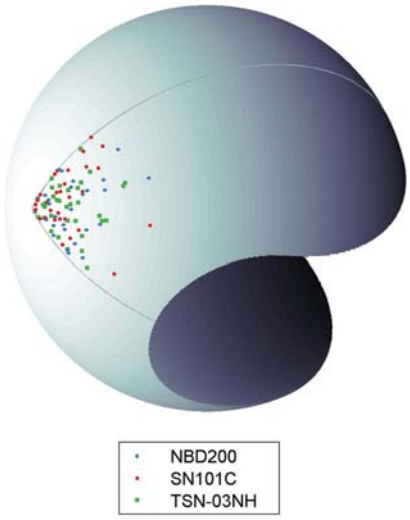

Figure 8. Map of locations of failure initiation for all tested specimens. Data projected onto a one-quarter domain of a C-sphere.

Figure 9. Example of a surface-located strength-limiting flaw in a SN101C C-sphere flexure strength specimen. This specimen had a strength of 770 MPa.

Presentations and Publications

A. A. Wereszczak, "IEA Annex III: Rolling Contact Fatigue," IEA IA-AMT Executive Committee Meeting, Porto, Portugal, 11 October 2005.

A. A. Wereszczak, "Strength of a C-Sphere Flexure Specimen," *30th Annual Conference on Composites and Advanced Ceramics*, Cocoa Beach, FL, Jan. 24, 2006.

A. A. Wereszczak, "IEA Annex III: Rolling Contact Fatigue," IEA IA-AMT Executive Committee Meeting, Calgary, Canada, 07 May 2006. A. A. Wereszczak, O. M. Jadaan, and T. P. Kirkland, "Hoop Tensile Strength of Ceramic Spheres Using a Diametrally Compressed 'C-Sphere' Specimen," in review, *Journal of the American Ceramic Society*, 2006.

A. A. Wereszczak, O. M. Jadaan, H. -T. Lin, G. J. Champoux, and D. P. Ryan, "Hoop Tensile Strength Testing of Small Diameter Ceramic Particles," in press, *Journal of Nuclear Materials*, 2006.

ORNL/TM-2006/521 Report: "Rolling Contact Fatigue of Ceramics," A. A. Wereszczak, W. Wang, Y. Wang, M. Hadfield, W. Kanematsu, T. P. Kirkland, and O. M. Jadaan, 2006.

A. A. Wereszczak, W. Wang, O. M. Jadaan, and M. J. Lance, "Strength of a C-Sphere Flexure Specimen," *Ceramic Engineering and Science Proceedings*, 2006.

8. EMERGING TECHNOLOGIES

A. Processing and Characterization of Structural and Functional Materials for Heavy-Vehicle Applications

J. Sankar, Z. Xu, and S. Yarmolenko
North Carolina A &T State University
1601 East Market Street
Greensboro, NC 27411
(336) 256-1151, extension 2282; fax: (336) 256-1153; e-mail: sankar@ncat.edu

DOE Technology Development Manager: Jerry L. Gibbs
(202) 586-1182; fax: (202) 586-1600; e-mail: Jerry.gibbs@ee.doe.gov
ORNL Technical Advisor: D. Ray Johnson
(865) 576-6832; fax: (865) 574-6098; e-mail: johnsondr@ornl.gov

Contractor: Oak Ridge National Laboratory, Oak Ridge, Tennessee
Contract No.: DE-AC05-00OR22725
Subcontractor: North Carolina A&T State University, Greensboro, North Carolina

Objectives

- Produce doped strontium cerate thin film electrolytes with flame-assisted chemical vapor deposition (FA-CVD) for solid oxide fuel cells (SOFCs).
- Study the effect of the processing parameters on the porosity of the NiO/YSZ anode substrates.

Approach

- Study the experimental parameters of the FA-CVD process and deposit yttria-doped strontium cerate thin film electrolytes thin film coatings using this technique.
- Characterize the coatings using scanning electron microscopy (SEM) and X-ray diffraction (XRD).
- Study the composition of raw materials, pressing, and sintering parameters for the anode substrate fabrication.
- Use optimization technique to study the properties of the anode materials.

Accomplishments

- Obtained dense and thin yttria-doped strontium cerate thin film electrolyte coatings.
- A design matrix was developed and successfully used to develop the anode material for SOFC application.
- The effect of the processing variables and their levels on porosity and conductivity of the anodes were identified.

Future Direction

- Optimize the FA-CVD process to prepare protonic conductive electrolyte with designed stoichiometry.
- Characterize the electrical conductivity of the protonic conductive electrolytes.
- Standardize the fabrication process of the anode materials.
- Fabricate single SOFCs and conduct performance tests.

Introduction

Proton-conductive perovskite materials have been receiving more and more interests since it was, for the first time, reported by H. Iwahara et al. over twenty years ago [1]. These materials have already found applications in fuel cells [2,3], hydrogen separation [4-6], and hydrogen sensors [7]. State-of-the-art solid oxide fuel cells (SOFCs), one of the most well known types of fuel cells, use solid state oxygen ion conductive electrolytes, which permit only oxygen ions to transfer through it from the cathode to anode. When proton-conductive materials are used as electrolyte for SOFCs, it permits only hydrogen ions, i.e. protons, to migrate from the anode to the cathode. Proton-conductive perovskite electrolytes have many advantages over oxygen ion conductor electrolytes. When a proton conductor is used instead of an oxygen ion conductor, fuel circulation is unnecessary, because no water vapor is generated at the hydrogen electrode. Moreover, the operating temperature can be reduced to about 600-700°C, where reactions such as methane reformation are kinetically favorable without the need for costly catalysts. Therefore, fuel cells could be constructed from less expensive materials. Recently, acceptor-doped ABO_3 perovskite oxides (A^{2+}=Sr, Ba, and B^{4+}=Ce, Zr) which exhibit proton conduction, have received much attention as solid oxide electrolytes of the hydrogen–air fuel cells. Among many different proton-conductive perovskites, Barium cerates ($BaCe_xM_{1-x}O_{3-\delta}$) and strontium cerates ($SrCe_xM_{1-x}O_{3-\delta}$) doped with acceptors M (trivalent element, such as, Y or rare earth elements, Yb, Gd, Nd, Dy, etc.) found to have the highest conductivities.

Up-to-date, almost all the research efforts towards proton-conductive perovskites are focused on materials processing, microstructure, phase and electrochemical properties characterization [8-10]. In addition to widely used powder sintering methods to prepare electrolytes [11], thin film technologies are also favorable in applying proton-conductive perovskites as electrolytes in SOFCs. Thin films were essentially prepared with sol-gel techniques [12, 13], screen printing [14], ultrasonically atomized spray of powder colloid [15] and RF-magnetron sputtering techniques [16]. In this report, preparation of yttria-doped strontium cerate thin films with flame-assisted chemical vapor deposition (FA-CVD) technique will be presented for the first time. FA-CVD technique had been used to process yttrium-stabilized zirconia thin films on both dense and porous substrates [17, 18], ceria [19] and alumina [20], and so on. It is a cost-effective technique to prepare metal oxides. It is operated in ambient, so that it is made possible to coat on large area. It is especially important to scaling up this technique for industrial applications. In the present work, we demonstrate again that the FA-CVD technique is effective in preparing thin films of perovskite materials. The purpose of the study was to understand the effects of the operating conditions on the microstructure, phase and deposition rate in order to optimize the process.

The two most common designs of SOFCs are the tubular and the planar [21]. Planar cells are capable of generating high power densities in comparison with the tubular cells. Anode supported planar cells provide very high cycle efficiency and pollution free energy. However, the microstructure of the cell degrades with respect to time due to the high temperature operating conditions. This leads to the deterioration of the fuel cell [22] and subsequent decomposition. This problem causes the major concern towards the commercialization of the fuel cells. The current study was to improve the life and performance of the anode cell for the SOFCs in a long run. In the earlier studies, Muller *et al*. [23] and Lee *et al*. [24] did extensive studies on the porosity and the electrical measurements for anode material with varying proportions of size and mol. % of the raw materials and the sintering temperature. Takehisa *et al.* [25] have used varying sizes of NiO-YSZ composite particles to fabricate a porous anode structure. Clemmer *et al.* [26] have observed dramatic improvements in electrical conductivity with increase in Ni content. Lee *et al.* [27] have investigated the effect of microstructure on anode substrate on the unit cell performance. However, the earlier investigators have studied the effect of individual process variables on the performance of the anode material. It is imperative to consider all the contributing factors that affect the anode material performance. So, it was decided to use the statistical method to study the individual effects and the combined effects of the different processing parameters on the output variable.

Approach

A liquid fuel FA-CVD system similar to the one introduced in previous work [17] was used for strontium cerate thin film processing. The metal-organic reagents used in all the experiments were strontium 2-ethylhexanoate (Sr-2EH, 40%, Strem Chemicals, Inc.), Cerium 2-ethylhexanoate (Ce-2EH, 49%, Alfa Aesar) and yttrium 2-ethylhexanoate (Y-2EH, 99.8%, Alfa Aesar). High purity oxygen (99.999%, National Welders) was used as oxidant. In order to vary the substrate temperature in a relatively large range, air-blow cooling and oxy-acetylene flame heating under the substrate support were developed. They were used alternatively according to the requirement of the substrate temperature. The ranges and values of the parameters employed in the experiments were designed as shown in Table 1. Si(100) was used as substrates.

To investigate the effect of the total-metal concentration and substrate temperature on the microstructure and phase development in the coatings, a full arrangement of 18 experiments for the two parameters with three levels was designed with a duplicate. The experiments were also randomized in order to eliminate the temporal effect on the results.

Table 1. Experimental parameter design

Parameters	Ranges and values
Total flow rate of solution (cm^3/min)	2.0
Flow rate of oxygen (cm^3/min)	1600
Substrate temperature (°C)	900, 1050, 1200
Total-metal concentration (M)	2×10^{-3}, 4×10^{-3}, 6×10^{-3}
Atomizer-to-substrate distance (mm)	51
Deposition time (min)	20

The microstructures of the deposited films and composition of the coatings were characterized with SEM (Hitachi 3000N) and EDS (Oxford Instruments). The phases of the sintered materials were determined with X-ray diffraction (XRD, D8 Discover, Bruker AXS, Germany) with Cu $K_{\alpha1}$ radiation at λ=1.5406 Å.

The anode material was prepared by mixing the raw materials (graphite, NiO and YSZ) in different proportions, compacted uniaxially, sintered in air and finally reduced in H_2/Ar atmosphere. The graphite powder ratios and sintering temperatures used for the fabrication is shown in the Table 2. The NiO/YSZ ratio was 57.5/42.5 and the compaction pressure was 150 MPa. The sintered samples were reduced at 1000 °C. The different powder ratios, compaction pressure, the sintering temperatures and the reduction temperature were decided based on the literature. The different powders used were mixed together using ball milling technique. The die used for powder compaction was half-inch steel die. The measured output variables were porosity and the electrical conductivity.

Table 2. Composition and process parameters used for the experimental design

Independent variable	**Treatment level**		
	0 Low	1 Medium	2 High
Graphite volume fraction (vol %)	30	35	40
Sintering temp (°C)	1200	1250	1350

Results

Phase Characterization of the Cerate Thin Films

Fig. 1 shows the XRD spectra of the coatings of experiments SCY-1, 3, 5, 7, 9, 11, 13, 15, and 17 with the characteristic peaks of $SrCe_{0.85}Y_{0.15}O_{2.925}$ (Pattern 01-083-1157) and CeO_2 (Pattern 01-081-0792) at the bottom for reference. The diffraction spectra of the three coatings of the experiments SCY-1, 3, and 5 show a tendency of increased intensity of the perovskite characteristic peaks at 2θ = 29.728º with the increased substrate temperature at the lowest total-metal concentration of 2.0×10^{-3} M. At the total-metal concentration of level 1 and 2 (4.0×10^{-3}M and 6.0×10^{-3} M), the highest intensities of the perovskite peaks were found from the coatings deposited at the intermediate substrate temperature, i.e., 1050ºC. All the coatings show (131) and (122) peaks at about 2θ = 37.78º and 2θ = 39.47º (not labeled in the graph). Comparing all the spectra, it seems that the coating of SCY-15 deposited at 6.0×10^{-3} M and 1050ºC represent the best result of the perovskite phases. However, the characteristic peaks of fluorite CeO_2 phases can be

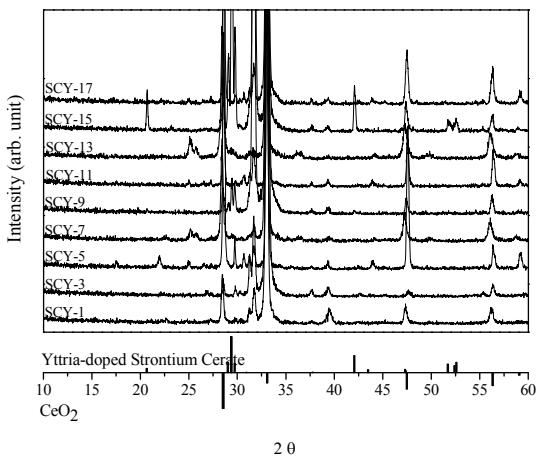

Figure 1 XRD spectra of yttria-doped strontium cerate coatings.

noticed in all the coatings. It shows the possibility of CeO_2 phase precipitation in the coatings caused by nonstoichiometry between Sr and Ce. Examination of the elemental ratios between Sr and Ce for the coatings SCY-2, 4 and 6 with EDS demonstrated the deficiencies of Sr. The atomic ratios of Sr to Ce were about 0.8. This implies that to achieve the stoichiometry of the $SrCe_{0.85}Y_{0.15}O_{2.925,}$ more starting chemical of Sr is needed in the solution. High temperature sintering of $BaCe_{0.85}Y_{0.15}O_{3-\delta}$ had experienced Ba evaporation and CeO_2 precipitation [28].

Microstructure of the Cerate Thin Films

The surface morphologies of all the coatings were examined with SEM. These micrographs shown in Figure 2 depict that the intermediate substrate temperature of 1050ºC produced smoothest surfaces. The grain sizes are not proportional to the substrate temperature. Both 900 and 1200ºC substrate temperatures produced large grains, rough surfaces consequently, while the substrate temperature of 1050ºC produced smallest grains. It is noteworthy to discern that the combination of substrate temperature of 1050 ºC and the total-metal concentration of 4.0×10^{-3}M generated the best quality coating in terms of morphology uniformity and surface smoothness. Cracks were apparently perceived in all the coatings, which demonstrate that there is a large difference in the coefficients of thermal expansion between the coating and substrate. The coefficient of thermal expansion for the coatings needs to be determined by further experiments.

Porosity and Conductivity of the Anodes

The graphite was used to obtain the desired porosity. The porosity calculations were based on the weigh and size measurements of the sample followed by the actual and the theoretical volume calculations. The four-point probe method was used for the conductivity measurements. The porosity and the conductivity results are shown in the Table 3. For each sample, three replicates were used and the results shown were averaged to one value.
The results show that the sintering temperature was the major variable that controls the porosity and the conductivity of the cell. Graphite content also had a role in controlling the porosity but it mostly depends on the sintering temperature values. Both graphite and the sintering temperature almost had a linear effect on the porosity and the conductivity values (Fig 3). For the samples sintered at 1200°C, with 30 vol. % of graphite content, the porosity value was 56.06 and for 40 vol. % of graphite content, the porosity was 58.96. But the porosity and the conductivity values had an inverse effect for the given sintering temperature. The reason was, the graphite oxidizes at lower temperature (~ 1000°C) compared to the maximum temperatures used and it directly leads to the formation of pores. So the difference in the graphite vol. % had some effect on the pore volume at the lower temperature sintering (i.e., at 1200°C). But at 1350 °C, the difference in the graphite volume did not make much of a difference in the porosity volume. This was because of the fact that at higher sintering temperature, the particle growth and particle fusion started taking place and it leads to reduced porosity and improved inter-particle connectivity. This replicates on the conductivity of the cell. At lower sintering temperatures, the inter particle connectivity was poor and that leads to poor electrical charge carrying paths. Whereas, at higher sintering temperature, the conductivity increases drastically due to the fact that it has more electron conducting path. Thus, the conductivity and the porosity values obtained for the samples sintered at 1350 °C were more suitable for the SOFC application.

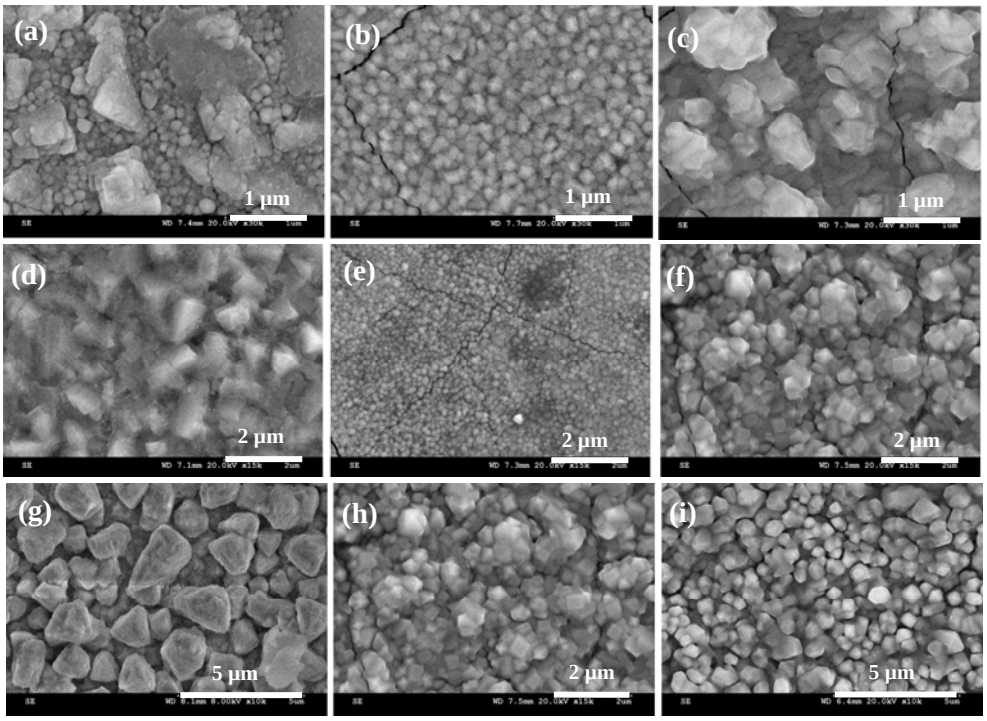

Figure 2. Micrographs of the $SrCe_{0.85}Y_{0.15}O_{2.925}$ coatings deposited at different conditions. The total-metal concentrations for the coatings shown in the first, second and the third rows are 2.0×10^{-3}, 4.0×10^{-3} and 6.0×10^{-3} M, respectively. Substrate temperatures for the coatings shown in the first, second and the third columns are 900, 1050 and 1200ºC, respectively.

Table 3. Porosity and Conductivity results for different processing conditions

Sintering Temp / °C	Graphite Vol %	Porosity Vol %	Conductivity Ω^{-1} cm^{-1}
1200	30	56.06	69.59
	35	56.85	69.27
	40	58.96	58.53
1250	30	52.53	147.99
	35	55.41	94.39
	40	57.66	81.70
1350	30	41.35	744.87
	35	37.08	686.19
	40	41.01	733.46

Conclusions

Yttria-doped strontium cerate coatings were developed with FA-CVD technique. XRD characterization revealed combined phase of the perovskite and fluorite in the coatings. EDS study found strontium depletion in the coatings as compared with the composition in the solution. The studies of the micrographs of the surface of the coatings also uncovered that both intermediate substrate temperature and total-metal concentration produced coating with smoothest surface.

The design matrix was developed and successfully used to develop the anode material for SOFC application. The results showed that the processing variables and their levels had a strong impact on the output variables. The porosity values had a controlling effect on the conductivity values. It indicates that the electrode performance can be optimized by controlling the porosity in order to achieve desired conductivity. The current work sparkle the idea of changing the ratios of NiO in the mixture to study the changes in conductivity values and also in the microstructure of the electrode.

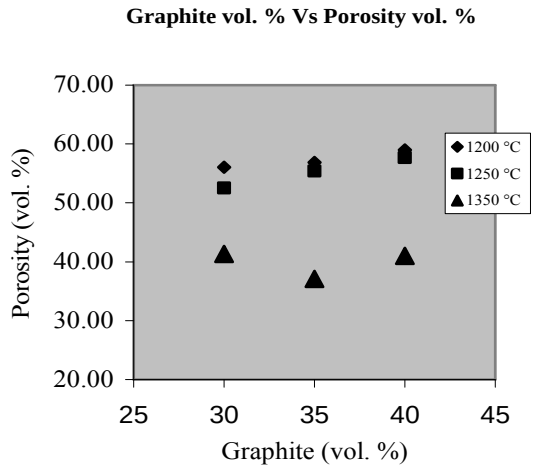

(a)

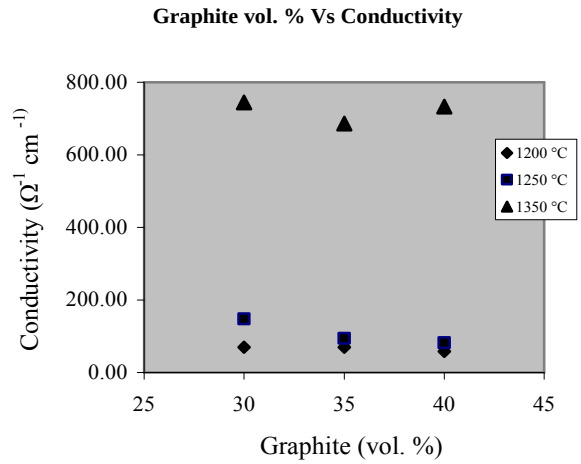

(b)

Figure 3. (a) Comparison of porosity values for different sintering temperatures (b) Comparison of Conductivity values for different sintering temperatures

References

1. H. Iwahara, H. Uchida and S. Tanaka, *Solid State Ionics,* **9-10**(1983) 1021-1025.
2. W. G. Coors, *J. Power Sources*, **118**(2003) 150-156.
3. S. Yamaguchi, H. Yugami, and S. Ikeda, J. Alloys and Compounds, **330-332**(2002) 911-915.
4. U. Balachandran, T. H Lee, S . Wang and S. E. Dorris, *Inter. J. Hydrogen Energy* **29** (2004) 291.
5. U. Balachandran, B. Mar, P . S . Maiya, R. L. Mieville, J. T. Dusek, J. Picciole, J. Guan, S. E. Dorris and M. LIU, *Solid State Ionics* **108** (1998) 363.
6. R. V. Siriwardane, J . A. Poster, E. P . Fisher, T. H. Lee, S . E. Dorris and U. Balachandran, *App. Surf. Sci.* **167** (2000) 34.
7. H. Iwahara, Y. Asakura, K. Katahira; M. Tanaka, *Solid State Ionics,* **168** (2004), 299-310.
8. F. Chen, O. T. Sørensen, G. Meng[a] and D. Peng**,** *Solid State Ionics,* **100**(1997) 63-72.
9. S. D. Flint, M. Hartmanová, J. S. Jones and R. C. T. Slade**,** *Solid State Ionics,* **86-88**(1996) 679-683.
10. R. Peng, Y. Wu, L. Yang and Z. Mao, *Solid State Ionics,* **177**(2006) 389-393.
11. W. Grover Coors and Dennis W. Readey, *J. Am. Ceram. Soc., 85* (2002) 2637-40.
12. V. Agarwal, M. Liu, *J. Mater Sci*, **32** (1997) 619-625.
13. S. Higgins, N. Sammes and A. Smirnova, Proceedings of the 26th Risø International Symposium on Materials Science: *Solid State Electrochemistry,* Editors: S. Linderoth, A. Smith, N. Bonanos, A. Hagen, L. Mikkelsen, K. Kammer,D. Lybye, P.V. Hendriksen, F.W. Poulsen, M. Mogensen, W.G. Wang Risø National Laboratory, Roskilde, Denmark 2005
14. G. Meng, P. Wang, Y.Gu and D. Peng, *Solid State Ionics,* **136-137**(2000)209-213.
15. T.H. Lee, S.E. Dorris and U. Balachandran, *Solid State Ionics,* **176**(2005) 1479-1484.
16. T. He, C. L. Jia, P. Ehrhart and P. Meuffels, *Solid State Ionics,* **89**(1996) 9-12.
17. Z. Xu, J. Sankar and S. Yarmolenko, *Surf. Coat. Technol.* **177–178** (2004) 52-59.
18. Z. Xu, S. Yarmolenko, J. Sankar, *NATO Science Series, II: Mathematics, Physics and Chemistry* (2005), 202 (Fuel Cell Technologies), 49-57.
19. W. B. Carter, G.W. Book, T.A. Polley, D.W. Stollberg, J,M. Hampikian, *Thin Solid Films* (1999), **347**(1999), 25-30.
20. B. Naoufal, *Surf. Coat. Technol*, **200**(2006) 4097-4103.
21. S.C. Singhal, *Solid State Ionics,* **152-153**(2002), 405-410.
22. M.J. Jorgensen, P. Holtappels, and C.C. Appel,. *Journal of Applied Electrochemistry,* **30**(2000), 411-418.
23. A.C Muller, D. Herbstritt, and E.I. Tiffee, *Solid State Ionics.* **152-153**(2002): 537-542.
24. J.-H Lee, H. Moon, H.-W. Lee, J. Kim, J-D. Kim, and K-H. Yoon, *Solid State Ionics,* **148**(2002), 15-26.

25. F. Takehisa, K. Murata, S. Ohara, H. Abe, M. Naito, and K. Nogi, *Journal of Power Sources*, **125**(2004), 17-21.
26. R. M. C. Clemmer, S.F. Corbin, *Solid State Ionics*, **166**(2004), 251-259
27. J. H. Lee, J.W. Heo, D.S. Lee, J. Kim, G.H. Kim, H.W. Lee, H.S. Song, and J.M. Moon, *Solid State Ionics*, **158**(2003), 225-232.
28. J. Wu, L.P. Li, W.T.P. Espinosa, and S.M. Haile, *J. Mater. Res.,* **19**(2004) 2366-2376

Publications and Presentations

1. Zhigang Xu, Gregory Young, Gukan Rajaram, Jag Sankar, "Proton Conductive Strontium Cerate Thin Films Processed Using Flame-Assisted Chemical Vapor Deposition", IMECE2006-15022, Proceedings of IMECE2006
   2006 ASME International Mechanical Engineering Congress and Exposition
   November 5-10, 2006, Chicago, Illinois, USA
2. G. Young, Z. Xu, G. Ramjram, J. Sankar, "Deposition of Yttrium Doped Strontium Cerate Thin Films by Combustion Chemical Vapor Deposition", presented in the 30th International Conference and Exposition on Advanced Ceramics and Composites, Cocoa Beach, FL, January 22-27, 2006
3. Zhigang Xu, Gukan Rajaram, Jag Sankar and Devdas Pai, "Electrophoretic deposition of YSZ electrolyte coatings for solid oxide fuel cells", *Surface and Coatings Technology,* **201**(2006), 4484-4488.
4. Zhigang Xu, Jag, Sankar, " Preparation and Characterization of Nano-crystallite Electrolyte for SOFCs", presented in the 2006 MRS Fall Meetings, November 27 - December 1, 2006
   Boston, MA.

B. Powder Processing of Nanostructured Alloys Produced by Machining

S. Chandrasekar, K. P. Trumble, and W. D. Compton
College of Engineering
Purdue University, IE, GRIS
315 North Grant Street
West Lafayette, IN 47907-2023
(765) 494-3623; fax: (765) 494-5448; e-mail: chandy@purdue.edu

DOE Technology Development Manager: Jerry L. Gibbs
(202) 586-1182; fax: (202) 586-1600; e-mail: Jerry.gibbs@ee.doe.gov
ORNL Technical Advisor: D. Ray Johnson
(865) 576-6832; fax: (865) 574-6098; e-mail: johnsondr@ornl.gov

---

Contractor: Oak Ridge National Laboratory, Oak Ridge, Tennessee
Prime DOE Contract No.: DE-AC05-00OR22725
Subcontractor: Purdue University, West Lafayette, Indiana

Objective

- Develop manufacturing technologies for producing bulk nanostructured alloys with enhanced mechanical properties for transportation applications.

Approach

- Create nanostructured chips and particulate by machining alloys of aluminum, titanium, and iron under controlled machining conditions.
- Develop machining methods for direct production of bulk forms (e.g, sheet, bar) with nano-scale microstructure.
- Characterize microstructure, structure and mechanical properties of nanostructured chip particulate and bulk forms.
- Develop low-temperature consolidation routes for converting the chip particulate into monolithic and composite materials without significant coarsening of the nanocrystalline microstructures.
- Characterize microstructure, mechanical properties, and performance of the bulk forms after the consolidation.

Accomplishments

- Produced nanostructured chips of a variety of alloys and metals—including Al6061-T6, commercially pure titanium, stainless steel, steels, and Inconel—by machining. The nanostructured chips are up to three times as strong as the bulk material. The grain size in most cases is ~ 100 nm.
- Developed a new process, large-strain extrusion-machining (LSEM), to directly produce bulk forms (e.g. sheet, bar) with ultra-fine grained (UFG) microstructure and enhanced mechanical properties.
- Developed a new Modulation –Assisted Machining (MAM) method for making nanostructured particulate of controlled size (30-500 micrometers) and shape (e.g., equi-axed, platelet, needle) directly by chip formation.
- Developed innovative, low-temperature processing routes for producing bulk nanostructured alloys from chip particulate using polymeric binders. These polymer-bonded alloys show promising enhancements in hardness and wear properties.

- Developed low-temperature consolidation routes that limit coarsening in Al6061-T6. Achieved a high degree of densification and interparticle bonding in room temperature powder extrusion of nanostructured Al6061-T6.
- Developed high temperature, high-strength nanostructured alloys, for example, Inconel 718, Waspaloy, with extraordinary thermal stability. The process involved a combination of nanostructure refinement by machining and creation of ultra-fine fine-scale precipitates in the nanostructured matrix by thermal ageing after the machining.

Future Direction

- Continue development of the extrusion machining process to make sheets of nanostructured Al and Mg alloys for potential automotive applications.
- Continue development of low-temperature consolidation routes to produce bulk monolithic and/or composite alloys with nanocrystalline microstructure.
- Characterize microstructure and properties of the bulk forms to demonstrate retention of nanostructures and enhanced mechanical properties.
- Determine tensile and wear properties of bulk forms to demonstrate integrity of the consolidated alloy samples and guide application.
- Initiate intensive efforts to scale-up these processes for prototype applications in the transportation and energy sectors.

Introduction

This program builds on the recent discovery of a low-cost means of producing nanostructured materials in essentially any alloy via machining. A notable achievement has been the development of a large-strain extrusion machining process (LSEM) for direct production of bulk forms, such as sheet and bar, with an ultra-fine grained (UFG) microstructure. These bulk forms, with or without additional thermo-mechanical processing, can serve as pre-cursor materials for component applications. Particulate having controlled size and shape can be produced directly by a unique modulation-assisted machining (MAM) process. The chips and particulates may be used as continuous or discontinuous reinforcements in metal or polymer matrices to create advanced composites; or consolidated into monolithic bulk forms using low-temperature shear-based consolidation processes with a binding agent (e.g., polymer).

Progress from FY 2006 in four main areas is highlighted in this report: (1) LSEM for direct production of sheet and bar with an UFG microstructure (2) particulate production by MAM (3) production of bulk alloys by low-temperature pressing of particulate using a very thin layer of polymer as binder and (4) continued development of high-strength nanostructured alloys with extraordinary thermal stability.

Approach

Two routes were pursued for the creation of bulk forms with nanocrystalline and/or UFG microstructures. The first involved a modified version of conventional chip-formation machining process called LSEM. In LSEM, the chip is produced with a controlled geometry by constraining its shape and size at the point of its formation. This method combines inherent advantages afforded by large strain deformation in chip formation by machining, with simultaneous dimensional control of extrusion in a single step of deformation. The resulting sheet offer enormous promise for ground transportation applications. Second, by incorporating controlled superimposed modulation with a conventional machining process, nanostructured chips could be directly created in micron-sized particulate form. The particulate have controlled size and shape, a tight particle size-distribution, and macroscopic dimensions resembling those of powders used in P/M processes. This process called MAM has provided a cost-effective solution to the problem of making nanostructured particulate suitable for consolidation. The resulting particulate

has served as pre-cursor material for shear-based consolidation processes such as powder extrusion and pressing with a polymer binder, and reinforcements for metal and polymer matrices in composites processing.

Bulk Al 6061T6 alloys have been have been produced using a low-temperature consolidation pressing process wherein a very thin layer of polymer is used as a binder. The polymer bonding is a new approach in which a thermosetting polymer resin is used, together with high-pressure compression molding in a steel die to yield a structure consisting of low-volume fractions of polymer bonding the nanostructured metal particles. The goal of this approach is to bond the machining chip particulate with as fine a polymer bond layer as possible. Previous work has established that premixing the particulate and liquid thermoset and pressing in a steel die is preferred to pressing the powder alone followed by infiltration. Although the metal volume fraction that can be achieved is comparable, a significant fraction of the residual pores in the preform in the infiltration route are closed or otherwise inaccessible to the infiltrant leading to more residual porosity. Although less residual porosity occurs pressing a mixture of the liquid epoxy and alloy particulate, there still is residual porosity, mostly in large epoxy regions larger alloy particles exhibit did not pack well. In an attempt to overcome the packing limitation, experiments were conducted using the equi-axed particles now being produced by the modulation-assisted machining method.

Another avenue of investigation has explored creation of high-strength, high-temperature nanostructured materials such as titanium and nickel-based alloys, with exceptional thermal stability of the microstructure. We have demonstrated a means of extending the temperature range for structural applications of nanomaterials through the introduction of a dispersion of second-phase precipitates, whose thermal stability determines the temperature at which the strength deteriorates. Precipitate-stabilized nanostructured materials synthesized from solution-treated Inconel 718 were found to be extremely stable even after prolonged heat treatment for 500 h at temperatures as high as one-half of the melting point. The enhanced thermal stability of the material's strength results from retention of both the fine microstructure and the fine precipitate phase coexisting at the high temperatures. This novel microstructure was created by first subjecting solution-treated Inconel 718 to severe plastic deformation (SPD) by machining, followed by thermal aging of the chip to create fine-scale precipitates. The principles developed herein appear to be equally well-applicable to a variety of precipitation-treatable materials systems such as P 13 stainless steels and Waspaloy. This class of materials is designated - Highly-Stable Nanostructured Materials (HSN).

Results

Bulk Nanostructured Materials by LSEM

Figure 1 illustrates a plane strain LSEM process wherein material (chip) of controlled thickness and an UFG microstructure is produced by machining and extrusion imposed in a single step using a specially designed tool. In this configuration, an LSEM tool moves into a disk-shaped workpiece rotating at a constant peripheral speed, V. The tool consists of two components – a bottom section with a sharp cutting edge inclined at a rake angle (α) (Figure 1); and a wedge-shaped top section that acts as a constraining edge. Both sections are made of a hard material. The machined material is simultaneously forced through an 'extrusion' die formed by the bottom rake face and the top constraining edge, thereby, effecting dimension and shape control. It is important to note that LSEM, unlike conventional machining, involves constrained chip formation where the deformed chip thickness is controlled *a priori*. LSEM can be considered a generalization of ECAP with the exemption that the thickness of the material at the tool exit can be larger or smaller than that at the inlet. This exemption ensures the imposition of levels of strain that are

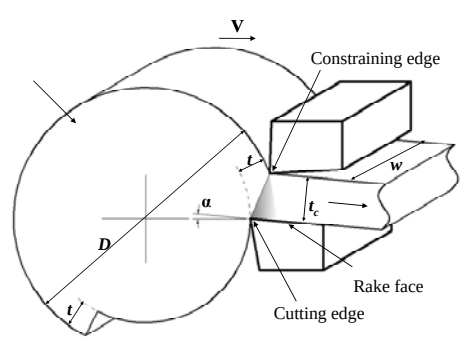

Figure 1. Schematic of LSEM process

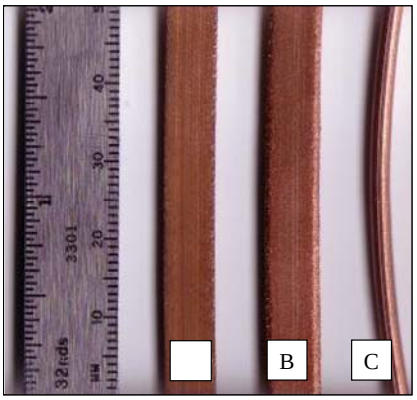

Figure 2. Bulk forms made by LSEM

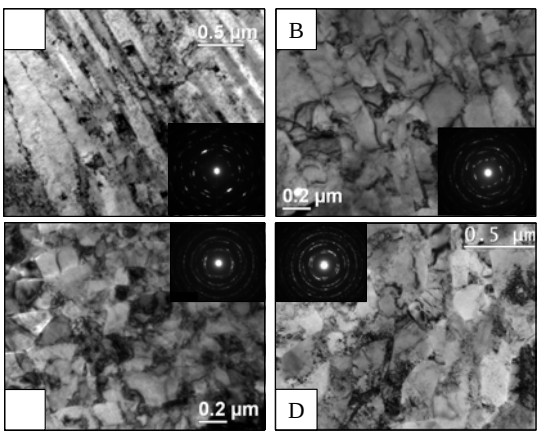

Figure 3. TEM images and SAD patterns (insets) of copper subjected to different levels of strain in LSEM. A: $\gamma = 2.2$ (elongated), B: $\gamma = 4.3$ (mix of elongated and equi-axed), C: $\gamma = 7.4$ (equi-axed) and D: $\gamma = 11$ (equi-axed).

sufficiently high to induce formation of an UFG microstructure in a single-step deformation process.

Figures 2A) – 2C) show examples of bulk sheet and bar samples of copper created by the LSEM process. Figure 3 shows TEM images of microstructure of bulk copper samples with different levels of strain made by the LSEM, and the corresponding selected area diffraction (SAD) patterns (inset). The sequence of images A, B, C and D, illustrates the progressive refinement of microstructure and formation of UFG structures with increasing strain; these are consistent with previously observed dependence of microstructure on strain**.** An elongated UFG microstructure is seen at a relatively small strain value (Figure 3A, $\gamma = 2.2$). With increasing strain, an increased level of grain sub-division and formation of equi-axed grains are observed (Figure 3B, γ=4.3). Larger strains lead to essentially equi-axed UFG structures with grain sizes of ~ 250 nm (Figures 3C and 3D). In consonance with this progressive refinement of the microstructure, the diffraction pattern can also be seen to progressively evolve from what is practically a smeared single-crystal pattern (Figure 3A) to one that is indicative of larger misorientation angles (Figures 3C and 3D). The TEM analysis also showed the microstructure to be reasonably uniform over much of the chip thickness, with the exception of a small region near the edges, consistent with the distribution of the strain.

Table 1 gives hardness (including standard deviation) of the bulk copper created with the different levels of strain by the LSEM. In all cases, the hardness values are substantially greater than that of the bulk copper. The highest hardness of ~ 160 kg/mm^2 is essentially indistinguishable from that of UFG copper microstructures created by machining or ECAE. The standard deviations on the hardness values are small, less than 4% of the mean, indicating relative uniformity of the material strength across most of the sample thickness.

Recent tests have shown that this LSEM can be applied to a variety of metals (e.g., copper, titanium, Al 6061-T6, tantalum) resulting in bulk sheet samples with UFG microstructures. Furthermore, by combining a scaled-up version of the LSEM tool used here, with an appropriate machine, large scale production of nanostructured sheet and bar material appears very feasible. These will be taken up in the coming year. The process offers exciting opportunities for creating bulk sheets of Al, Mg and Ti alloys for ground transportation applications.

Nanostructured Particulate by Modulation-Assisted Machining (MAM)

The machining process imposes large shear strains on the order of 1-10 in the chip resulting in significant microstructure refinement. While the chip has an UFG microstructure, the macroscopic shape and size of the chip are generally uncontrolled in conventional machining (note LSEM is an exception to this as shown earlier). Recently, a new machining method with superimposed low-frequency vibration (0-500Hz), referred to as modulation assisted machining (MAM), has demonstrated the ability to control the chip formation process. This control of chip formation in

MAM has been exploited to develop a novel process for producing particulate metals with controlled sizes and shapes, and having a nanocrystalline or UFG microstructure. The basis of this process is the observation that the chip dimensions and aspect-ratios are established geometrically by the discrete cutting events, which in turn are determined by machining and modulation parameters. Control of machining and modulation parameters provides the capability to produce particulate of different shapes and sizes in a deterministic way. The effectiveness of this process for making particulate with sizes in the range of 20 µm to 2,000 µm and with shapes as diverse as platelet, needle and equi-axed, has been demonstrated for a wide variety of materials (e.g. titanium, stainless steel, tantalum, Al alloys). Both the particle shape and the particle size distribution can be tightly controlled by adjusting the modulation parameters.

Figure 4 shows nanostructured Al6061-T6 alloy particulate (chips) in the form of needle and platelet produced by changing the modulation frequency in

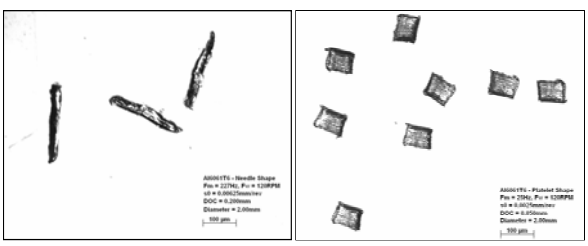

Figure 4. Al6061-T6 alloy particulate (chips) in the form of needle and platelet.

identical machining conditions. The needle and platelet particles were produced from a d=6mm diameter bar rotating at frequency f_w= 360rpm. Additional MAM tests have shown production of equi-axed particles and filaments during similar turning operations. The needle and platelet particles demonstrate the shape control and related effects of MAM on the particle surface area. For comparison, the needle particles in Figure 4 were produced with MAM conditions which produce a particle volume that is identical to the volume of the platelet particle. The needle and platelet particles develop high surface-areas compared to spherical shaped particles of the same volume. The sphericity (ratio of surface area of equivalent volume sphere to surface area of the particle) is ~0.77 for the needle particulate and ~0.65 for the platelet particulate. This comparison demonstrates the extraordinary control of particle size and shape control by MAM and the ability to create very high-aspect ratio, high surface-area particulates. Typical particle sizes are in the range of 20 µm to 2,000 µm. Preliminary TEM analysis has shown the particles to have UFG microstructures. The Vickers hardness of the particulate was found to be substantially higher than that of the bulk material consistent with the UFG microstructure.

The MAM process offers considerable scope for low-cost production of nanostructured particulate of micron-sized dimensions, extremely suitable for powder consolidation and spraying processes.

Bulk Al Alloys using a Polymer Bonding Agent

Die press bonding has been used to produce bulk Al-6061-T6 samples from nanostructured 6061 T6 particulate using a small amount (<10%) of epoxy as binder. Figure 5A) shows the results of pressing the nominal 50-150 µm Al alloy particulate, produced by MAM, with Buehler Epoxide resin at 800 MPa pressure in a steel die, followed by curing at 100°C for 1 hour. A thin "glue line" of epoxy is present at all the boundaries but the high strength of the particles seems to preclude any significant component of their densification due to particle plasticity. On the other hand, the fraction of epoxy + porosity is similar to composites produced by the same process, but using higher aspect ratio particulate produced by milling machining chips. A potential property advantage of the equiaxed particle composites may be less anisotropy compared to those made with anisometric particles; this aspect is yet to be quantified.

The effect of removing the native surface oxide from the particles before bonding was also investigated. The same procedure as above was followed except that the particles were stripped in a 10% NaOH solution for 10 minutes under ultrasonication and then rinsed in distilled water and dried in air. The resulting composite is shown in Fig. 5B). Overall, more uniform packing was observed, but the overall packing density (and porosity) levels were comparable to the composites made without pre-cleaning the particles in this way. An intriguing observation is that the interparticle bond ("glue line") appears to be thicker with the pre-cleaned particles.

Epoxy and porosity volumes as low as 6% have been achieved so far, and preliminary nanohardness measurements show little or no loss of hardening

imparted in producing the chips, consistent with separate measurements of coarsening-softening kinetics in this alloy.

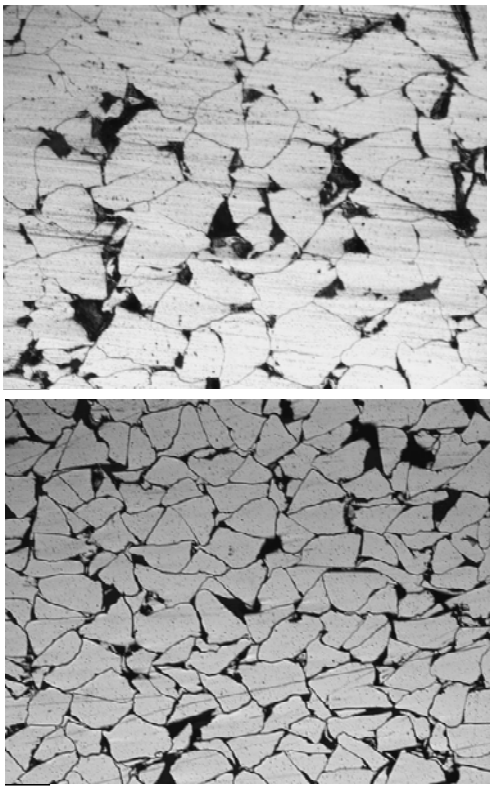

Figure 5. Polymer-bonded Al alloy systems.

Pressing experiments soon to be carried out in an autoclave are likely to reduce the porosity to minimal levels. Work in the next year will proceed to tensile testing in order to evaluate the degree of bonding. Although high strength and ductility are not predicted, the high hardness should impart improved wear resistance together with the shaping advantages of powder processing. Applications for lightweight, wear-resistant components are envisioned.

Highly Stable Nanostructured Materials (HSN)

The utility of the extraordinary strengths of nanostructured materials is typically limited by their low thermal stability. We have demonstrated a means of extending the temperature range for structural applications of nanomaterials through the introduction of a dispersion of second phase precipitates, whose thermal stability determines the temperature at which the strength deteriorates. This demonstration has been realized in a model high-temperature alloy system-Inconel 718; the resulting material is called HSN Inconel.

Figure 6 illustrates the nanostructured material composed of grains typically 100 nm in size produced from solution-treated microcrystalline Inconel 718 (grain size ~50 μm in the initial state) due to plastic shear strains of ~6 imposed using a -20° rake angle tool. The microstructure is composed primarily of equi-axed grains, along with some elongated structures. The diffraction pattern inset in Figure 6 indicates the presence of large angle grain boundaries in this nanostructured material. The Vickers microhardness value of this microstructure was 550 kg/mm^2 (~5.4 GPa), nearly twice that of the undeformed bulk, microcrystalline solution-treated material (300 kg/mm^2). Figure 7 illustrates the much improved ultimate tensile strength of this nanostructured material compared to the bulk microcrystalline material. Nanostructured Inconel is seen to possess a peak tensile strength of ~1.3 GPa, more than twice the yield strength of the bulk material (~600MPa). As expected its ductility is limited, but the tensile fracture surface showed vein-like features typical of micro-scale plasticity during crack propagation and fracture. Interestingly, the micrometer-scale features on this fracture surface are not characteristic of fracture surfaces of conventional nanocrystalline materials that usually show sub-micrometer scale dimpled features.

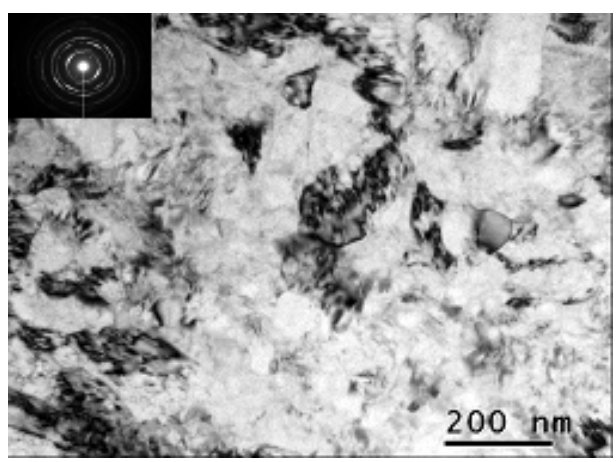

Figure 6. TEM micrograph of nanostructured Inconel 718 (shear strain ~6). Grain size ~100 nm.

When this high-strength nanostructured material was heat treated at 600°C (~ one-half the melting point), a rapid strengthening was found that can be associated with the formation of second-phase precipitates. A peak hardness value of 630 kg/mm^2 (~ 6.2 GPa) is reached after about 6 hours of annealing. In contrast, precipitation of the intermetallic γ" and γ' phases to achieve peak precipitation strengthening in the conventional microcrystalline structure usually involves a lengthier heat treatment process due to the characteristically sluggish precipitation kinetics. Additional evidence for the extraordinary strengthening and thermal stability comes from measurements of stress-strain curve of HSN Inconel after 6 hours of heat treatment at 700°C. The material has a failure stress of 1.4 GPa as illustrated

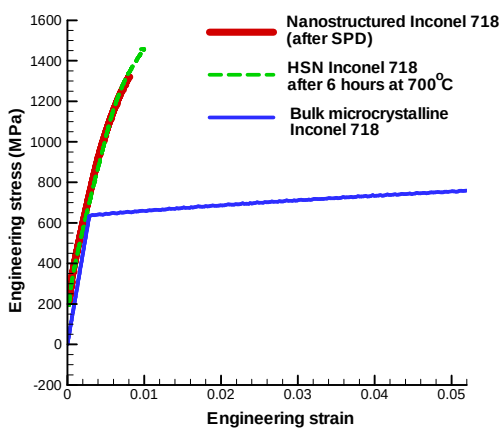

Figure 7. Stress-strain curves for Inconel-718

in Figure 7. The measurements also indicate an expected, albeit, modest improvement in the ductility of the HSN Inconel. Much more noteworthy, however, is the observation that this tensile strength following the heat treatment at 700°C is very comparable to, if not markedly greater than, that of the HSN Inconel prior to the heat treatment. This reinforces our observation of the extraordinary stability of the tensile strength of HSN Inconel.

In the nanostructured state, the large diffusion coefficient and the large number of nucleation sites resulting from SPD of the solution-treated material allow a rapid precipitation of a fine dispersion. Furthermore, the Ni-Nb intermetallic γ" phase, that can significantly contribute to material strength, is characterized by a very fine and dense dispersion of coherent, disc shaped precipitates, that are distributed in the matrix. In the nanostructured matrix, this phase is more likely to precipitate on the grain boundaries. This preferential precipitation can aid efficient pinning of the grain boundaries and enhance thermal stability. Thermal stability is also aided by the stability of the fine precipitate phase, which has been reported to have large activation energy for coarsening of ~1000 kJ/mol. This ensures the stability of the fine precipitate phase and consequent retention of strength in the nanostructured Inconel even after prolonged annealing at 600°C, resulting in its designation as a Highly-Stable Nanostructured (HSN) material.

The materials design principle propounded above can be generalized to other precipitation-treatable materials and offer a new line of development for this important class of structural materials. Other material systems that form stable, fine precipitate phases, for example, special Al alloys, P-series stainless steels, Waspaloy, can be expected to behave in a similar manner in the nanostructured state. Exceptional thermal stability and retention of the material strength are ensured by the stable, fine precipitate phase and the fine microstructure coexisting at high temperatures for significant lengths of time, resulting in a class of HSN materials with enormous potential for high-strength and/or high-temperature applications. These avenues will be investigated in detail in the coming year.

Publications

P. Iglesias, M. D. Bermudez, F. J. Carrion, S. Chandrasekar, and W.D. Compton, A study of the wear behavior of polymer-matrix composite containing discontinuous nanocrystalline alloy reinforcements, *Tribology International,* **40**, 479 (2006).

M. R. Shankar, B. C. Rao, S. Lee, S. Chandrasekar, A. H. King, and W. D. Compton, Severe plastic deformation of titanium at near ambient temperature, *Acta Materiala*, **54**, 3691 (2006).

Y. Uluca, B. C. Rao, M. Ravi Shankar, T. L. Brown, J. B. Mann, S. Chandrasekar, and W. D. Compton, Low-cost ultra-fine grained materials from aerospace machining chips, *SAE Journal of Aerospace*, (2006).

S. Lee, J. Hwang, M. Ravi Shankar, S. Chandrasekar and W. Dale Compton, Large strain

deformation field in machining, *Metallurgical and Materials Transactions* A, **37,** 1633 (2006).

W. Moscoso, M. R. Shankar, J. B. Mann, W. D. Compton, and S. Chandrasekar, Bulk nanostructured materials by large-strain extrusion machining, *Journal of Materials Research*, in press, to appear in January 2007.

S. Swaminathan, M. R. Shankar, B. C. Rao, W. D. Compton, S. Chandrasekar, A. H. King, and K. P. Trumble, Severe plastic deformation and nanostructured materials by machining, *Journal of Materials Science*, in press, to appear in January 2007.

Presentations

S. Chandrasekar et al., Severe Plastic Deformation and Nanostructured Materials by Machining, Sandia National Labs, Albuquerque, NM, June 2006.

S. Chandrasekar et al., Severe Plastic Deformation and Nanostructured Materials, Indian Inst. Sci., Bangalore, India, March 2006.

S. Chandrasekar, J. B. Mann and M. R. Shankar, Nanostructured Materials by Machining, Timken Company, Canton, OH, April 2006.

S. Chandrasekar, Manufacturing Innovations, State of Indiana Advancing Manufacturing Summit, Purdue University, West Lafayette, IN, May 2006.

J. B. Mann et al., Modulation-Assisted Machining for Particulate Production, Presentation before Army Research Labs panel, Purdue University, West Lafayette, IN, July 2006.

S. Chandrasekar, Severe Plastic Deformation and Nanostructured Materials, Naval Post Graduate School, Monterrey, CA, June 2006.

S. Chandrasekar et al., Advanced Manufacturing Technologies, State of India Senate Sub-Committee on Science and Technology, Indianapolis, IN, 2006.

J. B. Mann et al., Modulation-Assisted Machining for Particulate Production, US Army Benet Labs, Watervliet, NY, August 2006.

J. B. Mann et al., Modulation-Assisted Machining for Particulate Production, US Army Aberdeen Arsenal, MD, September 2006.

S. Chandrasekar et al., Measurements of Strain in Severe Plastic Deformation, UFG 2006, Kloitsersee, Germany, September 2006.

K. P. Trumble et al., Severe Plastic Deformation of Difficult-to-Deforma Materials at Ambinet Temperature, UFG 2006, Kloistersee, Germany, 2006.

K. P. Trumble et al., Consolidation of Nanostructured Chip Particulate by Powder Extrusion, TMS meeting, Orlando, FL, March 2006.

A. H. King et al., Large Strain Deformation Maps for Copper, TMS meeting, March 2006.

K. P. Trumble, Severe Plastic Deformation and Nanostructured Materials, Max Planck Institute, Stuttgart, Germany, September 2006.

Related Patents

Four patent applications pertaining to the machining technology for making bulk and particulate materials have been filed in May 2006. Two of these technologies have already been licensed.

C. Deformation Processes for the Next-Generation Ceramics

P. F. Becher
Oak Ridge National Laboratory
P.O. 2008, MS 6068
Oak Ridge, Tennessee
(865) 574-5157; fax: (865) 574-6098; e-mail: becherpf@ornl.gov

DOE Technology Development Manager: Jerry L. Gibbs
(202) 586-1182; fax: (202) 586-1600; e-mail: Jerry.gibbs@ee.doe.gov
ORNL Technical Advisor: D. Ray Johnson
(865) 576-6832; fax: (865) 574-6098; e-mail: johnsondr@ornl.gov

Contractor: Oak Ridge National Laboratory, Oak Ridge, Tennessee
Contract No.: DE-AC05-00OR22725

Objectives

- Promote plastic deformation of oxide ceramics by the application of electric fields for application to densification and shape forging of nanocrystalline ceramics.
- Characterize thermal and mechanical properties to assess influence of nanocrystalline microstructures for gaining improved performance for wear and other components.

Approach

- Collaborate with members of both the Pennsylvania State University and the Korea Institute of Machinery and Materials to develop fabrication technology to be able to fabricate dense monolithic nanocrystalline (i.e., grain sizes <100-nm) bodies.
- Characterize the potential for enhanced plasticity in ceramics resulting from sub-micron grain size on materials and from the application of applied electric fields with North Carolina State University researchers.
- Characterize the effects of nanometer scale microstructures on the mechanical and wear performance of ceramics.

Accomplishments

- In collaboration with Korea Institute of Machinery and Materials, it was demonstrated that dense nanocrystalline (grain size < 100 nm) could be produced through the use of a two-step sintering cycle and control of the composition.
- Demonstrated large reduction in tensile flow stress in a dense submicron grain sized zirconia ceramic containing 2.5 mol % yttria with the application of an applied D. C. electric field and showed that flow stress reduction increased to over 90% with increase in both permanent strain and strain rate.

Future Direction

- The fracture and wear properties of nanocrystalline ceramics will be examined to seek approaches for developing ceramics with substantially improved wear resistance.

Introduction

In addition to lower specific weight, ceramics have a number of attractive properties for application as components in various heavy-vehicle systems. However, many heavy-vehicle components require ceramics with complex shapes as well as function. Furthermore the demanding service conditions necessitate improved mechanical reliability together with fracture and/or wear resistance. Underlying the performance and use of ceramics is their tendency to fail in a brittle fashion except at temperatures generally well above 1000°C. Complex shape forming processes for ceramics are relegated to approaches based on powder processing as a result of the excessive temperatures for hot forming. On the other hand, metallic alloys can be hot worked at temperatures below 1000°C to not only form the desired shape but also to enhance their properties.

In ceramic systems, one needs to combine processing to tailor microstructures with novel concepts that offer the potential to enhance deformation. One such concept that has seen considerable interest is that of superplastic deformation of submicron-grain-sized ceramics above 1000°C.[1] Recent studies suggest that reducing the microstructure to achieve grain sizes <100 nm could lead to permanent/plastic deformation in ceramics at quite modest temperatures.[2,3] Recent studies have shown that the application of electric fields can reduce the yield stress or increase the creep rates of ceramic systems.[4] To date, this has not been exploited to determine the effects on the deformation of nanocrystalline oxides. The present study seeks to examine the influence of true nanocrystalline microstructures on the mechanical properties of ceramics, as well as approaches to economically fabricate nanocrystalline ceramics monoliths.

Hardness values generally obey the Petch-Hall behavior with the hardness rising as the grain size is reduced. However, results show that when the grain size is ~20 nm, the room temperature hardness then decreases as the grain size continues to be decreased.[1,2] This behavior has two important implications for applications of interest here. One is that some permanent deformation might be achieved in ceramics with grain sizes <30 nm, and this might offer improved reliability. More likely of interest is the fact that ceramics with grain sizes below 100 nm but above the softening point will be extremely hard, and that offers substantial advantages in overcoming wear problems in rolling stock. In addition, surface roughness of as-sintered ceramics decreases as the grain size decreases. In fact, the as-sintered surfaces of alumina substrates with grain sizes <500 nm exhibit a mirror-like finish without any surface preparation. This feature should be applicable to the fabrication of low-friction components.

Approach

This project involves two major thrusts. The first is a collaborative effort with researchers at the Korea Institute of Machinery and Materials on the sintering of nanocrystalline silicon nitride ceramics. In addition, collaborations continue with researchers at Pennsylvania State University, who are fabricating nanocrystalline oxides. These efforts are aimed at finding approaches to produce sizeable monolithic bodies for subsequent evaluation. The second thrust focuses on the mechanical and friction and wear behavior of nanocrystalline ceramics and the influence of external parameters [e.g., stressing rate, temperature, environment (e.g., air, vacuum)], and electric fields on the plastic deformation behavior.

Fabrication of Nanostructured Ceramics: Densification of nanocrystalline ceramics has typically involved the use of applied pressure to achieve dense sub-100-nm grain sized samples. In those few cases where pressureless sintering has been employed successfully, long hold times at the sintering temperatures were required to achieve densities ≥95% of theoretical, which allows undesired grain growth to occur. On the other hand, a two step sintering cycle offers a viable alternative approach.[5] This involves first heating to a temperature sufficient to achieve densities of ≥75% of theoretical followed by rapidly lowering the temperature to a level to obtain sufficient boundary diffusion. Using an extend hold time at the lower temperature results in the removal of pores trapped on boundaries while minimizing grain growth during the final stage of densification.

Deformation Behavior in Nanostructured Materials: Baseline deformation data will be established through studies of high purity, dense submicron grain size zirconia ceramics in order to evaluate the influence of nanocrystalline microstructures. These studies will then be extended to <100-nm grain sized ceramics. This will include

(a) nanostructured ceramics to explore for the softening effects observed in nanocrystalline metals by evaluating both the creep response over a range of temperatures and applied stresses, and the yield stress as a function of strain rate and temperature, and (b) the influence of external factors (e.g., electric fields) that have been shown to enhance deformation processes in ceramics with micrometer grain sizes. Modeling studies will be conducted to describe the deformation behavior and to address such phenomenon as space charge/solute segregation coupled with electric field effects. Additionally, the fracture, hardness, and wear response of nanocrystalline oxides will be evaluated to assess their application in wear components.

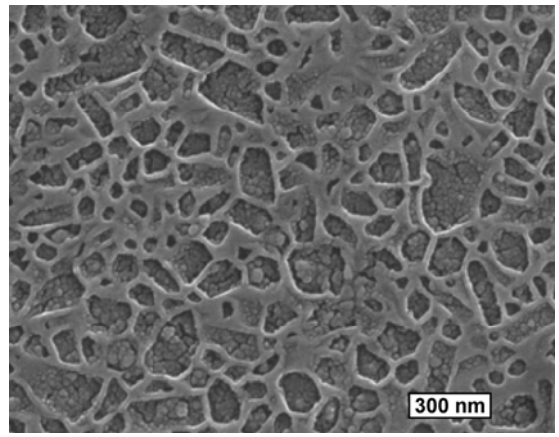

Figure 1. Dense nanocrystalline silicon nitride ceramic produced by two-step sintering.[6]

Results

Fabrication of nanocrystalline ceramics

The ability to fabricate dense bulk nanocrystalline ceramics represents a substantial barrier to their eventual application. In the present project, the fabrication of bulk nanocrystalline zirconia has been achieved using a combination of colloidal and granulation processing methods in conjunction with novel two-step sintering cycles working with researchers at Pennsylvania State University. In addition, bulk nanocrystalline silicon nitride ceramics have been fabricated using a similar approach to sintering working with researchers at the Korea Institute for Machinery and Materials.[6]

In both cases the sintering cycle involves heating to a peak temperature with a very abbreviated hold there followed by lowering the temperature by ≤ 200°C and holding there for 10 to 20 hours. The first step is designed to allow the ceramic body to reach a density in excess of 75% of the theoretical density. The second step allows further densification to occur by grain boundary diffusion. The key is to inhibit grain coarsening such that pores are retained at grain boundaries where they can pin boundaries, as well as be removed by diffusion. These collaborative studies make it possible to fabricate materials with a range of microstructures with grain sizes less than 100 nm where nanocrystalline effects are expected to have the greatest impact.

Electric field effects on plastic deformation

Collaborations with Prof. Hans Conrad and Dr. Kang Jung of North Carolina State University have assessed the reduction in flow stress in zirconia ceramics due to the application of an applied direct current (dc) field. Earlier studies of the enhancement of deformation by the application of electric fields to dense nanocrystalline zirconia ceramics subjected to ***compressive*** stresses suggested that the field effects were small. On the other hand, previous observations on oxides[4] exhibited substantial effects in oxides subjected to tensile loading. Our current studies seek to understand how superplastic behavior might be promoted at lower temperatures. These studies seek to determine how to enhance plasticity in that can also be employed to form nanocrystalline ceramics.

Re-evaluation of the electric field effects in the compression test results suggested that the magnitude of the electric field was much lower than expected due to the higher resistivity of the dense SiC push rods required to support the compression loads as compared to the resistivity of the lower density electric heating element grade of SiC used as pull rods in prior tensile tests. If this resulted in a much lower applied electric field in the compression tests, the reduction in the flow stress with the field applied versus not applied would be expected to be quite small. To test this, the current tensile tests at 1450°C included to electrode configurations: (1) the voltage applied directly through a circuit consisting of the upper and lower low resistivity SiC pull rods and the zirconia tensile sample and (2) the circuit path of a SiC sleeve with an air gap separating the sleeve from the ZrO2 sample that was connected to the lower low resistivity SiC pull rod. In

configuration 2, the maximum applied field was ~3.3 V/cm while in configuration 1 fields of up to ~46 V/cm were achieved. Using configuration 2 with an applied field of ~3.3 V/cm, the reduction in flow stress induced by the field was ≤10% of that obtained with configuration 1 where an applied field of 46 V/cm was achieved. Thus, one can attribute the minimal electric field effects on the flow stress reduction in the earlier compression tests to a substantial reduction in the actual applied electric field achieved.

With configuration 1, the tensile flow stress at 1450°C was reduced by upwards of 90% with increase in strain and strain rate with the application of an electric field of 46 V/cm. In order to accurately assess the impact of the electric field on the flow stress, one must account for the increase in specimen temperature due to Joule heating, which additional test results indicate minimal (~25°C) rise in temperature due to Joule heating.

The flow of vacancies needed for material transport and dislocation motion by applying stress and an electric field. The direction of the vacancy flux is a function of the sign of the applied stress (i.e., vacancies flow to regions under compression). This applies locally to vacancy flow in the deformation of a polycrystalline ceramic where vacancies move from grain boundaries under tension to those in compression while ions/atoms move in the reverse direction. The presence of space charge zones at grain boundaries also impacts the deformation.[7] Such zones are due to the migration of solute atoms (e.g., Y) that concentrate at the boundaries. As a result, the reduction in the flow stress ($\Delta\sigma_E$) is a function of the electric field (E):

$$\Delta\sigma_E = ZeEx_{SC}/\Omega \quad , \qquad (1)$$

where Z is the valence of the ion (Zr^{+4} in this case); e is the electronic charge (1.6 x 10^{-19} coulomb)s; Ω is the atomic volume of Zr; X_{SC} is the width of the space charge zone at the grain boundaries.

Based on the flow stress reduction (~6 MPa) at 1450°C due to an applied field of 46 V/cm, the space charge zone width is calculated to be 4 to 5 nm. The width of the space charge zone is also related to the Debye length of the material:

$$X_{SC} = \beta\lambda \qquad (2)$$

where it is a proportionality factor in the range of 2 to 5. The value of X_{SC} calculated from the current results are consistent with values obtained from studies of the ionic conductivity of zirconia ceramics.[8] However, theoretical treatments show that the Debye length (δ) in ionic solids increases as both the bulk solute content and temperature are decreased.[9,10] The increases in the Debye length due to decreases in temperature and solute content will be reflected as increases in the space charge width. One should then expect that the decrease in flow/yield stress brought about by application of an electric field would increase as the temperature decreases.

Conclusions

Until now, the ability to fabricate dense bulk nanocrystalline ceramics has been a major barrier to their evaluation for heavy vehicle applications. With the advances in the fabrication technology, one can now assess the wear resistance and electrochemical performance of nanocrystalline nitrides and oxides, respectively. The demonstration of electric field effects on deformation offer opportunities for deformation forming of nanocrystalline ceramics to reduce the temperatures required for densifying sub-100 nm grain sized ceramics.

References

1. T. G. Nieh and J. Wadsworth, "Superplastic Behavior of a Fine-Grained Yttria-Stabilized, Tetragonal Zirconia Polycrystal (Y-TZP)," *Acta Metall et Mater.*, **38**, 1121–1133 (1990).

2. H. Conrad and J. Narayan, "On the Grain Size Softening in Nanocrystalline Materials," *Script. Mater.*, **42**, 1025–30 (2000).

3. M. Yoshida, Y. Shinoda, T. Akatsu, and F. Wakai, "Deformation of Monoclinic ZrO_2 Polycrystals and Y_2O_3-Stabilized Tetragonal ZrO_2 Polycrystals below the Monoclinic-Tetragonal Transition Temperature," *J. Am. Ceram. Soc.*, **85**(11), 2834–36 (2002). Ibid, "Superplasticity-Like Deformation of Nanocrystalline Monoclinic Zirconia at Elevated Temperatures," *J. Am. Ceram. Soc.*, **87**(6), 1122–25 (2004).

4. H. Conrad, "Thermally Activated Plastic Flow of Metals and Ceramics with an Electric Field or Current," *Mater. Sci. Eng.* **A322**: 100-107 (2002).

5. I.-W. Chen and X.-H. Wang, "Sintering Dense Nanocrystalline Ceramics Without Final-Stage Grain Growth," *Nature*, **404**, 168–71 (2000).

6. H.-D. Kim, Y.-J. Park, B.-D. Han, M.-W. Park, W.-T. Bae, Y.-W. Kim, H.-T. Lin and P. F. Becher, *Scripta Mater*., **54**: 615-19 (2006).

7. H. Conrad, "Space Charge and the Dependence of the Flow Stress of Ceramics on an Applied Electric Field," *Scripta Mater*., **44**, 211–16 (2001).

8, X. Guo, J. Maier, "Grain Boundary Blocking in Zirconia: A Schottky Barrier Analysis," *J. Electrochem. Soc*. **148** (3) E121– E126 (2001).

9. K. L. Kliewer and J. S. Koehler, "Space Charge in Ionic Crystals. I. General Approach with Application to NaCl," *Phys. Rev. A*, **140** (4A), 1226–40 (1965).

10. M. F. Yan, R. M. Cannon, H. K. Bowen, and R. L. Coble, "Space-Charge Contribution to Grain-Boundary Diffusion," *J. Am. Ceram. Soc*., **60** (3–4),120–27(1977).

This document highlights work sponsored by agencies of the U.S. Government. Neither the U.S. Government nor any agency thereof, nor any of their employees, makes any warranty, express or implied, or assumes any legal liability or responsibility for the accuracy, completeness, or usefulness of any information, apparatus, product, or process disclosed, or represents that its use would not infringe privately owned rights. Reference herein to any specific commercial product, process, or service by trade name, trademark, manufacturer, or otherwise does not necessarily constitute or imply its endorsement, recommendation, or favoring by the U.S. Government or any agency thereof. The views and opinions of authors expressed herein do not necessarily state or reflect those of the U.S. Government or any agency thereof.

Printed on recycled paper

A Strong Energy Portfolio for a Strong America

Energy efficiency and clean, renewable energy will mean a stronger economy, a cleaner environment, and greater energy independence for America. Working with a wide array of state, community, industry, and university partners, the U.S. Department of Energy's Office of Energy Efficiency and Renewable Energy invests in a diverse portfolio of energy technologies.

For more information contact:
EERE Information Center
1-877-EERE-INF (1-877-337-3463)
www.eere.energy.gov